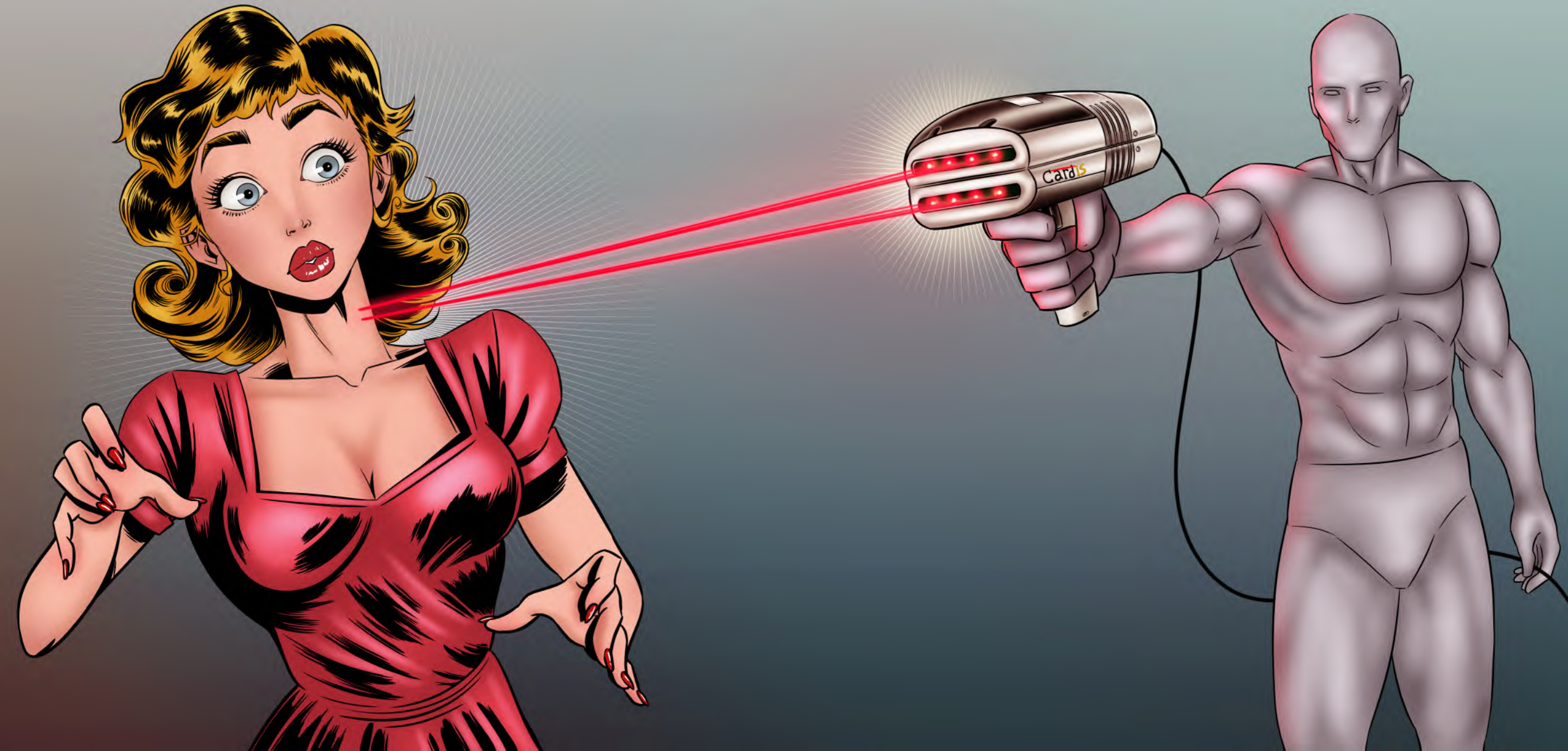
Cardis

FACULTY OF ENGINEERING AND ARCHITECTURE

Laser-Doppler Vibrometry as Non-Invasive Technique for the Real-Time Assessment of Cardiovascular Health

Simeon Beeckman

Doctoral dissertation submitted to obtain the academic degree of
Doctor of Biomedical Engineering

Supervisors

Prof. Patrick Segers, PhD - Prof. Nilesh Madhu, PhD

Department of Electronics and Information Systems
Faculty of Engineering and Architecture, Ghent University

GHENT UNIVERSITY

ISBN null
NUR 954
Wettelijk depot: null

Members of the Examination Board

Chair

Prof. Sabine Wittevrongel, PhD, Ghent University

Other members entitled to vote

Danilo Babin, PhD, Ghent University
Kasper Claes, PhD, imec
Prof. Yanlu Li, PhD, Ghent University
Prof. Jef Vandemeulebroucke, PhD, Vrije Universiteit Brussel

Supervisors

Prof. Patrick Segers, PhD, Ghent University
Prof. Nilesh Madhu, PhD, Ghent University

Man Is as Old as His Arteries

Thomas Sydenham (1624–1689)

PREFACE

TABLE OF CONTENTS

Preface iv

Table of contents iv

Abbreviations and symbols xi

Graphical Abstract xvii

Summary xxiv

Samenvatting xxx

1 Introduction 1
- 1.1 Background and clinical rationale . . . 1
- 1.2 Objectives . . . 3
- 1.3 Structure . . . 4
- 1.4 List of peer-reviewed publications . . . 5

I Clinical Rationale and State-of-the-Art in Pulse Wave Velocity Estimation 7

2 Clinical rationale 9
- 2.1 Physiology of the arterial system . . . 9
  - 2.1.1 The heart anatomy and function . . . 9
  - 2.1.2 Arterial function, anatomy and modelling . . . 12
    - 2.1.2.1 The windkessel model . . . 12
    - 2.1.2.2 Arterial wall composition . . . 15
    - 2.1.2.3 Compliance and distensibility for arterial stiffness assessment . . . 16
    - 2.1.2.4 Pulse wave propagation . . . 18
  - 2.1.3 Arterial stiffening and associated cardiovascular disease risk . . . 22

2.2 State-of-the-art in measuring arterial stiffness and its challenges . . . 25
2.2.1 Arterial tonometry . . . 25
2.2.2 MRI . . . 26
2.3 Laser Doppler vibrometry . . . 29
2.3.1 The InSiDe project and CARDIS device . . . 31
2.4 Biomedical signal processing . . . 33
2.4.1 The 1D biomedical digital signal . . . 33
2.4.2 Pattern recognition . . . 35
2.4.2.1 Matrix profile . . . 35
2.4.2.2 Template matching . . . 36
2.4.3 The stochastic nature of biomedical signals . . . 37
2.4.3.1 Beamforming . . . 38
2.4.3.2 Independent component analysis (ICA) . 40
2.4.4 Machine learning . . . 42
2.4.4.1 Supervised learning and logistic regression 42
2.4.4.2 Deep learning . . . 45

II Laser-Doppler Vibrometry Carotid-Femoral Signal-Quality Enhancement and Pulse Transit Time Estimation 51

3 Laser Doppler Vibrometry Signal Quality for Carotid-Femoral Pulse Wave Velocity 53
3.1 Introduction . . . 54
3.2 Methods . . . 56
3.3 Materials and methods . . . 56
3.3.1 The CARDIS device . . . 56
3.3.2 Study population and available database . . . 57
3.3.3 Visual scoring of the data . . . 58
3.3.4 Template matching . . . 58
3.3.4.1 Constructing the templates . . . 60
3.3.4.2 Template matching and beat selection . . 61
3.3.4.3 LDV traces classification based on template matching - finding threshold values 63
3.3.4.4 LDV traces classification based on template matching - defining quality score and testing on the CARDIS dataset . . . 65
3.3.4.5 A logistic regression model for signal classification based on template matching 66
3.3.5 Matrix profile . . . 67

3.3.5.1 Signal classification based on the matrix profile . . . 67
3.3.5.2 A logistic regression model based on the matrix profile . . . 69
3.3.6 Relation between signal quality and physiological variables . . . 69
3.4 Results . . . 69
3.4.1 Visual scoring . . . 69
3.4.1.1 Carotid-carotid measurements . . . 69
3.4.1.2 Carotid-femoral measurements . . . 70
3.4.2 Template matching . . . 70
3.4.2.1 Carotid-carotid (CC) measurements . . . 70
3.4.2.2 Carotid-femoral (CF) measurements . . . 73
3.4.3 Matrix profile . . . 74
3.4.3.1 Quality metric results . . . 74
3.4.3.2 Logistic regression models performance 74
3.4.4 Signal quality vs. physiological variables . . . 75
3.5 Discussion . . . 75
3.6 Conclusion . . . 80

4 Beamforming Laser Doppler Vibrometer Sensor Arrays 81
4.1 Introduction . . . 82
4.2 Materials & baseline method . . . 84
4.2.1 The CARDIS database . . . 84
4.2.2 Brute-force PTT estimation . . . 85
4.3 Beamforming for PTT estimation . . . 87
4.3.1 Signal model . . . 87
4.3.2 Time alignment of the $s_m(n)$ . . . 88
4.3.3 Compensating for α_m . . . 89
4.3.4 Estimating w_m and the enhanced signal $y(n)$ . . . 90
4.3.5 Beamformer-driven ICA . . . 92
4.4 Experimental results and discussion . . . 93
4.5 Conclusions . . . 97
4.6 Addendum . . . 97
4.6.1 Premise of the expanded analysis . . . 98
4.6.2 Expanded results and discussion . . . 98

5 Real-Time Pulse Wave Velocity Estimation 101
5.1 Introduction . . . 102
5.2 Materials and methods . . . 104
5.2.1 Dataset . . . 104
5.2.2 LDV device . . . 105

5.2.3 Automatic algorithm for PTT and PWV estimation 106
5.2.3.1 Identification of the fiducial points . . . 107
5.2.3.2 Automatic quality control 109
5.2.3.3 PTT estimation 111
5.2.4 Validation and Ablation Analysis 114
5.2.4.1 Validation of cfPWV estimation 114
5.2.4.2 Confidence level of the cfPWV estimation 114
5.2.4.3 Ablation analysis 115
5.3 Results 116
5.3.1 Validation of the algorithm 116
5.3.1.1 Validation of cfPWV estimation 116
5.3.2 Threshold tuning and ablation analysis 117
5.3.3 Beat-to-beat analysis 119
5.4 Discussion 120
5.5 Conclusion 122

III Investigating Heart-Carotid Pulse Transit Time for Arterial Stiffness Assessment 125

6 Heart-Carotid Pulse-Transit Time 127
6.1 Introduction 128
6.1.1 Carotid-femoral pulse-wave velocity 129
6.1.2 Heart-carotid pulse-wave velocity 129
6.2 Materials & methods 131
6.2.1 The LDV-prototype specifications 131
6.2.2 Study population and data collection 131
6.2.3 Analysis of heart-carotid LDV data 132
6.2.3.1 Data properties & preprocessing 132
6.2.3.2 Heart-carotid pulse-transit time calculation 133
6.2.3.3 Heart-carotid PTT with age and blood pressure 136
6.2.3.4 Intra- and inter-operator variability . . . 136
6.3 Results 137
6.3.1 Correlation with clinical parameters and sphygmocor cfPTT 137
6.3.2 Relation between hcPTT methods 138
6.3.3 Intra- and inter-operator variability 140
6.3.4 Sphygmocor cfPTT agreement with clinical parameters 142
6.4 Discussion 145
6.4.1 Feasibility of LDV-based hcPTT 145

6.4.2 hcPTT as biomarker of arterial stiffness? 146
6.4.3 LDV-based hcPTT compared to other techniques . 148
6.4.4 Study limitations 149
6.5 Conclusions 149

7 Deep-Learning Based ECG-free Heart-Carotid Pulse Transit Time Estimation 151
7.1 Introduction 152
7.1.1 Pulse transit time estimation 152
7.1.2 Automated PTT estimation 154
7.2 Methods 156
7.2.1 Applied principle for PTT calculation 156
7.2.2 Manual PTT estimate (reference method) 156
7.2.3 ECG-based automated PTT estimation 157
7.2.4 Template matching-based PTT estimation 158
7.2.5 Data-driven PTT approach 160
7.2.5.1 ECG-proxy as learning target 160
7.2.5.2 DNN structure and training 161
7.2.5.3 Application to PTT calculation 163
7.2.6 Experiment 166
7.3 Results 167
7.4 Discussion 169
7.4.1 DNN-model validation for heartbeat onset prediction 169
7.4.2 TM- vs DNN-based PTT estimation 171
7.4.3 Future applications 172
7.4.4 Remaining challenges 173
7.5 Conclusion 173

IV Conclusions 175

8 Conclusions and Perspectives 177
8.1 Signal quality 177
8.2 The potential of heart-carotid PWV 179
8.3 Deep learning application and findings 180
8.4 Alternative tools for arterial pulse detection 181
8.5 The InSiDe-alpha device 184
8.6 Final thoughts 184

V Appendices 187

A Appendix **189**

Acknowledgements **192**

Bibliography **193**

ABBREVIATIONS AND SYMBOLS

The following list summarizes the most commonly used abbreviations and symbols in this dissertation.

Abbreviations

1D	One-Dimensional
3D	Three-Dimensional
CVD	Cardiovascular Disease
LDV	Laser Doppler Vibrometry
SNR	Signal-to-Noise Ratio
ECG	Electrocardiography
PCG	Phonocardiography
SCG	Seismocardiography
PPG	Photoplethysmography
EEG	Electroencephalography
MRI	Magnetic Resonance Imaging
PC-MRI	Phase-Contrast Magnetic Resonance Imaging
DNN	Deep Neural Network
ICA	Independent Component Analysis
AI	Artificial Intelligence
ReLU	Rectified Linear Unit
ROC	Receiver Operating Characteristic
AUC	Area Under Curve
BMI	Body Mass Index
CC	Carotid-Carotid
CF	Carotid-Femoral
HP1	Handpiece One
HP2	Handpiece Two
CCT	Cross-Correlation Threshold
BQT	Beat-Quality Threshold
RQT	Recording-Quality Threshold
SD	Standard Deviation

DN	Dicrotic Notch
PAT	Pulse Arrival Time
Base	LDV probe positioned at the base of the heart
Apex	LDV probe positioned at the apex of the heart
MC	Mitral Valve Closure
IVC	Isovolumic Contraction
AO	Aortic Valve Opening
RE	Rapid Ventricular Ejection
AC	Aortic Valve Closure
MO	Mitral Valve Opening
RF	Rapid Ventricular Filling
S2	Second Heart Sound
DBP	Diastolic Blood Pressure
SBP	Systolic Blood Pressure
OP	Operator
CV	Coefficient of Variation
SE	Standard Error
US	Ultrasound
PEP	Pre-Ejection Period
TM	Template Matching
MSE	Mean Squared Error
MP	Matrix Profile

Symbols

dx	Distance between LDV measurement sites [m]
C_A	Area compliance [mm^2/mmHg]
∂A	Change in cross-sectional area [mm^2]
∂P	Change in intra-arterial pressure [N]
D_A	Distensibility [1/mmHg]
C	Capacitance [mL/mmHg]
T_{sys}	Duration of systole [s]
PP	Pulse pressure [mmHg]
SV	Stroke volume [mL]
TAC	Total arterial compliance [mL/mmHg]
$n_{p,i}$	Sample index of the i-th R-peak [/]
$\delta(n)$	Kronecker delta function [/]
$E'(n)$	Target signal derived from convolved ECG pulse train [a.u.]
$g(n)$	Gaussian filter function [/]
Q_R	R-peak score: ratio of correctly predicted R-peaks to total R-peaks [/]

$\hat{I}$	Number of correctly predicted R-peaks in the model output [/]
$A_{\min}$	Minimum amplitude threshold for peak detection [a.u.]
$\zeta_{m,i}$	Bounded SNR-based quality metric for peak i in channel m [/]
P_s^m	Signal power around a detected peak in channel m [a.u.]
P_v^m	Noise power around a detected peak in channel m [a.u.]
$Q_{vent}(t)$	Ventricular outflow rate [mL/s]
d_i^m	Distance between successive detected peaks in channel m [samples]
$\boldsymbol{\zeta}$	Vector of average SNR-based quality metrics for all channels [/]
ζ_m	Average SNR-based quality metric for channel m [/]
γ	Threshold factor for minimum number of valid PTT estimates [/]
N_S	Number of unique subjects with a final PTT estimate [/]
$P_d(t)$	Diastolic pressure decay [kg/m³]
τ	Windkessel model time constant [s]
PWV	Pulse wave velocity [m/s]
$cfPWV$	Carotid-femoral PWV [m/s]
$hcPWV$	Heart-carotid PWV [m/s]
PTT	Pulse transit time [s]
$cfPTT$	Carotid-femoral PTT [s]
$hcPTT$	Heart-carotid PTT [s]
V	Volume of accelerated blood [mL]
dP	Instantaneous applied pressure to a blood vessel [mmHg]
A	Cross-sectional surface area [mm^2]
h	Vessel wall thickness [mm]
r	internal vessel radius [mm]
ρ_b	Density of blood [g/mL]
E	Young's modulus of the vessel wall [Pa]
E_{inc}	Incremental Young's modulus [Pa]
f_D	Doppler frequency shift [Hz]
λ_0	Laser wavelength [nm]
$v(t)$	Vibrating target velocity [nm/s]
f_0	Laser frequency [Hz]
$Q(t)$	Quadrature-phase signal [a.u.]
$I(t)$	In-phase signal [a.u.]
f_s	Sampling frequency [Hz]
N	Signal length [samples]
m	Recurring pattern length [samples]
$s(n)$	Target (underlying) signal [a.u.]

$v(n)$	Noise component [a.u.]
$x(n)$	Observed signal [a.u.]
Q_{MP}	Matrix-profile based LDV signal-quality index [%]
Q_{TM}	Template-matching based LDV signal-quality index [%]
Q_{vis}	LDV signal visual score [/]
Q_1	First template matching signal quality feature
n_{peaks}	Number of detected skin acceleration peaks [/]
$\text{max}_{\text{peaks}}$	Maximum expected number of peaks or heartbeats [/]
Q_2	Second template matching signal quality feature [/]
d_{peak_n}	Time delay between the peak of each LDV-acceleration epoch and the peak of the template [ms]
A_s	Maximum amplitude of a subsequence [a.u.]
A_{MP}	Average relative maximum amplitude of a subsequence in a matrix-profile motif [a.u.]
A_{ref}	Maximum amplitude of the reference subsequence [a.u.]
$t_{\text{d,MP}}$	Average relative time-instant of the subsequence peaks in the motif [ms]
n_{MP}	Matrix-profile based subsequence-number signal quality feature [/]
n_{exp}	Expected number of subsequences in the motif [/]
n_{mtf}	Effective number of subsequences in the motif [/]
α_m	Channel-dependent scale factor [/]
τ_m	Channel-dependent time delay [/]
$\widetilde{j}$	Segment index
$\widetilde{k}$	Sub-segment index [/]
m_{ref}	Reference channel index [/]
$\widetilde{J}$	Total number of overlapping segments [/]
$\widetilde{K}$	Total number of sub-segments [/]
$\widetilde{N}$	Segment length [samples]
$\tilde{x}(n)$	Aligned and compensated signal [a.u.]
$\widetilde{\mathbf{x}}(n)$	Vector of compensated signals [a.u.]
$\widetilde{\mathbf{v}}(n)$	Vector of aligned noise [a.u.]
$h_m(n)$	Delay filter for channel m [/]
α_m	Scale factor for channel m [/]
$\widehat{\alpha}_m$	Estimated scale factor [/]
τ_m	Time delay for channel m [samples]
T_m	Delay to be applied for alignment [samples]
w_m	Weighting factor for channel m [/]
$\mathbf{1}$	All-ones vector [/]
$\mathbf{w}$	Weight vector [/]
$E_{m,j}$	Energy of segment j in channel m [a.u.]
$E_{m_{\text{ref}},j}$	Energy in reference channel segment j [a.u.]

$E_{m,\widetilde{j},\widetilde{k}}$	Energy in sub-segment $\widetilde{k}$ of segment $\widetilde{j}$ in channel m [a.u.]
$y(n)$	Enhanced output signal [a.u.]
ρ	Pearson cross-correlation coefficient [/]
K	Tuning factor for threshold sensitivity [/]
PTT_{hbeat}	Median PTT value for a single heartbeat [ms]
PTT_{mean_mean}	Mean of means of PTT values across all heartbeats [ms]
PTT_{mean_median}	Mean of medians of PTT values across all heartbeats [ms]
PTT_{median_median}	Median of medians of PTT values across all heartbeats [ms]
k_i	Number of cf-peak pairs in the i-th heartbeat [/]
PTT_1	hcPTT calculated using the first heartsound and carotid foot [ms]
PTT_2	hcPTT calculated using the second heartsound and carotid dicrotic notch [ms]
$\mathrm{ECG}(n)$	ECG signal at sample n [a.u.]
I	Number of R-peaks (heartbeats) in ECG [/]
J	Number of valid PTT estimates [/]
PTT_j	PTT estimate for the j-th beat [ms]
$\boldsymbol{PTT}$	Vector of all valid PTT estimates [ms]
$P_{x,m}$	Power of the observed signal at channel m [a.u.]
$P_{v,m}$	Power of the noise at channel m [a.u.]
SNR_m	Signal-to-noise ratio at channel m [/]
PTT_m	Pulse transit time for channel m [ms]
$\hat{E}'(n)$	DNN output signal for a 4-second LDV segment [a.u.]
$\hat{E}'_m(n)$	Reconstructed DNN output for carotid channel m [a.u.]
$\mathrm{ECG}'(n)$	Pulse train of Kronecker delta functions at R-peak locations [/]

GRAPHICAL ABSTRACT

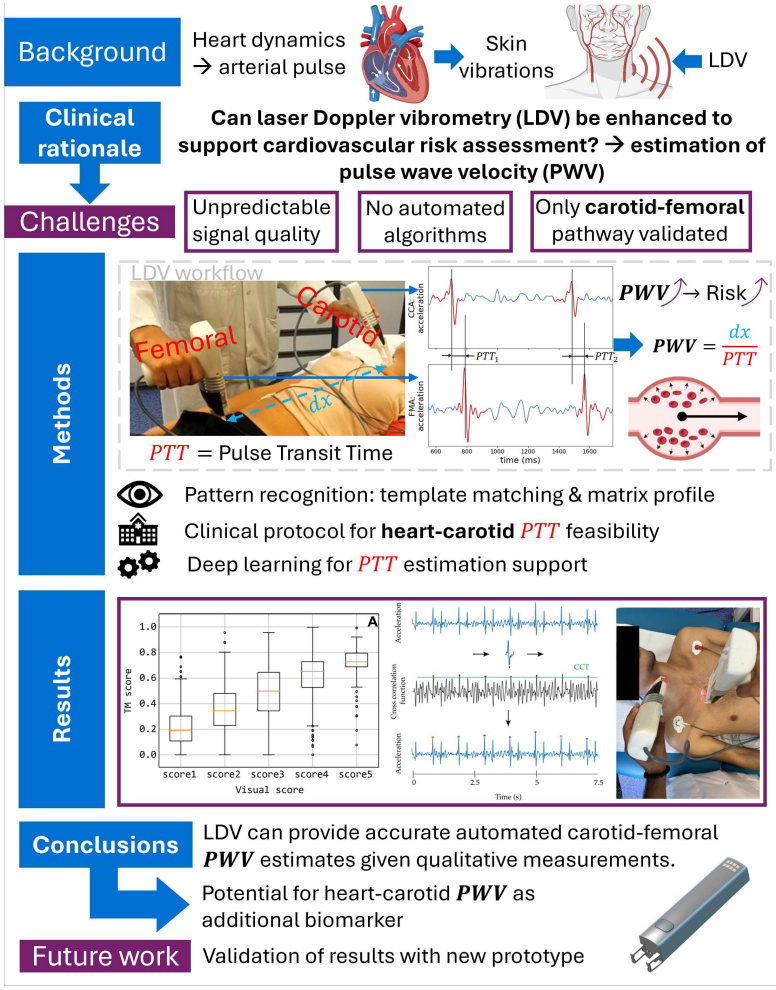

Figure 1: Graphical abstract.

SUMMARY

SHORT ABSTRACT

BACKGROUND: Cardiovascular disease (CVD) is the leading cause of death in economically developed countries, of which a significant subset is untimely. Additionally, the socio-economic impact of non-fatal cardiovascular events such as stroke or myocardial infarction, highlights the need for accessible screening tools. Existing technologies are often costly, require operator expertise, and are confined to dedicated medical facilities. The InSiDe-project aims to introduce a novel, user-friendly cardiovascular screening technique using laser Doppler vibrometry (LDV), which measures skin displacement caused by cardiac pulses. By assessing pulse transit time (PTT) between the carotid and femoral artery measurement sites, the system estimates pulse wave velocity (PWV) – a key biomarker of arterial stiffness and CVD risk. This thesis explores the potential applications of LDV in enhancing arterial stiffness assessment.

PART II: LDV enables a fast and non-invasive (potentially even non-contact) acquisition of cardiovascular signals but suffers from the complexity and interpretability of the measured signals and inconsistent signal quality, both across and within subjects. To address this, a real-time signal-quality metric was developed using features of recurring heartbeat related patterns, exploring two distinct signal pattern detection techniques: matrix profile and template matching. This can guide operators during measurements to improve overall signal quality. Algorithms were then created to compute PTT using these patterns. It was found that both methods allowed for reliable pattern detection leading to indicative quality metrics.

Besides detecting patterns, we also explored a method to enhance the quality of the signals to process. Using 'beamforming', we exploited the availability of multiple LDV-channels (6 signals per handpiece/measurement site) to enhance signal quality. Signals were time-aligned and combined using weights based on signal-to-noise ratios. It was found that analysis based on beamformed signals yielded a more robust PTT estimate than benchmark methods.

PART III: While carotid-femoral PWV is a clinically feasible and well-accepted standard method to assess arterial stiffness, it cannot measure the stiffness of the most compliant segment of the aorta. Therefore, we explored an alternative PWV-pathway from the heart to the carotid artery, which includes the ascending aorta. A feasibility study assessed four ways to estimate heart-carotid PTT using two measuring positions on the heart and two different features on the signals measured on the heart and carotid artery, associated with opening and closure of the aortic valve. The most effective method used the second heart sound (aortic valve closure) and carotid dicrotic notch, with the LDV probe aimed at the base of the heart where the most consistent signals could be recorded.

During the development phase, we always co-registered the ECG signal to support signal processing and to provide a reference indication of the onset of cardiac contraction. Future LDV technology, however, should not include ECG. We therefore developed a deep neural network (DNN) to infer heartbeat timings from carotid LDV signals alone. This enabled ECG-free segmentation of heartbeats and automated heart-carotid PTT calculation with a stronger agreement to ground-truth.

CONCLUSION: This work presents algorithmic enhancements to an LDV prototype for improved cardiovascular assessment. Real-time signal quality metrics and beamforming techniques support carotid-femoral PTT estimation, while a deep learning model enables ECG-free heart-carotid PTT measurement. The heart-carotid pathway shows potential as a complementary biomarker to carotid-femoral PWV. Despite promising results, broader clinical adoption requires improved hardware and signal stability to overcome current limitations.

LONG ABSTRACT

BACKGROUND

Cardiovascular disease (CVD) is responsible for about one-third of all deaths in economically developed countries, with many considered untimely. Non-fatal events like stroke, heart attacks, and heart failure also have major personal and societal consequences. To assess CVD risk, especially in people with hypertension, clinicians often use the SCORE2 and SCORE2-OP models. These tools estimate the 10-year risk of fatal and non-fatal cardiovascular events in individuals aged 40 and older. The 2024 European Society of Cardiology guidelines recommend using additional risk assessment tools for people under 40 with risk factors like high blood pressure, smoking, or obesity. These tools are also useful for those with borderline clinical indicators. Supplementary diagnostics

such as ECG, vascular ultrasound, and arterial stiffness measurements are advised in these cases.

Arterial stiffness, which increases with age, is a strong predictor of cardiovascular disorders. It is commonly measured using pulse wave velocity (PWV), which reflects how fast a pulse wave travels through the arteries. PWV is typically derived from the pulse transit time (PTT), defined as the temporal delay between the arrival of the pulse wave at two anatomically distinct measurement sites, divided by the distance separating these sites. Higher PWV indicates stiffer arteries and greater cardiovascular risk. Traditional PWV measurement methods like MRI, ultrasound, and applanation tonometry are often expensive, require expert operators, and are typically limited to specialized medical facilities. These limitations have driven interest in alternative approaches to assess PWV.

One promising method is laser Doppler vibrometry (LDV), which uses laser light to infer vibrations – originating from cardiac contraction and the propagating pulse – on the skin surface with minimal contact. When applied to the neck and groin simultaneously, LDV can measure carotid-femoral PWV. This technique has been developed and tested in EU-funded projects (CARDIS and InSiDe), resulting in a working prototype used in two clinical studies (named CARDIS and InSiDe) and each involving 100 patients. To support the development of the device, parallel development of algorithms to extract clinically relevant information from LDV measurements was necessary.

The PhD pursued three primary objectives. First, it aimed to develop a real-time signal quality index to enhance the reliability and efficiency of pulse wave velocity (PWV) measurements by enabling the identification of high-quality signal segments during acquisition. Second, a pseudo real-time algorithm for estimating carotid-femoral PWV was to be implemented, allowing for near-instantaneous analysis and feedback suitable for clinical settings. Third, the feasibility of heart-carotid PWV as an alternative biomarker for arterial stiffness was investigated, with the goal of expanding the diagnostic toolkit for vascular health assessment.

PART II: Laser-Doppler vibrometry carotid-femoral signal-quality enhancement and pulse transit time estimation

LDV offers a non-invasive and relatively rapid method for assessing arterial stiffness, but its effectiveness can be limited by variable signal quality. This variability is observed both across subjects, within a subject over the duration of the measurement and over the six sensors within a single LDV handpiece. To address this, a real-time signal quality metric was developed, designed to enhance measurement reliability by guiding the operator during

acquisition. The metric was based on features extracted from automatically detected recurring patterns in the LDV signals, presumed to correspond to heartbeat-induced perturbations. Two algorithms – matrix profile analysis and template matching – were employed for pattern detection. This quality metric was integrated into the measurement interface to provide real-time feedback.

Building upon insights gained from the signal quality analysis, dedicated algorithms were developed for PTT estimation, utilizing the previously identified waveform patterns to enable robust and automated feature extraction. The resulting algorithm, termed CAPE (Continuous Automatic PWV Estimation), employs template matching for the automated selection of fiducial points and facilitates beat-to-beat analysis of LDV signals in near real-time. CAPE was evaluated using a multichannel LDV database comprising 100 patients (CARDIS: 50 male, 50 female). By incorporating real-time signal quality control, the framework selectively analyzed high-quality data segments. In the subset of patients meeting these quality criteria, CAPE demonstrated strong concordance with reference measurements obtained via applanation tonometry, confirming its potential for reliable and efficient carotid-femoral PWV estimation in clinical settings.

To further improve signal fidelity, a beamforming approach was introduced, exploiting the multidimensional nature of the LDV data. This method aligned the six sensor signals in time and combined them into a single trace with enhanced signal-to-noise ratio (SNR), using a segment-wise weighted sum based on blind SNR estimation. Template matching performed on the resulting beamformed signals yielded more robust PTT estimates compared to conventional methods. This was tested on a high-quality subset of the CARDIS database.

PART III: Investigating heart-carotid pulse transit time for arterial stiffness assessment

Although carotid-femoral PWV remains the clinical reference standard due to its extensive validation, alternative measurement pathways may provide complementary insights into arterial stiffness, particularly in vascular regions not encompassed by the standard route. One such alternative is the heart-carotid pathway, which includes the proximal ascending aorta, contributing most to the buffering capacity of the aorta due to its high compliance. A feasibility study was conducted using LDV data from the INSIDE clinical trial, comprising 100 participants (55 male, 45 female), to evaluate the potential of this pathway. The study investigated two heart measurement sites – specifically, LDV probe placement at the right second intercostal space (close to the base of the heart) and the fifth left intercostal

space (close to the apex of the heart) – in combination with two heart-carotid fiducial point combinations for PTT estimation: (i) the first heart sound paired with the foot of the carotid pulse wave, and (ii) the second heart sound paired with the carotid dicrotic notch. This resulted in four heart-carotid PTT estimation strategies. The derived PTT values were analyzed for correlation with established markers of arterial stiffness, including age and systolic blood pressure. The most robust method, demonstrating the highest statistically significant correlations and the lowest inter- and intra-operator variability, involved targeting the base of the heart and using the second heart sound in conjunction with the carotid dicrotic notch for PTT calculation.

During the development phase, ECG was measured in parallel with LDV as support for algorithmic validation. As future LDV systems are not expected to incorporate electrocardiography (ECG) functionality, an alternative approach was required to enable automated segmentation of cardiac cycles for heart-carotid PTT estimation. To address this, a deep neural network (DNN) architecture was developed and trained on carotid LDV signals to predict the onset of cardiac cycles, thereby enabling ECG-independent heartbeat segmentation. During training, the target output was not the raw ECG signal but a simplified proxy signal encoding only the relevant temporal markers for heartbeat onset detection. This abstraction facilitated effective learning of the underlying cardiac rhythm from LDV data alone. The resulting DNN-based method enabled fully automated heart-carotid PTT estimation, demonstrating strong correlation with reference values obtained in the heart-carotid feasibility study. Notably, this approach proved more inclusive than traditional template-matching techniques, yielding valid PTT estimates for a significantly larger proportion of the patient cohort.

CONCLUSION

This work introduced several algorithmic advancements to enhance the performance of an existing LDV prototype. Real-time signal quality metrics support optimal device positioning, while beamforming improves the robustness of PTT estimation. The heart-carotid pathway was validated as a potential complementary biomarker to carotid-femoral PWV. Finally, a deep learning-based method was developed to enable automated, ECG-free heart-carotid PTT estimation, with the potential to broaden the applicability of the methodology to scenarios involving sparse physiological signals.

LDV has demonstrated its potential for accurate arterial stiffness assessment in patients exhibiting high SNR measurements. However, despite the integration of a real-time signal quality index, the technique remains susceptible to signal degradation, which can limit applicability across broader

patient populations. To position LDV as a competitive alternative to current state-of-the-art arterial stiffness assessment technologies, further advancements in hardware design and signal acquisition stability are essential.

SAMENVATTING

KORTE SAMENVATTING

ACHTERGROND: Cardiovasculaire aandoeningen vormen de belangrijkste doodsoorzaak in economisch ontwikkelde landen, waarvan een aanzienlijk deel als voortijdig overlijden wordt beschouwd. De socio-economische gevolgen van niet-fatale cardiovasculaire gebeurtenissen, zoals beroertes en hartinfarcten, zijn bijzonder groot en hadden mogelijk kunnen worden vermeden mits toegankelijke screeningsmethoden. Bestaande technologieën voor screening zijn vaak duur, vereisen gespecialiseerde vaardigheden van de gebruiker en worden enkel gehanteerd in gespecialiseerde medische centra. Het InSiDe-project beoogt een innovatieve, gebruiksvriendelijke screeningstechniek te introduceren op basis van laser-Doppler vibrometrie (LDV). LDV laat toe om kleine huidverplaatsingen, veroorzaakt door het kloppende hart en de arteriële puls in slagaders, op te meten. Door de pulstransittijd (PTT) tussen de meetlocaties op de *arteria carotis* (hals) en *arteria femoralis* (lies) te bepalen, kan het systeem de polsgolfsnelheid (PWV) schatten, die een belangrijke biomarker voor arteriële stijfheid en cardiovasculair risico is.

DEEL II: LDV laat toe om op een snelle en niet-invasieve manier cardiovasculaire signalen te registreren, maar wordt beperkt door de complexiteit en moeilijke interpretatie van de gemeten signalen alsook door een inconsistente signaalkwaliteit, wat leidt tot een grote variabiliteit van signalen en signaalkwaliteit zowel tussen als binnen proefpersonen. Om dit probleem aan te pakken werd een realtime signaalkwaliteitsindex ontwikkeld, gebaseerd op kenmerken van terugkerende hartslaggerelateerde patronen in het signaal. We onderzochten hierbij twee verschillende patroonherkenningstechnieken: matrixprofielanalyse en template matching. Deze kwaliteitsindex helpt de operator tijdens de meting om de algehele signaalkwaliteit te verbeteren. Vervolgens werden algoritmen ontwikkeld om PTT te berekenen op basis van deze herkende patronen. Beide methoden bleken betrouwbare patroonherkenning mogelijk te maken, wat leidde tot kwaliteitsmetingen die indicatief waren voor het kwaliteitsniveau van inkomende meetdata.

Naast patroonherkenning werd ook onderzocht hoe de signaalkwaliteit zelf verbeterd kon worden (na de metingen), waarbij gebruik kan worden gemaakt van het gegeven dat op één enkele meetlocatie 6 parallelle kanalen worden geregistreerd. Met behulp van '*beamforming*' kunnen deze kanalen in de tijd worden uitgelijnd en gecombineerd via gewichten gebaseerd op signaal-ruisverhoudingen, om tot één samengesteld en kwalitatiever signaal te komen. Analyse op basis van deze *beamformed* signalen leverde robuustere PTT-schattingen op dan de betrokken referentiemethoden.

DEEL III: Hoewel hals-lies PWV momenteel een klinisch haalbare en goed geaccepteerde standaard is voor het beoordelen van arteriële stijfheid, kan deze methode geen inzicht verschaffen in de eigenschappen van de meest elastische segmenten van de aorta. Daarom werd een alternatieve PWV-route onderzocht, rechtstreeks van het hart naar de halsslagader, die wél het meest elastische segment (de opstijgende aorta) omvat. In een haalbaarheidsstudie werden vier methoden voor het schatten van de hart-hals PTT geëvalueerd, gebaseerd op twee meetposities op het hart en twee verschillende signaalkenmerken gemeten ter hoogte van het hart en de halsslagader. Deze twee kenmerken waren gerelateerd aan het openen en sluiten van de aortaklep. De methode waarbij gebruik werd gemaakt van het tweede hartgeluid (sluiting van de aortaklep) en de dicrotische notch in het carotissignaal, met de LDV-sonde gericht op de basis van het hart, bleek meest effectief met de meest consistente signalen.

Tijdens de ontwikkelingsfase werd het electrocardiografie-signaal (ECG) steeds mee geregistreerd ter ondersteuning van de signaalverwerking en als referentie voor het identificeren van het begin van de hartcontractie. Aangezien toekomstige LDV-systemen geen ECG-functionaliteit zullen bevatten, werd een diep neuraal netwerk (DNN) ontwikkeld om het begin van de hartcontractie rechtstreeks uit de carotis-LDV-signalen af te leiden. Op die manier kunnen LDV-signalen eenduidiger worden gesegmenteerd, onafhankelijk van het ECG, wat beter toelaat om hart-hals PTT op een geautomatiseerde manier te berekenen, met een sterke overeenkomst met manueel bepaalde referentiewaarden.

CONCLUSIE: Dit doctoraatsonderzoek leverde meerdere verbeteringen op voor LDV-gebaseerde metingen van arteriële stijfheid en verhoogt het potentieel voor klinische toepassing van LDV in cardiovasculaire opvolging.

LANGE SAMENVATTING

ACHTERGROND

Cardiovasculaire aandoeningen (CVD) zijn verantwoordelijk voor ongeveer een derde van alle sterfgevallen in economisch ontwikkelde

landen, waarvan een aanzienlijk deel als voortijdig overlijden wordt beschouwd. Niet fatale gebeurtenissen zoals beroertes, hartinfarcten en hartfalen hebben eveneens ingrijpende persoonlijke en maatschappelijke gevolgen. Om het risico op CVD te beoordelen, vooral bij personen met hypertensie, maken artsen vaak gebruik van de SCORE2- en SCORE2-OP modellen. Deze modellen laten toe om het 10-jaarsrisico op zowel fatale als niet fatale cardiovasculaire gebeurtenissen te schatten bij personen van 40 jaar en ouder. Voor personen jonger dan 40 jaar met risicofactoren zoals hoge bloeddruk, roken of obesitas heeft de *European Society of Cardiology* in 2024 een nieuwe richtlijn opgesteld, waarbij ze aanbeveelt om aanvullende risicobeoordelingsinstrumenten te gebruiken om het CVD risico correcter te kunnen inschatten. Deze instrumenten zijn ook nuttig voor patiënten met klinische grenswaarden voor bijvoorbeeld de bloeddruk. In dergelijke gevallen worden aanvullende diagnostische technieken zoals ECG, vasculaire echografie en metingen van arteriële stijfheid aanbevolen.

Arteriële stijfheid, die toeneemt met de leeftijd, is een sterke voorspeller van cardiovasculaire aandoeningen. Arteriële stijfheid wordt doorgaans onrechtstreeks gemeten via de polsgolfsnelheid (PWV), die de snelheid weergeeft waarmee een drukgolf zich door de slagaders voortplant. PWV wordt meestal afgeleid uit de pulstransittijd (PTT), gedefinieerd als de tijdsvertraging tussen de aankomst van de puls op twee anatomisch verschillende meetlocaties, gedeeld door de afstand tussen deze locaties. Een hogere PWV duidt op stijvere slagaders en een verhoogd risico op cardiovasculaire aandoeningen. Traditionele methoden om PWV te meten zoals MRI, echografie en applanatietonometrie zijn vaak duur, vereisen gespecialiseerde vaardigheden van de gebruiker en zijn doorgaans beperkt tot gespecialiseerde medische centra. Deze beperkingen hebben geleid tot een toenemende interesse in alternatieve methoden voor het meten van PWV.

Een veelbelovende methode is laser-Doppler vibrometrie (LDV), waarbij laserlicht wordt gebruikt om trillingen op het huidoppervlak, veroorzaakt door het samentrekken van het hart en de propagerende arteriële puls, met minimale contactbelasting te detecteren. Wanneer LDV gelijktijdig wordt toegepast op de hals en lies, kan de carotis-femorale PWV worden gemeten. Deze techniek werd ontwikkeld en getest in twee aansluitende door de EU gefinancierde projecten (CARDIS en InSiDe), wat resulteerde in een werkend LDV-prototype dat werd ingezet in twee klinische studies (verder CARDIS en InSiDe genoemd) met in totaal elk 100 patiënten. Ter ondersteuning van de ontwikkeling van het apparaat was parallelle ontwikkeling van algoritmen nodig om klinisch relevante informatie uit LDV-metingen te extraheren.

Het doctoraatsonderzoek, uitgevoerd binnen de context van het InSiDe project, had drie hoofddoelstellingen. Ten eerste werd beoogd een realtime signaalkwaliteitsindex te ontwikkelen om de betrouwbaarheid en efficiëntie van PWV-metingen te verbeteren door het identificeren van hoogwaardige signaalsegmenten tijdens de meting. Ten tweede was het de doelstelling om een pseudo realtime algoritme te implementeren voor het schatten van de hals-lies PWV, met als doel onmiddellijke analyse en feedback mogelijk te maken in een klinische context. Ten derde werd de haalbaarheid onderzocht van hart-hals PWV als alternatieve biomarker voor arteriële stijfheid, met als doel het uitbreiden van het diagnostisch arsenaal voor de beoordeling van vasculaire gezondheid.

DEEL II: Verbetering van signaalkwaliteit en schatting van pulstransittijd met Laser-Doppler Vibrometrie voor de carotis-femorale route

Laser-Doppler Vibrometrie (LDV) biedt een niet invasieve en relatief snelle methode voor het beoordelen van arteriële stijfheid, maar de effectiviteit ervan wordt beperkt door een sterk variabele signaalkwaliteit. Deze variabiliteit doet zich zowel voor tussen verschillende proefpersonen, binnen de meting van één proefpersoon en tussen de zes verschillende sensoren binnen één enkele LDV-meetkop. Om dit probleem aan te pakken, werd een realtime signaalkwaliteitsindex ontwikkeld die de betrouwbaarheid van de metingen verhoogt door de operator tijdens de meting te begeleiden. Deze index is gebaseerd op kenmerken die worden geëxtraheerd uit automatisch gedetecteerde terugkerende patronen in de LDV-signalen, waarvan wordt aangenomen dat ze overeenkomen met hartslaggerelateerde verstoringen. Twee algoritmen, matrixprofielanalyse en template matching, werden toegepast voor patroonherkenning. De kwaliteitsindex werd geïntegreerd in de meetinterface om realtime feedback te bieden.

Vervolgens werden specifieke algoritmen ontwikkeld voor de schatting van de pulstransittijd (PTT), waarbij de eerder geïdentificeerde golfvormpatronen werden benut voor een robuuste en geautomatiseerde extractie van kenmerkende punten op de gemeten golfvormen. Het resulterende algoritme, CAPE (Continuous Automatic PWV Estimation), maakt gebruik van template matching voor de automatische selectie van kenmerkpunten en maakt beat-to-beat analyse van LDV-signalen in quasi realtime mogelijk. CAPE werd geëvalueerd op basis van de CARDIS LDV-databank (50 mannen, 50 vrouwen). Integratie van realtime signaalkwaliteitscontrole laat toe om een meer selectieve analyse uit te voeren, op basis van hoogwaardige signaalsegmenten. Binnen de subset van patiënten die aan minimale kwaliteitscriteria voldeden, toonde CAPE een sterke overeenkomst

met referentiemetingen verkregen via applanatie tonometrie, wat de betrouwbaarheid en klinische toepasbaarheid van het systeem bevestigt voor het schatten van hals-lies PWV.

Om de signaalintegriteit verder te verbeteren, werd een '*beamforming*' benadering geïntroduceerd die de beschikbaarheid van data gemeten langsheen 6 parallelle kanalen optimaal benut. Deze methode synchroniseert de zes sensorkanalen in de tijd en combineert ze tot één verbeterd signaal met een verhoogde signaal-ruisverhouding (SNR), via een segmentgewogen som gebaseerd op blinde SNR-schatting. Template matching toegepast op deze *beamformed* signalen resulteerde in robuustere PTT-schattingen dan conventionele methoden. Deze aanpak werd gevalideerd op een subset van hoge kwaliteit binnen de CARDIS-database.

DEEL III: Onderzoek naar hart-carotis pulstransittijd voor de beoordeling van arteriële stijfheid

Hoewel hals-lies PWV de klinische referentiestandaard blijft vanwege de uitgebreide validatie, kunnen alternatieve meetposities aanvullende inzichten bieden in arteriële stijfheid, met name in vaatsegmenten die buiten het bereik van de standaardmethode vallen, zoals het meest elastische deel van de aorta. Een van deze alternatieven is de hart-hals route, die *wel* de proximale opstijgende aorta omvat. Dit deel van de aorta draagt het meest bij aan de bufferfunctie van de gehele slagader vanwege haar hoge compliantie. In het kader van een haalbaarheidsstudie werd hart-hals PWV geëvalueerd aan de hand van LDV-data uit de InSiDe klinische studie, bestaande uit 100 deelnemers (55 mannen, 45 vrouwen). Er werden hierbij twee meetlocaties op het hart onderzocht, namelijk plaatsing van de LDV-sonde op de tweede intercostale ruimte rechts (dicht bij de hartbasis) en de vijfde intercostale ruimte links (dicht bij de apex van het hart). Deze twee locaties werden elk gecombineerd met twee combinaties van fiduciale punten voor PTT-bepaling: (i) het eerste hartgeluid gecombineerd met het begin van de carotispuls, en (ii) het tweede hartgeluid gecombineerd met de dicrotische notch in het carotissignaal. Dit resulteerde in vier strategieën voor het schatten van de hart-hals PTT. De verkregen PTT-waarden werden geanalyseerd op correlatie met bekende determinanten van arteriële stijfheid, waaronder leeftijd en systolische bloeddruk. De meest robuuste methode, met de hoogste statistisch significante correlaties en de laagste inter- en intra-operatorvariabiliteit, betrof de meting aan de basis van het hart en gebruik van het tweede hartgeluid in combinatie met de dicrotische notch.

In de haalbaarheidsstudie werd het electrocardiogram (ECG) mee opgemeten als referentie voor het identificeren van de start van de

hartcontractie. Aangezien toekomstige LDV-systemen naar verwachting geen ECG zullen bevatten, was een alternatieve aanpak nodig om automatische segmentatie van hartcycli voor hart-hals PTT mogelijk te maken. Hiervoor werd een diep neuraal netwerk (DNN) ontwikkeld en getraind op carotis-LDV-signalen om het begin van hartcycli te voorspellen, waardoor ECG-onafhankelijke segmentatie van hartslagen mogelijk werd. Tijdens de training werd niet het ruwe ECG-signaal gebruikt als doeluitvoer, maar een vereenvoudigd proxiesignaal dat enkel de relevante temporele markers voor het detecteren van de start van de hartcontractie bevatte. Deze abstractie maakte effectieve training mogelijk op basis van LDV-data alleen. De resulterende DNN-gebaseerde methode maakte volledig geautomatiseerde hart-hals PTT-bepaling mogelijk, met een sterke correlatie met de referentiewaarden uit de haalbaarheidsstudie. Opmerkelijk is dat deze aanpak inclusiever bleek dan traditionele template-matching technieken, doordat ze bij een aanzienlijk groter deel van de patiëntengroep geldige PTT-schattingen opleverde.

CONCLUSIE

Dit werk introduceerde verschillende algoritmische verbeteringen om de prestaties van een bestaand LDV-prototype voor het meten van arteriële stijfheid te optimaliseren. Realtime signaalkwaliteitsmetingen ondersteunen een optimale positionering van het apparaat, terwijl beamforming de robuustheid van de PTT-schatting verhoogt. De hart-hals route werd gevalideerd als een potentiële aanvullende biomarker naast de hals-lies PWV. Ten slotte werd een op *deep learning* gebaseerde methode ontwikkeld om geautomatiseerde, ECG-vrije hart-hals PTT-schatting mogelijk te maken, met het potentieel om de methode uit te breiden naar alternatieve klinische toepassingen van LDV.

LDV heeft zijn potentieel aangetoond voor nauwkeurige beoordeling van arteriële stijfheid bij patiënten met metingen met een hoge signaal-ruisverhouding. Desondanks blijft de techniek, zelfs met de integratie van een realtime signaalkwaliteitsindex, gevoelig voor signaaldegradatie, wat de toepasbaarheid bij een bredere populatie kan beperken. Om LDV te positioneren als een volwaardig alternatief voor de huidige geavanceerde technologieën voor het meten van arteriële stijfheid, zijn verdere verbeteringen in hardwareontwerp en stabiliteit van signaalacquisitie essentieel.

CHAPTER 1

INTRODUCTION

1.1 BACKGROUND AND CLINICAL RATIONALE

Cardiovascular disease (CVD) accounts for approximately one-third of all deaths in Western countries, of which a subset is generally considered to be premature [1, 2]. Also non-fatal cardiovascular events, such as such as stroke, myocardial infarction and heart failure, have significant individual and societal impact and come with a high socio-economic cost [3, 4].

To evaluate an individual's risk of developing CVD, particularly among patients with hypertension, clinicians commonly employ the SCORE2 and SCORE2-OP (Older Persons) risk stratification models [5, 6]. These tools estimate the 10-year probability of both fatal and non-fatal cardiovascular events, incorporating various biophysical parameters, and are validated for use in individuals aged 40 years and older.

According to the 2024 guidelines from the European Society of Cardiology on hypertension management, additional risk assessment tools should be considered for individuals who fall outside the SCORE2/SCORE2-OP eligibility criteria, such as those under 40 years of age with elevated blood pressure, smoking habits, or obesity [2]. Early risk evaluation in these populations aims to support timely preventive interventions. This recommendation also extends to patients with borderline clinical indicators, such as blood pressure readings near diagnostic thresholds or intermediate SCORE2/SCORE2-OP risk estimates (5–10%). In such cases, supplementary diagnostic modalities are advised to enhance

cardiovascular risk profiling and guide clinical decision-making. These modalities include electrocardiography (ECG), vascular ultrasound and arterial stiffness measurements.

Arterial stiffness is a biomarker that is a known predictor of cardiovascular complications and increases with chronological age [7–10]. The metric most commonly used to assess arterial stiffness is pulse wave velocity (PWV) [11]. It is measured as $PWV = dx/PTT$ from a pulse transit time (PTT), the time delay between the arrival of a pulse wave at two different points on the arterial tree, and the distance dx between those two points. PWV quantifies the speed with which a pulse wave, generated by the contracting heart, travels through the arteries. It increases for increasingly stiff arteries. Particularly the large arteries and their characteristic elastic behaviour is indicative of vascular age, as it deteriorates with increasing indicators of cardiovascular disease risk [12–14].

A plethora of technologies and their derived devices to measure PWV exist already, such as magnetic resonance imaging [15], ultrasound [16] or applanation tonometry [17], to name the most prominent. However, these methods suffer from some common drawbacks, namely that they are typically expensive due to the required high-end equipment, expert staff and/or time-consuming nature of the technique, resulting in them being used in dedicated medical facilities only. Another challenge is the required operator expertise of the state-of-the-art. Further issues such as patient comfort could additionally be an incentive for the search for alternative methods.

One such novel alternative is the application of laser Doppler vibrometry (LDV) to assess arterial stiffness [18, 19]. LDV measures the displacement of a vibrating surface over time using laser light, with high temporal and spatial resolution [20–22]. LDV can also detect skin vibrations that have been induced by underlying cardiac contractions and propagation of the arterial pulse over the arterial tree, generating mechanical waves that propagate to the skin. When simultaneously applied to the neck and groin of a patient, it can measure the time of pulse wave arrival in the carotid and femoral artery respectively, leading to carotid-femoral PWV [23].

Within 2 successively EU-funded projects, CARDIS (H2020, Grant agreement ID: 644798, 2015 to 2019, doi: 10.3030/644798) and InSiDe (H2020, Grant agreement ID: 871547, 2020 to 2024, doi: 10.3030/871547), a consortium led by Medtronic and imec developed multi-beam LDV prototypes aimed to measure arterial stiffness. At the start of this PhD, a working LDV prototype existed (the CARDIS device, see Figure 2.13) [18, 19, 24], which was also used in a clinical study where LDV data was acquired in 100 patients [23, 25, 26].

1.2 Objectives

The research performed within this PhD thesis was done within the context of the InSiDe project, with as the general objective to enhance the LDV signal acquisition and processing and explore alternative PWV assessment methods.

First, the prototype developed with the preceding CARDIS project did not include any form of intuitive real-time signal-quality control. Measurements were conducted with a fixed length at 20 seconds and signal quality assessment was at the mercy of the operators device positioning according to their expertise (or lack thereof) with other, similar probe-based technologies. From inspection of the data measured by this device, it was found that the average quality was subpar [27]. In order to get a robust estimate of PTT, and consequently PWV, signal features associated with the arrival of the pulse wave have to be discernible. The features get hampered by noise from motion artefacts, or lack of physiologically sound signal. Naturally, this means that for a noisy signal, no reliable PWV values could be estimated. This issue seemed to occur especially for measurements at the femoral artery and for subjects with an elevated BMI. A quality metric that could inform the operator in real-time, suggesting a repositioning if necessary, would strengthen the case for LDV applied to arterial health. The first objective of this thesis is therefore to: **develop algorithms that assess signal quality for real-time feedback**.

Secondly, following an improvement to average signal quality in carotid and femoral LDV measurements, PTT and PWV should be be derived from the data in an automated manner. Ideally, the operator performs a measurement, with little to no delay between the end of the measurement and the returning of a reliable PWV value. The second objective is therefore: **the development of a pseudo-real-time carotid-femoral PWV estimation algorithm**.

Third, the advantage of an LDV device that it can measure very small displacement (nanometer range), may open up other avenues of assessing arterial stiffness. A major drawback of carotid-femoral PWV is its arterial pathway. While extensively researched and proven to be a robust metric for arterial stiffness [28, 29], carotid-femoral PWV does not infer the ascending part of the aortic arch, which accounts for a large part of the elastic capabilities of the arterial stiffness [30]. Subsequently, arterial stiffening should have the highest impact on this part of the aorta, but is not apparent from carotid-femoral PWV. The proposed corollary biomarker is heart-carotid PWV, which aims to assess PWV along the path from the aortic valve to the carotid artery. However, since heart-carotid PWV has not been

investigated thoroughly, little is known on conventions surrounding PTT, *dx* and PWV. Hence, a third objective is to explore **the potential of heart-carotid PWV as an additional biomarker to carotid-femoral PWV**.

1.3 STRUCTURE

This dissertation is structured according to 4 distinct parts:

1. **Part I – Clinical Rationale and State-of-the-Art in Pulse Wave Velocity Estimation.** The first part of this book introduces the rationale behind the widespread clinical investigation of arterial stiffness. Its association with cardiovascular disease will be explained as well as the underlying anatomical structures that influence the stiffness of human vasculature. The concept of PWV will be introduced as a metric for arterial stiffness, and several ways of estimating PWV will be derived theoretically. Next, state-of-the-art technologies for the measurement of PWV will be discussed. Specifically an overview of LDV will be provided as a potential solution for some of the pitfalls of the other technologies in the field.

2. **Part II – Laser-Doppler Vibrometry Carotid-Femoral Signal-Quality Enhancement and Pulse Transit Time Estimation.** Part II will address the efforts made in regards to the design, construction and validation of LDV-signal quality metrics. First, this is done via two pattern recognition techniques in matrix profile and template matching, both of which detect recurring waveforms that correspond with the arrival of the pulse wave at the associated LDV-measurement site. These methods will be validated using a logistic regression model. Next, signal-to-noise ratio will be improved by leveraging the multi-beam build of the CARDIS device. This *beamforming* will combine multiple signals per handpiece in a smart, piecewise manner and return a single, enhanced signal from which arterial stiffness will be assessed and compared with benchmark methods. Finally, a real-time implementation of a PWV estimation algorithm will be discussed. The determined heuristics of the algorithm are largely based on insights gained from the signal-quality analysis using pattern recognition methods.

3. **Part III – Exploring Heart-Carotid Pulse Transit Time for Arterial Stiffness Assessment.** While carotid-femoral PWV is standard, alternative arterial pathways for PWV assessment like heart-carotid may offer complementary insights, especially into the stiffness of the

ascending aorta. A feasibility study will be discussed which assessed two different heart measurement sites for the LDV measurements. PTT was calculated using two distinct combinations of heart and carotid signal features. This led to 4 potential heart-carotid PTT estimation methods which will be compared and evaluated against each other using several arguments. Initially, PTT was extracted from the LDV data, through rigorous visual inspection of signal features, with parallel ECG measurements as a vital supporting element. Since future LDV prototypes should not include ECG, a deep neural network (DNN) was developed to infer heartbeat timings from carotid LDV signals alone. This enabled ECG-free segmentation of heartbeats and provided an automated heart-carotid PTT calculation method, in addition to others relying on template matching or ECG.

4. **Part IV – Conclusions.** The individual chapters of this dissertation will discuss their encapsulated results within their respective frames, but part IV delivers an overview of the key results, bringing them together to be discussed in a broad, global sense. This part will provide an assessment of the current state of the LDV device and its biomedical application.

1.4 List of peer-reviewed publications

Accepted and published papers as (co-)first author

- Template matching and Matrix Profile for Signal Quality Assessment of Carotid and Femoral Laser Doppler Vibrometer Signals, *S. Seoni*, S. Beeckman* et al., Frontiers in Physiology, vol. 12, 11 January 2022, doi: https://doi.org/10.3389/fphys.2021.775052 (* joint first author)*

- Enhancing Multichannel Laser-Doppler Vibrometry Signals with Application to (Carotid-Femoral) Pulse Transit Time Estimation, *S. Beeckman et al., 45th Annual International Conference of the IEEE Engineering in Medicine & Biology Society (EMBC), 24-27 July 2023, pp. 1-7, doi: 10.1109/EMBC40787.2023.10340553*

- Heart-Carotid Pulse-Wave Velocity via Laser-Doppler Vibrometry as a Biomarker for Arterial Stiffening: a Feasibility Study, *S. Beeckman et al., Physiological Measurement, vol. 46(4), 22 April 2025, doi: https://doi.org/10.1088/1361-6579/adcb85*

Papers under review as first author

- Deep-Learning Based ECG-free Heart-Carotid Pulse Transit Time Estimation from Laser Doppler Vibrometry, *S. Beeckman et al., submitted to Medical & Biological Engineering & Computing*

Papers under review as co-author

- Real-Time Beat-to-Beat Pulse Wave Velocity Estimation: A Quality-Driven Approach using Laser Doppler Vibrometry, *S. Seoni et al., submitted to Medical & Biological Engineering & Computing*

I

Clinical Rationale and State-of-the-Art in Pulse Wave Velocity Estimation

CHAPTERS

2 Clinical rationale **9**

CHAPTER 2

CLINICAL RATIONALE

2.1 PHYSIOLOGY OF THE ARTERIAL SYSTEM

First a broad summary is given on the anatomy and function of the human cardiovascular system, with an emphasis on the arterial system. The concept of arterial stiffness and its relation to hemodynamic functionality and cardiovascular disease is next. This is followed by a brief overview of several state-of-the-art solutions for measuring arterial stiffness with the added rationale behind laser Doppler vibrometry as an alternative technology in development.

2.1.1 The heart anatomy and function

The heart is in essence an organic pump that sustains the circulatory system, carrying oxygenated blood and nutrients throughout the rest of the cardiovascular system, shown in Figure 2.1 [31]. Oxygen gets transferred from inspired air in the lungs to oxygen-poor blood in the lungs. Oxygenated blood is then transported via the pulmonary vein to the heart. It is then pumped into the aorta (about 2 cm in diameter close to the heart), further down the large arteries leading to smaller arteries, arterioles (diameter 30-100 μm) and capillaries (diameter 8 μm) where, finally, the oxygen diffuses into the surrounding tissue, along with exchange of nutrients and waste products [32]. The total blood volume is compartmentalised by this branching tree-like structure, whose branches gradually decrease in caliber with successive generations.

After the blood loses its oxygen content and picks up CO_2, it travels back to the heart via the veins that coincide into the vena cava. The heart then completes the circulatory system by pumping this received blood to the lungs via the pulmonary artery.

In brief, the heart itself consists of two distinct sides, each with an atrium and a ventricle. Blood flows into the atria first, then to the ventricles from where it is ejected into either the aorta for the left side or the pulmonary vein for the right side. Figure 2.2 shows the anatomy of a healthy heart. Going forward, we will focus on the left side of the heart, responsible for the receiving and projection of oxygen-rich blood into the aorta and systemic arteries.

Through evolution, the heart had to become a self-regulating and self-sustaining entity [33, 34]. This means that no external energy can drive its mechanism, as is the case with human-made electrically-driven pumping devices. This forces the heart to operate into two distinct phases. One is where it delivers energy outwards in the form of mechanical work and where it ejects blood into the vasculature (systole). The other phase requires the heart to relax and take in (chemical) energy via oxygenated blood that is circulated through the coronary arteries, delivering oxygen to the myocardial fibers in the left ventricle (diastole). This energy is then converted into potential and kinetic energy when the heart contracts, at the time where the cardiac muscle receives an electric starting signal in the form of an R peak in electrocardiagram (ECG) signals. Of the whole cardiac cycle duration, about 30% amounts to systole in resting conditions; the remaining 70% is diastole. Figure 2.3 provides a graphical overview of these two phases.

Valves such as the mitral and aortic valves play a critical role in maintaining the heart's pulsatile flow by ensuring unidirectional blood movement between chambers and into the systemic circulation. The mitral valve, located between the left atrium and left ventricle, opens during diastole to allow ventricular filling and closes at the onset of systole to prevent backflow. The aortic valve, situated between the left ventricle and the aorta, opens during systole to permit ejection of blood into the aorta and closes during diastole to maintain arterial pressure.

These valves operate in a tightly coordinated sequence, and their function is audibly reflected in the heart sounds heard during auscultation. The first heart sound corresponds primarily to the closure of the mitral and tricuspid valves, marking the beginning of systole, while the second heart sound is generated by the closure of the aortic and pulmonary valves, signaling the end of systole and the onset of diastole. A low-pitched third heartsound can be observed during early diastole, signaling the rapid-filling

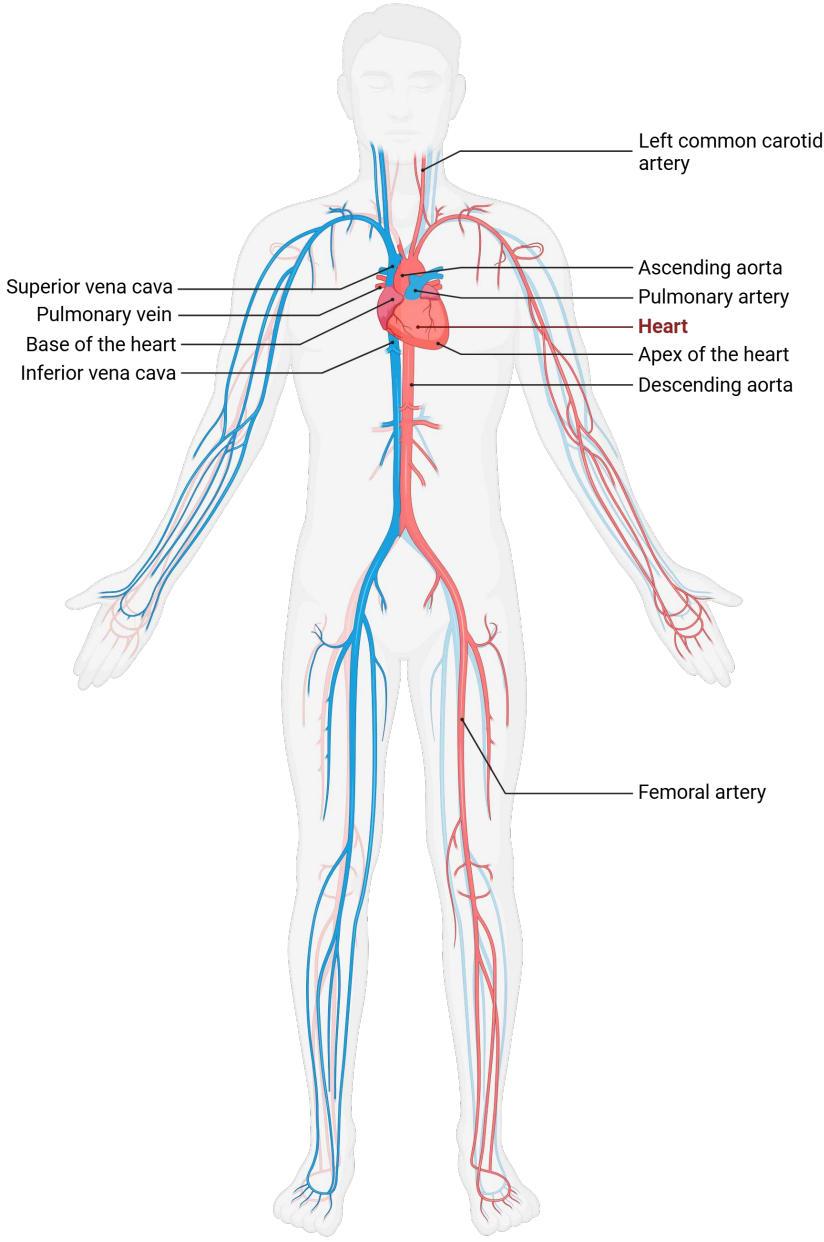

Figure 2.1: Schematic representation of the human cardiovascular system. Blood vessels containing oxygen-rich blood are marked in red, while oxygen-poor blood travels through the blue vessels. Several arteries and veins that are relevant to future chapters are indicated. Created in Biorender.

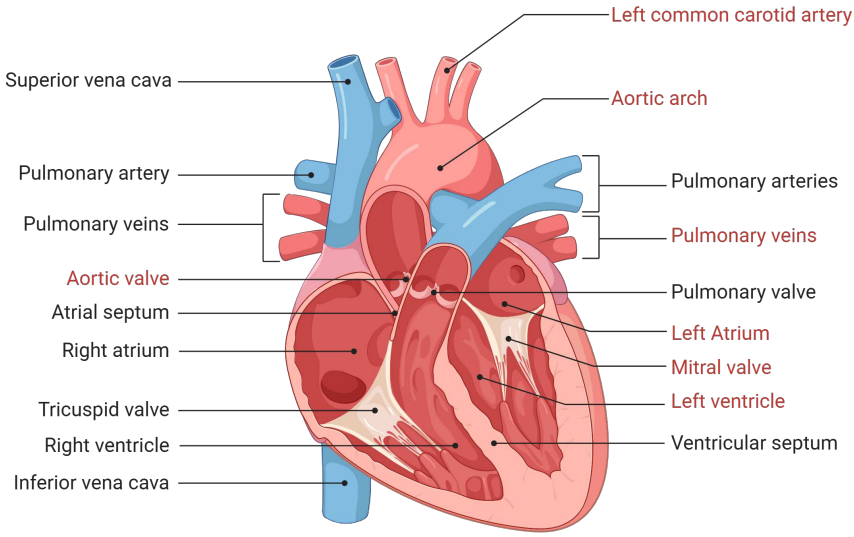

Figure 2.2: The anatomy of the human heart. The main components are indicated. Those that correspond to the left side of the heart are highlighted in red. Created in Biorender.

phase of the ventricles. These acoustic events are not only diagnostic markers but also physiological indicators of the mechanical integrity and timing of valvular function.

2.1.2 Arterial function, anatomy and modelling

2.1.2.1 The windkessel model

Aside from their function as conduits, (large) arteries also act as a buffering reservoir for blood [32, 35, 36] and they enable continuous blood flow through the systemic vasculature. The aorta and large elastic arteries expand during ventricular systole, storing blood volume which is released during diastole, ensuring continuous flow down the arterial tree. Their branching structure constitutes an eventual drop in blood flow in the microcirculatory beds as opposed to the high pulsatility closer to the heart. This inherent degree of distensibility of these vessels will determine storage capacity, something that is commonly referred to as (local) vessel compliance or area compliance C_A (units in $mm^2/mmHg$). C_A is defined as the ratio of the change in cross-sectional area ∂A and the change in intra-arterial pressure ∂P that drives ∂A. Area compliance normalized for cross-sectional area (the diastolic area is commonly used) gives distensibility D_A (units in $1/mmHg$).

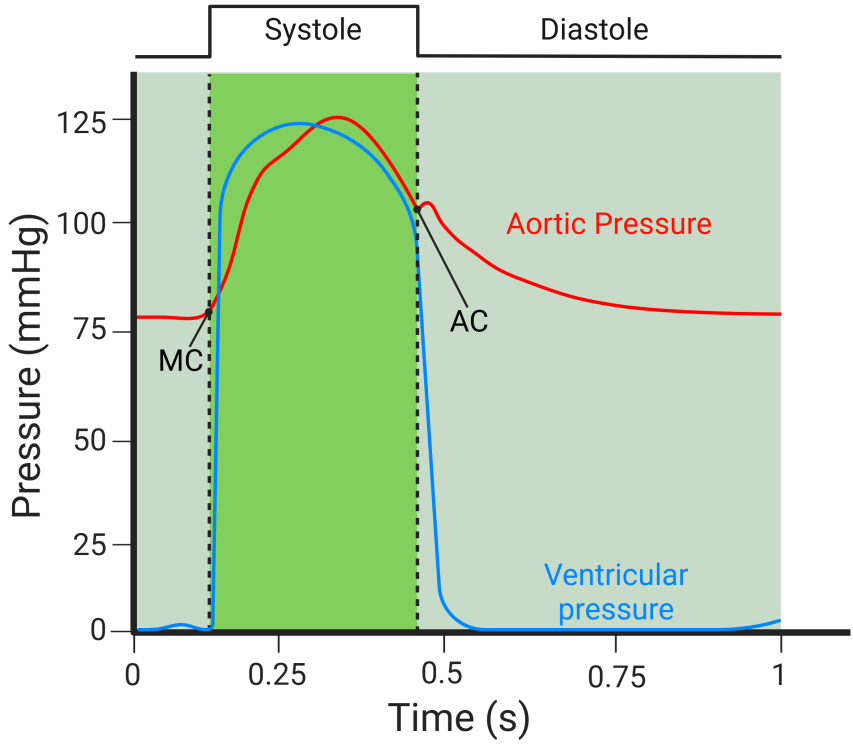

Figure 2.3: Aortic and ventricular pressure expressed in time for an example, healthy subject. Systole and diastole are distinctly indicated as well as the timepoints at which the mitral and aortic valve close (MC & AC respectively).

When observing the complete arterial system with parameters such as the total arterial compliance (TAC, units in mL/mmHg) and stroke volume (SV), we get to PP = SV/TAC [37, 38]. PP refers to pulse pressure, which is the difference between peak systolic and diastolic arterial pressure. For a healthy individual 120/80 mmHg is the desired readout on state-of-the-art blood-pressure measurement devices, yielding a PP of 40 mmHg [2].

Arterial stiffness determines the degree of expansion in large blood vessels which accommodates increases in blood volume. In general, arterial stiffness is inversely proportional to C_A and D_A, and is directly proportional to pulse pressure. Arterial stiffening typically manifests itself in an increased pulse pressure in the elderly [39, 40], as arterial stiffness increases with age following a loss of compliance [41, 42].

The volume buffering effect of large arteries can be modeled using a windkessel-model (Figure 2.4). It borrows its name from a closed-volume water tank with a certain capacitance C (modeling TAC; units in mL/mmHg), used by fire brigades where the intermittent water volume

arriving in the tank, due to an oscillating pump, fills the volume to a degree making the water flow rate out of the actual firehose with resistance R (units in $\frac{\text{mmHg}}{\text{mL/s}}$) be constant. The rough outline of the mechanism can easily be fit to what is observed in the (left) cardiovascular system. The windkessel represents the storage capacity for blood of the large arteries, with the resistance representing the bifurcations and narrowing of the peripheral blood vessels.

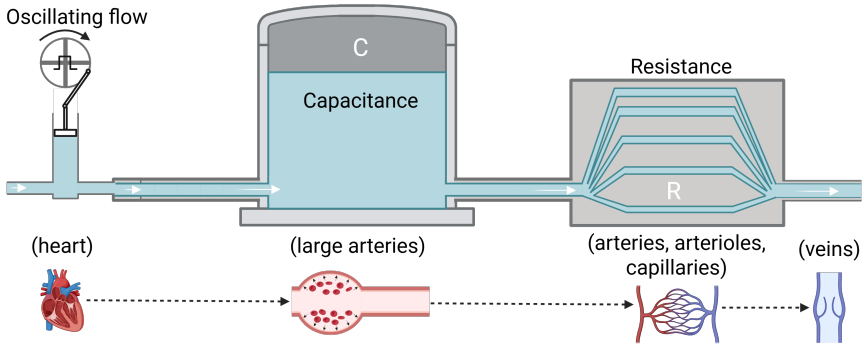

Figure 2.4: A schematic overview of the windkessel model with its oscillating inlet flow, storage capacitance in the windkessel and resistance. Physiological parallels are provided in addition. Figure made in Biorender.

Because stroke volume is a function of instantaneous changes over the duration of systole T_{sys}, it can be expressed as an integral of ventricular outflow rate $Q(t)$, commonly expressed in units of mL/s.

$$\text{SV} = \int_0^{T_s} Q(t)dt \tag{2.1}$$

$Q_{vent}(t)$ can then be decomposed as:

$$Q_{vent}(t) = Q_r(t) + Q_c(t) \tag{2.2}$$

$Q_r(t)$ is the part of the flow rate that is associated with R, the total resistance to blood flow under pressure. This resistance is attributed to the bifurcations and narrowing of blood vessels in the peripheral vasculature – something that follows from Poiseuille's law where flow resistance of a vessel is inversely proportional with its diameter to the fourth power. The flow rate $Q_c(t)$ is the component of $Q_{vent}(t)$ which is stored following the elastic expansion of the arterial wall due to the arterial compliance. Furthermore, the windkessel model constitutes the following equation, from volume conservation in a resistive-compliant system and with the assumption that no inflow occurs during diastole:

$$P_d(t) = P_0 \cdot e^{-t/\tau} \tag{2.3}$$

In the equation above, P_0 refers to the end-systolic arterial pressure. (2.3) is also dependent on a time constant $\tau = R \cdot C$, which has units in seconds. It determines the diastolic pressure decay over time for a system with specific arterial resistance and compliance, dictating that for a decreased C, and consequently increased arterial stiffness, the diastolic pressure will drop faster since the time to release the stored blood in the arterial wall will be shorter as well. This leads to τ being a major determinant in pulse pressure, and by association also arterial stiffness [39, 40, 43].

While the windkessel model explains the concepts of arterial stiffness and peripheral resistance, with their effects on blood pressure and flow, it can still be expanded upon by adding several more elements. A limiting factor is that it is a so-called 'lumped-parameter model', meaning that each parameter is a mathematical scalar without taking any physical dimensions into account. More in-depth approaches model each parameter as time and space variant values, yielding pressure and flow waves travelling along the axial dimension of the modelled vessels [44, 45].

2.1.2.2 Arterial wall composition

Arteries are distensible conduits that expand, storing blood during systole, as well as elastic energy in the arterial wall, and consequently recoil using that elastic energy to squeeze the stored blood during diastole. During heavy resistance exercise, intra-arterial blood pressures can reach extreme values, with measurements up to 480/350 mmHg reported in healthy individuals [46]. These values reflect acute physiological responses, including the Valsalva maneuver and vascular compression, rather than baseline cardiovascular mechanics. It follows that specialised tensile properties are required to withstand these pressure gradients. The two main components that contribute to this are the proteins elastin and collagen, as they are about 30 and 50% respectively of the dry weight of the aortic wall [47, 48].

Viewing a typical cross-section of a large elastic artery, elastin and collagen are built in concentric layers, or *lamellae*, in the arterial media, see Figure 2.5. For the human aorta, this amounts to $\pm$ 60 lamellae [49]. This number decreases with the vessel dimensions in peripheral arteries, which also switch to more muscular-type arteries, losing the concentric organization. Elastin is by far the most distensible, carrying the load on the arterial wall at low resting stresses. Conversely, collagen is much less distensible but has a significantly higher yield strength, which is the stress at which the tissue begins to irreversibly deform [50, 51].

It follows then that for an increasing wall stretch, first elastin distends until progressively more of the helical collagen fibers start to carry the load [52, 53]. The vessel stops expanding and starts recoiling due to the more resilient elastin. Since collagen is distinctly more stiff than elastin, arterial stiffness will be higher during systole, as the vessel is distended more [54].

Arteries proximal to the heart have material properties that make them highly distensible [30], as discussed previously. Subsequently, distal arteries change in geometric (reduced dimensions) and material (less elastin, more collagen) ways [55]. By extent, these more distal arteries are stiffer, have reduced storage capacities and will have an associated increased pulse pressure. Since these arteries have more smooth muscle cells in their media, they are referred to as muscular arteries, as in Figure 2.5 [56, 57]. The reduced compliance of the vasculature along the axial direction due to geometric and elastic material changes also affect the speed at which the travelling pulse waves propagate.

This description of the arterial wall composition is ultimately a simplified one. From various *ex-vivo* studies, it has become clear that arterial tissues are anisotropic, meaning that material properties differ along different directions due to fiber structure [58]. They also exhibit viscoelastic behaviour, where internal friction causes heat loss during vessel wall expansion and contraction [59]. Finally, it is also the non-linear relation between stress and strain for these tissues that challenges biomechanical modelling of the arterial wall beyond classic material science [60].

2.1.2.3 Compliance and distensibility for arterial stiffness assessment

The relation between arterial pressure and lumen cross-sectional area is non linear, following from what was explained previously. The relation can be described using different mathematical expressions, but a way to phenomenologically capture the non-linear relation over a wide pressure range is an arctan function which was fitted to experimental data [61]. Langewouters et al. applied pressures ranging from 0 to 200 mmHg to thoracic and abdominal aortic segments. This can be observed in the top panel of Figure 2.6. Of interest to us is the physiological pressure range of 80 to 120 mmHg. From this empirically found expression, area compliance C_A and distensibility D_A can be derived, leading to PWV.

Local arterial compliance C_A coincides with the local slope of the pressure-area curve in the physiological pressure range. From the experimentally-found arctan function [61], it can also be expressed as a function of pressure, see the second panel in Figure 2.6. The maximum value for C_A is reached for sub-physiological pressures. When observing

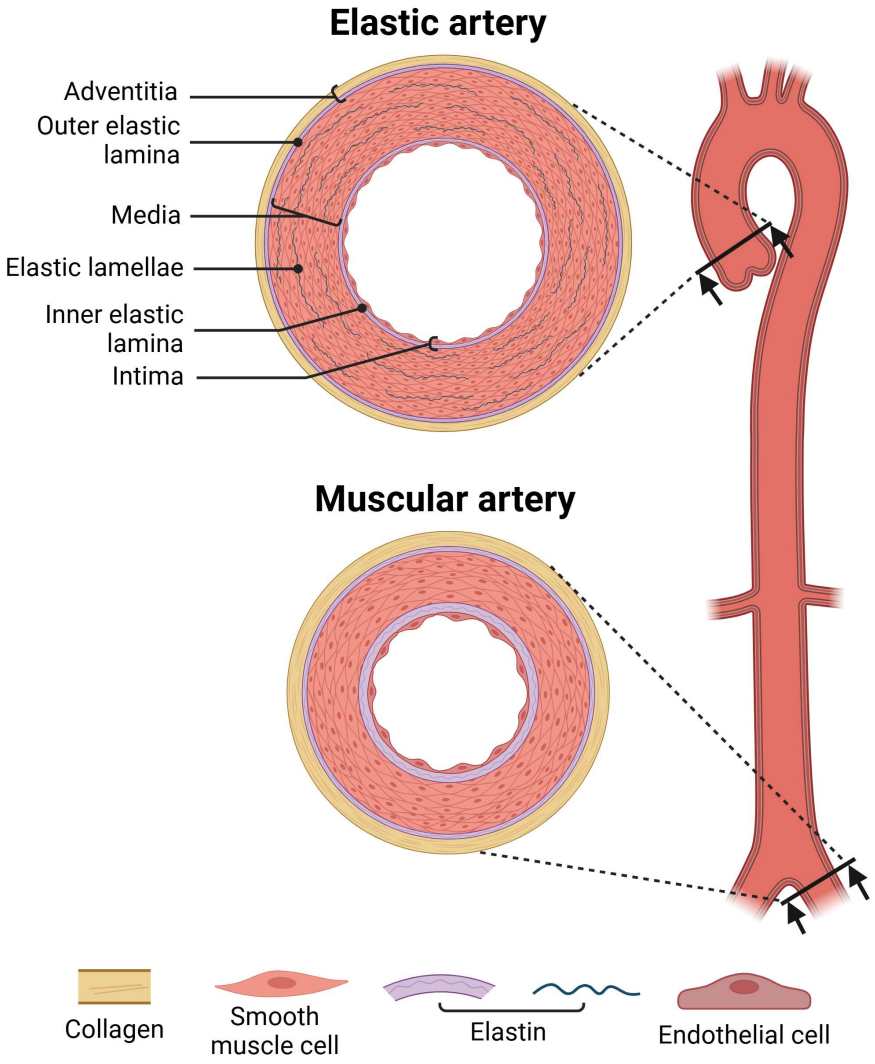

Figure 2.5: A schematic cross section of the ascending, descending and abdominal aorta is given, alongside two cross sections of a distinctively elastic part of the aorta, and a more muscular part situated more downstream. The layers and components of the arterial wall are indicated. Made in Biorender.

physiological ranges, C_A is (non-linearly) reduced with increasing pressure, which is pressure-dependent stiffening.

C_A normalised for cross-sectional area, yielding D_A can be observed from the third panel in Figure 2.6. It follows from the definition of C_A that $D_A = \frac{\delta A/A}{\delta P}$, which is the ratio of the *relative* change in cross-sectional area and change in arterial pressure.

D_A and C_A are inherently localised parameters that depend on wall tissue properties and vessel dimensions and describe the mechanical properties of the vessel wall. To compute them local pressures are ideally used as well, something that can prove to be difficult when it comes to the large vessels of interest e.g. the ascending aorta. While technologies such as ultrasound and MRI can, in theory, assess this [16, 62], they have limitations. In general, while of interest for phenotyping specific arterial sites, getting the required pressure and area values to compute local stiffness C_A and D_A, is too tedious for large-scale clinical use.

From these expressions of D_A and C_A, a measure for pulse wave velocity (PWV) can be derived. But in order to get there, the Bramwell-Hill equation is needed. In the next section we will derive this in a stepwise, intuitive manner.

2.1.2.4 Pulse wave propagation

For blood flow in an elastic artery, the famous Bramwell-Hill equation is noted as follows [63, 64]:

$$\text{PWV} = \sqrt{\frac{V \cdot dP}{\rho_b \cdot dV}} \tag{2.4}$$

With pulse wave velocity (PWV) the term used to describe the speed of the traveling pulse wave, V the volume of the accelerated blood, dP the instantaneously applied pressure on the vessel with cross-sectional surface area A, ρ_b as the density of blood and dV as the volume expansion of the elastic tube. Another expression derived from (2.4) is the Moens-Korteweg equation [65, 66].

$$\text{PWV} = \sqrt{\frac{E \cdot h}{2\rho_b \cdot r}} \tag{2.5}$$

Here, wave speed is expressed in terms of wall thickness (h), internal vessel radius (r), ρ_b and the Young's modulus of the vessel wall E (Pa). The latter characterizes the linear relationship between applied stress and

resulting strain in an idealized linear elastic material. However, this model can be extended to better capture the inherently nonlinear mechanical behavior of the arterial wall during expansion, replacing E with E_{inc} [51, 67]. E_{inc} denotes the incremental modulus of elasticity, representing the rate of change in stiffness from a reference situation as collagen fibers progressively engage and bear a greater proportion of the applied load during arterial wall deformation. The expression assumes a thin, homogeneous and isotropic vessel wall and that the blood behaves as a Newtonian, incompressible fluid.

From (2.4), (local) PWV can be expressed as a function of distensibility; PWV $= \sqrt{\frac{1}{\rho_b \cdot D_A}}$. This implies that PWV is indeed also a pressure-dependent metric, as seen in the bottom panel of Figure 2.6 [68, 69]. Because PWV is *measured* over a larger segment of the vasculature, contrary to the *local* PWV derivations of (2.4) and (2.5), it has the potential for encapsulating more global indicators for cardiovascular disease risk.

There is a clear distinction between the theoretical mechanics of pulse wave propagation in an idealized, long, uniform tube, as described by Equations 2.4 and 2.5, and the complex behavior observed in the in-vivo arterial system. In reality, arteries exhibit branching, variations in diameter and wall composition, and are subject to wave reflections. These anatomical and physiological complexities introduce significant challenges in accurately estimating pulse wave velocity (PWV). Hence, PWV is measured in practice by estimating the pulse transit time (PTT), the time it takes for the pulse wave to travel the distance dx between two points on the arterial tree [8].

$$PWV = \frac{d}{\text{PTT}} \tag{2.6}$$

The most commonly used PWV measurement is between the carotid and femoral arteries. This metric has some obvious limitations. For one, dx being measured on the surface level of subjects, albeit with an added correction factor [29]. Another one is the fact that (2.4) makes assumptions that are not valid in a real setting e.g. no wave and/or flow reflections [70]. The primary limitation, however, lies in the fact that the two measurement sites are not situated along the same arterial pathway; instead, the pulse waves recorded at each location propagate through anatomically distinct but parallel vascular routes (see Figure 2.7). Still, through extensive and exhaustive clinical trials investigating this matter, it was found that carotid-femoral PWV is a robust predictor for cardiovascular disease risk [8, 29, 71].

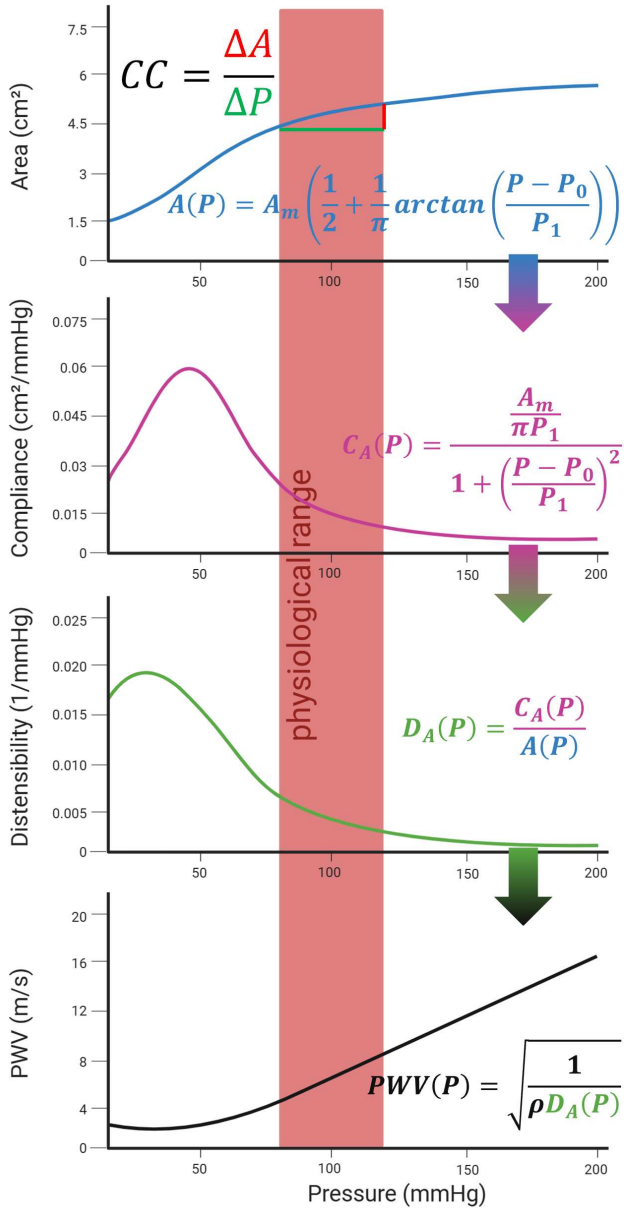

Figure 2.6: A schematic representation of the pressure-area relationship expressed as an arctan function in the top panel. The second panel shows area compliance as a function of pressure. A_m, P_1 and P_0 are all empirically found parameters based on experimental data. A_m is the max cross-section at high pressures, P_0 the pressure at the point of maximum compliance and P_1 is a measure the steepness of the pressure-area relation. From panel 1 and 2, distensibility and PWV (via the Bramwell-Hill equation) can be derived as seen in panel 3 and 4 respectively. Figure adapted from [31].

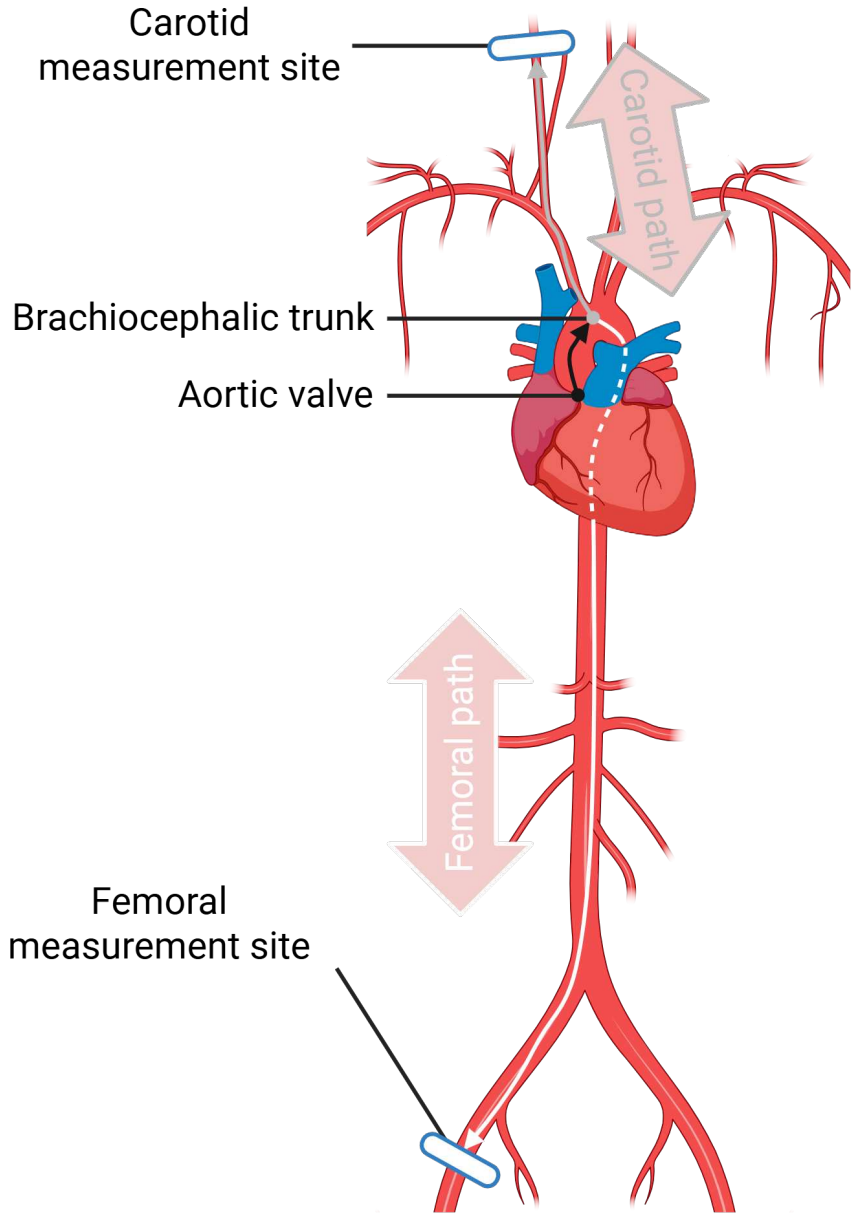

Figure 2.7: Schematic representation of the two principal arterial pathways along which pulse waves propagate toward the carotid and femoral measurement sites, as assessed in techniques such as applanation tonometry or LDV. The black arrow traces the segment from the aortic valve to the brachiocephalic trunk, representing an arterial portion not included in the conventional carotid–femoral PWV pathway. The gray arrow indicates the route toward the right common carotid artery, while the white arrow delineates the descending path toward the femoral artery, highlighting the directional divergence of these vascular trajectories.

Crucially for this work, PWV increases with increased arterial stiffness [72]. Assuming that the ratio of vessel wall thickness and radius stays constant for large arteries [49], an increased PWV can then be related to a change in wall composition, its intrinsic properties and consequently its E_{inc}, see 2.5. More specifically, changes in the vessel wall media, which holds the bulk of composite material that determines the wall elasticity and hence, stiffness.

It is of note that arterial stiffness, and by extent also its associated measured PWV, can be determined by more factors besides the *passive* interpretation of stiffness due to aging [73]. Smooth muscle cell stiffness and tone, calcification of the media and atherosclerosis, changes in the cross-linking between collagen and elastin, thickening of the vessel wall through fibrosis and endothelial cell dysfunction all can have profound effects on (local) arterial stiffness [7].

So, while PWV is not the only metric for arterial stiffness, it has become clinical routine for *in-vivo* state-of-the-art medical technology [7, 8, 74–76]. It contains information on potential remodelling of the vessel wall, if controlled for the pulsatile pressure dependence of arterial stiffness in general [77, 78]. To fully understand the potential of PWV as a biomarker, it behoves understanding the associated pathological spectrum.

2.1.3 Arterial stiffening and associated cardiovascular disease risk

Increased chronological and biological age is associated with an increase in arterial stiffness due to elastin degradation in the large elastic arteries [31, 79]. When elastin starts to degrade (it has an estimated half-life of 40 to 50 years), the collagen patterns dispersed in this joint-protein matrix progressively carries more of the applied wall stress [80]. Being the less resilient of the two causes these vessels to start to lose their windkessel function over time [41]. Aside from the loss of elastin, the vessel walls also experiences growth and remodeling with aging and disease, affecting arterial stiffness [77, 78, 81, 82].

Exasperating the gradual elastin decrease is the fact that elastin, is mainly synthesized in the arterial media during fetal and infantile growth, making the protein quite literally irreplaceable [83, 84]. As an individual grows, this elastin deposition stretches along, introducing permanent intramural stresses. Later in life, the wear on elastin manifests into vessel dilation, elongation and increased tortuosity [85].

Elevated large artery stiffness in turn leads to several detrimental effects on cardiovascular health. It causes an increase in systolic blood pressure [86], and consequently pulse pressure, which increases shear stress

in the arterial wall leading to wall degradation, dilation and aneurysms [7, 87]. Arterial stiffening also reduces coronary artery perfusion pressure [88–90]. This happens because of reflected waves arriving back at the heart more rapidly for stiffer arteries [91–93]. For low PWV values, these waves arrive during diastole, augmenting diastolic pressure needed for coronary perfusion. For high PWV's the reflected waves arrive during late systole, constructively interfering with systolic pressure, increasing pulse pressure and lowering diastolic pressure. Such a reflected wave is an accumulation of smaller reflections from many individual reflection sites e.g. changes in wall diameter, bifurcations [94, 95].

Next, it promotes left ventricle remodeling due to an increased systolic load, which causes ventricular dysfunction and can lead to heart failure [96–100]. Finally, an increased pulse pressure leads to an increase in pulsatility at the level of the microvasculature close to organs that require high blood flow and have low resistance vascular beds e.g. the kidneys, brain and placenta [101–106].

Elevated pulsatile blood pressure and flow result in barotrauma and increased shear stresses respectively, damaging microvasculature in low resistance organs [50]. This may be followed by target organ failure (e.g. kidney and cerebrovascular disease), and further stiffening of the vessel wall [107, 108]. All of these cardiovascular events can be predicted independently by carotid-femoral pulse wave velocity [7, 96, 109–111]. To make these predictions requires knowledge of PWV ranges associated with cardiovascular risk.

Reference values for normal and abnormal PWV values were obtained and set in a large-scale multicenter study [112]. Normal average PWV ranges were found starting from 6.2 m/s for < 30 year olds up to 10.9 m/s for > 70 year olds. Average PWV values for people of that same age range increase to 7.7-14.0 m/s when investigating patients with grade II or III hypertension, showing a leap in PWV with increased blood pressure. It was also shown that this increased PWV with blood pressure is not simply attributed to increasing blood pressure with age.

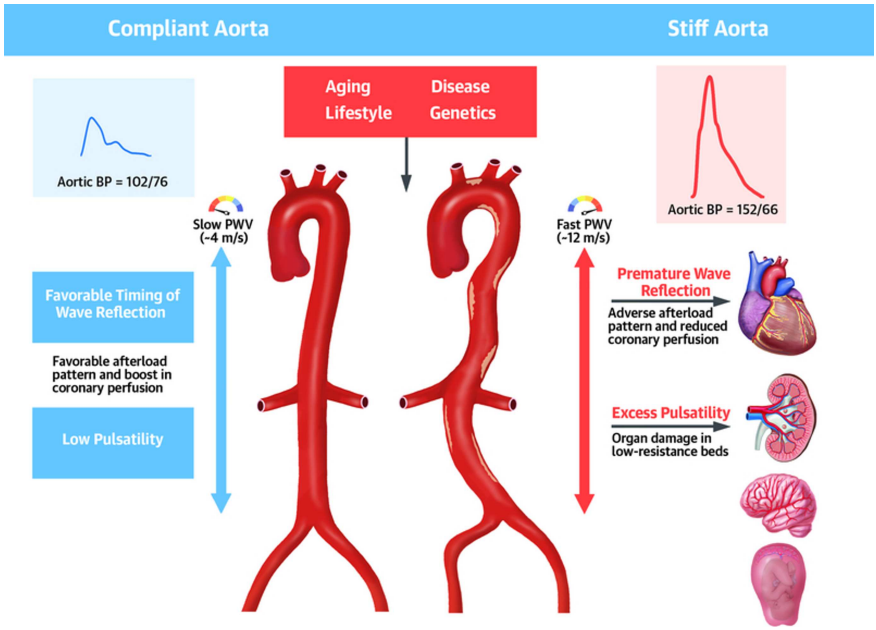

Figure 2.8: The central illustration presents two representative aortic phenotypes. The aorta on the left is compliant, demonstrating effective Windkessel (buffering) function, which corresponds to a low PWV and PP. In contrast, the aorta on the right is characterized by increased stiffness, dilation, and tortuosity. These pathological features are associated with elevated PWV and PP, which may impair coronary perfusion and contribute to end-organ damage. Figure adapted from [7].

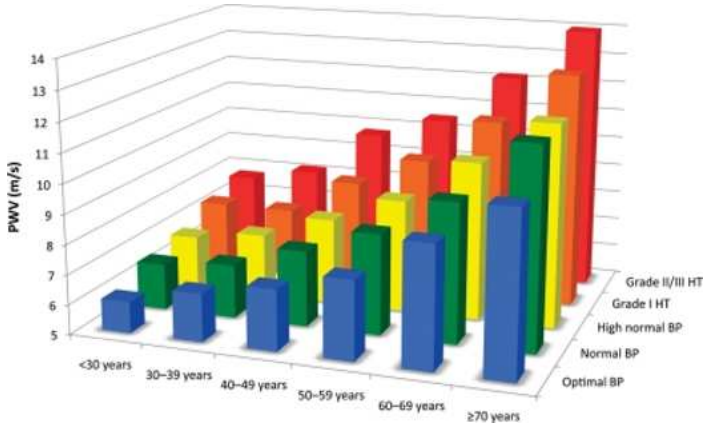

Figure 2.9: Mean PWV values according to age and blood pressure in the multicenter study to establish reference values for carotid-femoral PWV; Figure cited from [112].

2.2 State-of-the-art in measuring arterial stiffness and its challenges

Over the last years, many devices have been released that measure pulse wave velocity [113]. The work presented in the following chapters of this book is based on data measured by an LDV-device that is intended to join this cohort of medical technology. First, two existing, validated technologies will be discussed here whose measurement data are considered *ground truth* for the experiments performed in this thesis.

2.2.1 Arterial tonometry

Arterial pressure waveforms can be measured non-invasively via applanation tonometry applied to subcutaneous peripheral arteries e.g. the radial, carotid or femoral artery [114–116]. A probe, installed with piezoelectric sensors, is pressed onto the skin and perpendicular to the underlying artery of interest. If possible, the compression exerted by the probe pushes (and partially flattens) the artery against neighbouring stiffer tissues such as bone, cartilage or muscle, fixing the artery in place. In doing this, tangential forces are eliminated and the sensors couple to the intra-arterial pressure, yielding high-quality recordings.

While central aortic blood pressure can be derived from these peripheral waveforms through mathematical transformations [117, 118], the application of interest to this work remains arterial stiffness and PWV. To allow for the estimation of transit times via consecutive measurements at 2 arterial sites, the ECG is typically co-recorded such that time delays, relative to the R-peak of the ECG, can be obtained as with e.g. the Sphygmocor system [75, 109, 119]. When taking a carotid measurement for a sufficiently large number of heartbeats, leading to several clean pressure waveforms, the time delay between start of systole and arrival of the pulse wave in the carotid can be derived together with the R peaks in the ECG signal. This is referred to as carotid pulse arrival time, which could lead to a PWV metric describing aortic pressure, but will be an underestimation of the real PWV in that arterial segment due to the isovolumic contraction period (time between start of systole and opening of the aortic valve) being included in the time delay.

Following this, a second measurement can be performed at the femoral artery. Including ECG, femoral pulse arrival time can be calculated, given enough qualitative pressure waveforms were measured. At this point, the carotid-femoral pulse transit time is then calculated from the difference of femoral and carotid pulse arrival times. From here, only a tape measure is required to measure the distance between carotid and femoral measurement sites to get carotid-femoral PWV. This methodology is commonly accepted

as a highly reliable manner of assessing arterial stiffness and will be considered a reference for carotid-femoral PWV throughout this thesis [17].

Drawbacks to this method are: (i) it has a significant learning curve. Especially at the femoral artery, measurements can be difficult to conduct in a qualitative manner, in particular for individuals with a femoral artery situated deep in the tissue of the inner thigh. (ii) It can become uncomfortable for the patient when the probe is being pressed with excessive force (either through necessity to guarantee qualitative measurements or user inexperience) and (iii) the device setup is dependent on the inclusion of ECG and the taking of separate carotid and femoral measurements, increasing the duration of the average measurement protocol, making it less suited for adoption by first responders e.g. at the general practitioner (GP) level.

Note that the most recent version of the Sphygmocor system (Sphygmocor XCEL) has replaced the femoral tonometer measurement by a thigh cuff-based measurement of the femoral waveform, which allows for simultaneous measurements and discarding the ECG.

2.2.2 MRI

Magnetic resonance imaging (MRI) is a widely accepted medical imaging technology. Its phase-contrast variant (PC-MRI) is a specialized MRI technique used primarily to quantify and visualize the velocity of moving fluids, most commonly blood flow in vessels or cerebrospinal fluid in the brain and spine. [88, 120–122]. From these data, estimation of PWV on a longer segment of the aorta is feasible as well i.e. aortic PWV [15, 123–129]. Crucially, aortic PWV includes the proximal, ascending part of the aorta (the most distensible part) in its considered pathlength, something that is excluded when working with carotid-femoral PWV.

In order to measure aortic PWV, flow wave profiles at multiple points on the aorta are required. Transit time between the ascending and descending aorta is to be derived. Phase-contrast MRI provides the user with images taken at several points on the aortic arch, perpendicular to the aortic centerline. From this, flow profiles for the entire cross section at every considered point, for one cardiac cycle, are derived and transit time can be calculated. The timepoints of the foot of these flow waves is compared between the waves of the different points on the aortic arch. From the time delays found in this way, transit time can be calculated in a reliable fashion as this avoids the effect of early reflected waves.

The biggest drawback of this technique is the limited temporal resolution of the flow curves. In Figure 2.11, the curves span 50 points, over an averaged cardiac cycle of 870 ms, resulting in a temporal resolution of 17.4

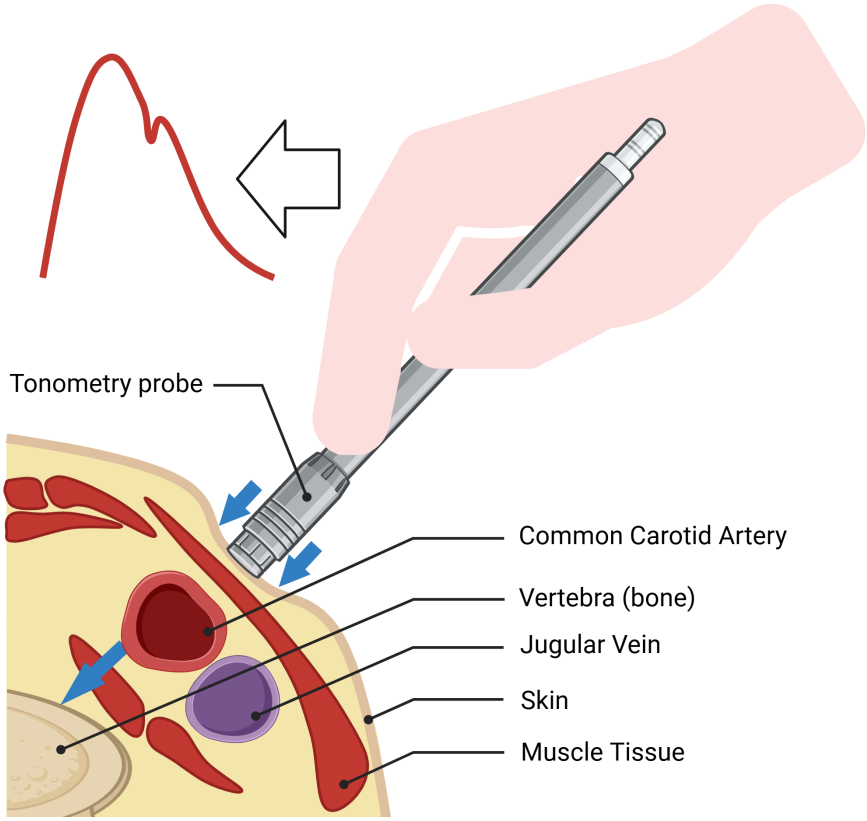

Figure 2.10: Working principle for arterial tonometry exemplified for the carotid artery in the neck. The probe is pressed against the skin, locking the carotid artery in place between it and a rigid region of tissue e.g. bone. The transducers in the probe then pick up pressure gradients following the arrival of pulse waves. This results in arterial pressure profiles being measured, of which an example is drawn in the top left corner. Figure made in Biorender.

ms. Especially for short path lengths or subjects with stiff aortas, leading to short transit times, this proves to be a challenge. The analysis presented in chapter 6 was impacted because of this temporal resolution limitation.

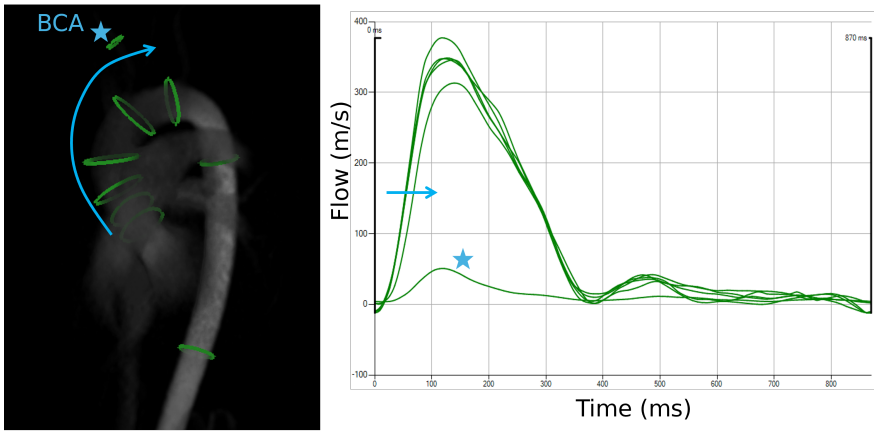

Figure 2.11: An example of phase-contrast MRI images in 3D and over time (4D-flow MRI), with several planes indicated where flow is measured, is displayed in the left panel. From those images flow profiles are derived as seen in the right panel. One plane on the brachiocephalic artery (BCA) is also drawn to illustrate the difference in flow profiles with the aorta. The data presented herein originates from one of the MRI acquisitions performed in conjunction with LDV measurements, as part of the experimental protocol detailed in Chapter 6.

2.3 Laser Doppler vibrometry

Laser Doppler vibrometry (LDV) was developed and applied to aerospace and mechanical engineering first in the 1970s [130]. Its non-contact principle was deemed ideal for the precise modus operandi required for measuring vibrations on moving, hot or fragile components. In the following decades, as the technology improved, LDV was extrapolated to other fields such as civic infrastructure (e.g. bridge health), automotive industries, micro-electromechanical systems and finally: biomedical diagnostics [131].

The basic configuration of LDV is an optical interferometer, where one laser is reflected on a vibrating target, moving with velocity $v(t)$ and consequently captured again. The technology is based on the Doppler effect, a photonic principle relating the out-of-plane velocity of the illuminated target to a phase shift f_D picked up by the laser due to reflection. λ_0 is the laser wavelength, and $f_0 = 1/\lambda_0$ its frequency.

$$f_D(t) = \frac{2 \cdot v(t)}{\lambda_0} \tag{2.7}$$

To extract the Doppler shift f_D, the reflected signal is coherently mixed with a reference signal prior to detection by a photodiode. The photodiode then converts the received optical power into a current from which the amplitude and direction of the vibrating target can be extracted. The practical execution comes in the form of a Mach-Zehnder interferometer, as illustrated in Figure 2.12. Panel A shows the theoretical principle of the interferometer for a single-point LDV. Two laser beams are generated. The measurement beam is lead towards the vibrating target, which it hits, consequently reflects on and is then received again. The second beam, known as the reference beam, does not illuminate any vibrating surfaces but is instead first split from and later combined again with the measurement beam. The recombined signal is picked up by a detector, the photodiode in our case.

Panel B shows a schematic of the practical build of an LDV device containing six parallel interferometers [18, 19, 24, 132], resulting in a multi-beam LDV. The system is homodyne, meaning that the reference and measurement beams both have the same frequency f_0, resulting in a less complex configuration. The Figure also indicates that lasers are coupled into the system using optical antennas (or grating couplers) before being split into the separate beams. The measurement beam is also transmitted and received through transmitter-receiver optical antennas. This part of the system, encapsulating the interferometers is referred to as the photonic package of the

LDV device. Additionally, panel B shows the inclusion of an optical system, equipped with an array of lenses that determine the depth of focus for the measurement beams.

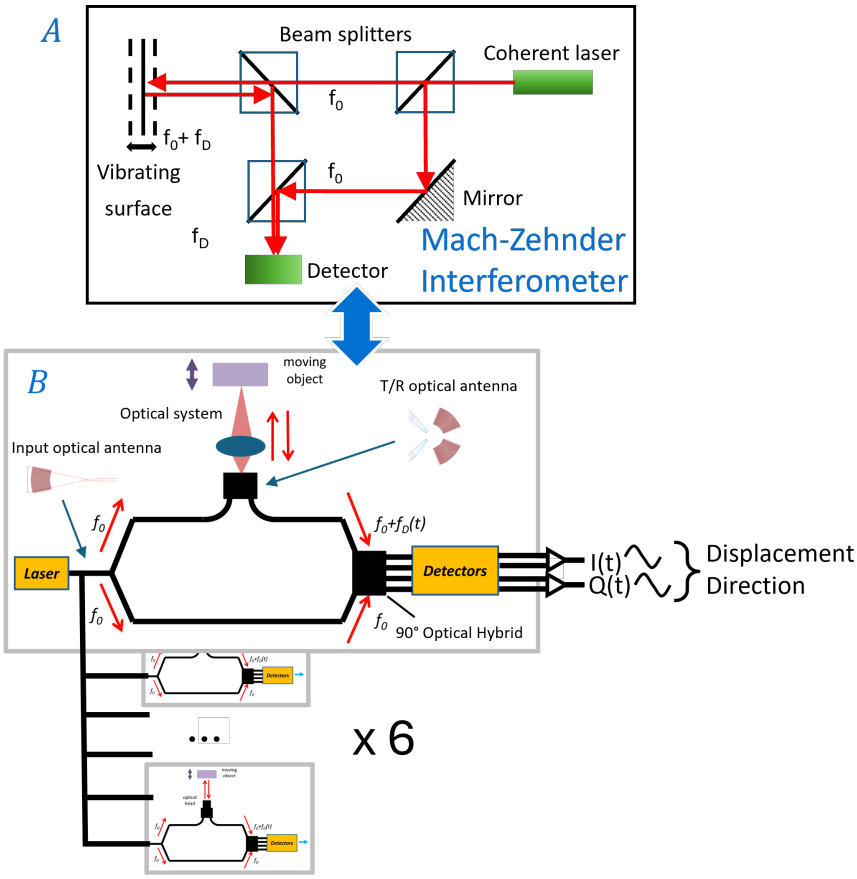

Figure 2.12: Panel A illustrates the theoretical operation of a Mach-Zehnder interferometer. In this setup, a laser source emits two coherent beams of frequency f_0: a measurement beam directed toward a vibrating target and a reference beam. Upon reflection from the moving surface, the measurement beam acquires a Doppler-induced phase shift, resulting in a frequency component f_D. The interference between the measurement and reference beams at the detector yields phase-sensitive information about the target's motion. Panel B presents a schematic of the practical implementation, consisting of a six-sensor array integrated on a photonic chip. Laser light is coupled into and out of the chip via optical transmit/receive (T/R) antennas. The measurement beam is directed to the moving surface through a lens system, while both the reference and reflected measurement beams are guided to photodetectors. These generate electrical quadrature signals $Q(t)$ and $I(t)$, which encode both displacement and direction of motion.

2.3.1 The InSiDe project and CARDIS device

Figure 2.13 shows the LDV device of Figure 2.12 at work. In panel A, the operator points the two handpieces of the device at the neck of the subject. One handpiece is equipped with a handle, resulting in a pistol-like grip. The second handpiece is mounted on top of the first one, but can be uncoupled and pointed at other regions of the body while the first handpiece remains. In this way, neck-groin (panel B) or chest-neck (panel C) measurements can be conducted, something that will result in carotid-femoral and heart-carotid LDV data from which different measures of pulse wave velocity are endeavoured to be estimated in the later chapters of this thesis.

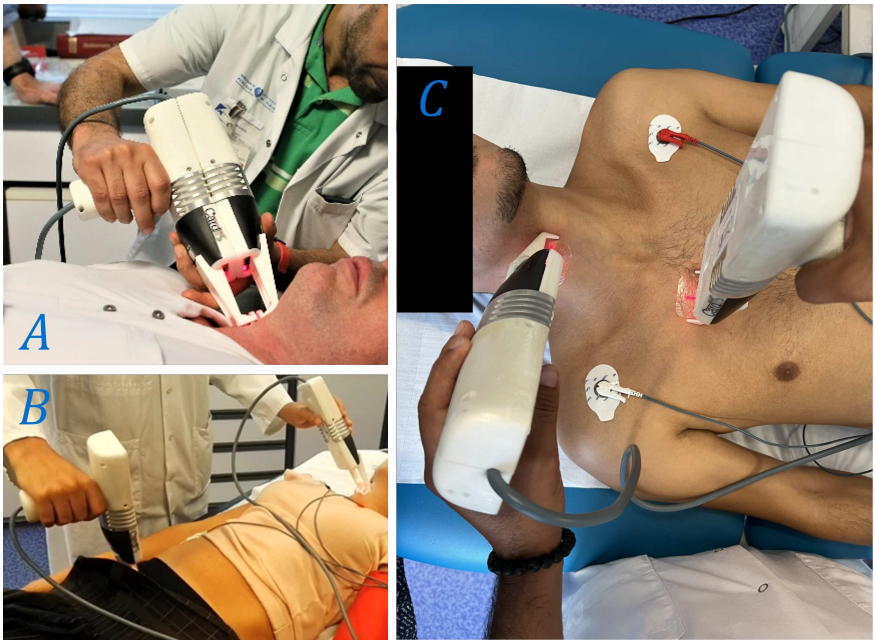

Figure 2.13: The CARDIS device measuring skin displacement via LDV. Panel A: the device measures carotid-carotid. Panel B: example of a carotid-femoral measurement. Panel C: A heart-carotid measurement with one of the two handpieces pointed at the second right intercostal space on the thorax.

The device in panel C of Figure 2.12 is the LDV prototype designed and constructed within the scope of the H2020 project called CARDIS (Grant agreement ID: 644798). The prototype will be referred to as the CARDIS device. The main result from CARDIS that is of relevance for this thesis is the existence of this device *with* proven carotid-femoral PWV assessment capabilities as well as the availability of an LDV database [19–23].

Naturally, since the CARDIS device was an early prototype, many points for improvement were apparent. The CARDIS device is heavy and

wired, making it difficult to handle. It also requires the application of retroreflective tape to the measurement site to ensure ample reflected laser light, adding to the measurement duration and potentially interfering with the vibrations of the skin. By the time of project completion, the associated software did not yet provide intuitive feedback to the operator both during and after the measurement. Still, CARDIS was promising enough to validate a follow-up H2020 project.

The project goals of InSiDe (Grant agreement ID: 871547) were many. Over the entire consortium, ranging from industrial, technical to clinical and investigational partners, the main objectives could be summarized as:

1. Development of a new photonic package with a four-beam LDV chip for 4 sensing locations (opposed to the previous 6).
2. 1310 nm solid-state laser assembly on a micro-optical bench (previously: $\lambda_0 = 1550$ nm).
3. Development of imaging optics capable of measuring vibrations on bare skin by implementing an auto-focus element in the optical system.
4. Development of electronics for control of the laser interferometer with onboard real-time signal processing capability.
5. Development of algorithms for translation of the interferometer signals to measurement results relevant for monitoring and diagnosis of selected cardiovascular risk factor (e.g. carotid-femoral PWV).
6. Development of a new clinical investigational device that can be used for clinical feasibility studies.
7. Validation of the updated technology for several cardiovascular conditions (i.e. vascular aging, carotid stenosis and cardiac arrhythmia).
8. Outline a path to industrialization and manufacturability.

In short, a handheld, battery-operated split device was to be engineered, which can be operated as one unit, as well as two separate units and can conduct timed recordings in order to measure arterial stiffness and cardiac contraction patterns. All data used in the presented analyses was measured by the CARDIS device.

2.4 Biomedical signal processing

To better understand the later chapters, key concepts of signal processing and statistical signal analysis are presented. This is not meant as an exhaustive introduction to biomedical signal processing but more as a refresher of the concepts exploited in the later chapters.

2.4.1 The 1D biomedical digital signal

In nature, biomedical signals $x(t)$ are analogue i.e. continuous over time, with time index t. However, digital technology necessitates that any continuous signal is represented as an array of discrete points sampled from the original signal [133]. The sampling frequency $f_s = \frac{1}{T_s}$, which describes the number of samples taken per second, plays a crucial role in accurately capturing the original signal in the sampled, discrete-time signal $x(n) = x(nT_s)$, with n the discrete sample index. While a high sampling frequency can closely approximate the original signal, it may not always be practically feasible and could be considered excessive in certain contexts.

Deciding on the appropriate sampling frequency involves examining the original signal and estimating its frequency content. A signal can be decomposed into a combination of different sinusoids with varying frequencies, a process known as Fourier decomposition [133–135]. To preserve the frequency content, the sampling frequency must be sufficiently high. According to the Nyquist theorem [136], the sampling frequency must be at least twice the highest frequency component present in the signal (f_m) to avoid information loss due to aliasing.

$$f_s \geq 2 \cdot f_m \tag{2.8}$$

Figure 2.14 illustrates an example ECG signal sampled under two conditions: once at a rate satisfying the Nyquist criterion, and once at a sub-Nyquist rate. The latter demonstrates how insufficient sampling frequency leads to aliasing, distorting the representation of the original signal.

The information embedded within biomedical signals is of critical importance, necessitating the use of optimal signal representation techniques to facilitate its extraction. The Fourier transform is a widely employed method that enables the analysis of signals in the frequency domain, providing insights into their spectral composition . Given that biomedical signals exhibit variability in amplitude ranges, noise characteristics, and frequency content, attributable to differences in physiological origin, acquisition resolution and application context, the selection of appropriate analytical methodologies must be tailored to the specific requirements of each application.

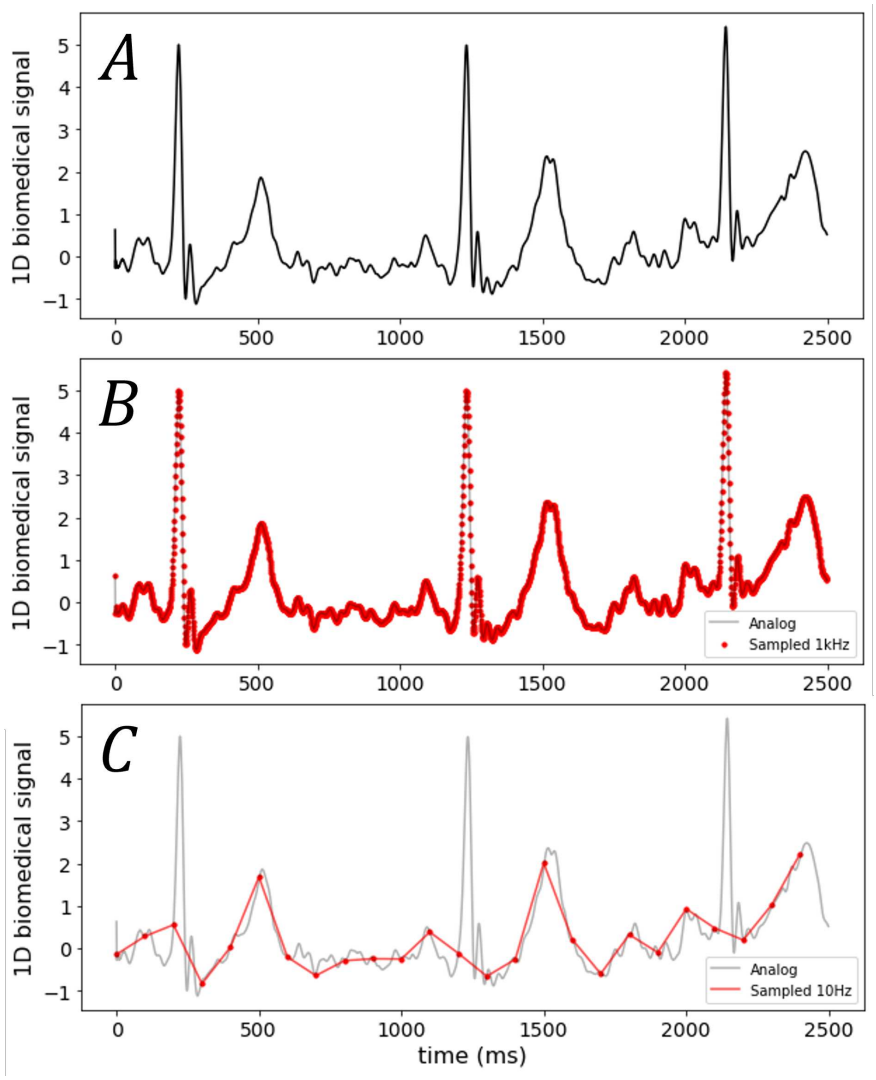

Figure 2.14: Panel A: An example of an analog biomedical signal (ECG) exhibiting three recurring waveforms over a 2.5-second interval, shown as a continuous-time signal. Panel B: The same signal sampled at a frequency of $f_s = 10,\text{kHz}$. The red dots represent individual sample points, which are sufficiently dense to accurately capture the shape and content of the original analog waveform. Panel C: The signal sampled at a lower frequency of $f_s = 10,\text{Hz}$, which violates the Nyquist criterion (ECG frequencies typically fall in the range of 0.5 to 150 Hz [137]). As a result, the red-dotted sampled signal fails to preserve the essential features of the original waveform, demonstrating the effects of aliasing.

For instance, electroencephalograms (EEG) contain different frequencies that correspond to various brain activities at specific times. Electrocardiograms (ECG) display stationary, rhythmic waveforms related to heart rhythms, with frequency content and temporal morphology that change during certain cardiac events or conditions related to the electrical activity of the myocardium. Electromyograms reflect the electrical activity and activation of muscle fibers, showing distinct frequency and time domain changes during muscle contractions. In the analysis of such signals, primary objectives often include the identification of recurring temporal patterns or the detection of anomalies.

2.4.2 Pattern recognition

When analyzing LDV skin vibration signals, a key challenge lies in identifying recurring waveform patterns that correspond to physiological events, such as heartbeats. Detecting these patterns is essential for assessing signal quality and for enabling accurate physiological measurements, such as PWV. Pattern matching techniques are well-suited to this task, as they allow for the retrieval of similar waveform segments across time-series data. Within the scope of this dissertation, two techniques, matrix profile and template matching, are particularly relevant to Parts II and III. These methods facilitate the detection of heartbeat-related patterns, which in turn provide insights into the quality of the LDV signal and the reliability of derived PWV estimates. A brief overview of both techniques is provided below, along with illustrative examples.

2.4.2.1 Matrix profile

The matrix profile is a powerful tool for time series analysis for identifying patterns as well as anomalies [138–142]. It borrows its name from the matrix profile structure, a 1D array which annotates the signal it is applied to. This structure is constructed by calculating the distance between a subsequence of the signal at time index n, and with a length of m, and all other subsequences of equal length in the signal using a sliding window approach. The value of the matrix profile at that index n becomes the minimum of the all calculated distances, and this for every n for the signal with a total length of N. The 'distance' calculated for the matrix profile can be any measure of similarity between two sequences, with the one most often used being the Euclidean distance [142]. The result can indicate how similar the closest match of the subsequences of the signal is and where it can be found.

Regions with low values in the matrix profile indicate the presence of closely matched subsequences in the original signal segment. Conversely, high values in the matrix profile suggest the presence of anomalies, also

called discords. This dual purpose, together with the lack of predefined field-specific knowledge are the definite strengths of the matrix profile technique. The method only depends on the hyper-parameter 'm', the length of subsequences investigated, and the choice of a suitable distance metric.

Building on the matrix profile structure, algorithms have been developed that search for complete motifs i.e. collections of similar waveforms containing more than two subsequences of the original signal [141–143]. In other words, motifs can be found that indicate all points in a given signal where a similar waveform is located. Figure 2.15 shows an example of the matrix profile being constructed for an LDV measurement, of which three seconds are highlighted. For an extended application of this technique to LDV data, we refer to chapter 3.

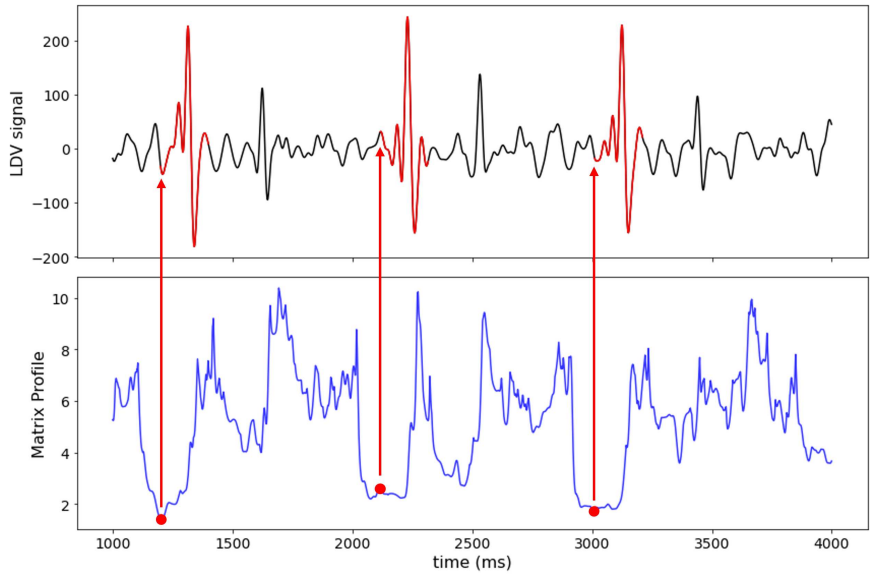

Figure 2.15: Example of the matrix profile technique performed on a skin-acceleration signal measured by the LDV prototype introduced in section 2.3. The top graph shows this LDV signal. The bottom graph is the annotating matrix profile on which the best recurring motif is indicated by red dots. The equivalent recurring pattern in the LDV signal is indicated and highlighted in red. $m = 200$ in this example.

2.4.2.2 Template matching

Template matching is a technique used to identify segments of a signal that match a predefined template [27, 144–147]. This method involves sliding the template across the signal and calculating a similarity measure at each position, often a cross-correlation function. The segments with the highest similarity scores are considered matches. This is determined by a threshold

value set for the cross-correlation function. The magnitude of this threshold has an immediate impact in the number and quality of the detected matches. For the application of template matching to LDV signals, see chapters 3, 4, 5 and 7. Further details and figures regarding the construction of the carotid and femoral templates are provided in chapter 3.

Both matrix profile and template matching are capable of identifying recurring patterns in time-series data; however, they differ in their methodological requirements and susceptibility to error. Template matching necessitates the manual construction of a representative template and the tuning of multiple hyperparameters, such as similarity thresholds, often requiring iterative refinement. In contrast, matrix profile relies primarily on the selection of a single parameter, the subsequence length m, which is informed by domain knowledge. While matrix profile offers a more automated and parameter-efficient approach, it may occasionally prioritize patterns that are statistically conserved yet clinically irrelevant. In such scenarios, the use of a well-constructed template can make template matching the more suitable technique, as it enhances the specificity and clinical relevance of the detected patterns.

2.4.3 The stochastic nature of biomedical signals

A *stochastic signal* is one that exhibits inherent randomness and cannot be predicted exactly, even with complete knowledge of its past values. Unlike *deterministic signals*, which can be described by explicit mathematical functions and fully determined at any point in time, stochastic signals are better characterized by their statistical properties, such as their mean, variance, and autocorrelation structure. In biomedical applications, many signals – such as ECG, EEG or LDV – exhibit stochastic behavior due to the complex, composite and dynamic nature of physiological processes [133, 134].

Several factors contribute to the stochastic nature of biomedical signals. First, intrinsic physiological variability results from the complex, nonlinear interactions among biological subsystems. For example, even under resting conditions, the intervals between heartbeats vary due to autonomic nervous system modulation [148, 149]. Second, measurement noise, including electronic noise, quantization error, and motion artifacts (especially true for LDV), introduces random perturbations into recorded signals [150, 151]. Third, environmental influences such as temperature fluctuations and electromagnetic interference further contribute to variability, making the observed signal a noisy and often incomplete reflection of the underlying physiological activity [152, 153].

Biomedical signals with a stochastic nature, such as LDV measurements of skin vibrations, can be modeled as combination of deterministic signal $s(n)$ and additive noise components $v(n)$ as

$$x(n) = s(n) + v(n) \tag{2.9}$$

To extract $s(n)$ from $x(n)$, thereby separating $s(n)$ from $v(n)$, we encounter a fundamental challenge in the broader field of signal processing: source separation. This challenge is often modeled as the well-known 'cocktail party problem' [154].

The cocktail party problem involves separating individual sources of sound from a mixture of sounds, analogous to distinguishing different biomedical signals from a composite signal [133]. This problem is named after the challenge of focusing on a single conversation in a noisy environment, such as a cocktail party, where multiple people are speaking simultaneously. In biomedical signal processing, the cocktail party problem is highly relevant. For example, separating EEG signals from background noise [155, 156] or isolating heart sounds from lung sounds in phonocardiogram (PCG) signals are critical tasks [157]. These applications require distinguishing the signal of interest from various overlapping signals.

Several techniques can be employed to address the cocktail party problem: (i) Beamforming uses spatial filtering, involving arrays with multiple sensors, to enhance the signal from a specific direction while suppressing signals from other directions [158–160]. It is particularly useful in scenarios where the spatial location of the signal sources is known. An application of beamforming to LDV data is presented in chapter 4. (ii) Blind source separation involves separating a set of signals into their individual components without prior knowledge of the source characteristics. Methods like independent component analysis (ICA) are commonly used for this purpose [161]. ICA has also been applied to LDV measurements in chapter 4.

2.4.3.1 Beamforming

Beamforming is a signal processing technique that functions as a spatial filter, analogous to spectral filters, but operating across sensor arrays distributed in space. Its primary objective is to enhance signals arriving from specific directions of interest while attenuating interference and noise from other directions. This is achieved by coherently combining the signals $(x_m(n))$ captured by the M array sensors in a directionally selective manner, resulting in an output signal $y(n)$:

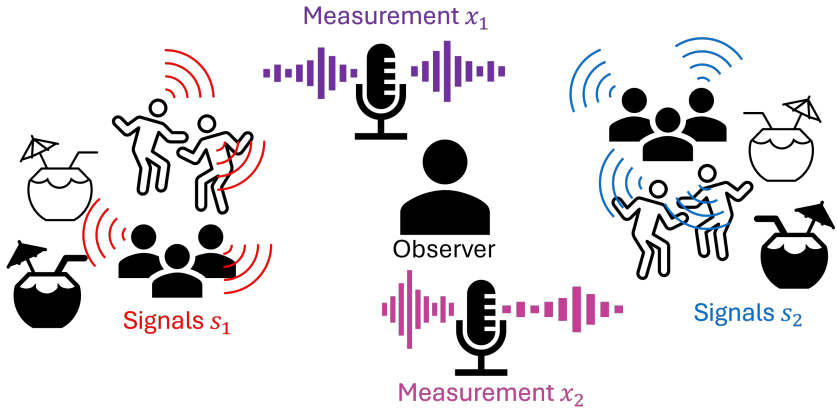

Figure 2.16: Conversations of two groups (s_1 and s_2 at a cocktail party are being recorded using two microphones, leading to two mixture measurements x_1 and x_2.

$$y(n) = \sum_{m=1}^{M} w_m x_m(n) \tag{2.10}$$

In this formulation, the weights w_m represent either scalar gains (in the time domain) or complex coefficients (in the frequency domain, e.g., when using the short-time Fourier transform). In the time domain, w_m may also represent finite impulse response filters applied to each sensor signal. The weights are designed to constructively combine signals from the desired direction and destructively interfere with signals from other directions.

In many practical scenarios, especially in acoustics and biomedical applications, the observed signals are the result of convolutive mixing in the time domain, meaning that each sensor receives a delayed and filtered version of the source signals:

$$x_m(n) = \sum_{j=1}^{J} h_{mj}(n) * s_j(n) \tag{2.11}$$

With $s_j(n)$ the j-th source signal, $h_{mj}(n)$ the impulse response from source j to sensor m, $*$ denoting the convolution operation and J the total number of sources.

To simplify this complex mixing model, beamforming is often performed in the frequency domain using a Fourier transform expressed using $X_m(f)$, $H_{mj}(f)$ and $S_j(f)$ as the Fourier transforms of $x_m(n)$, $h_{mj}(n)$ and $s_j(n)$ respectively. In this domain, the convolutive mixture is approximated as an instantaneous linear mixture with complex-valued coefficients at

each frequency bin. This transformation reduces the problem to a simpler form, where signal enhancement can be achieved through matrix operations rather than deconvolution, significantly reducing computational complexity as

$$X_m(f) = \sum_{j=1}^{J} H_{mj}(f) S_j(f) \tag{2.12}$$

The beamformed output in frequency domain becomes

$$Y(f) = \mathbf{w}^H(f)\mathbf{X}(f) \tag{2.13}$$

where $\mathbf{w}^H(f)$ is the conjugate transpose of the complex weight vector and $\mathbf{X}(f)$ is the vector of sensor signals at frequency f.

Beamforming techniques have been successfully applied in various domains, including EEG, where the assumption of instantaneous mixing is often valid even in the time domain. In such cases, spatial filtering can be used to isolate neural sources of interest, improving signal-to-noise ratio and aiding in source localization tasks [162]. While beamforming suggests spatial information, it can generally be applied to models that assume an instantaneous mixing even in time domain like $x(n) = As(n) + v(n)$ where A is the "steering" vector. In these cases, beamforming estimates a filter $\mathbf{w}$ such that $y(n) = \mathbf{w}^T\mathbf{x}(n)$ to maximize the contribution of the source of interest while minimizing the influence of sources considered interference.

2.4.3.2 Independent component analysis (ICA)

ICA is a computational technique used to decompose a multivariate signal into a set of additive components that are statistically independent and exhibit non-Gaussian distributions [161, 163]. The method enables the recovery of underlying source signals from observed mixtures without requiring prior knowledge of the source characteristics or the mixing process. ICA is particularly effective in blind source separation tasks, where the goal is to disentangle latent signals based solely on their statistical independence.

For example, in a scenario where multiple people are speaking simultaneously, ICA can help isolate each person's voice from the combined audio recording (if the mixtures are instantaneous). The relevance is explained via an example. Starting from Figure 2.16, Let the original source signals be denoted as:

$$\mathbf{s}(n) = \begin{bmatrix} s_1(n) \\ s_2(n) \end{bmatrix} \tag{2.14}$$

Assume that the microphones record two linear mixtures of the two sources:

$$\mathbf{x}(n) = \mathbf{A} \cdot \mathbf{s}(n) \tag{2.15}$$

where $\mathbf{x}(n) = \begin{bmatrix} x_1(n) \\ x_2(n) \end{bmatrix}$ is the observed signal vector and $\mathbf{A}$ is a 2×2 unknown instantaneous mixing matrix (for convolutive mixtures a Fourier transform is required as previously illustrated with beamforming) containing mixing coefficients that are combined with the original source signals. The goal of ICA is to estimate a demixing matrix $\mathbf{W}$ such that:

$$\mathbf{u}(n) = \mathbf{W} \cdot \mathbf{x}(n) \tag{2.16}$$

where $\mathbf{u}(n) \approx \mathbf{s}(n)$ are the estimated independent components. The steps of the general ICA algorithm start with centering and whitening the observed signal data. The mean of each observed signal is subtracted from it for the centering step, yielding $\tilde{\mathbf{x}}(n)$. Whitening means applying a linear transformation to $\tilde{\mathbf{x}}(n)$ to make the components uncorrelated and their variance becoming equal to 1, which can be expressed as:

$$\mathbf{z}(n) = \mathbf{V} \cdot \tilde{\mathbf{x}}(n) \tag{2.17}$$

where $\mathbf{V}$ is a whitening matrix such that $\mathbb{E}[\mathbf{z}(n) \cdot \mathbf{z}^T(n)] = \mathbf{I}$, where $\mathbf{I}$ is the identity matrix and $\mathbb{E}$ refers to the *expected value* operator.

To get the unmixing matrix $\mathbf{W}$ from $\mathbf{u}(n) = \mathbf{W} \cdot \mathbf{z}(n)$, with maximally independent components in $\mathbf{u}(n)$, the non-Gaussianity needs to be maximized. This is because the central limit theorem dictates that a linear mixture of independent non-Gaussian variables (such as two individuals speaking) tends to be more Gaussian than the original variables. This optimization procedure is most often done by maximizing kurtosis or negentropy [161, 163, 164].

The recovered signals $\mathbf{u}(n)$ approximate the original sources $\mathbf{s}(n)$, up to permutation and scaling:

$$\mathbf{u}(n) \approx \mathbf{P} \cdot \mathbf{D} \cdot \mathbf{s}(n) \tag{2.18}$$

where $\mathbf{P}$ is a permutation matrix and $\mathbf{D}$ is a diagonal scaling matrix.

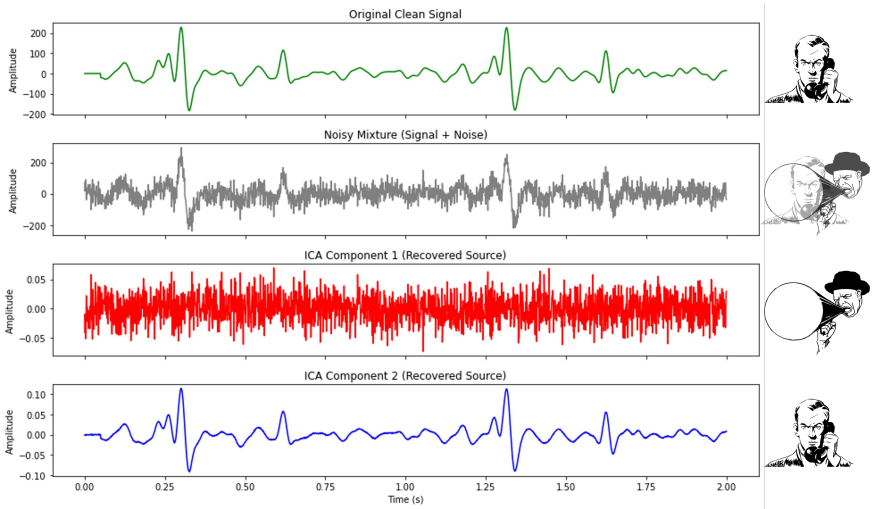

Figure 2.17: ICA applied to a noisy mixture of an LDV-measurement segment s_1 and Gaussian noise s_2. From top to bottom, first the original signal is portrayed. The second graph shows one of the two mixture signals in this experiment (x_1 and x_2), followed by the two independent ICA components (u_1 and u_2). From these two components, first the noise and then the recovered clean signal can be recognized.

2.4.4 Machine learning

With the surge in capabilities of artificial intelligence (AI) in recent years, especially for generative AI, an understanding of the broad scope of these methods is required. Especially for a sensitive field such as healthcare, optimized tools such as diagnostic AI assistants are in constant demand [165, 166]. AI in general aims to build intelligent systems that mimic human cognition for reasoning, learning and problem-solving while often being specialized and optimized for specific applications like image recognition [167]. Machine learning is a subset of AI. It specifically encapsulates systems that learn from data as opposed to being explicitly programmed (which is the case with knowledge-based systems). For the scope of this dissertation, we will focus on the supervised-learning branch of machine learning.

2.4.4.1 Supervised learning and logistic regression

A machine learning model can learn trends and properties present in data, given labels that represent them. This form of machine learning is supervised learning, referring to the requirement of said training labels during the model training. In general, the model learns to map input features $\mathbf{x}$ to the target output label y that they correspond to. During training, a loss function measures the error between the model's prediction at a given point and

the target output. Optimization at that point adjusts the model to minimize the error going forward. This process takes place over the entire training dataset. When generalized correctly, the model will be able to predict an accurate output given new, 'unseen' data (referring to data not present in the training dataset).

The model output and target labels are continuous values for *regression* models. When they are discrete values, the model performs *classification*. A popular classifier is the logistic regression model which (contrary to its name suggests) is a supervised learning algorithm for binary classification problems [168–170]. Some examples of binary classification are distinguishing healthy from diseased, qualitative from not qualitative etc. The main reason for its popularity is its interpretability, with its coefficients directly linked to individual feature influence, helping identify which features are useful or redundant for a specific application. Logistic regression was used for a part of the analysis in chapter 3.

Any logistic regression model output is interpreted as a probability (value between 0 and 1) that a given input, with feature vector $\mathbf{x} = [x_1, x_2, \ldots, x_N]^T$ (e.g. x_1: systolic blood pressure, x_2: age, etc.), belongs to class 1 (e.g. 'Diseased') as:

$$h_\theta(\mathbf{x}) = P(y = 1 \mid \mathbf{x}; \theta) = g(\theta^\top \mathbf{x}) \tag{2.19}$$

with $g(z) = \frac{1}{1+e^{-z}}$ the sigmoid function and $\theta = [\theta_1, \theta_2, \ldots, \theta_N]^T$ the weight vector. The sigmoid function guarantees an output between 0 and 1, monotonic behaviour (steady evolution) and if $\mathbf{x}$ moves towards characteristic features of class 1: $h_\theta(\mathbf{x}) \to 1$ with $h_\theta(\mathbf{x}) \to 0$ as $\mathbf{x}$ moves away from characteristic features of class 1. $h_\theta(\mathbf{x})$ indicates probability $y = 1$ given $\mathbf{x}$ and parametrized by θ. Consequently $P(y = 0 \mid \mathbf{x}; \theta) = 1 - h_\theta(\mathbf{x})$, leading to a compact representation (with y either 1 or 0):

$$P(y \mid \mathbf{x}; \theta) = h_\theta(\mathbf{x})^y (1 - h_\theta(\mathbf{x}))^{1-y} \tag{2.20}$$

Given I feature vectors $\mathbf{x}_i$ and corresponding class labels y_i, the likelihood $P(y \mid \mathbf{x}; \theta)$ (also noted as: $\mathscr{L}_\theta$) is

$$\mathscr{L}_\theta = \prod_{i=1}^{I} P(y_i \mid \mathbf{x_i}; \theta) \tag{2.21}$$

To find an optimal θ the *log* likelihood $\mathscr{LL}_\theta$ is maximized by gradient *ascent* [168–170]. The iterative process towards an optimum is training the classifier.

The trainable weights reflect the power of the N included features in the feature vectors $\mathbf{x}_i$. b is the bias term. The threshold value on the likelihood is 0.5, meaning that should $P(y = 1 \mid \mathbf{x}; \theta) > 0.5$, then for class 0 (e.g. 'Healthy') it holds that: $P(y = 0 \mid \mathbf{x}; \theta) \leq 0.5$.

Usually a learnable bias term θ_0 is added to the definition of $h_\theta(\mathbf{x})$:

$$h_\theta(\mathbf{x}) = \frac{1}{1 + e^{-\theta_0 - \theta^\top \mathbf{x}}} \tag{2.22}$$

A visual aid is given with Figure 2.18. The horizontal axis represents values resulting from the combination of the features in $\mathbf{x}$ with the trained weights $\mathbf{w}$ and bias b. The sigmoid function maps these resulting values onto a $0-1$ space shown on the y-axis. With 0.5 as the threshold value between class 0 and class 1, two regions are created for binary classification purposes.

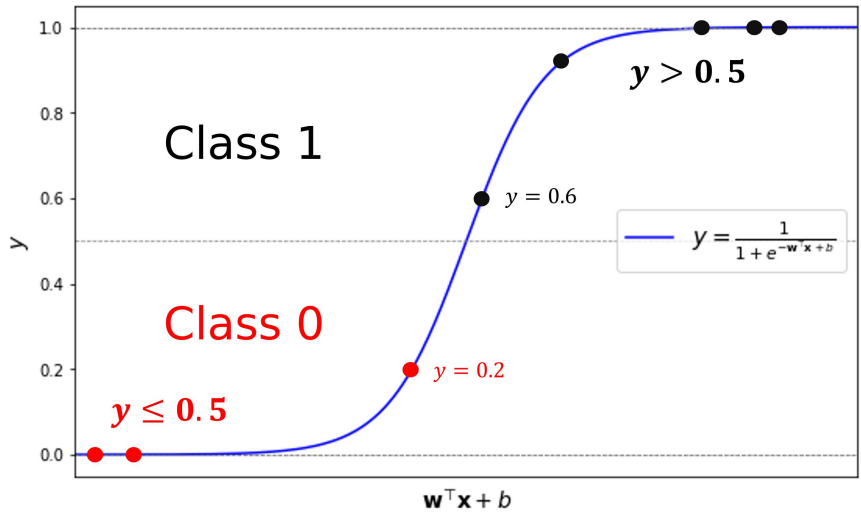

Figure 2.18: Working principle of the sigmoid function in logistic regression. Input features that result in a y-value smaller than or equal to 0.5 are classified as 'class 0', indicated in red. $y > 0.5$ gets classified as 'class 1', indicated in black.

Classifier model performance (such as logistic regression models) can be assessed by calculating its sensitivity and specificity, see chapter 3. These concepts take into account the number of correct and incorrect classifications the model makes for both class 0 and 1. A visual tool that is often used for this purpose is the confusion matrix of which an example is shown in Figure 2.19. A model is considered accurate if the rate of correct classifications (true positives and true negatives) is much higher than the rate of incorrect ones (false positives and false negatives).

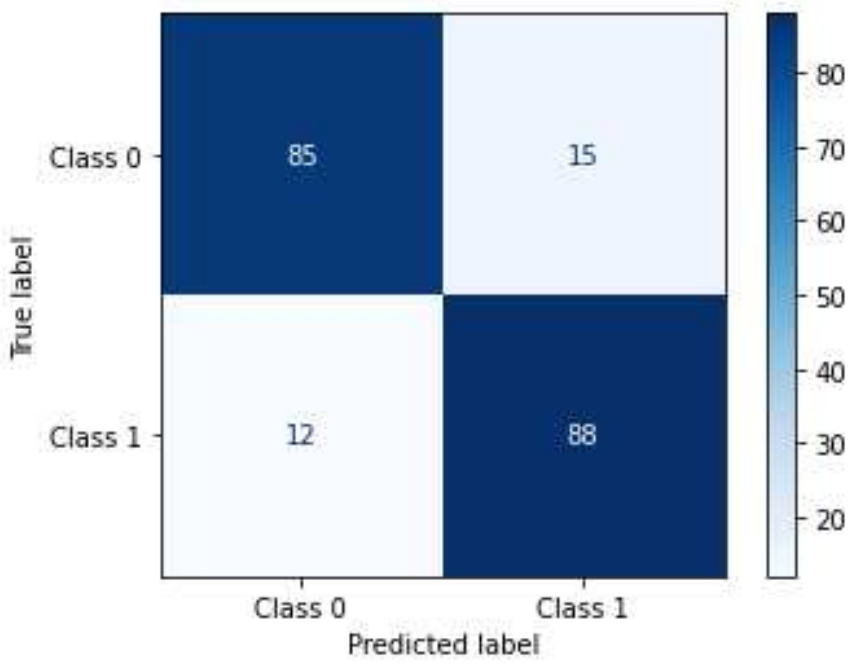

Figure 2.19: Example of a confusion matrix constructed to evaluate the performance of a logistic regression model. Going from left to right and top to bottom, the first cell shows the number of true positives. Here, the model classifies an input datapoint as belonging to class 0, while its real class does indeed belong to that class. Second, there is the number of false negatives, followed by the number of false positives. Finally there is the number of true negatives.

2.4.4.2 Deep learning

Deep learning is a subset of machine learning that employs neural networks with multiple layers, known as deep neural networks (DNNs), to model complex, non-linear patterns in data. At its core, a neural network is composed of interconnected layers of units called neurons, each of which performs a computation similar to logistic regression. Specifically, each neuron computes a weighted sum of its inputs, adds a bias term, and passes the result through a non-linear activation function, such as the sigmoid or ReLU (Rectified Linear Unit) function.

In fact, logistic regression can be viewed as a single neuron in a neural network: it takes input features, applies weights and a bias, and outputs a probability via the sigmoid function. Deep learning extends this concept by stacking many such neurons across multiple layers. These models are typically trained using supervised learning, where the training dataset includes both input features and corresponding target labels. While deep networks

can also be used in unsupervised or self-supervised settings, supervised learning remains the most common paradigm.

An example of supervised deep learning is U-Net and U-Net inspired networks – relevant for chapter 7 – that are popular for biomedical image and signal processing [171–174]. U-Net was introduced by Ronneberger et al. in 2015 to address the challenge of segmenting biomedical images with limited annotated data, a common constraint in medical imaging tasks [175]. The U-Net architecture is particularly effective for biomedical image segmentation due to its ability to capture both global context and fine details.

U-Net is a convolutional DNN architecture, shown in Figure 2.23, characterized by its use of convolutional layers where the learnable 'weighted sum' computed by individual neurons includes a convolution operation, analogous to digital filtering, exemplified in Figure 2.20. In this context, these filters are often called kernels with typically small dimensions e.g., a 3×3 matrix. Convolutional layers, characterized by fewer parameters than fully connected neural networks, generate feature maps that emphasize distinct patterns such as edges, textures, and other pertinent features in two-dimensional biomedical images. These layers are integral components of the U-Net architecture, which consists of two primary sections.

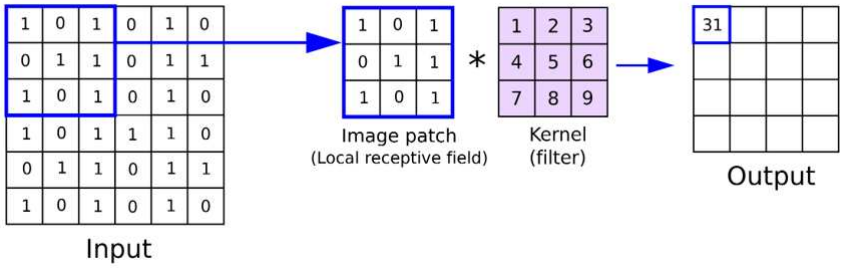

Figure 2.20: Example of one convolution operation in a convolutional layer with a 3×3 kernel. The operation returns a feature map with altered dimensions according to: Output size $= \left\lfloor \frac{N+2P-K}{S} \right\rfloor + 1$, going from 6×6 for the input to 4×4 for the output. $N = 6$ is the size of the input, $K = 3$ the size of the kernel, $P = 0$ the amount the input is zero padded and $S = 1$ is the stride of the convolution. $\lfloor x \rfloor$ is the 'floor' operation. Figure implemented from [176].

First, there is the contracting path or *encoder*. This part captures context through successive convolutional and pooling layers, which progressively reduce the spatial dimensions of the feature maps while increasing the depth, i.e. creating more feature channels. Each convolutional layer

is typically followed by a ReLU activation function and a max-pooling layer that downsamples the feature maps. The ReLU activation function: $\mathrm{ReLU}(x) = \max(0,x)$ introduces nonlinearity which allows for learning of more complex patterns in data that are not possible with just linear transformations. An example of a pooling operation is given in Figure 2.21.

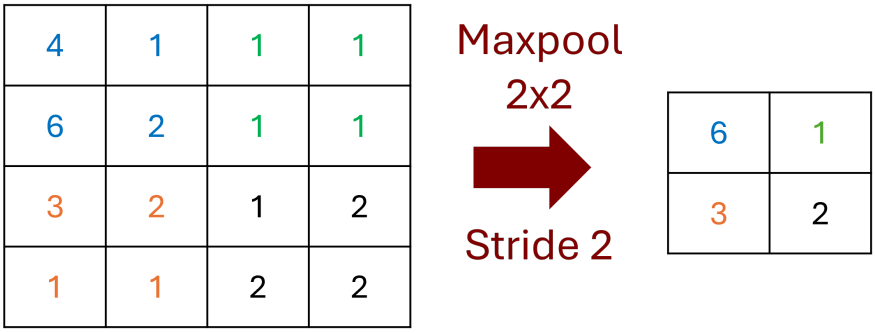

Figure 2.21: Example of a max pool operation. This example utilizes a 2×2 filter operation with stride (the number of pixels by which the convolutional filter moves across the input image or feature map) equal to two. The input is a 4×4 feature map. The output has dimensions 2×2.

Second is the expansive path or *decoder*. It aims to recover spatial information through upsampling and concatenation with high-resolution features from the contracting path. The upsampling is usually performed using transposed convolutions (also known as deconvolutions) to reconstruct an output from the feature maps that has the same dimensions as the input. An example is provided in Figure 2.22. The concatenation step (also referred to as skip-connections) ensures that the network retains fine-grained details that are crucial for accurate processing of the model output for medical purposes e.g. the preservation of edges for image segmentation. The skip connections between the encoder and decoder merge feature maps from the contracting path directly with the expanding path. In this way, U-Net combines low-level detail information with high-level contextual information across the network. This helps recover spatial hierarchies lost during pooling operations in the contracting phase.

A DNN is trained using a designated training dataset, which must be sufficiently large and representative of the target application domain to ensure effective generalization. The size of the training dataset should scale proportionally with the complexity and capacity of the network architecture. During training, the model iteratively processes the entire training dataset over multiple epochs. Training involves minimizing a loss function that quantifies the difference between predicted and true labels. Common

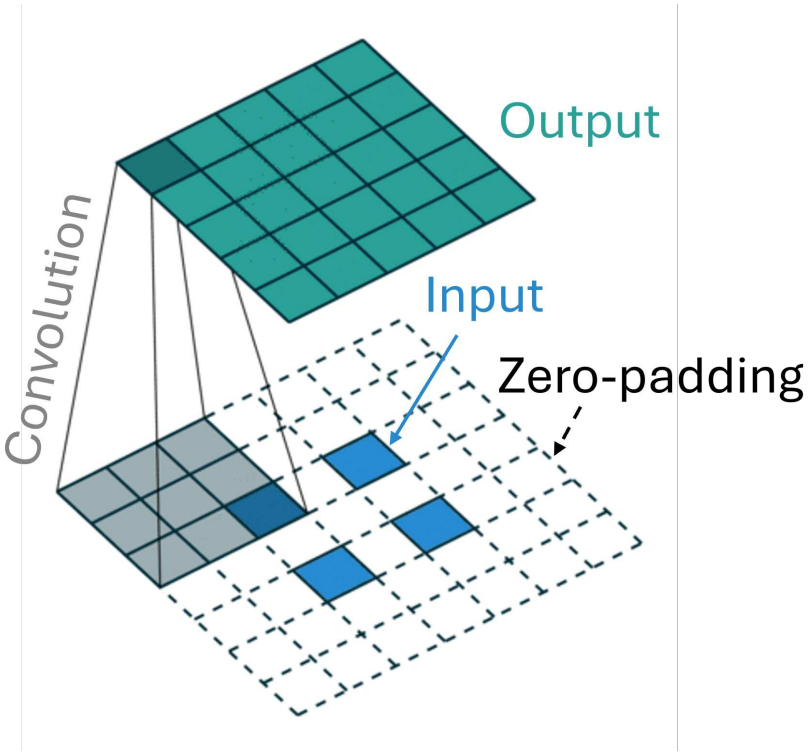

Figure 2.22: An example of a transposed convolution (or deconvolution) with a kernel of size 3×3. The input feature map has been zero-padded to achieve a higher-dimensional output. Figure adapted from [177]

choices include mean-squared error or cross-entropy loss and Dice coefficient loss, the latter two being particularly suited for segmentation tasks. Optimization is typically performed using stochastic gradient descent or adaptive methods such as Adam (Adaptive Moment Estimation).

At regular intervals, the models performance is evaluated using a separate validation dataset. This dataset consists of previously unseen examples and serves to provide an intermediate assessment of its accuracy and helps in tuning hyperparameters or implementing early stopping. Upon completion of the training phase, the model is evaluated on a third dataset, the test set, which also comprises unseen data. This final evaluation provides an unbiased estimate of the model's performance and generalization capability on new, real-world data.

U-Net can be adapted to 3D or 1D applications where the architecture is also of significant interest when the objective is to learn both short and long-range dependencies in the input data. This is particularly relevant in tasks such as heart rhythm analysis from ECG or PCG data [178–181],

where capturing temporal patterns at multiple scales is crucial for accurate interpretation and diagnosis. Performance metrics used to evaluate a model vary depending on the specific task and the nature of the input-output data.

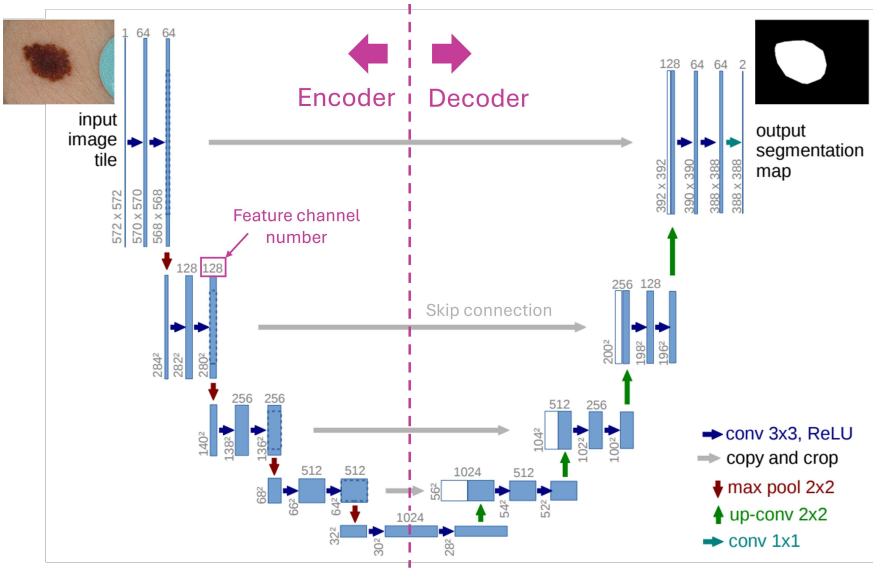

Figure 2.23: The original U-Net architecture with an added example of input medical image and output segmentation. The encoder and decoder parts of the network are indicated. The individual operations are colour-coded. Figure adapted from [174, 175]

II

Laser-Doppler Vibrometry Carotid-Femoral Signal-Quality Enhancement and Pulse Transit Time Estimation

CHAPTERS

3 Laser Doppler Vibrometry Signal Quality for Carotid-Femoral Pulse Wave Velocity **53**

4 Beamforming Laser Doppler Vibrometer Sensor Arrays **81**

5 Real-Time Pulse Wave Velocity Estimation 101

CHAPTER 3

LASER DOPPLER VIBROMETRY SIGNAL QUALITY FOR CAROTID-FEMORAL PULSE WAVE VELOCITY

POSITIONING OF THE CHAPTER

This chapter is a copy of the publication *Template matching and Matrix Profile for Signal Quality Assessment of Carotid and Femoral Laser Doppler Vibrometer Signals* (Seoni, S.*, Beeckman, S.*, Li, Y., Aasmul, S., Morbiducci, U., Baets, R., Boutouyrie, P., Molinari, F., Madhu, N., & Segers, P., Frontiers in Physiology, vol. 12, 11 January 2022,doi: https://doi.org/10.3389/fphys.2021.775052) [27] (* co-main author). The sections in introduction, methods, results and discussion on matrix profile were conceptualized and written by the author. The represented analyses in those sections were performed by the author. The publication as a whole was proofread and finetuned by the author in conjunction with prof. Segers, prof. Madhu, prof. Morbiducci, prof. Molinari and dr. Seoni.

ABSTRACT

Background: Laser-Doppler Vibrometry (LDV) is a laser-based technique that allows measuring the motion of moving targets with high spatial and

temporal resolution. To demonstrate its use for the measurement of carotid-femoral pulse wave velocity, a prototype system was employed in a clinical feasibility study. Data were acquired for analysis without prior quality control. Real-time application, however, will require a real-time assessment of signal quality. In this study, we (1) use template matching and matrix profile for assessing the quality of these previously acquired signals; (2) analyze the nature and achievable quality of acquired signals at the carotid and femoral measuring site; (3) explore models for automated classification of signal quality.

Methods: Laser-Doppler Vibrometry data were acquired in 100 subjects (50M/50F) and consisted of 4–5 sequences of 20-s recordings of skin displacement, differentiated two times to yield acceleration. Each recording consisted of data from 12 laser beams, yielding 410 carotid-femoral and 407 carotid-carotid recordings. Data quality was visually assessed on a 1–5 scale, and a subset of best quality data was used to construct an acceleration template for both measuring sites. The time-varying cross-correlation of the acceleration signals with the template was computed. A quality metric constructed on several features of this template matching was derived. Next, the matrix-profile technique was applied to identify recurring features in the measured time series and derived a similar quality metric. The statistical distribution of the metrics, and their correlates with basic clinical data were assessed. Finally, logistic-regression-based classifiers were developed and their ability to automatically classify LDV-signal quality was assessed.

Results: Automated quality metrics correlated well with visual scores. Signal quality was negatively correlated with BMI for femoral recordings but not for carotid recordings. Logistic regression models based on both methods yielded an accuracy of minimally 80% for our carotid and femoral recording data, reaching 87% for the femoral data.

Conclusion: Both template matching and matrix profile were found suitable methods for automated grading of LDV signal quality and were able to generate a quality metric that was on par with the signal quality assessment of the expert. The classifiers, developed with both quality metrics, showed their potential for future real-time implementation.

3.1 INTRODUCTION

The aorta and large central arteries fulfil key physiological functions in the circulation, whereby their structure is apt to their function. They consist of complex composite soft tissues, concentrically organized in lamellar units, where sheets of elastin intertwine with layers of vascular smooth-muscle

cells in a matrix of collagen and other proteins composing the extra-cellular matrix [49]. This allows the aorta and large arteries to distend when the heart contracts and blood is ejected into the aorta and store elastic energy in the arterial wall, which is used during the relaxation phase of the heart to maintain blood pressure and drive the perfusion of organs and tissues. This function is also referred to as the "windkessel" or buffering function of the large arteries, and ensures that the pulsatile blood flow generated by the heart is transformed into a near steady flow when reaching the smaller arteries [35]. It prevents excessive maximal (systolic) and too low minimal (diastolic) blood pressure. Arterial stiffening leads to a loss of this buffering function with detrimental effects on nearly all organ systems, and especially low resistance organs such as the brain, the kidneys and the heart itself [7]. Arterial stiffening has received large attention over the past 3 decades, and there is a consensus that assessment of arterial stiffness is especially relevant in the assessment of an individual's risk for cardiovascular disease and death [8, 75].

Because of the distensible nature of arteries, cardiac contraction generates a wave (detectable as a change in pressure, flow or arterial diameter). This wave initially propagates from the heart to the periphery, but increases in complexity as it interacts on its way with the branching arterial tree and gets shaped because of wave reflection and transmission [7, 9, 182, 183]. The wave speed, or pulse wave velocity (PWV), is directly linked with the distensibility of the arteries (the stiffer the artery, the higher PWV) [63], and the current clinical standard method to measure arterial stiffness is by measuring the pulse wave velocity [11]. In essence, the method is simple and straightforward: one detects the pulse at two locations a distance dx apart, and from the time delay, PTT, between the signals, one gets PWV = dx/PTT. Despite the simplicity of the concept, there are still many hurdles in measuring PWV in practice, mainly related to the non-availability of sites to directly measure the pulse along the path of the aorta in a non-invasive way and without the need of clinical scanners [11]. Accessible sites closest to the aorta are the neck (carotid artery) and groin (femoral artery) and carotid-femoral PWV is considered the best possible proxy for aortic PWV [8].

Several sensors can be used to detect the pulse in the neck and groin [11, 184], including applanation tonometry, ultrasound (pulsed Doppler recordings) or accelerometers. Motivated by the relatively high cost of equipment, the required level of expertise by the operator or contact-based nature of the measurement, we and others have explored the use of laser Doppler vibrometry to detect the motion of the skin atop the carotid and/or femoral arteries in response to the passage of the arterial pulse [20–22, 185, 186].

To eliminate motion drift and amplify the fast displacements associated with the arrival of the foot of the pulse [186], we have been using skin acceleration as the basic signal from which to derive time delays between the neck and groin for measuring carotid-femoral PWV.

The feasibility of the method has been shown using industrial-type LDV sensors [22], and we have been working on the design and development of a multi-beam handheld device. The core of the device is a silicon photonics chip integrated in a micro-optical system which allows for flexible and compact multi-array designs [18, 19]. A first prototype (consisting of 2 connected yet separable handheld pieces to measure in the neck and groin with each 6 laser beams) was developed within the context of the H2020-funded project CARDIS and included a clinical feasibility study whereby carotid-femoral PWV was assessed in 100 patients and compared with a reference method based on applanation tonometry [25]. Measurements were performed with a minimal visual feedback during the measurements and and all the analyses were carried out in off-line modality.

A next generation version of the device is under development and will provide real-time measurement of carotid-femoral PWV. To do so, we need real-time assessment of the quality of incoming data to decide whether or not data records are of an acceptable quality for subsequent processing. This is, however, not a trivial assessment as there is little reference as to what makes LDV signal recordings appropriate for PWV estimation.

The aim of this study is therefore to identify a strategy to objectively and automatically assess the LDV-signal quality and set criteria for future use of this technology in arterial pulse detection. To do that we will use the existing CARDIS database of LDV recordings at the carotid and femoral measurement sites and subject them to two different strategies: the template matching and the matrix profile will be tested for (1) analysing the nature and achievable quality of the recorded signals, and (2) exploring models for an automated classification of LDV-signal quality.

3.2 METHODS

3.3 MATERIALS AND METHODS

3.3.1 The CARDIS device

Technical details on the optics and overall design of the CARDIS device have been described in [19]. Briefly, the device consists of two handpieces (handpiece 1 contains the handgrip of the device, handpiece 2 is the add-on part of the device: we refer to Figure 3.1 for an illustration of the device and the positioning of the handpieces), each sending out 6 laser beams

(wavelength 1550 nm), positioned along a line and 5 mm apart. The handpieces can be used separately for measurement of carotid-femoral PWV, or attached to measure signals on locations 25 to 50 mm apart, e.g. to locally measure pulse wave propagation along the carotid artery. A retro-reflective tape is attached to the skin at the measurement location to enhance reflection of the laser light, and the device is equipped with a spacer to ensure an appropriate optical focus distance and to stabilize measurements.

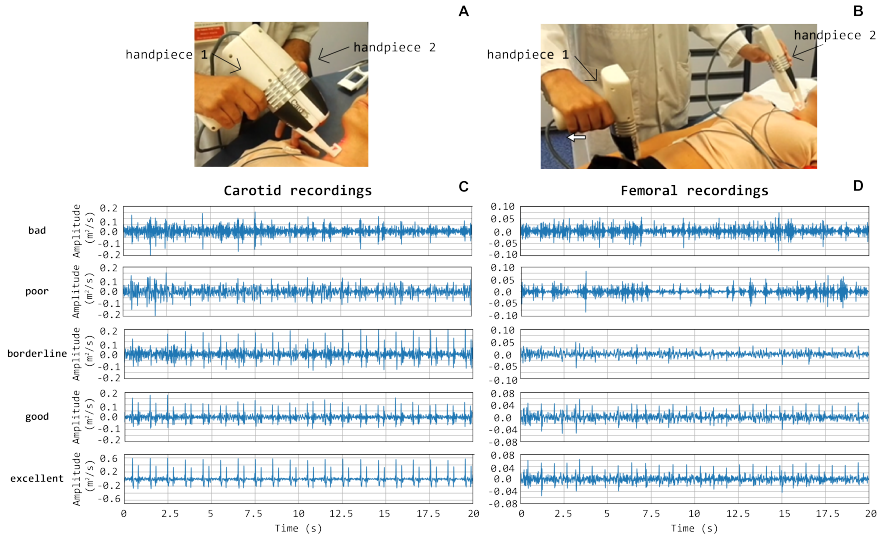

Figure 3.1: CARDIS device in configuration to measure carotid-femoral **(A)** and local carotid PWV **(B)**. **(C)** and **(D)** display representative tracings on the carotid **(C)** and femoral **(D)** measuring site receiving a visual grading score of 1 to 5. Especially in the excellent tracings, the foot-of-the-wave waveforms are clearly visible, with the same for the dicrotic notch waveforms in the local carotid case.

3.3.2 Study population and available database

The data used in this study were acquired with a clinical feasibility study in 100 patients, conducted at the Hôpital Européen Georges Pompidou (HEGP) in Paris, France, to assess the ability of the CARDIS device to measure signals in a configuration with simultaneous carotid-femoral or carotid-carotid recordings. Patients were in the age range 19-85 and presented with mild to stage 3 hypertension, controlled or not [25]. For each subject, 4 to 5 datasets, each consisting of 20 second traces on 12 channels measured with the two handpieces, were acquired. In detail, the analysed database was made of 410 datasets (4920 waveforms) from carotid-femoral recordings, and of 407 datasets (4884 waveforms) from carotid-carotid recordings. Raw IQ (In-phase and quadrature) LDV-data were acquired at a

sampling frequency of 100 kHz, and LDV-displacement data were down-sampled to 10 kHz upon demodulation. A low-pass filter with cut-off frequency of 30 Hz was applied to LDV displacement data, which were differentiated twice to yield acceleration. The same low-pass filtering strategy was applied after each differentiation operation.

3.3.3 Visual scoring of the data

A graphical interface displaying all the LDV acceleration signals derived from the six channel recordings per each handpiece was implemented in MATLAB environment (The MathWorks, Naticks MA, US). The acceleration signals were visually scored by an expert operator (Segers P.) on a 5-level grade scale taking values Q_{vis} according to table 3.1.

Table 3.1: The 5-levels grade scale taking values Q_{vis}

Quality score Q_{vis}	Quality	Description
Score 1	Bad	Acquisition with no evidence of repeatable features that may be linked to the detection of a pulse
Score 2	Poor	Very noisy acquisition not suitable for analysis, but with identifiable pulses within the noisy trace
Score 3	Bordeline	Acquisition affected by noise but presenting clear repeatable patterns. Advanced signal processing algorithms could remove the noise and allow to detect the foot of the pulse wave with reasonable affordability
Score 4	Good	Acquisition with sharp and pronounced peaks at the foot (and dicrotic notch), with relatively low noise levels between successive pulse peaks
Score 5	Excellent	Acquisition with very sharp and pronounced peaks at the foot (and dicrotic notch), with low noise levels in between the peaks. Signals of textbook quality

Note that the presence of brief artefacts in the 20 second acquired traces was not used as a criterion to score the signal quality. As such, signals qualified as excellent may still demonstrate a brief episode of poor data. Overall, the femoral data were of a markedly lower Q_{vis} 'quality' than traces recorded at the carotid artery, which impacted the rating. Therefore, the Q_{vis} quality score 3 (borderline) was given to femoral traces that appeared to be of a much lesser quality than $Q_{\text{vis}} = 3$ rated carotid traces. Such a borderline score was assigned when 5-10 beats were discernible in the signal. Representative carotid and femoral signals receiving the different scores are displayed in Figure 3.1.

3.3.4 Template matching

Template matching technique is an effective approach for the automatic detection of a priori identified patterns in signal recordings [145, 146] and images [144]. A good-quality carotid LDV acceleration signal presents two sharp peaks for each heartbeat: the first peak corresponds to the systolic

rapid upstroke of pressure and demarcates the foot of the arterial pulse; the second peak denotes the wave that is generated at the moment of closure of the aortic valve (the dicrotic notch). The LDV-femoral recording is devoid of clearly identifiable features related to the dicrotic notch because of the distance of the measurement site from the heart, whose final effect is filtering the recorded LDV pulses, in the femoral artery. An example of displacement, acceleration and ECG signals together are shown in Figure 3.2.

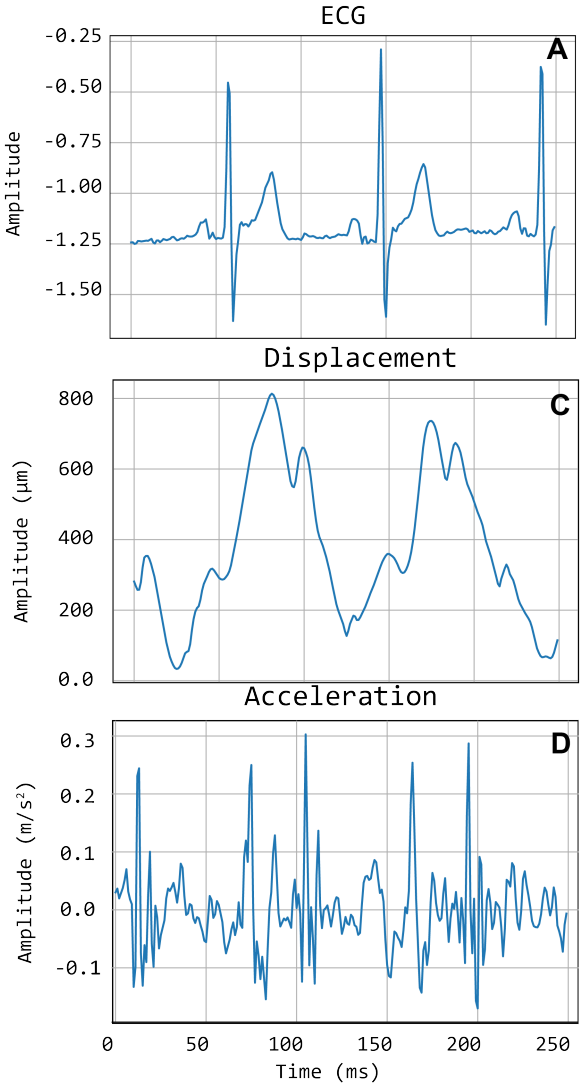

Figure 3.2: *An example of Cardis data.* ***(A)*** *shows the ECG signals,* ***(B)*** *shows the displacement signal and* ***(C)*** *the corresponding acceleration signal.*

3.3.4.1 Constructing the templates

High-quality carotid and femoral LDV-acceleration traces were adopted for template construction. Traces with visual score value Q_{vis} of 4 and 5 were selected. To avoid subject-specific biasing in template construction, only one 20 s recording (from the acquired channel with highest Q_{vis}) per subject was selected. Based on these selection criteria, 135 carotid LDV-acceleration traces from 20 different subjects and 40 femoral LDV-acceleration traces from 10 different subjects were identified as suitable for template construction in the CARDIS dataset. The selected carotid LDV-acceleration traces were from both handpieces.

The selected traces, characterized by the presence of sharp and pronounced peaks at the foot (and dicrotic notch for carotid recordings), were then segmented in epochs, each one corresponding to a single heartbeat. LDV-acceleration trace segmentation was carried out using ECG synchronous recordings (available for each subject in the CARDIS dataset, on which automatic R-peak detection was carried out, see Figure 3.3). Over each LDV trace single epochs were then defined within a time interval within the occurrence of two consecutive R peaks in the ECG trace (Figure 3.3A). By construction of the visual inspection classification, some of the identified single epochs might still not be of adequate quality for template construction, because of the presence of short-time artifacts/noise (Figure 3.3B). The lower quality single epochs in a LDV-acceleration trace were identified according to the following strategy: (1) for each LDV segmented trace a correlation matrix R_{ij} was built up, each element of the matrix being the Pearson-correlation coefficient between epochs i and j, used as a measure of their shape similarity; (2) a threshold value of the correlation coefficient was defined and single epochs with an average correlation coefficient with all the other epochs lower than the threshold was discarded, since they were not sufficiently similar in shape to the other epochs in the recorded trace (Figure 3.3C); (3) for each LDV-acceleration trace an 'individual template' was built up by averaging only the identified highly correlated epochs (Figure 3.3D); (4) by adopting the same approach with the carotid and femoral LDV-acceleration traces, the final carotid and femoral 'population templates' were obtained (Figure 3.4).

Template construction is based upon the definition of a strategy to treat the issue of the different time length of single epochs (intra-individual RR variability) [187, 188] and of the individual templates as well. Hence, the time length of single epochs should be defined on the basis of what the template should represent. In the case under study, the carotid LDV-acceleration template longer than 350 ms will include by construction the foot of the wave (first peak) and the dicrotic notch (second peak). Here

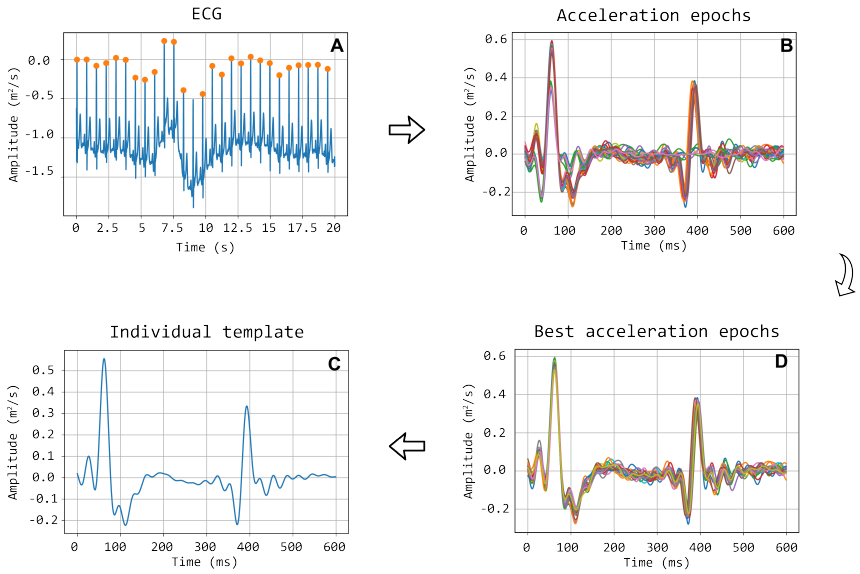

Figure 3.3: *Workflow detailing the construction of the template. Illustration of selection of good quality epochs using the correlation coefficient.* ***(A)*** *ECG signal with detected R peaks, which are used to segment the acceleration signal into heartbeat epochs* ***(B)****. After the correlation matrix analysis, only the good epochs maintained* ***(D)****. In* ***(C)*** *the final individual template, calculated as the average of the good epochs, is displayed.*

we speculate that a carotid LDV template incorporating the second peak may degrade in performance, as the distance between the two peaks is (intra-individually as well as inter-individually) variable. In figure 3.5, carotid and femoral LDV-acceleration templates constructed for different (predefined) time length are displayed. In detail, time lengths of 300, 400 and 500 ms were considered for the femoral LDV-acceleration template, and time lengths of 200, 400 and 600 ms for the carotid LDV-acceleration template. The impact of the time length in the LDV template performance when used for the automatic assessment of the quality of the CARDIS data was evaluated.

3.3.4.2 Template matching and beat selection

The matching between the templates and the LDV-acceleration traces in the CARDIS dataset was performed by applying a local moving-window function calculating the Pearson's correlation coefficient between the LDV template and the 20 s-long acceleration trace at each time step, as displayed in Figure 3.6. The locations of peaks in the time series resulting from this moving-window cross-correlation operation identify the time instants where the sliding template is similar to a segment of the LDV-acceleration trace.

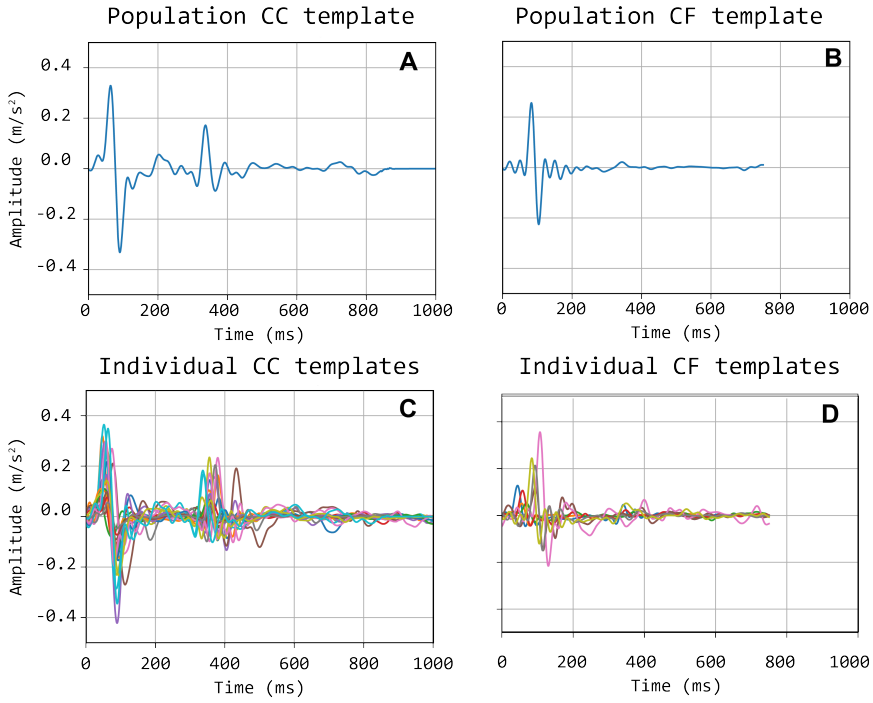

Figure 3.4: *Bottom **(C & D)**: individual carotid (CC) and femoral (CF) templates; Top **(A & B)**: population-average carotid and femoral templates.*

Setting a threshold for the value of the cross-correlation coefficient then demarcates the correspondence level above which segments of the LDV-acceleration trace can be considered similar to the template. Based on the set threshold value, single segments corresponding to single heartbeats in the LDV trace can be considered of sufficient or not sufficient quality.

To further improve the identification of high-quality heartbeats in the LDV recorded traces, two further selective criteria were added. Firstly, all the LDV-acceleration peaks in the recorded trace with an amplitude lower than the 80% of the average peak amplitude were not considered. Then, if two successive peaks were detected within a time window shorter than 500 ms, the second peak was discarded and only the first one was considered. The latter criterion was adopted to avoid the dicrotic notch detection (second peak), especially when the shorter carotid template was used. An explanatory example of peak detection, presenting the LDV-acceleration trace, the moving-window cross-correlation function and detected peaks is displayed in Figure 3.7.

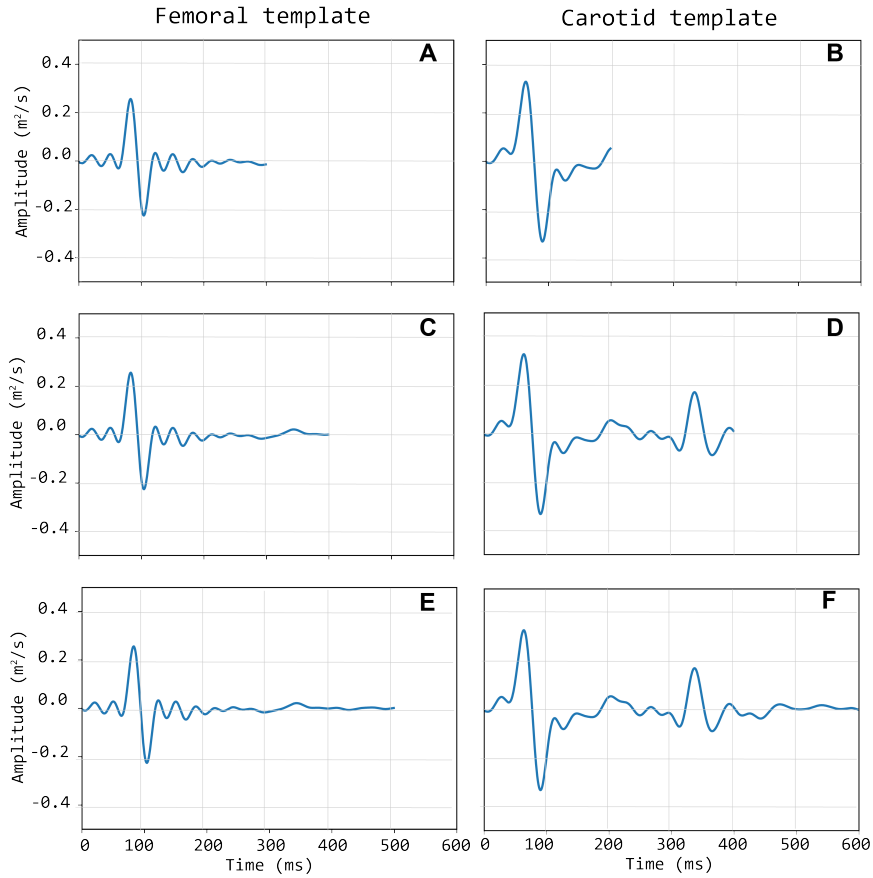

Figure 3.5: *Left column **(A, C & E)**: three different length of the femoral template; Right column **(B, D & F)**: three different lengths of the carotid template.*

3.3.4.3 LDV traces classification based on template matching - finding threshold values

The performance of the template matching algorithm in classifying the quality of the CARDIS dataset was evaluated by comparison with visual score classification, according to the following scheme: acceptable heartbeat (label 1), corresponding to Q_{vis} values 4 or 5; not acceptable heartbeat (label 0) corresponding to Q_{vis} values 1 or 2. Signals with Q_{vis}-values of 3 are discarded in this analysis as these signals are difficult to assign an absolute and correct classification (see discussion). The template matching-based c classification, as also mentioned before, depends upon the threshold value for the moving-window correlation function and the number of detected heartbeats in the LDV-acceleration trace, which have to be appropriately set.

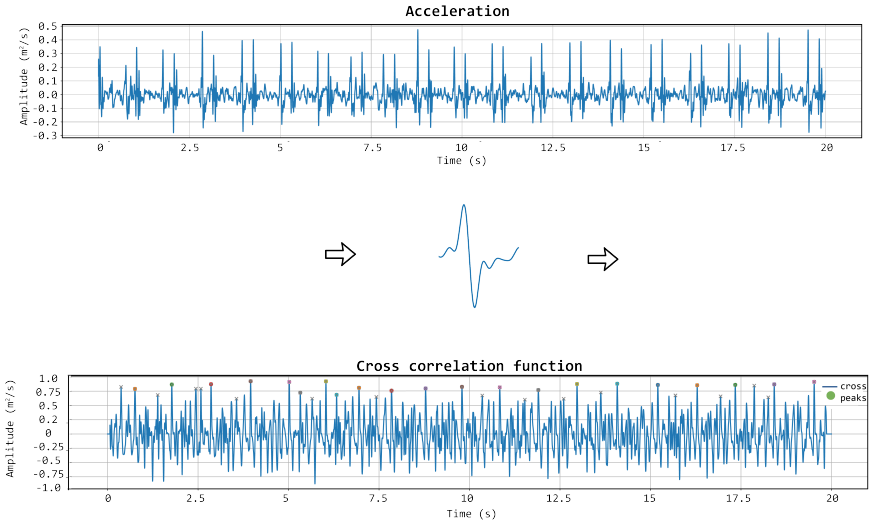

Figure 3.6: *The template matching algorithm is shown. The chosen template (displayed in the middle row of the figure) is iteratively correlated with the acceleration signal to get the cross correlation function. In that function, the appropriate peaks are then identified.*

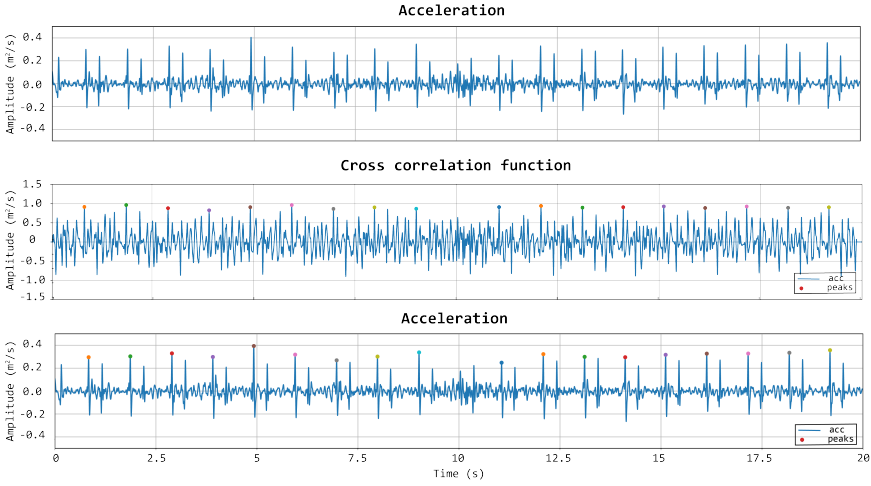

Figure 3.7: *First row: acceleration signal. Second row: normalised cross-correlation function and its maximum values of the acceleration signal with the femoral template of 500 ms. Last row: acceleration signal with the detected peaks using the template matching method.*

Here, we considered: true positive (TP) an acceptable LDV trace (based on Q_{vis} classified by the template matching as acceptable; false negative (FN) an acceptable LDV trace classified by the template matching as not acceptable; true negative (TN) an unacceptable LDV trace classified by the template matching as not acceptable; false positive (FP) an unacceptable LDV trace classified by the template matching as acceptable. On this basis, sensitivity and specificity values of the classifier are defined as:

$$\text{Sensitivity} = \frac{TP}{TP+FN} \tag{3.1}$$

and

$$\text{Specificity} = \frac{TN}{TN+FP} \tag{3.2}$$

Sensitivity and Specificity were then used to build up the Receiver Operating Characteristic (ROC) curves and their area under the curve (AUC) was used to assess the performance of the classifier. Moving-window cross-correlation coefficient threshold values and number of detected heartbeats yielding the highest AUC were defined on the complete CARDIS dataset, and this for each one of the template lengths in time.

3.3.4.4 LDV traces classification based on template matching - defining quality score and testing on the CARDIS dataset

Once the best performing carotid and femoral templates time length and the associated moving-window cross-correlation threshold values were identified, a quality score (Q_{TM})was estimated for each 20 s LDV-trace recording, based on two main features.

The first feature (Q_1) is the number of the detected acceleration peaks (n_{peaks}), normalized with the maximum expected number of peaks or heartbeats in the 20 s LDV-trace recording ($\text{max}_{\text{peaks}}$). This value was empirically set equal to 26 to ensure a maximal feature value of 1 in the investigated database:

$$Q_1 = \frac{n_{\text{peaks}}}{\text{max}_{\text{peaks}}} \tag{3.3}$$

The second feature (Q_2) is defined as the average time delay between the occurrence of maximum value of each LDV-acceleration epoch in the recorded trace and the occurrence of the peak value on the template (d_{peak_n}), normalized to the template time length (N):

$$Q_2 = \frac{\sum_{n=1}^{n_{\text{peaks}}}(1-\frac{d_{\text{peak}_n}}{N})}{\text{max}_{\text{peaks}}} \tag{3.4}$$

When the peaks in the template and in each LDV epoch are all perfectly aligned, and when all the peaks in the LDV-trace are detected (i.e., $Q_1 = 1$), feature Q_2 is equal to 1, indicating good quality of the LDV trace recording. The final score based on template matching can be computed as the mean value of the partial scores Q_1 and Q_2:

$$Q_{\text{TM}} = \frac{1}{2}(Q_1 + Q_2) \tag{3.5}$$

By construction, the score Q_{TM} was set up so that the value is within the range $[0, 1]$ (with $Q_{\text{TM}} = 0$ representing the worst possible signal quality and $Q_{\text{TM}} = 1$ indicating that the signal is of excellent quality). Q_{TM} was calculated for all the traces in the CARDIS database and compared to the corresponding assigned visual score Q_{vis}, which is treated as the ground truth.

3.3.4.5 A logistic regression model for signal classification based on template matching

Q_{TM} Was a heuristically derived quality metric with equal weighting on the sub-components. Now we use logistic regression models to find a better weighting of the contributions of Q_1 and Q_2, and automatically map this to a predicted quality of the signal. Logistic regression models are chosen since they can be well applied to binary classification problems, and are typically used in medical research [168–170] when a two-class classifier is required. These predictions were then compared to the ground truth labels (given by the visual scores).

Logistic regression models were trained and tested with the two template-matching derived scores (3.3) and (3.4) as features, on both carotid and femoral LDV-acceleration traces. For this purpose, again the LDV traces visually scored with Q_{vis} equal to 1 or 2 were labeled 0, and LDV traces visually scored with Q_{vis} equal to 4 or 5, were labeled 1. Again, signals with Qvis score 3 were not included in the analysis.

The data available in the CARDIS database was split such that 80% was used for training the logistic regression model and the remaining 20% used for testing purposes. The training-testing set partition was randomly iterated 1000 times while storing the model accuracy every iteration, so that the overall accuracy distribution of the logistic regression model approach could be assessed.

Of note, all features used to train logistic regression models were normalized via standardization. This allowed the logistic regression-model coefficients to be interpreted as the corresponding feature weights, granting

information about which feature was most influential in labeling an LDV trace.

The accuracy distributions of logistic regression models trained on template-matching and the later discussed matrix-profile derived features were evaluated.

3.3.5 Matrix profile

The matrix profile is a data structure that annotates a time series [141, 142]. It allows for exact, simple and fast [139] similarity search or discord discovery and is among the state-of-the-art techniques in the field of discrete time-series analysis [140, 143]. The matrix profile has been used in processing biological signals like EEG [138], ECG and gait cycles [142]. It was applied here to accurately identify recurring waveforms in the LDV-acceleration data. Every such waveform is a subsequence of the original sequence or time series. These subsequences, taken togegher, are collectively called a motif. We gauged the quality of an LDV-measurement via several features determined by its best motif. The strength of the matrix profile lies in the fact that it does not require a template or other input parameters except for the length m of the desired motif subsequences. Analogous to the template matching analysis, waveforms were subsampled to 1 kHz. We set m to 200 ms, similar to the optimal length of the template described in previous sections.

3.3.5.1 Signal classification based on the matrix profile

A quality metric (Q_{MP}) was constructed based on three features of the matrix profile-generated motif as seen in (3.6). This metric was constructed so that its possible values lie between 0 and 1.

$$Q_{\mathrm{MP}} = A_{\mathrm{MP}}\, t_{\mathrm{d,MP}}\, n_{\mathrm{MP}} \tag{3.6}$$

The first feature used in calculating (Q_{MP}) is the average relative maximum amplitude of a subsequence in the motif (A_{MP}) computed as in (3.7). The maximum amplitude of a subsequence A_s was compared with the maximum amplitude of the reference subsequence A_{ref}. This reference is the first subsequence identified by the matrix profile (the minimum of the matrix profile) and subsequently included in the motif. In good quality measurements, most maximum amplitudes of subsequences in the motif were similar.

$$A_{\mathrm{MP}} = \frac{1}{n_{\mathrm{mtf}}} \sum_{n=1}^{n_{\mathrm{mtf}}} \frac{A_s}{A_{\mathrm{ref}}} \tag{3.7}$$

The second feature, the average relative time-instant of the subsequence peaks in the motif ($t_{d,MP}$), is computed as in (3.8). The time-instant of the subsequence peak was compared with that of the reference. This value was then normalized over the length of the subsequence m. Ideally, all subsequences in the motif represent the same heartbeat-related waveform with peaks at similar time instants. For poor quality signals, these time instants tended to randomly vary over the length of the subsequence.

$$t_{d,MP} = \frac{1}{n_{mtf}} \sum_{n=1}^{n_{mtf}} (1 - \frac{d_{peak}}{m}) \tag{3.8}$$

Lastly, the third feature (n_{MP}) was calculated as the expected amount n_{exp} versus the effective amount n_{mtf} of subsequences in the motif, shown in (3.9). n_{exp} was estimated based on a discrete-Fourier-transform analysis of the entire signal recording. More specifically, the peak corresponding to the heartbeat during the measurement was identified as the most prominent peak in the signal spectrum, in the range 0.5 - 1.5 Hz. The effective amount of subsequences in the motif n_{mtf} was based on how many heartbeats the matrix-profile technique was able to pick up.

$$n_{MP} = \frac{n_{mtf}}{n_{exp}} \tag{3.9}$$

Before a subsequence is included in the motif, three criteria decide the inclusion: (1) If a subsequence maximum amplitude was lower than 0.8 times the reference maximum amplitude it was excluded from the motif. (2) If the time instant of the peak deviated 30 ms or more from that of the reference, the subsequence was also removed from the motif. (3) If two subsequences were closer than 0.8 times the expected time delay between two subsequent heartbeats, the one with the lower matrix-profile value (higher similarity to the reference) of the two was preserved, the other was removed. The applied thresholds levels were determined empirically from excellent and poor quality signals. Figure 3.8 shows an example of a signal being scored by first finding the motif so that as many heartbeats as possible are present within it, then calculating the features of that motif. Both the relative amplitude and time-instant of subsequence peak features of one subsequence in the motif are indicated on the Figure.

The auto-generated matrix-profile based quality metric was computed for all carotid-carotid and femoral-carotid datasets and results were compared to the visual scores.

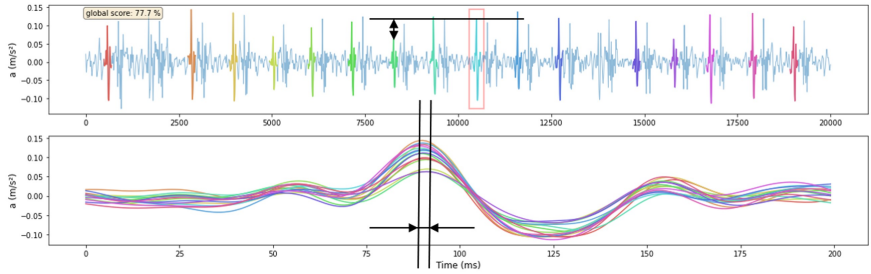

Figure 3.8: *Example of one signal being scored by the features that are derived from the Matrix-Profile-identified motif. The amplitude feature of one subsequence is shown in the upper figure, the reference is indicated with a red square. The time-instant of subsequence peak feature is shown in the lower figure where all subsequences shown in the upper figure are time-aligned. Signal score is shown in the upper left corner of the upper Figure. The visual score of this signal is 4.*

3.3.5.2 A logistic regression model based on the matrix profile

Similar to template matching, we also designed logistic regression models using the previously discussed matrix-profile derived features. These models allowed for more freedom in weighting the features to come to a better classification result. Models were trained and tested on the three features mentioned above. Signals were labeled and available data was split into training and testing sets analogous as in the previously discussed template-matching case.

3.3.6 Relation between signal quality and physiological variables

Lastly, we investigated the existence of possible associations of quality of the LDV-acceleration traces with age, body mass index (BMI) and systolic blood pressure. The statistical analysis was performed using Q_{MP} as quality score variable. In detail, the existence of a linear correlation was tested using the Pearson-correlation coefficient on both CC and CF datasets, with data analysed per handpiece. For all analyses, significance was assumed for $p < 0.05$.

3.4 Results

3.4.1 Visual scoring

3.4.1.1 Carotid-carotid measurements

By visual inspection, about 12% of all LDV-acceleration traces were qualified as bad and close to 30% as poor (Figure 3.9, panel B). Which implies that about the 42% of the recorded LDV traces was evaluated to not be

of sufficient quality for further analysis. About 22% of all recordings was scored from good to excellent, and are deemed suitable for further analysis. About 37% of the traces was visually scored borderline, i.e. these traces might be of sufficient quality for further analysis with advanced processing. The number of LVD traces scored with Q_{vis} 4 or 5, and recorded using handpiece 2 was higher than the number using handpiece 1. For handpiece 1, channel 1 scored almost systematically very low; the best channels were channels 3 and 4. For the second handpiece, the best channels were channels 2 and 3.

3.4.1.2 Carotid-femoral measurements

The bottom row of Figure 3.9 illustrates that, concerning femoral LDV-acceleration traces (handpiece 1), 20% of all recordings was qualified as bad, and another 32% as poor, meaning that over 50% of all recordings is not usable for analysis. About 15% of the measured signals get a score good to excellent, deemed immediately suitable for analysis. Best channels are channels 3 and 4 with 21.9% (beam 3) and 19.5% (beam 4) of the recordings good to excellent. For handpiece 2 (carotid recordings), about 20% gets a score good to excellent. This is less than what was obtained for handpiece 2 for the carotid-carotid recordings, where close to 25% of all recordings were rated good to excellent. On the other hand, less signals received grade 1 and 2. Best channels are channels 4 (24.9%) and 5 (24.1% of the recordings scoring good to excellent).

3.4.2 Template matching

3.4.2.1 Carotid-carotid (CC) measurements

From the analysis carried out on the complete CC dataset, it emerged that using the carotid template of 200 ms length guarantees the best performance in terms of specificity, setting the cross-correlation threshold to 0.74 and the minimum number of detected heartbeats per trace to 15 (AUC = 0.89, sensitivity 74%, specificity 89%; template of 400 ms length: AUC = 0.89, sensitivity 81%, specificity of 83%; template of 600 ms length: AUC = 0.92, sensitivity 87%, specificity 86%). For each template length, the corresponding confusion matrix is presented in Table 3.2. The adoption of specificity for the evaluation of the performance of the template matching strategy was dictated by the need of maximizing the removal of LDV traces with inadequate quality. More in detail, it emerged that in general the template matching performed excellently in correctly classifying visual scores 1 and 5, while accuracy decreased for visual scores 2 and 4 (Table 3.2). Interestingly, using the shorter template length of 200 ms led to score 42% of the LDV acceleration traces visually scored 3 (borderline) as acceptable data.

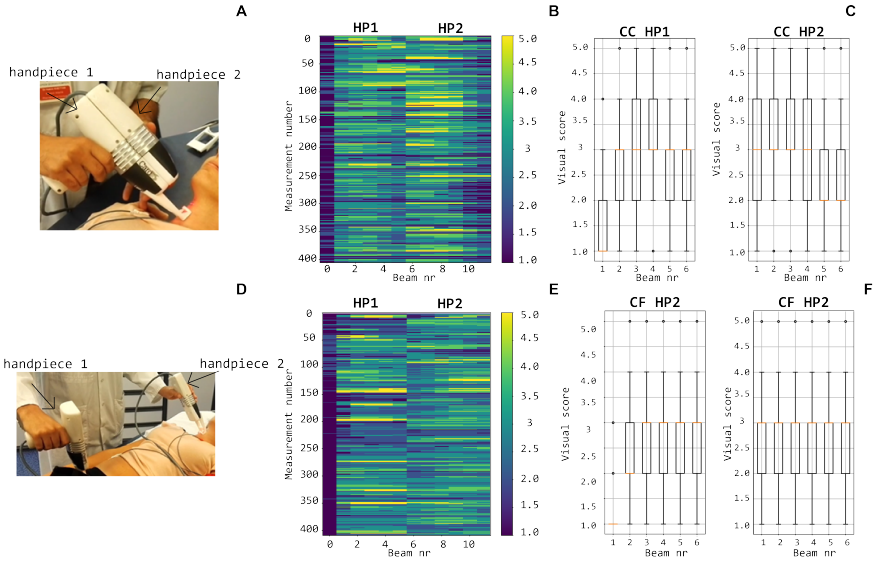

Figure 3.9: Top row: visual scoring of signals measured with handpiece 1 and 2 during local carotid measurements **(A)** with overall grades shown in **(B)** and box plots and mean values per channel in **(C)**. Bottom row: visual scoring of signals measured during carotid-femoral PWV measurements **(D)** with overall grades shown in **(E)** and box plots and mean values per channel in **(F)**.

Table 3.2: Confusion matrices of signal classification done by the hand-engineered classification model constructed with template matching. Signals classified in this table were measured at the carotid and the templates used were the carotid population templates.

	Template of 200ms		Template of 400ms		Template of 600ms	
Carotid recordings	TM score 0	TM score 1	TM score 0	TM score 1	TM score 0	TM score 1
score 1	97%	3%	97%	3%	97%	3%
score 2	86%	14%	86%	14%	82%	18%
score 3	58%	42%	55%	45%	44%	56%
score 4	29%	71%	30%	70%	15%	85%
score 5	8%	92%	19%	81%	6%	94%

The level of agreement obtained between Q_{TM} and Q_{vis} on the CC recordings dataset, with template matching adopting a 200 ms template length, is presented in Figure 3.10. This suggests that the median of the Q_{TM} values, computed on traces that have a $Q_{\text{vis}} = 3$, could be adopted as a threshold value for the automatic quality checking of an LDV trace (i,e. in the case under study, traces with a $Q_{\text{TM}} > 0.5$ could be considered of adequate quality; note that, manually setting these thresholds is not required for the logistic regression models since this is implicitly learnt in the training).

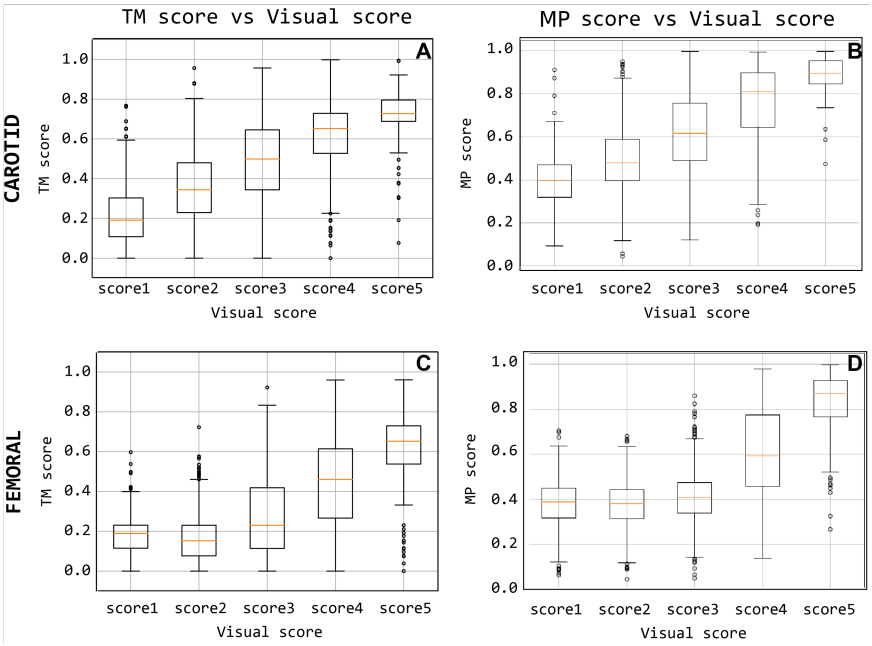

Figure 3.10: *Quality score comparison between visual score and the template-matching-derived and matrix-profile-derived. Subfigures* ***(A)*** *and* ***(C)*** *display the score based on the template matching and* ***(B)*** *and* ***(D)*** *quality score based on the matrix profile.*

The accuracy distributions of logistic regression models trained on quality scores derived from template-matching are displayed in figure 3.11 (3.11A- 3.11B). On average, the accuracy on traces acquired using handpiece 2 is higher than handpiece1 (85±1.6% and 80±1.70%, respectively; the results are summarized in Table 3.3).

Table 3.3: Table containing the average performance of the logistic regression models trained on features derived by both template matching and matrix profile methods. Results are shown per handpiece of the measuring device. Average classification accuracy as well as its standard deviation are given.

	Template Matching		Matrix Profile	
Accuracy	Average	Std	Average	Std
Carotid-carotid HP1	80%	1.75%	82%	1.64%
Carotid-carotid HP2	85%	1.63%	88%	1.53%
Femoral-carotid HP1	87%	1.31%	86%	1.43%
Femoral-carotid HP2	81%	1.96%	85%	1.71%

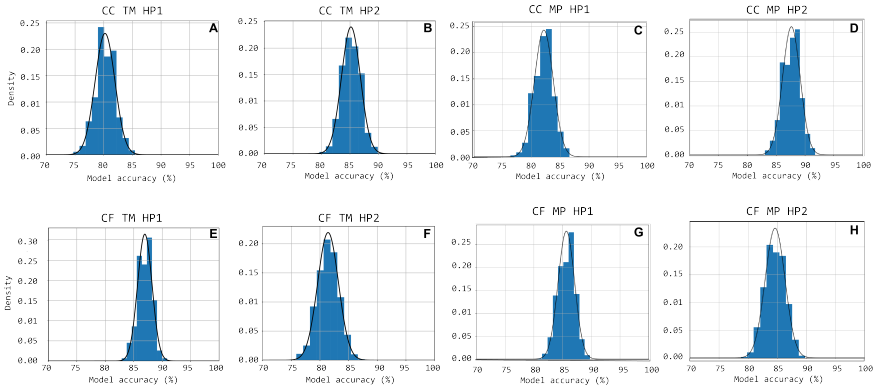

Figure 3.11: *Accuracy distributions for 1000 random train-test set partitions and subsequent logistic regression models trained. The accuracy distribution is shown cumulatively through bar-charts with the equivalent Gauss-curve plotted on top of it. Subfigures* ***(A)****,* ***(B)****,* ***(C)*** *and* ***(D)*** *show this for CC HP1, CC HP2, CF HP1 and CF HP2 cases respectively.*

3.4.2.2 Carotid-femoral (CF) measurements

From the analysis carried out on the complete CF dataset, it emerged that using the carotid template of 500 ms length guarantees the best performance in terms of specificity, setting the cross-correlation threshold to 0.56 and the minimum number of detected heartbeats per trace to 10 (AUC = 0.89, sensitivity 77%, specificity 92%; template of 400 ms length: AUC = 0.88, sensitivity 76%, specificity of 91%; template of 300 ms length: AUC = 0.87, sensitivity 72%, specificity 92%).The confusion matrices are shown in Table 3.4 for each template.

Table 3.4: Confusion matrices of signal classification done by the hand-engineered classification model constructed with template matching. Signals classified in this table were measured at the femoral and the templates used were the femoral population templates.

	Template of 300ms		Template of 400ms		Template of 500ms	
Femoral recordings	TM score 0	TM score 1	TM score 0	TM score 1	TM score 0	TM score 1
score 1	96%	4%	96%	4%	96%	4%
score 2	91%	9%	89%	11%	91%	9%
score 3	68%	32%	64%	36%	65%	35%
score 4	33%	67%	28%	72%	27%	73%
score 5	8%	92%	6%	94%	7%	93%

As for the carotid traces, the performance of the template matching algorithm was based on the specificity values, in order to remove the bad quality signals. More in detail, the template matching strategy shows excellent performance for the classification of visual scores 1 and 5 (accuracy

of 96% and 93% respectively), while the accuracy decreases for class 2 and class 4 (91% and 72% respectively). In the femoral case, the method classified a majority of LDV traces with a visual score of 3 (borderline) as inadequate. Indeed, considering the template of 500 ms, the template matching method classified 65% of score 3 as inadequate signals and the other 35% (borderline)as adequate.

The level of agreement obtained between Q_{TM} and Q_{vis} on the CF recordings dataset, using the 500 ms template length, is shown in Figure 3.10C. The results indicate that from the median Q_{TM} values scored Q_{vis} = 3, a threshold value could be adopted for the automatic quality checking of the LDV trace (i,e. in the case under study, traces with a $Q_{TM} > 0.23$ could be considered of adequate quality; again, this threshold is not required when working with the logistic regression models.)

The accuracy distributions of logistic regression models trained on quality scores derived from template-matching are displayed in figure 3.11(3.11E and 3.11F). On average, the accuracy on traces acquired using handpiece 1 is higher than handpiece 2 (87±1.3% and 81±1.9%, respectively; the results are summarized in Table 3.3).

3.4.3 Matrix profile

On good quality data, i.e., those visually scored at 4 or 5, the matrix profile technique was able to include nearly all heartbeats in the motif. On poor quality data the matrix profile was unable to identify most heartbeats because of noise or artifacts in the measurement. On some measurements that contain pure noise, the matrix profile picked up random noisy waveforms that were less prevalent and differed much compared to the desired foot-of-the-wave waveform.

3.4.3.1 Quality metric results

The signals measured at the carotid measuring site were given a matrix profile-derived quality score that is compared with their visual scores in figure 3.10B. A positive, linear relation between the two scoring methods is observed for the carotid-carotid database.The same information is shown for the femoral measuring site in figure 3.10D. The difference between poor and good quality signals is apparent. Signals with visual score 1,2 or 3 have significantly lower Q_{MP} than those with visual score 4 or 5.

3.4.3.2 Logistic regression models performance

Figure 3.11C,D,H show the accuracy distributions of the repeated logistic regression model-training experiment for signals measured in the neck with the different handpieces. All accuracy averages are above 80% with 82%

(±1.64%) and 88% (±1.53%) for carotid-carotid recordings with handpiece 1 and 2, respectively. For carotid-femoral recordings, carotid data recorded with handpiece 2 yielded an accuracy of 85%± 1.71%. The distributions were assumed to be normally-distributed after a Shapiro-Wilk test and thus the Gauss-curves are drawn onto the subfigures of Figure 3.11.

The same data for the femoral data (measured with handpiece 1 during carotid-femoral recordings), is shown in figure 3.11G. An average accuracy of 86% with a standard deviation of 1.43% is observed. All accuracy statistics of the different measurement situations are summarized in table 3.3.

3.4.4 Signal quality vs. physiological variables

The results from the correlation analysis between Q_{MP} and age, BMI and systolic blood pressure are shown in figure 3.12 for the femoral data (carotid-femoral recording, handpiece 1; CF HP1) and the carotid-carotid recordings with handpiece 2 (CC HP2) showing the strongest trends. Significant negative correlations were found between age and Q_{MP} for CF HP1 ($\rho = -0.253$, P<0.05) and CC HP2 ($\rho = -0.365$, P<0.001). The correlation with BMI (figure 3.12B) was significant only for the femoral recording ($\rho = -0.304$, P<0.01) while the correlation with systolic blood pressure was significant only for CC HP2 ($\rho = -0.206$, P<0.05)(figure 3.12C). In a multivariate regression model including both age and systolic blood pressure, the correlation between carotid signal quality and systolic blood pressure was no longer significant (due to the correlation between age and systolic blood pressure). In contrast, in a multivariate model of femoral signal quality, both age and BMI remained significantly correlated with signal quality. The same relations are found when repeating the analysis with Q_{vis} or Q_{MP} (data not shown).

3.5 Discussion

The potential of Laser-Doppler Vibrometry (LDV) for non-contact measurement of physiological (cardiovascular) signals has been reported since about 2000 in explorative studies [21, 186, 189, 190] making use of bulky industry-time devices, and the technique has been suggested for measurement of carotid-femoral PWV by [22]. An important technological breakthrough to enable LDV-based measurements in a clinical setting is the use of silicon photonics to miniaturize and integrate the optical components onto chips [18] that are easily built in into hand-held devices as the CARDIS prototype used in this study. That prototype was used in a clinical feasibility study where measurements were performed on the carotid and femoral artery and we previously reported on the agreement of LDV-based

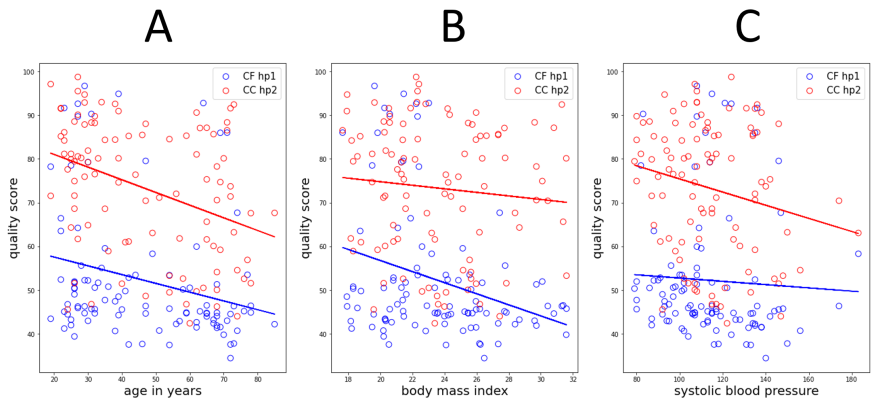

Figure 3.12: *Correlation analyses of the matrix profile-based quality score with age, BMI and systolic blood pressure, shown in subfigures* ***(A)****,* ***(B)*** *and* ***(C)*** *respectively. Only data in the CC HP2 and CF HP1 cases is shown. Trendlines of the data are also drawn.*

carotid-femoral PWV with a reference method [25]. In that paper, data was processed off-line and algorithms for foot detection relied on the ECG and gating was applied on carotid and femoral tracings to ensure identification of the correct characteristic points on the waveforms. Further developments aim for ECG-independent measurements and will require a more stringent quality assessment in real-time application to ensure that data is captured from which transit times can be derived. Unlike the CARDIS device, future versions of the device will provide real-time feedback on signal quality and valid measurements will only be accepted after a minimal number of data samples have been retrieved from signals passing predefined quality criteria. In this paper, we explored two possible strategies for such quality assessment, template matching and matrix profile, and benchmarked them using visual scoring as reference.

The visual grading was done by what we considered an expert observer, but is inherently subjective. The graphical user interface that was developed showed all data within one single window for reasons of efficiency, but inevitably leads to a weighed appreciation where data from different channels do get, to some extent, a degree of relative scoring. This mainly applies to the scores good (4)-excellent (5) where recordings of certain channels could have likely received different rankings if they had been individually assessed without the knowledge of the signal on the other channels. This remark may also pertain to the grade borderline. As future use of the device will target acquiring the best possible signals in a given subject, we particularly focused on signals graded 4 or 5. Figure 3.9 provides a visual overview of observed quality across the complete database. Each handpiece of

the device is equipped with 6 channels in line, spanning 2.5 cm with the aim to have minimally one channel that detects a strong signal. It is clear that channel 1 on handpiece 1 systematically yields very low scores, which was attributed to a hardware problem with inadequate alignment of the optical components during device assembly. For carotid measurements, the middle channels 3 and 4 yielded the the highest quality signals (as expected), but this shifted to channels 2 and 3 for handpiece 2. Also, the overall signal quality was slightly higher for handpiece 2. We speculate that the use of the spacer underneath handpiece 1 may contribute to the difference in signal quality between both handpieces. These data can be compared to the data from handpiece 2 during carotid-femoral measurement, where handpiece 2 is now equipped with a spacer (see Figure 3.9 for the measuring configurations). The mean signal quality is now in the same range as it was for handpiece 1 on the local carotid measurements. An extra factor, however, is the fact that carotid-femoral measurements are technically more demanding, requiring the simultaneous acquisition of signals at 2 distinct locations. The same conclusions can be drawn on the basis of the automatically calculated sores Q_{TM} and Q_{MP}.

In essence, one very good to excellent channel recording on each of the handpieces should guarantee a reliable transit time estimation from one handpiece to the other. This was achieved in 27% of the local carotid datasets and in 13% of the carotid-femoral datasets mainly due to the suboptimal femoral recording that is more challenging due to fact that the operators has to manipulate two sensors on two distinct locations as well as the deeper positioning of the femoral artery leading to weaker signals. That does not imply that the remaining datasets cannot be processed (especially when the ECG is available; see [25]) or that LDV would not be suitable as measuring technique; we just speculate that these results can be drastically improved with real-time feedback on the signal quality upon measurement.

The main objective of this paper was to explore different methods for an automated signal quality assessment, where we first explored template matching. The template should minimally contain the foot fingerprint of the wave, apparent on both the carotid and femoral measuring locations. That pattern turned out to be fairly robust across the tested population. Even though the amplitude of acceleration signals was lower at the femoral measuring site, the pattern of the foot is quite similar on both measuring locations. A practical choice that has to be made is on the length of the template. For carotid signals, it may be relevant to extend the template such that it also encompasses the dicrotic notch. We preferred the shorter template of 200 ms (which does not extend beyond the dicrotic notch) as the time delay between the wave's foot and the dicrotic notch is not constant but varies in between subjects and also within one subject from cycle

to cycle due to physiological variations in blood pressure and heart rate. The shorter template was found to result in a somewhat higher specificity in correctly classifying poor signals, but overall, the performance of the carotid templates with different lengths was not very different, as can be observed from the confusion matrix (Table 3.2). On the other hand, for the femoral artery, we preferred the longest template of 500 ms which should detect epochs characterized by one prominent peak, the foot of the wave, followed by a long tail of low amplitude signals.

We then determined optimal thresholds levels for the magnitude of the cross-correlation and the number of detected beats using ROC analysis, whereby we maximized the classification performance of a binary classifier on the basis of Q_{TM}. In this exploratory study, that analysis was done on the complete database and further optimizations should be done on the used features and repeating the analysis with a separate training and testing data set. Using the resulting thresholds, the agreement between Q_{TM} and Q_{vis} was overall satisfactory. The logistic regression model analyses learned that a template matching approach is a valuable option to automatically classify signal quality as acceptable or not acceptable with an accuracy of over 80%.

As a second method, we considered the matrix profile as a technique to identify recurring patterns in the LDV-measurements in an automatic manner [191], with very few control parameters. The potential advantage of a matrix profile approach over template matching is that no prior knowledge is required on the shape of the signal feature that one is looking for. Also, using the matrix profile allows the generation of a 'user-dependent' template in situ. Signal quality was quantifiable using features of the motifs found by the matrix profile and combined into the quality metric Q_{TM}, which showed a good agreement with the ground truth of visual scores as can be observed from Figure 3.10.

As for the template matching approach, the average accuracy of a logistic regression model trained and tested on features derived from motifs provided by the matrix profile technique is in all cases higher than 80%. Overall, only relatively small differences are observed between the two techniques. Both techniques perform similarly well which suggests that both, or a combination of the two, can be used for classifying new, future data into 'bad, unusable' or 'good, usable'. This allows us to state that a logistic regression model suffices, along with the signal features and techniques that are considered, to accurately assess incoming data in future real-time applications.

In our logistic model training, we purposely discarded datasets visually labelled 'borderline' (score 3) as these data were simply hard to classify

visually in an unequivocal way. That difficulty is relatively well reflected in the values of the quantitative metrics for these signals (figure 3.10) and the performance of the classifiers as quantified by the confusion matrix (table 3.2 and 3.4). Especially for the carotid artery, automated classification leads to a close to fifty-fifty percent labeling of data as acceptable or not acceptable. For the femoral recordings, there is a larger tendency to classify signals with visual score 3 as not acceptable. This is in line with our own perception that femoral data may have received higher scores than carotid data of a similar quality, and underlines the need for objective tools to score signal quality.

Interestingly, the quality score, exemplified by Q_{MP}, correlates negatively with age and especially with BMI when signals are measured in the groin on the femoral artery. This observation supports the operator impression that measuring good quality LDV-signals on more obese subjects is consistently more challenging. The deeper the positioning of the artery and the more surrounding tissue, the stronger the signal attenuation. Such relation with BMI was absent for neck recordings. Also, skin inelasticity or thickness is expected to play a role on the transmission of intra-arterial vibrations and likely contributed to the observed negative correlation between and signal quality at the carotid and femoral locations in the study populations. The negative correlations between signal quality and age for carotid-carotid recordings with handpiece 2 were less strong, and were not found for the other carotid recordings (carotid-carotid handpiece 1 or carotid-femoral handpiece 2 recordings). A possible explanation may be the use of the spacer for these latter measurements, which may mechanically interfere with the transmission of the vibrations from within the artery to the skin and exert an effect on the recordings. Overall, this effect is considered minor, but it may nonetheless be a factor contributing to observed differences in the recordings.

The CARDIS prototype has a laser wavelength of 1550 nanometer which is insufficiently reflected by the skin. We therefore attached retroreflective patches to the skin at the measurement locations to enhance reflection. The next-generation prototype aims for measurements without the retroreflective patch to facilitate practical use. A wavelength of 1300 nanometer, for which there is a relative peak in skin reflectance [192], will be used but the impact of skin pigmentation or sweating on data quality will have to be investigated.

In this study, signal quality was assessed off-line on 20 second recordings. Future developments will focus on real-time assessment of data quality as data is being captured and where the considered techniques will be used for epoch detection and subsequent quality quantification. Although

a template-matching approach has the benefit that prior knowledge can be used to assess incoming data from the start, we assume that both techniques provide similarly useful features and that both are suitable for real-time implementation. It may be an option to hybridize the two techniques to come to a stronger, even more robust algorithm when implementing them into the device.

3.6 CONCLUSION

In conclusion, template matching and matrix profiling are methods suitable for the automated assessment of the signal quality of acceleration data measured from the skin in the neck and groin using laser Doppler velocimetry. Both methods allow to identify epochs in a data stream, and provide quantifiable features that can be combined into a quality score, or be used as input for logistic regression models for an automated classification of signals as acceptable or not acceptable. Models based on both methods yielded an accuracy of minimally 80% in our CARDIS database of carotid and femoral recordings, reaching as high as 87% for the femoral data.

CHAPTER 4

BEAMFORMING LASER DOPPLER VIBROMETER SENSOR ARRAYS

POSITIONING OF THE CHAPTER

This chapter is based on the publication *Enhancing Multichannel Laser-Doppler Vibrometry Signals with Application to (Carotid-Femoral) Pulse Transit Time Estimation* (Beeckman, S., Li, Y., Aasmul, S., Baets, R., Boutouyrie, P., Segers, P., & Madhu, N., 45th Annual International Conference of the IEEE Engineering in Medicine & Biology Society (EMBC), 24-27 July 2023, pp. 1-7, doi: 10.1109/EMBC40787.2023.10340553) [193]. Conceptualization and methodology for this paper were tackled by the full list of authors. The author performed the presented analyses and wrote the conference proceeding in conjunction with prof. Madhu. This chapter only deviates from the conference proceeding in section 4.6, were an extension to the analysis is presented.

ABSTRACT

Pulse-wave velocity (PWV) can be used to quantify arterial stiffness, allowing for a diagnosis of this condition. Multi-beam laser-doppler vibrometry offers a cheap, non-invasive and user-friendly alternative to measuring PWV, and its feasibility has been previously demonstrated in the H2020 project CARDIS. The two handpieces of the prototype CARDIS device measure skin displacement above main arteries at two different sites,

yielding an estimate of the pulse-transit time (PTT) and, consequently, PWV. The presence of multiple beams (channels) on each handpiece can be used to enhance the underlying signal, improving the quality of the signal for PTT estimation and further analysis. We propose two methods for multi-channel LDV data processing: beamforming and beamforming-driven ICA. Beamforming is done by an SNR-weighted linear combination of the time-aligned channels, where the SNR is blindly estimated from the signal statistics. ICA uses the beamformer to resolve its inherent permutation and scale ambiguities. Both methods yield a single enhanced signal at each handpiece, where spurious peaks in the individual channels as well as stochastic noise are well suppressed in the output. Using the enhanced signals yields individual PTT estimates with a low spread compared to the baseline approach. While the enhancement is introduced in the context of PTT estimation, the approaches can be used to enhance signals in other biomedical applications of multi-channel LDV as well.

4.1 INTRODUCTION

The large arteries, and specifically the aorta, play a central role in the blood circulation. Their structure allows the vessel wall to distend during heart contraction, storing elastic energy, which is used during the consequent relaxation to drive the blood flow [49]. This way, a near-continuous flow is assured at the smaller arteries that provide organ perfusion. This 'buffer' function [35] deteriorates significantly when these large arteries stiffen, leading to poorer blood flow and consequent organ damage – especially in low resistance organs such as the heart itself [7, 8, 75].

A metric that allows for quantifying arterial stiffening is the pulse-wave velocity (PWV) [8, 11]. Especially carotid-femoral PWV has been studied and showed a significant relationship with arterial stiffness. The speed of the pulse-wave induced by heart-contraction increases with arterial stiffness. If we measure the arrival time of the pulse-wave at two points on the arterial tract, separated by a distance dx, it holds that $\text{PWV} = \frac{dx}{PTT}$, where PTT is the delay in the pulse arrival time across the two points. We refer to PTT as the pulse-transit time.

Aside from the current state-of-the-art measurement methods, such as applanation tonometry and ultrasound [11, 184], an alternative approach based on laser-doppler vibrometry (LDV) [20–22] has also been applied to the measuring of PWV. This cheaper, more user-friendly method measures skin displacement above large arteries such as the carotid and femoral arteries, based on which the pulse arrival time and PTT can be estimated. A feasibility study was previously conducted using industrial LDV devices

[22]. In the scope of the H2020 CARDIS project, a first prototype was constructed with two handpieces, with which skin displacement could be simultaneously measured at two different locations. Each handpiece captured data using six laser *beams* with a wavelength of 1550nm, where the inter-beam distance was 5mm. The displacement signals obtained were differentiated twice, yielding acceleration. The time-point of the arrival of the pulse wave was then detected via the point of maximum acceleration.

Several datasets were obtained with this prototype [25]. However, despite the availability of multi-channel data on both handpieces, PTT and PWV estimates were based on a laborious combination of the individual channels across both handpieces.

Since the underlying signal captured by all the channels in a single handpiece is the same, *linearly* combining the channels could yield an output with a better signal-to-noise ratio. Such methods of combining signals from spatially separated sensors to enhance a desired (target) signal fall under the umbrella of *beamforming* [158, 159, 194, 195]. A beamformer is essentially a spatial filter that, like its temporal/spectral counterpart, combines signals captured by spatially distributed sensors to extract signals coming from desired *directions* while suppressing interference and noise from unwanted ones. Since the original problem in the time-domain is a convolutive mixing, beamforming is typically applied in the transform (Fourier) domain, where the signal model reduces to an *instantaneous* mixture with complex coefficients at each frequency. This simplifies the subsequent enhancement as it simplifies to a straightforward matrix multiplication instead of a deconvolution. Such methods have also been applied to electroencephalography (EEG) data e.g. [162], where an instantaneous mixing model is directly applicable in time domain.

Unlike conventional beamforming or the methods applied to EEG signal processing, however, the signal model for LDV captures cannot be straightforwardly transformed into an instantaneous mixing model in the frequency or the time domain [160]. In this contribution, therefore, we investigate how to adapt and apply beamforming to multichannel LDV data. We also show how to extend the framework to incorporate more sophisticated approaches such as independent component analysis (ICA) [161]. While the approach will be demonstrated in the context of carotid-femoral PTT estimation, the underlying signal model and concepts can be applied to a wide range of applications using multichannel LDV - which is being explored in the scope of the follow-up H2020 project InSiDe.

The paper is structured as follows: we first present the CARDIS data and the 'brute-force' baseline PTT estimation method. Next, we present the

signal model for the multichannel LDV data. Based on this model we first adapt the beamforming strategy to perform a signal-to-noise ratio (SNR)-weighted averaging of the channels. Lastly, we show how, with the adapted signal model, ICA can also be applied and how the permutation and scaling ambiguity associated with ICA can be resolved. The approaches are then compared in terms of the quality of the PTT estimates obtained from the enhanced signals. It will be demonstrated that individual PTT estimates obtained on the beamformed or ICA processed signals are more reliable (lower variance) than that obtained from the baseline method. Further, the SNR estimates computed in the course of the beamforming provide valuable, additional information regarding the reliability and quality of different segments of the signal - opening up new possibilites for such signal analysis.

4.2 MATERIALS & BASELINE METHOD

4.2.1 The CARDIS database

The CARDIS device consists of two handpieces (HP) - which we will refer to as HP1 and HP2. While the reader is referred to [18, 19] for the details, the prototype is illustrated in Fig. 4.1, along with typically captured signal traces, for convenience. Note the six channels per handpiece, which capture the skin displacement. To guarantee that sufficient light is reflected by the skin back to the device, application of retro-reflective tape on the measurement site was required. Finally, to ensure stability of positioning and an optimized focus distance during the measurements, a spacer is included in the build.

Data can be gathered simultaneously with both handpieces, each of which is located at a separate measurement site – such as above the carotid and femoral artery to get a carotid-femoral PWV estimation, or on measurement sites that are $25-50$mm apart, to measure local pulse wave propagation in e.g. the carotid artery. Note that while the developed approaches are illustrated on the carotid-femoral setup, they are equally applicable to other setups as well.

The carotid-femoral LDV-data used in this analysis were acquired in a clinical feasibility study at the Hôpital Européen Georges Pompidou (HEGP) in Paris, France. Data was gathered from 100 subjects with varying ages (19-85), sex, BMI, and history with cardiovascular risk-factors and illnesses (from mild to stage three hypertension) [25]. For every subject, four to five sets of measurements were conducted, resulting in 410 datasets for the carotid-femoral database. Each measurement contained six LDV signals per handpiece, yielding skin-displacement data sampled at

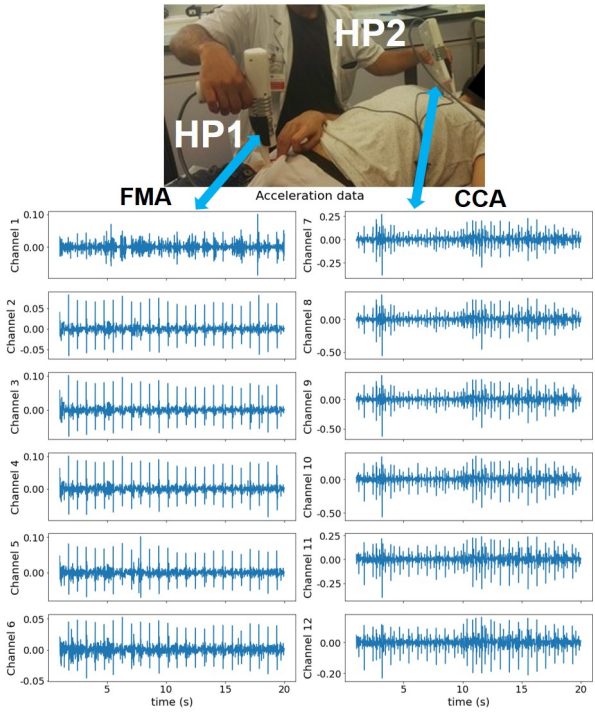

Figure 4.1: The CARDIS device being used during a carotid-femoral measurement. Handpiece 1 measures skin displacement above the femoral artery and handpiece 2 above the carotid artery. 20-second recordings for the 12 beams are displayed. Channel 1-6 correspond with handpiece 1 and channel 7-12 to handpiece 2.

$f_s = 10$kHz. This was passed through a linear-phase low-pass filter with a cut-off frequency of 30 Hz to suppress high-frequency noise. Filtering was applied in a zero-phase manner. The signal was then differentiated twice to yield acceleration data – which is a more robust feature as the differentiation removes any drift in the displacement signal.

4.2.2 Brute-force PTT estimation

To validate the applicability of LDV for PWV estimation, the carotid-femoral PTT estimate was calculated and compared with ground truth data, which was obtained using applanation tonometry. As mentioned previously, PTT is defined as the time delay between the arrival of the pulse wave at the carotid artery and the femoral artery. It should be noted that, since the arterial pathway from the heart to the carotid artery is shorter than that from heart to femoral, the pulse wave should always be detected first at the carotid. The time of arrival of the pulse at each measurement point is taken as the instant of maximum acceleration for

a given heartbeat. Demarcation of the pulse arrival time and the PTT computation is illustrated in Fig. 4.2 where one channel each from HP1 and HP2 are considered. By pooling the estimates across the 36 possible channel combinations between HP1 and HP2, more robust PTT estimates can be obtained.

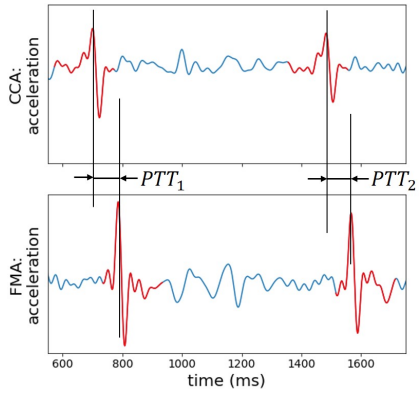

Figure 4.2: Example matching of simultaneously measured carotid and femoral LDV-traces. Two corresponding heartbeats from which pulse-transit times can be calculated are indicated in red. Y-axis is not labelled because the scale is arbitrary.

As the above example illustrates, computing the PTT consists of first identifying the heart cycles in the acceleration signals of the carotid-femoral channel-pair considered, followed by identifying the pulse arrival time in each channel and for each cycle. However, the problem is that either or both channels may not pick up the pulse in each beat - because of insufficient reflection of the beam or movement of the handpiece or insufficient skin displacement. Further, as the heart rate can also change during a measurement, an online estimation of the heart rate (and, thus, the location of a cycle) becomes necessary. Thus, the following procedure was adopted for estimating the PTT from a given recording.

First, a beat-detection algorithm based on *template matching* [145, 146] was applied to each of the 12 traces (we term the acceleration signal of a channel as a *trace*). Template matching is a pattern recognition technique which essentially consists of computing the normalised cross-correlation between a so-called template (here, the characteristic waveform of the acceleration signal when the pulse traverses the measurement point) and the trace at different time-lags. For time-lags where the segment of the trace 'matches' well with the template, the normalised cross-correlation will be high (ideally ≈ 1) – indicating the presence of the pulse-wave. An empirically selected threshold of 0.7 was selected and at time instants where this value was exceeded, it was be assumed that a beat was detected. As the

acceleration signal demonstrates different characteristic wave pattern at the carotid (HP1) and femoral (HP2) measurement points, separate templates were used each case, and were obtained offline by an ensemble average across all recordings. The length of the carotid template was 200ms and that of the femoral was 500ms (please see [27] for details).

Next, *matching* beat-pairs were identified using the carotid as reference (typically more carotid beats are detected compared to femoral). When a pulse is detected on *any* of the carotid channels, all femoral channels are examined for pulses within a time-window of 200ms of this pulse (two matching beat-pairs are indicated in Fig. 4.2). The range of 200ms was chosen to accommodate a wide range of PWVs while minimising the risk that a *subsequent* beat on the femoral is matched (i.e., carotid detects beat P and is matched to beat $P+1$ on the femoral). Since a 200ms beat period corresponds to the unlikely heart rate of 300bpm, such confusion is avoided. Finally, PTTs were calculated from *each* matching beat pair in the 36 trace combinations. The *median* value of these was taken as the final PTT estimate.

In addition to being laborious (template matching applied to 12 channels, exhaustive search for a matching beat in the femoral channels for each beat found on a carotid channel,...) this approach implicitly includes data from noisier channels as well. With no way of indicating which estimate comes from a good or from a bad channel, this leads to a wide spread of the results. Hence we investigate the linear combination of all channels at a handpiece to generate a single output signal with improved SNR. This should reduce the spread of the PTT estimates and offer potential to reduce the computational complexity as well.

4.3 Beamforming for PTT estimation

4.3.1 Signal model

For any handpiece, the acceleration signal at a channel $m \in \{1,2,\ldots,6\}$ is modelled as:

$$x_m(n) = s_m(n) + v_m(n)\,, \tag{4.1}$$

where $s_m(n)$ is the underlying target signal *in channel m* and $v_m(n)$ is the noise in that channel. We further assume:

$$s_m(n) = \alpha_m s(n-\tau_m)\,, \tag{4.2}$$

i.e., the target signal is received at each channel with a channel-dependent scale factor α_m and delay τ_m.

The channel-dependent delay in (4.1) makes it difficult to form the enhanced output ($y(n)$) by a weighted linear combination of the form:

$$y(n) = \sum_m w_m x_m(n)\,, \tag{4.3}$$

while ensuring a constructive addition of the desired component $s(n)$. The general solution requires the estimation of optimal individual *filters* $w_m(n)$ for each channel – which is not a straightforward problem (see, e.g., [196]). However, the model of (4.2) allows for a simpler alternative: by time-aligning the target components $s_m(n)$, (4.1) reduces to:

$$x'_m(n) = \alpha_m s(n) + v'_m(n)\,, \tag{4.4}$$

allowing for the application of (4.3). We address, next, the blind estimation of the time-delays τ_m and the optimal weighting factor w_m. Since the underlying signal $s(n)$ is essentially unknown, a blind estimation of τ_m and α_m is always subject to an offset and a scale ambiguity respectively - i.e., any solution of the kind $\widehat{\tau_m} = \tau_m + T$ and $\widehat{\alpha_m} = \mathscr{C}\alpha_m$, where T and $\mathscr{C}$ are constants, is acceptable – the constant values being subsumed into the definition of $s(n)$. The ambiguities vanish, however, if we estimate the scale and delay with respect to the signal component in a *reference* channel m_{ref}. Thus, reinterpreting (4.1) and (4.2) with respect to a reference channel m_{ref} we obtain:

$$\begin{aligned} x_m(n) &= \alpha_m s(n-\tau_m) + v_m(n) \quad \forall m \neq m_{\text{ref}} \\ x_{m_{\text{ref}}}(n) &= s(n) + v_{m_{\text{ref}}}(n) \end{aligned} \tag{4.5}$$

where α_m and τ_m are now with respect to the signal component in the reference channel.

In general, the reference channel can be arbitrarily chosen for each handpiece – the middle channels ($m = 3,4$) being a logical choice. Alternatively, with the help of overall-quality estimated per channel over the whole recording – as in [27] – the 'best' channel (on average) may be chosen. In the following we denote this generically as m_{ref}.

4.3.2 Time alignment of the $s_m(n)$

As the signal component in channel m can either be advanced or delayed with respect to the signal component at channel m_{ref}, the reference signal $x_{m_{\text{ref}}}(n)$ is first shifted by a group delay of $D > \max\{\tau_m\}$ samples. This ensures that all other channels are shifted *causally* for time alignment. Thus, the reference signal becomes:

$$\tilde{x}_{m_{\text{ref}}}(n) = s(n-D) + \tilde{v}_{m_{\text{ref}}}(n)\,. \tag{4.6}$$

It is easy to see that delaying each $x_m(n)$ $(m \neq m_{\text{ref}})$ by $T_m = D - \tau_m$ ensures that the signal component is aligned with the reference. By cross-correlating $x_m(n)$ with $\tilde{x}_{m_{\text{ref}}}(n)$ an estimate of the time-delay can be obtained [159, 197]. The *integer* part of the delay corresponds to the time-lag at which the cross-correlation peak is observed. The delay estimate can be further refined to account for *fractional* shifts. This can be done by a simple three-point parabolic fit around the observed cross-correlation peak, or by more sophisticated methods (see, e.g., [198]). Having estimated T_m, generic delay filters $h_m(n)$ can be obtained by (truncated) sinc functions [199] of order $L \geq 2D$:

$$h_m(n) = \text{sinc}\Big(n - T_m\Big). \tag{4.7}$$

This formulation of the delay filter allows us to account for fractional sample shifts. It is easy to see that the filter reduces to a shifted Kronecker's delta function when T_m is an integer – as we expect.

4.3.3 Compensating for α_m

By appropriately compensating α_m, we can express the signal at *each* channel as:

$$\tilde{x}_m(n) = s(n-D) + \tilde{v}_m(n), \tag{4.8}$$

which, as we subsequently show, allows for an intuitive definition of the weighting factors w_m in (4.3). We exploit the observation that $s(n)$ is characterised by high-energy regions corresponding to the traversal of a pulse. Thus, comparing energies of $x_m(n)$ to $x_{m_{\text{ref}}}(n)$ (or their time-aligned versions) at these regions can yield a reasonable idea of α_m.

While identification of high-energy regions can be done using template matching (as in Sec. 4.2.2), this requires extra computation and the availability of templates. Therefore, we present a more generic method based on the *statistics* of the signal energy – so the approach is also applicable where prior knowledge of templates are unavailable.

We segment $x_{m_{\text{ref}}}(n)$ and $x_m(n)$ (or their time-aligned versions) into J non-overlapping segments of length N samples, where N is roughly the length of a pulse waveform (≈ 200ms). The energy $E_{m,j}$ (resp. $E_{m_{\text{ref}},j}$) is obtained as:

$$E_{m,j} = \sum_{n=0}^{N-1} \Big(x_m(n+jN)\Big)^2. \tag{4.9}$$

Subsequently, as we are interested in the high-energy segments, the 85^{th} percentile of the energies was calculated. This threshold was empirically

found to be a good balance between accounting for the variation of the received pulse energy in the trace and not being biased by the low-energy segments which mainly contain channel-dependent noise. Based on this, α_m can be estimated as:

$$\widehat{\alpha}_m = \sqrt{\frac{\text{perc}\Big(\{E_{m,j}\},85\Big)}{\text{perc}\Big(\{E_{m_{\text{ref}},j}\},85\Big)}} \tag{4.10}$$

The distribution of the energies are illustrated for an example dataset in Fig. 4.3 and the 85$^{\text{th}}$ percentiles are shown as vertical lines in the colour of the corresponding distribution.

Based on $\widehat{\alpha}_m$ above and $h_m(n)$ from (4.7), we modify the signal of each channel as:

$$\tilde{x}_m(n) = \frac{1}{\widehat{\alpha}_m} h_m(n) * x_m(n) \;\approx s(n-D) + \tilde{v}_m(n)\,, \tag{4.11}$$

where $*$ represents the discrete-time convolution operator.

4.3.4 Estimating w_m and the enhanced signal $y(n)$

Using (4.5) and (4.11) and stacking the signals into an $M-$dimensional column vector for each time-instant yields:

$$\widetilde{\mathbf{x}}(n) = \mathbf{1}\, s(n-D) + \widetilde{\mathbf{v}}(n)\,, \tag{4.12}$$

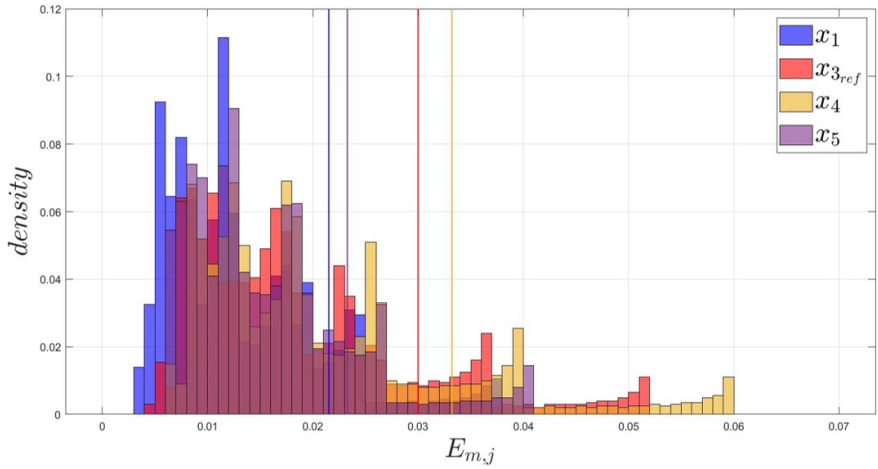

Figure 4.3: Distribution of the segmented energies for 4 channels in a sample dataset. The 85$^{\text{th}}$ percentiles are displayed by vertical lines, and in the colour chosen for the corresponding channel.

where $\widetilde{\mathbf{x}}(n) = \left[\tilde{x}_1(n), \quad \tilde{x}_2(n), \quad \ldots, \quad \tilde{x}_M(n)\right]^T$, $\mathbf{1}$ is an $M \times 1$ vector of ones and $\widetilde{\mathbf{v}}(n)$ is similarly defined to $\widetilde{\mathbf{x}}(n)$. This model now allows the computation of the enhanced signal as in (4.3) and an intuitive way to define the weights would be to make them proportional to the SNR at each channel.

However, computing a *single* set of weights over the whole recording would not be optimal, since the quality of the underlying received signal is time-variant in each channel (as can be seen in Fig. 4.1). Thus, we propose to segment $\tilde{x}_m(n)\ \forall m$ into $\widetilde{J}$ *overlapping* segments of length $\widetilde{N} \approx$ 1s, and derive optimal weights for each segment independently. A 50% overlap is considered to avoid edge effects during the subsequent weighted combination.

To estimate the SNR of each channel m in segment $\widetilde{j}$, we expand upon the idea in Sec. 4.3.3. We first partition segment $\widetilde{j}$ into $\widetilde{K} = 2000$ sub-segments of $\widetilde{N}/\widetilde{K} = 5$ samples and compute the energy $E_{m,\widetilde{j},\widetilde{k}}$ of every sub-segment $\widetilde{k}$. Indices $(m,\widetilde{k})$ where $E_{m,\widetilde{j},\widetilde{k}} > 85^{th}$ percentile (for channel m and segment $\widetilde{j}$) are then extracted. This is done separately for all channels. Next, we compare the selected $\widetilde{k}$ across all M channels and only retain those sub-segment indices that occur in a *majority* of the channels. The signal energy in segment $\widetilde{j}$ for each channel (denoted as $P_s(m,\widetilde{j})$) is finally computed as the *average* of the energies $E_{m,\widetilde{j},\widetilde{k}}$ in the *retained* sub-segments $\widetilde{k}$. Since the desired signal $s(n)$ is time-aligned across the channels, when the energy of a particular sub-segment $\widetilde{k}$ lies beyond the 85^{th} percentile in multiple channels, it is likely that this is not a spurious energy peak, but that occasioned by $s(n)$. This selection thus avoids noise sub-segments in a channel from biasing the signal energy estimate.

A similar procedure is applied to estimate the noise energy $P_v(m,\widetilde{j})$, but here we select segment indices where $E_{m,\widetilde{j},\widetilde{k}} < 15^{th}$ percentile. Comparison of sub-segment indices across channels is not required in this case.

The final SNR and the resultant combination weights $w_m(\widetilde{j})$ are then obtained, for segment $\widetilde{j}$, as:

$$\mathrm{SNR}(m,\widetilde{j}) = \frac{P_s(m,\widetilde{j})}{P_v(m,\widetilde{j})} \tag{4.13}$$

$$w_m(\widetilde{j}) = \frac{\mathrm{SNR}(m,\widetilde{j})}{\sum_{m'=1}^{M} \mathrm{SNR}(m',\widetilde{j})}\,. \tag{4.14}$$

The beamformed signal of segment $\widetilde{j}$ is subsequently computed using (4.3) as:

$$y_{\mathrm{BF}}(n,\widetilde{j}) = \mathbf{w}^T(\widetilde{j})\mathbf{x}(n,\widetilde{j})\,. \tag{4.15}$$

The enhanced signal $y_{\mathrm{BF}}(n)$ is reconstructed from the segments $y_{\mathrm{BF}}(n,\widetilde{j})$ by the overlap-add method, after the application of an $\widetilde{N}$-point von Hann window. This tapered window reduces edge effects at the boundaries of the overlapping segments and, at 50% overlap, allows perfect reconstruction during overlap-add.

4.3.5 Beamformer-driven ICA

Given an *instantaneous* multi-channel mixture of the form:

$$\mathbf{x}(n) = \mathbf{A}\mathbf{s}(n)\,, \tag{4.16}$$

where $\mathbf{x}(n)$ is an $M-$dimensional vector of *observations* at time-instant n and $\mathbf{s}(n)$ is a $Q(\leq M)$-dimensional vector of underlying source activity. $\mathbf{A}$ is an $M \times Q$ *mixing* matrix yielding a linear combination of the sources in the observed signal. Under the assumption that the $s_q(n)$ are statistically *independent*, ICA [160, 196] can be applied to yield a $Q \times M$ *demixing* matrix $\mathbf{W}$. Applied to $\mathbf{x}(n)$ this yields: $\mathbf{y}(n) = \mathbf{W}\mathbf{x}(n)$, with statistically independent $y_{q'}(n)$. For non-Gaussian $s_q(n)$, such maximisation of statistical independence in the output implies that $y_{q'}(n)$ recover $s_q(n)$, subject to a *scale* ambiguity and arbitrary order of outputs (*permutation* ambiguity). Robustly resolving these ambiguities is an enduring challenge, usually requiring extra knowledge!

Our signal model after *time-alignment* may be written as (slightly abusing the notation in (4.12)):

$$\widetilde{\mathbf{x}}(n) = \boldsymbol{\alpha} s(n-D) + \widetilde{\mathbf{v}}(n)\,, \tag{4.17}$$

where $\boldsymbol{\alpha} = \Big[\alpha_1, \alpha_2, \ldots, \alpha_M\Big]^T$. This can be straightforwardly massaged into the standard ICA form of (4.16):

$$\widetilde{\mathbf{x}}(n) = \mathbf{A}\widetilde{\mathbf{s}}(n)\,, \tag{4.18}$$

with the noise subsumed into the definition of $\widetilde{\mathbf{s}}(n)$. Application of ICA then gives outputs $\mathbf{y}_{\mathrm{ICA}}(n)$, where $y_{\mathrm{ICA},q}(n)$ corresponds to $s(n-D)$ for some output channel q, and subject to an unknown scale. A simple correlation of each $y_{\mathrm{ICA},q}(n)$ with $y_{\mathrm{BF}}(n)$ can then be used to identify the correct output channel $q'-$ the one with the maximum correlation with $y_{\mathrm{BF}}(n)$. It is straightforward, then, to infer the scale as:

$$\alpha_{\mathrm{ICA}} = \frac{\mathbb{E}\Big\{y^2_{\mathrm{BF}}(n)\Big\}}{\mathbb{E}\Big\{y_{\mathrm{BF}}(n)y_{\mathrm{ICA},q'}(n)\Big\}}\,, \tag{4.19}$$

where $\mathbb{E}\{\cdot\}$ is the expectation operator.

Consistent with Sec. 4.3.4, ICA is similarly applied segment-wise and the final output obtained by overlap-add.

4.4 Experimental results and discussion

We start with a qualitative evaluation on a sample dataset: Fig. 4.4 depicts the captured signal on four channels of a handpiece, after scale compensation and time-alignment. To illustrate the weight computation of (4.14), three segments ($\widetilde{j}$) are highlighted in each channel, and the corresponding weights ($w_m(\widetilde{j})$) assigned to those segments are indicated. As can be seen, when using these four channels for beamforming, our blind SNR-estimation approach performs correctly, assigning a very low weight to channel 1 (essentially noise) and giving more-or-less similar weights to the other three channels (of similar quality). Also evident is the time-varying SNR in each channel (indicated by the changing weights) – indirectly validating the wisdom of segment-wise processing.

This is further highlighted in Fig. 4.5 which shows, for the same sample dataset as in Fig. 4.4, a different set of channels as well as the enhanced signals ($y_{\mathrm{BF}}(n)$ and $y_{\mathrm{ICA}}(n)$). Channel 1 is omitted for space reasons (and, as Fig 4.4 shows, this channel will not contribute to the output). It is instructive to note that despite all channels being of relatively good quality in Fig. 4.5, spurious peaks occur in individual channels – which are effectively removed in the enhanced signals.

Lastly, we test the benefit of the proposed beamforming and ICA-based enhancement for PTT estimation on a subset of the CARDIS carotid-femoral database. Only those datasets were taken that had at least one good quality channel per handpiece [27] (to allow reasonable PTT estimation with the baseline). A total of 54 datasets passed this threshold. For these datasets, the $y_{\mathrm{BF}}(n)$ and $y_{\mathrm{ICA}}(n)$ are obtained for each handpiece. Following this, PTT is estimated on these signals, in a similar manner as described in Sec. 4.2.2. These estimates were compared with those generated by the baseline ('brute-force') and the ground truth.

Fig. 4.6 shows the *error* of each method compared to the ground-truth as a function of the number of PTT estimates (i.e., the number of matching beat-pairs across which the PTT estimate is computed). For all methods the accuracy of the final PTT estimate improves with increasing number of timepoints at which a pulse-transit time estimation could be made. While all methods deviate somewhat from the applanation-tonometry reference values, between brute force, beamforming and ICA, results were mostly

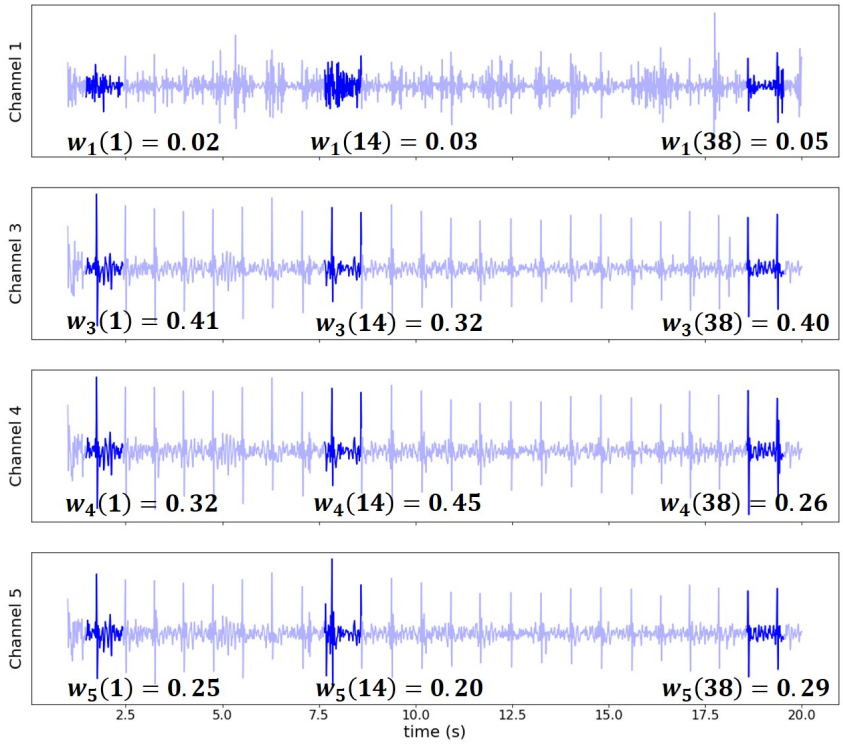

Figure 4.4: Weights w_m computed for four input channels. Three representative segments are highlighted. The correlation between the segment weights and the SNR is evident – indicating a good (blind) SNR estimation.

similar. This is not wholly unexpected: $y_{\mathrm{BF}}(n)$ and $y_{\mathrm{ICA}}(n)$ are obtained by linearly combining the different channels. Inherently, the brute-force search across all beat-pairs and all channels performs such a linear combination. As the *final* estimate is obtained from the median value in all cases, the results are expected to be rather homogeneous.

It is more instructive, therefore, to consider the distribution of the *individual* PTT estimates in all cases. This is depicted in Fig. 4.7, where the left sub-plot shows the distribution of the PTT-deviation about the median value and the right sub-plot shows the cumulative density. Both plots indicate a clear reduction of variance in the PTT estimates obtained after beamforming and ICA enhancement, whereas the brute-force method has a larger variance and several outliers. Between beamforming and ICA, for the purpose of PTT estimation, the performance is comparable, with the ICA being *marginally* better.

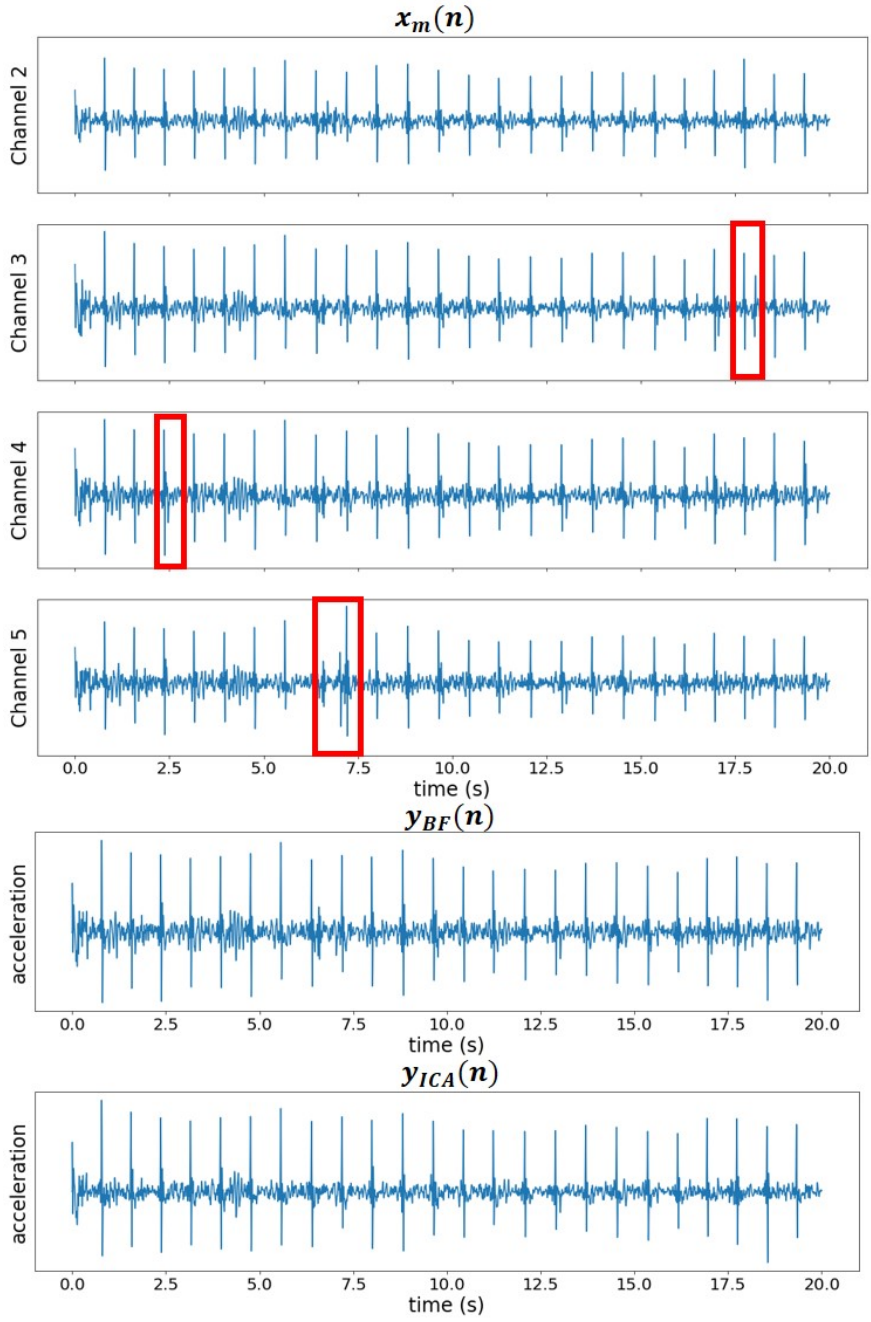

Figure 4.5: A selection of four input signals from the femoral recording, along with the beamformer & ICA enhanced outputs, for an example dataset. The segment-wise operation with time-varying weights effectively suppresses spurious pulses in individual channels (highlighted). The ICA also yields a cleaner signal compared to the beamformer.

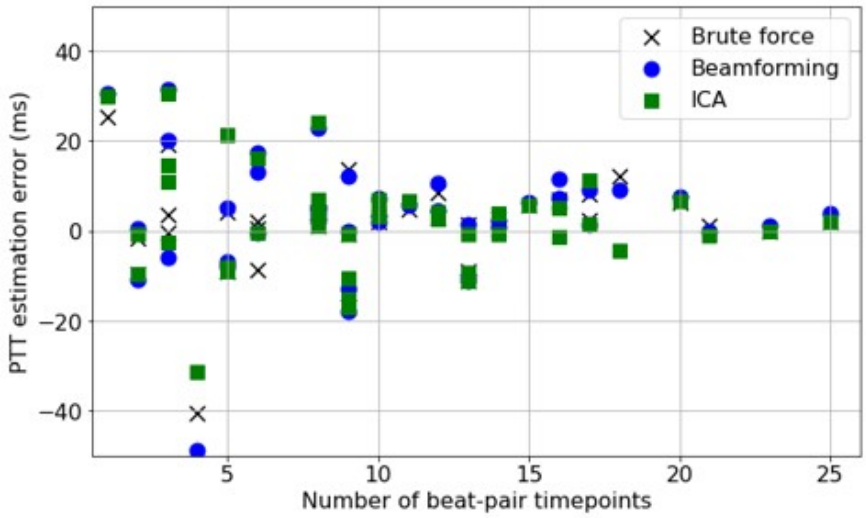

Figure 4.6: PTT estimation error for the different methods, compared to the ground-truth. The error is shown in function of the number of individual estimates obtained from matching beat-pairs. As the number of individual estimates increase, their median is closer to the ground truth.

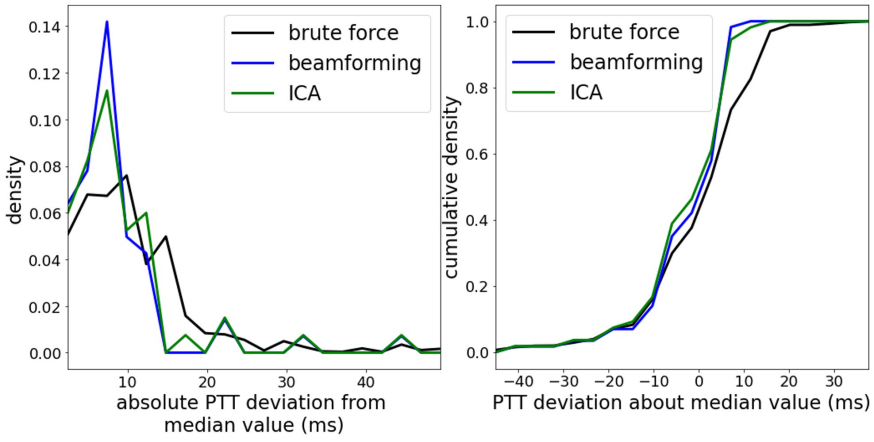

Figure 4.7: PTT-estimation distributions calculated via brute force, beamforming and ICA methods for ten example datasets. The median value was subtracted from the estimations.

4.5 Conclusions

We proposed two methods for the enhancement of multi-channel LDV signals, as applied to the task of pulse-wave velocity estimation. Data from a pilot study indicate that the desired signal component in each channel can be modelled as a scaled and time-shifted version of the true, underlying signal. Exploiting the fact that this underlying signal is characterised by high-energy peaks at instants of pulse traversal, an analysis of statistics of the short-term signal energy allows for an estimation of the scale factor, and correlation analysis yields the necessary time-shift for the signal alignment across the channels. By compensating the scale and time-aligning the signals across all channels of a handpiece, an SNR-weighted linear combination yields the beamformed signal. The SNR in each channel is *blindly* estimated, based on percentile statistics of the short-term signal energies and by cross-validating across channels – increasing the robustness of the estimates.

Experiments demonstrate that the weights assigned during beamforming reflect the signal quality in the channels – validating the SNR estimation. Further, the beamformed output shows a cleaner signal with spurious pulses in the individual channels being well suppressed. Because the ICA does not require an explicit compensation of the individual channel scale factors and is free to derive the optimal weighting in terms of maximising statistical independence, it yields sharper, better formed outputs compared to the beamformer.

Regarding the reliability of individual PTT estimations: the distribution of the estimates has low variance when estimated on the beamformed or ICA-enhanced outputs. In comparison, the estimates from the brute-force method exhibit a larger variance – indicating the influence of noisy and unreliable beat-pairs.

While we have demonstrated the benefit of the proposed approaches in the context of PWV estimation, the underlying ideas for blind SNR estimation and delay- and scale compensation can be more broadly applied to analyse the quality of, or enhance the signals from multidimensional LDV data in biomedical applications.

4.6 Addendum

The following subsections present an extended analysis that was not published in a peer-reviewed journal but was documented in a project deliverable for the InSiDe project. This analysis expands the dataset and evaluates whether the conclusions drawn in the preceding sections are substantiated by additional evidence.

4.6.1 Premise of the expanded analysis

This section introduces an extension of the previously presented work by applying the beamforming method to an alternative dataset. The dataset, referred to as InSiDe, is described in detail in Chapter 6. Briefly, it comprises 83 patients, each of whom underwent multiple LDV measurements. For the purposes of this analysis, only the carotid-femoral measurements were considered, with each patient contributing three such recordings. Additionally, carotid-femoral PWV reference values were obtained using the Sphygmocor system via arterial tonometry.

Following the LDV measurements, cfPWV was also assessed using the SphygmoCor system, serving as the ground truth. A secondary reference metric was derived from the LDV data. Simultaneously recorded ECG signals enabled the identification of heartbeat onsets, allowing segmentation of LDV signals into individual cardiac cycles. Carotid and femoral segments corresponding to the same heartbeat were paired, and pulse transit time was estimated by manually identifying fiducial points. For each measurement, the manual cfPTT was determined as the median value derived from five heartbeat pairs. These pairs were manually selected based on visual inspection, prioritizing segments with high signal quality in the vicinity of the relevant fiducial points.

The beamforming, ICA, and brute-force baseline methods described earlier were applied to all 249 measurements. cfPTT was estimated where signal quality permitted. Subject-level cfPTT values were calculated as the median of up to three measurement-level values per subject.

4.6.2 Expanded results and discussion

The correlation between the SphygmoCor-derived cfPTT values and the manually derived LDV-based cfPTT values was first assessed (Figure 4.8). Statistically significant correlations were observed at both the measurement level ($\rho = 0.646$, $p < 0.001$, $N = 165$) and the subject level ($\rho = 0.625$, $p < 0.001$, $N = 66$).

Figure 4.9 presents subject-level comparisons for cases where cfPTT estimates were available across all methods (N = 39). The manual cfPTT served as the reference. Among the automated methods, beamforming demonstrated the highest correlation with the manual reference ($\rho = 0.457$, $p = 0.003$), followed by ICA ($\rho = 0.375$, $p = 0.019$), and brute-force ($\rho = 0.255$, $p = 0.117$).

An alternative visualization is provided in Figure 4.10, which illustrates the absolute differences between automated and manual cfPTT estimates in terms of density and cumulative density. The results indicate

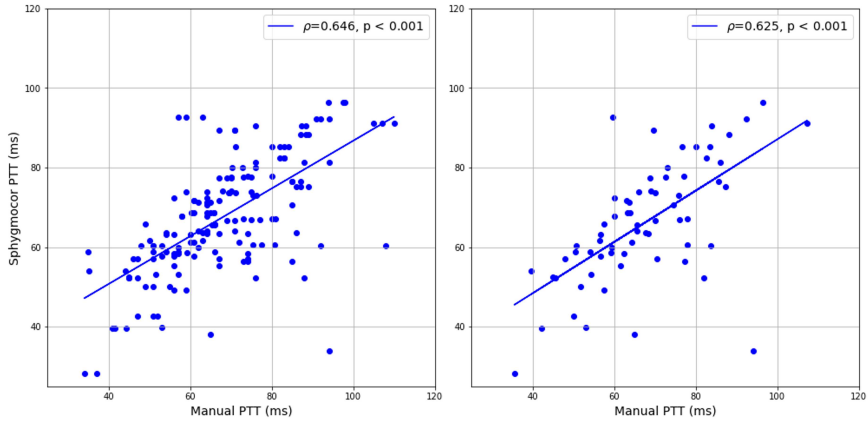

Figure 4.8: Comparison of manual cfPTT estimates derived from LDV data with cfPTT values obtained via the SphygmoCor system. The left panel presents data at the measurement level (three measurements per subject), while the right panel aggregates data at the subject level using the median of available measurements.

that beamforming and ICA yield estimates closer to the manual reference, with beamforming showing a slight advantage. The brute-force method exhibited larger deviations.

These findings are consistent with those discussed in Section 4.4, reinforcing and extending the conclusions regarding the efficacy of beamforming and ICA-based approaches for automated cfPTT estimation.

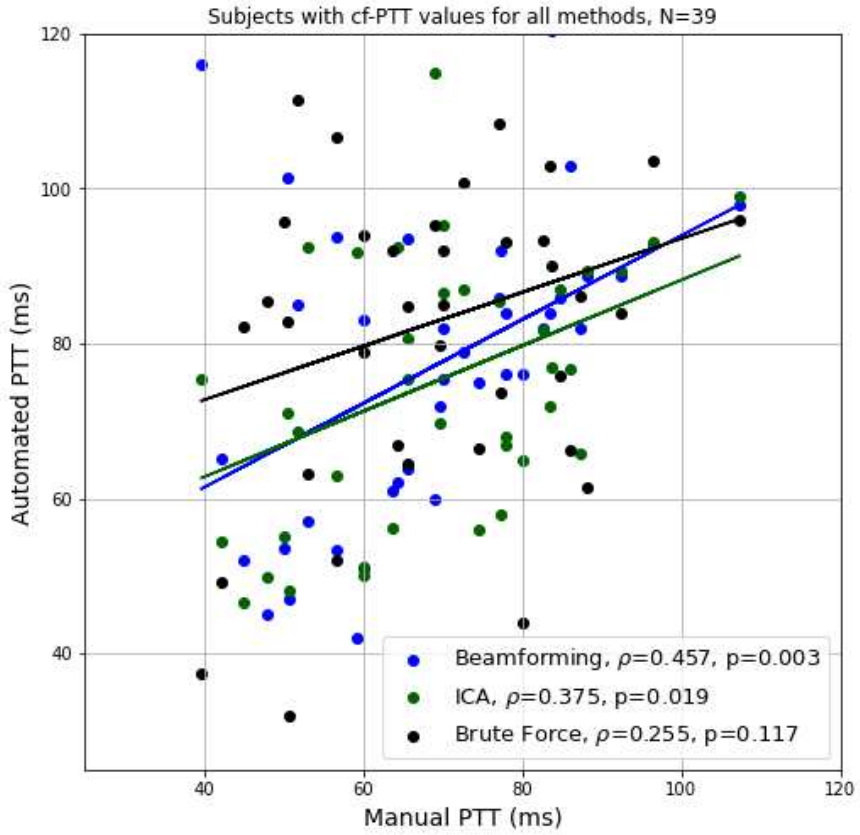

Figure 4.9: Correlation of automated cfPTT estimation methods (beamforming, ICA, brute-force) with manual cfPTT estimates at the subject level. Trendlines, correlation coefficients, and p-values are shown.

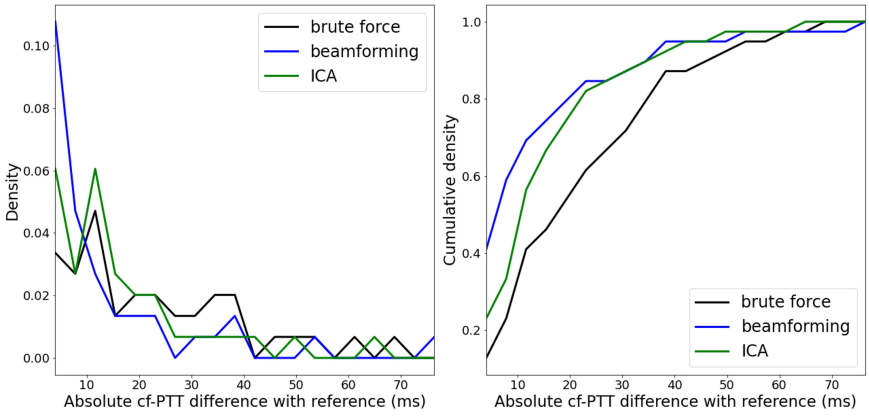

Figure 4.10: Density (left) and cumulative density (right) plots of the absolute differences between automated and manual cfPTT estimates. Beamforming and ICA methods show smaller deviations compared to the brute-force approach.

CHAPTER 5

REAL-TIME PULSE WAVE VELOCITY ESTIMATION

POSITIONING OF THE CHAPTER

This chapter is derived from the article titled *Real-Time Beat-to-Beat Pulse Wave Velocity Estimation: A Quality-Driven Approach using Laser Doppler Vibrometry* (Seoni, S., Segers, S., Beeckman, S., Salvi, M., Romanelli, M., Badhwar, S., Bruno, R. M., Li, Y., Aasmul, S., Madhu, N., Molinari, F. & Morbiducci U.). At the time of writing, this article was submitted to *Medical & Biological Engineering & Computing* for publication. The primary authorship and editorial work was conducted by Dr. Silvia Seoni. The development of real-time PWV estimation algorithms based on the quality metrics introduced in chapter 3 was a collaborative effort between the InSiDe-project partners at UGent and PoliTo. This chapter outlines those joint contributions.

ABSTRACT

Arterial stiffness, a key cardiovascular risk marker, is typically assessed via carotid-femoral pulse wave velocity (cfPWV), the gold-standard method. In this study, we introduce CAPE (Continuous Automatic PWV Estimation), an innovative framework for near real-time cfPWV estimation based on beat-to-beat analysis of Laser-Doppler Vibrometry (LDV) signals. CAPE integrates automatic fiducial point detection,

systematic signal quality control, and a cross-channel strategy to provide a highly reliable assessment of cf-PWV. The framework was evaluated using LDV signals acquired from 100 patients with mild to moderate essential hypertension, using a multichannel laser vibrometry system. CAPE calculates cf-PWV as the ratio of carotid-femoral distance to pulse transit time (PTT), which is the delay between carotid and femoral fiducial points. These points are detected using template-matching on the second derivative of LDV displacement signals. Signal quality in CAPE is ensured through an integrated quality assessment based on the number of automatically detected carotid-femoral peaks, which assigns confidence scores (acceptable or excellent) to the PWV measurements. When validated against the gold-standard applanation tonometry, CAPE achieved a mean bias of 0.25 ± 0.77 m/s, demonstrating high reliability and precision. The optimized framework estimates cf-PWV in 3 seconds, making CAPE ideal for clinical applications requiring real-time cardiovascular assessment.

5.1 INTRODUCTION

The aorta and large central arteries buffer the heart's pulsatile output by expanding with each beat to store elastic energy, which is released during relaxation to maintain continuous blood flow and stable pressure [35, 49]. With age or disease, arterial stiffening reduces the buffering capacity of arteries, increasing the risk of e.g. stroke, cardiac failure, chronic renal disease, end-organ damage [11]. Based on evidence, over the past few decades, arterial stiffness has been increasingly recognized as a key indicator of cardiovascular risk and mortality [8, 75].

Arterial stiffness can be evaluated by measuring the so-called pulse wave velocity (PWV) which refers to the speed at which pressure waves propagate through the arterial tree during the systolic contraction. High PWV values indicate reduced vessel distensibility, reflecting greater arterial stiffness [63]. PWV is typically measured between two arterial sites, one proximal and one distal, to assess the velocity along a segment of the arterial pathway of defined length. In this regard, carotid-femoral PWV is considered the gold-standard method for assessing arterial stiffness, where pressure waveforms are captured from the carotid and femoral arteries, located in the neck and groin, respectively [8]. PWV is determined by the ratio of the distance between two arterial sites, to the transit time of the pulse wave between the two measurement sites.

A non-invasive, commonly adopted technique for measuring PWV is applanation tonometry. Various algorithms can be implemented within applanation tonometry to enhance the accuracy of PWV measurements.

These algorithms have been developed to improve the accuracy of fiducial point detection and Pulse Transit Time (PTT) estimation, with the foot of the waveform often serving as the primary reference point [200, 201]. Foot-to-foot methods such as the diastole-minimum, maximum first derivative, maximum second derivative, and tangential methods are frequently employed, along with region-based approaches like the diastole-patching method [202] or region-based cross-correlation approach [203]. However, current automated PWV estimation methods often face challenges including operator dependency, sensitivity to signal noise, and lack of real-time quality assessment capabilities. These limitations can lead to unreliable measurements and require multiple recording attempts in clinical settings.

In some of the proposed implementations, applanation tonometry is combined with ECG signals, where the R-wave of the ECG provides a timing reference to allow for sequential measurements at the two measuring sites [204, 205]. Other technologies, such as ultrasound, Magnetic Resonance Imaging (MRI), and accelerometers, are also used to detect arterial pulses and estimate PWV [11, 206, 207]. Ultrasound-based devices, for instance, rely on Doppler signals or vessel wall motion tracking to measure PTT [208, 209]. Regional aortic stiffness can be measured using 4-Dimensional Flow Cardiac Magnetic Resonance [210, 211]. However, noninvasive PWV measurements present practical challenges hampering their large adoption [11], which have motivated the exploration of alternative methods. These practical limitations highlighted the need for more accessible and operator-independent measurement techniques. Laser-Doppler Vibrometer (LDV) has emerged as a promising non-contact technique, detecting skin motion overlying the carotid and femoral arteries, and offering a viable method for PWV estimation [21, 22, 185, 212]. There is a large body of literature confirming that LDV offers a simple, noninvasive, and operator-independent method for assessing arterial stiffness, with results comparable to established methods [21, 22, 212].

In previous studies, the feasibility of LDV for PWV measurements was demonstrated using industrial-grade sensors [22]. As part of the H2020-funded CARDIS project, a multi-beam handheld device was developed, incorporating a silicon photonics chip into a compact design, enabling flexible, multi-array configurations [19]. The prototype consists of two separable handheld units for simultaneous measurement of the neck and groin, each equipped with six channels with a laser beam. In a clinical feasibility study, carotid-femoral PWV (cfPWV) measurements from this device were compared to a reference method using applanation tonometry, yielding promising results [25]. Furthermore, Badhwar et al. [23] demonstrated the clinical validity of LDV-based measurements of carotid-femoral PWV (cfPWV) compared to standard reference techniques.

In this context, we present the framework CAPE (Continuous Automatic PWV Estimation), an automated algorithm for cfPWV estimation based on beat-to-beat analysis of high-quality LDV signals acquired over several heartbeats. The approach builds upon our previously validated methodology for automatic fiducial point detection and signal quality assessment, thoroughly described in [27], which is now embedded within CAPE to enable robust and confidence-classified cfPWV measurements. The main contributions of this paper are as follows:

- A near Real-Time automatic algorithm for cfPWV estimation using an LDV system (with results available within approximately 3 seconds after signal acquisition), enabling continuous cardiovascular monitoring with minimal operator intervention.
- The integration of automatic fiducial points detection with a quality criterion, ensuring accurate and reliable cfPWV estimation with systematic signal quality assessment.
- An LDV multichannel acquisition implementing a cross-channel strategy and an innovative beat-to-beat analysis for cfPWV estimation.
- Based on signal quality, a quality-controlled algorithm with integrated confidence level assessment for cfPWV measurement.

This paper is structured as follows: Section 2 provides a comprehensive overview of the proposed method, while Section 3 details the experimental results. Finally, Sections 4 and 5 offer a thorough discussion of the overall work.

5.2 MATERIALS AND METHODS

5.2.1 Dataset

The dataset used in this study was acquired as part of the CARDIS project [25]. The CARDIS project recruited 100 patients, both male and female, aged between 18 and 85 years, diagnosed with mild to moderate essential hypertension (systolic blood pressure ranging from 140 to 179 mm Hg and diastolic blood pressure ranging from 90 to 109 mm Hg). The study was conducted at the Georges Pompidou European Hospital (Paris, France), where patients referred by the Hypertension and Pharmacology units underwent carotid-femoral pulse wave velocity (cfPWV) assessment in the vascular laboratory as part of routine clinical care.

To ensure stable physiological conditions, all measurements were performed in the supine position following a 10-minute rest period, in accordance with the European Society of Hypertension guidelines [1]. Three consecutive measurements of blood pressure and heart rate were obtained using a validated oscillometric device (Colin Press-Mate BP monitor) immediately before cf-PWV acquisition.

The applanation tonometry measurements were acquired first using the SphygmoCor system (Atcor Medical, Australia), which served as the reference method in this study. On the same day and within the same clinical session, LDV signals were recorded using the CARDIS device from the carotid and femoral arteries. Although the two measurements were not simultaneous, the temporal gap was minimal, and both were acquired under comparable resting conditions to limit potential hemodynamic variability. The LDV signals used in this study were recorded in an ambulatory setting, replicating real-world conditions, allowing for the evaluation of CAPE's performance under conditions where motion artifacts might be more prevalent.

Exclusion criteria included secondary hypertension, established cardiovascular diseases such as a history of acute heart failure, unstable coronary heart disease, peripheral arterial disease, stroke, and arrhythmias. Additionally, patients with chronic inflammatory or infectious diseases were excluded from the study. The study received approval from the National Ethics Committee (Comité de Protection des Personnes) and is registered under ClinicalTrials.gov with ID: NCT03446430.

Raw LDV data in the form of in-phase and quadrature (IQ) signals were acquired at a sampling frequency of 100 kHz. The resulting LDV displacement signals were downsampled to 10 kHz upon demodulation. An IIR infinite impulse response low-pass filter with a cut-off frequency of 30 Hz was applied to LDV displacement recorded signals, which were then differentiated twice to obtain acceleration. Note: this filtering was also applied after *each* differentiation step to further suppress high-frequency noise. The filtering was performed using zero phase forward-backward filtering to avoid phase distortion and preserve the temporal integrity of the signal features.

5.2.2 LDV device

An extensive description of the CARDIS device and the embedded optical system is provided in Li et al. [19]. Briefly, the device comprises two main components: Handpiece 1, which includes the primary grip, and Handpiece 2, an auxiliary extension. The primary handpiece was placed at the femoral artery and the secondary handpiece at the carotid artery for simultaneous

measurement from the two arterial sites for carotid-femoral PWV measurements. Each handpiece projects a series of 6 laser beams (wavelength 1,550 nm) arranged linearly with a 5 mm interval between them. To enhance the reflection of the laser beams, a retro-reflective tape is applied to the measurement area on the skin. Additionally, the device includes a spacer to ensure optimal optical focus and stability during measurements. Figure 5.1 displays an illustration of the device and the positioning of these handpieces (a) and a measurements setup (b). A single measurement consists of six LDV signals acquired at the carotid site and six LDV signals acquired at the femoral site.

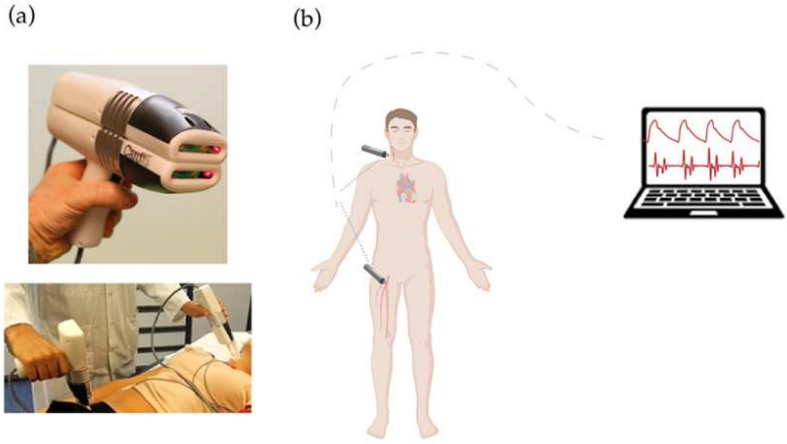

Figure 5.1: LDV device and the positioning of (a) the two handpieces and (b) a measurements setup.

5.2.3 Automatic algorithm for PTT and PWV estimation

An overview of the CAPE framework for the cfPWV analysis is presented in Figure 5.2. LDV signals are acquired using the CARDIS device from femoral and carotid sites. The panel of Figure 5.2 displays an example of LDV recording from one of the 6 channels (in terms of displacement signal) at the carotid site together with its second derivative (acceleration signal), the latter being used to identify the fiducial points for the PTT estimation. In detail, in the CAPE framework, the cf-PTT is defined as the time delay between the maximum of the second derivative (fiducial points) of the LDV displacement signals acquired at the carotid and femoral artery measurement sites. The adoption of the second derivative data, corresponding to skin acceleration, minimizes motion drift and enhances sensitivity to rapid changes associated with the pulse wave's arrival [186]. The second derivative was specifically chosen as it amplifies the sharp features of the

waveform while suppressing low-frequency motion artifacts, making it particularly suitable for accurate fiducial point detection. This approach has been shown to be more robust than using either the raw displacement signal or first derivative, especially in cases where baseline drift or patient movement might affect the measurements.

Initially, template matching is applied to accurately identify the fiducial points on the acceleration data [27]. Considering the six LDV signals acquired from each of the two handpieces (Figure 5.1), the proposed algorithm performs a cross-channel analysis of all the possible combinations of carotid-femoral peak pairs, resulting in 36 possible combinations per heartbeat. The CAPE algorithm aggregates these cf-peak pairs for each individual heartbeat, effectively capturing a comprehensive set of peak pairs that serves as a basis for PTT estimation.

To ensure reliable PTT measurements [29], a quality criterion is then applied to individual heartbeats as well as to the overall recording, aiming to preserve the accuracy of PTT measurements. Technically, for each cf-peak pair, the CAPE algorithm calculates the PTT by measuring the delay between carotid and femoral acceleration peaks. The PTT values from each possible combination are then aggregated to perform a beat-by-beat analysis, producing a single PTT value for each heartbeat. Finally, an overall PTT value is computed by averaging these beat-by-beat PTT estimates, yielding a comprehensive cfPWV measurement and an associated confidence level based on signal quality. Specifically, this confidence level is classified as acceptable or excellent, according to threshold values defined by guidelines criteria [29].

5.2.3.1 Identification of the fiducial points

In the CAPE framework, the template matching algorithm is employed to detect peaks in the LDV acceleration signals according to the strategy described in our previous study [27]. This algorithm identifies acceleration waveforms that closely match a pre-constructed template [213], [145]. For this study, two templates were used: one for the carotid site and one for the femoral site. These templates were generated by averaging LDV epochs from high-quality signal recordings. High-quality signals were defined using an expert-based visual scoring system, where only those rated as excellent (score = 5) were included. Details on the template generation can be found in [27]. Each template spans 200 ms centered around the peak of the LDV acceleration signal.

In our previous work [27], we evaluated multiple template durations and found that 200 ms offered the best performance for accurately detecting high-quality LDV acceleration peaks. Building on the previous study, here

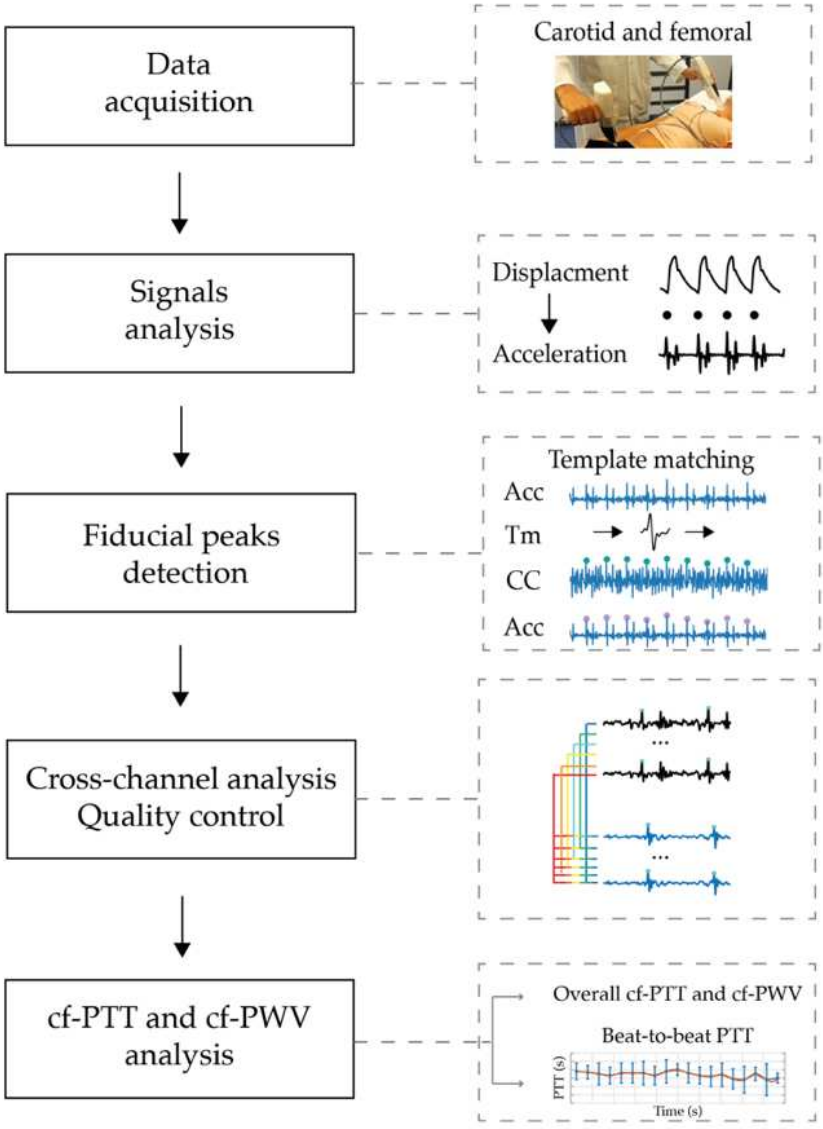

Figure 5.2: CAPE Framework: Starting with the displacement signals acquired by the CARDIS device, the CAPE algorithm calculates the second derivative (acceleration signals) and automatically identifies the fiducial points as the peaks of these acceleration signals. Following a cross-analysis of all cf-peak pairs and a quality control check, CAPE computes cf-PTT values. This process provides an overall PTT and cfPWV (carotid-femoral pulse wave velocity) value, along with a trend analysis of PTT values over time. In the figure, ACC, TM, CC, and cf represent the acceleration, the template, the cross-correlation function, and carotid-femoral.

we revised and expanded the approach to make the method more effective for clinical use and to enhance computational efficiency. Specifically, here, the cross-correlation function was employed to quantify the similarity between the template and LDV signals.

To detect fiducial points within the LDV signals, a threshold level based on the cross-correlation amplitude $r_{x,y}$, referred to as the Cross-Correlation Threshold (CCT), was established according to:

$$\mathrm{CCT} = K\frac{1}{N}\sum_{i=1}^{N}\left|r_{x,y}[i]\right| \tag{5.1}$$

where subscript x and y denote the LDV signal and the template, respectively, and N is the number of steps over which the cross-correlation is computed. Since the template is shorter than the LDV signal, it slides over the entire signal, with the cross-correlation calculated at each step. Consequently, N represents the total number of cross-correlation operations performed as the template slides over the LDV signal. A fiducial point is detected when the cross-correlation value is higher than CCT. The sensitivity and specificity of the peak detection process are controlled by the tuning factor K, which directly influences PTT estimation accuracy. An example of the way the fiducial peaks detection and the template matching algorithms operate is displayed in Figure 5.3.

The acquired signals from all 12 channels (6 from the carotid hand piece, and 6 from the femoral handpiece) are processed simultaneously, using separate templates for carotid and femoral LDV signals while maintaining the same K value for CCT calculations. In this configuration, the algorithm can detect up to 36 cf peak pairs per heartbeat, based on the possible combinations of six carotid peaks and six femoral peaks. CAPE then aggregates the cf-peak pairs for each heartbeat, effectively capturing a comprehensive set of peak pairs for a detailed analysis of the specific heartbeat.

5.2.3.2 Automatic quality control

Signal quality is crucial for accurate PTT estimation. To ensure reliable measurements, we introduced a quality control criterion aimed at discarding low-quality and incorrectly detected peaks that could compromise the accuracy of PTT calculations. An example of the LDV acceleration signals acquired from each one of the two handpieces, where the two modules of quality criterion assessment are applied, is presented in Figure 5.4. The quality assessment framework operates at two different levels: individual heartbeat or signal segment evaluation, (*local*) and overall recording quality evaluation (*global*). This local-global approach is founded on the previous

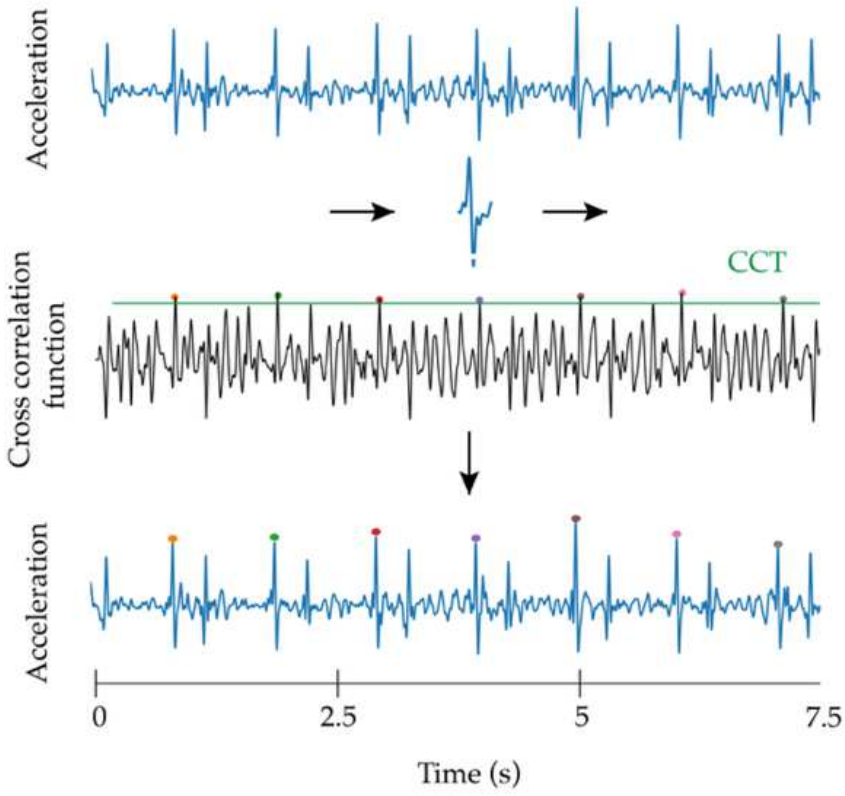

Figure 5.3: Fiducial peaks detection using the template matching algorithm. The template moves among the signals and the cross-correlation function is computed (third line). The last line displays the acceleration signals with the detected peaks, that correspond to the Cross-correlation values higher than the Cross-Correlation Threshold (CCT, green line in the figure). In this example, $K = 2.5$. The template is not scaled to the signals and has a duration of 200 ms.

finding that the LDV acceleration signal quality can be effectively quantified through the number of accurately detected fiducial points [27].

At the first *local* quality control level the Beat Quality Threshold (BQT) module, defining the minimum number of carotid-femoral peak pairs (cf-peak pairs) required to classify a heartbeat as reliable for its use in delay estimation, is applied. If the number of detected cf-peak pairs is lower than BQT, the heartbeat is discarded since the PTT estimation may lack accuracy and could lead to unreliable results. Conversely, if the number of identified peak pairs within a heartbeat is higher than BQT, the estimation of the delay becomes more robust, increasing the likelihood of accurate PTT estimates.

The second *global* quality control level implements the Recording Quality Threshold (RQT) module, which establishes the minimum number

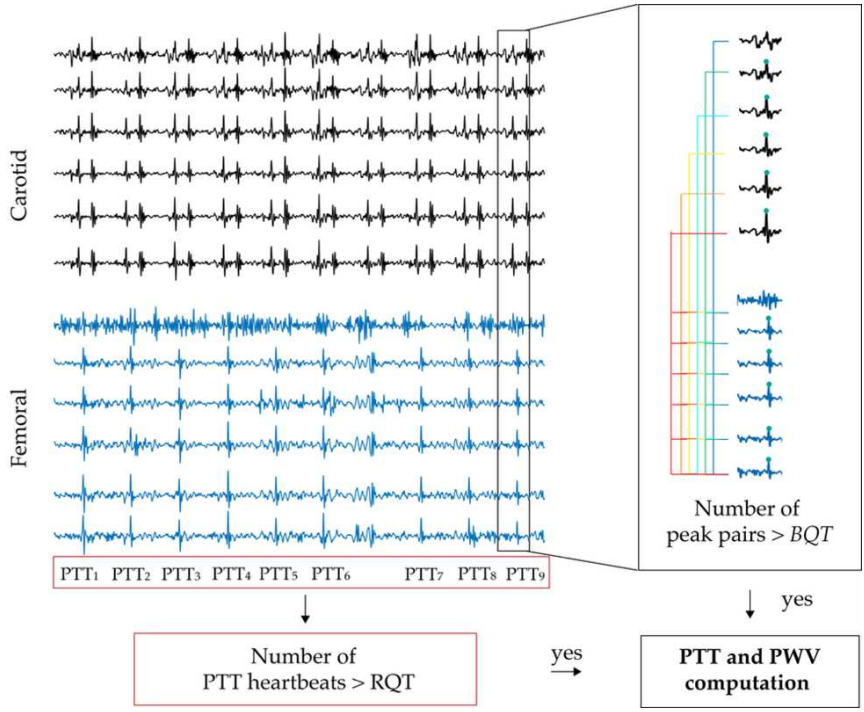

Figure 5.4: Quality criterion for the cfPWV estimation. The black box represents the first module on the number of peak pairs (Beat Quality Threshold, BQT), while the red box the second module on the number of good heartbeats (Recording Quality Threshold, RQT).

of high-quality heartbeats required for a recording to be considered valid. This ensures that in recordings with an insufficient number of high-quality heartbeats, the algorithm will not provide any estimate of cfPWV, as the entire acquisition is considered unaffordable for PTT estimation. The tuning of the threshold values for signal quality selection was conducted in accordance with international guidelines [29], ensuring that the algorithm meets the required standards for accuracy and reliability.

5.2.3.3 PTT estimation

The cfPWV estimation is based on a three-step process of delay computation. Figure 5.5 illustrates an example of a combination of cf-peak pairs used in the cfPWV estimation process. First, for each cf-peak pair, the algorithm calculates the PTT as the temporal distance between the two acceleration cf-peaks (green square). Then, if a heartbeat presents a higher number of cf-peak pairs than BQT, the algorithm computes the median value of all delays of the corresponding heartbeat (PTT_{hbeat}). In this way, heartbeats that do not meet the BQT threshold are excluded from the estimation.

Finally, when the number of valid heartbeats is higher than the RQT, the algorithm computes the overall PTT for the entire recording, denoted $\overline{PTT}$, in terms of median value of all PTT_{hbeat} values.

As recommended by the expert consensus document on the measurement of aortic stiffness by Van Bortel et al. [29], the final cfPWV is computed as follows:

$$PWV = 0.8 \cdot \frac{dx}{\text{PTT}} \tag{5.2}$$

Where dx is the directly measured straight distance between the carotid and femoral sites, PTT is the computed delay, and 0.8 is a correction factor. The proposed algorithm offers two distinct analyses: an overall cfPWV estimation over the entire recording, and a time-based assessment of cfPWV variation, providing a detailed beat-to-beat evaluation of cfPWV trends. A final comprehensive overview of the CAPE framework is displayed in Figure 5.6.

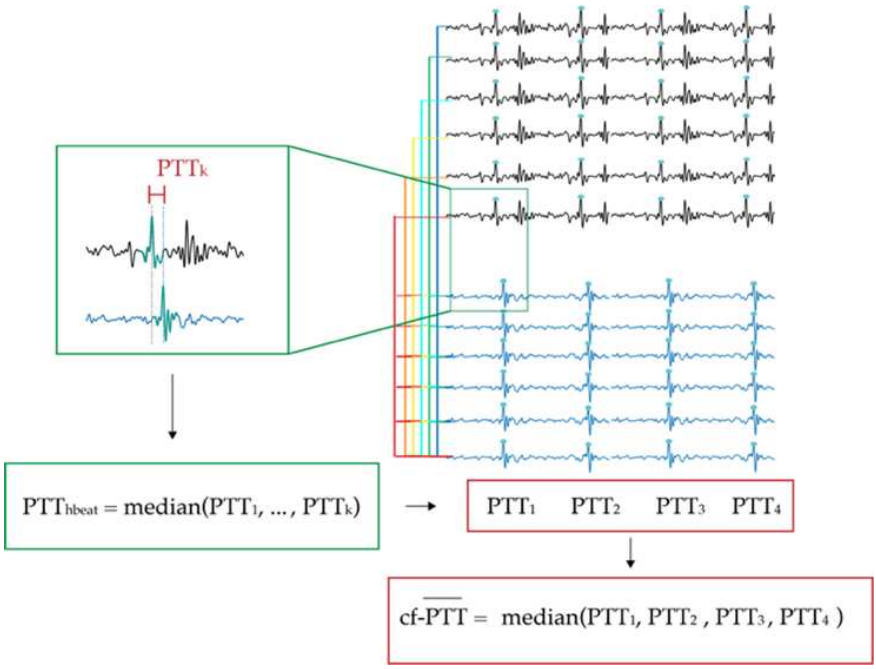

Figure 5.5: Automatic Estimation of Final cf-PTT: CAPE first computes the pulse transit time (PTT) between all peak pairs (green square) within each individual heartbeat (indicated by the green rectangle). It then determines the final PTT value by taking the median of the PTT values across all heartbeats (indicated by the red rectangle).

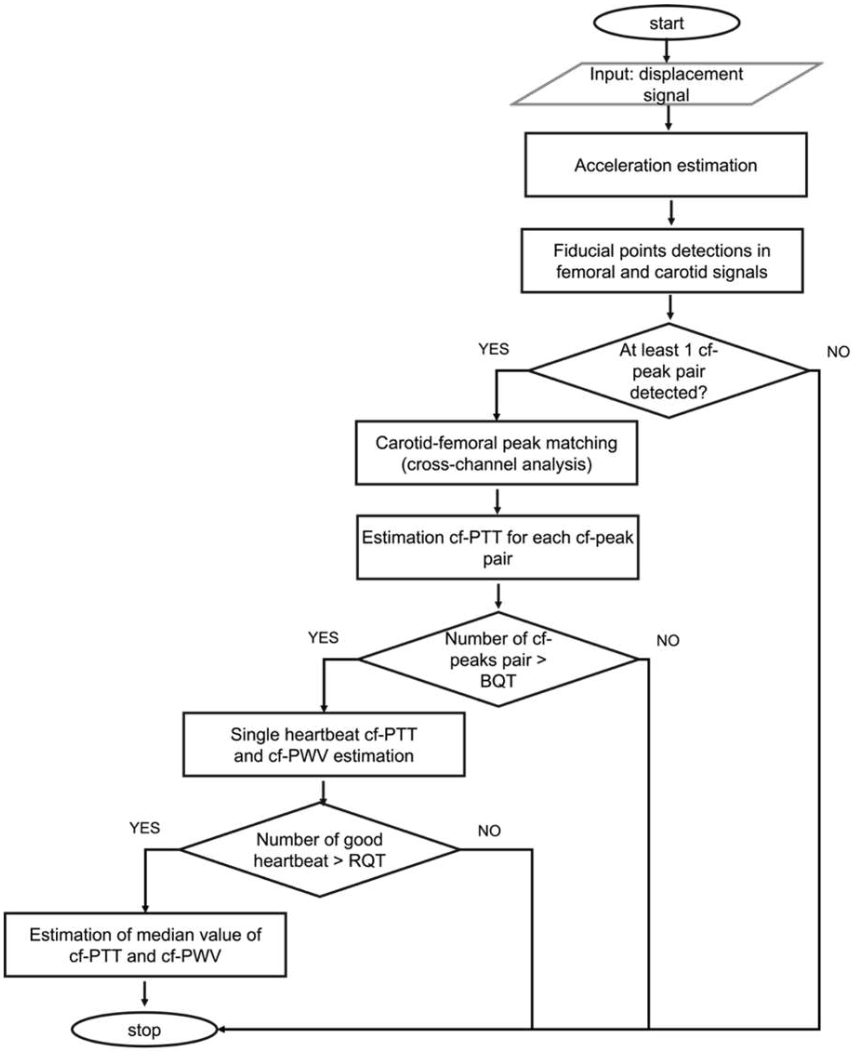

Figure 5.6: A comprehensive overview of the CAPE framework.

5.2.4 Validation and Ablation Analysis

5.2.4.1 Validation of cfPWV estimation

The automatic algorithm for cfPWV estimation was validated against applanation tonometry measurements (SphygmoCor System) [214], considered as the gold standard. The equivalence of the applanation tonometry-based and of the LDV-based approaches was tested through Bland-Altman analysis [215, 216], calculating the mean differences between the two estimated cfPWV data, along with their standard deviations. Following international guidelines criteria [29], two cfPWV measurements are considered equivalent if the mean difference is less than 0.5 m/s with a standard deviation (SD) below 0.8 m/s.

Based on guidelines, measurements are classified into three quality grades:

- Excellent: mean difference < 0.5 m/s and SD < 0.8 m/s
- Acceptable: mean difference < 1.0 m/s and SD < 1.5 m/s
- Poor: mean difference > 1.0 m/s or SD > 1.5 m/s

To optimize the PWV estimation, a systematic tuning and ablation analysis was conducted for three key variables (K, BQT, and RQT) of the CAPE framework:

- The value of K was varied from 1 to 5, in increments of 0.5.
- The value of BQT was varied from 10 to 20, in increments of 5.
- The value of RQT was varied from 5 to 15, in increments of 5, considering a recording duration of 20 seconds.

5.2.4.2 Confidence level of the cfPWV estimation

The CAPE framework, implementing an adaptive validation approach through dynamic adjustment of BQT and RQT thresholds, enables quality-dependent accuracy levels. This flexibility allows the algorithm to operate effectively across varying signal quality conditions, with three distinct response modes:

- Low-quality signals: The algorithm automatically withholds PWV estimation when signal quality falls below minimum thresholds, preventing unreliable measurements.

- Moderate-quality signals: For signals meeting basic quality measurements, the algorithm provides acceptable PTT estimates, ensuring usable measurements while acknowledging potential limitations in precision.
- High-quality signals: When the signal quality is high, the algorithm delivers an excellent measurement with high accuracy PTT estimates.

Following established guidelines [29], two distinct threshold configurations were implemented to optimize the algorithm performance. The first configuration focuses on high-precision measurements, optimized specifically for high-quality signals to deliver maximum accuracy in PTT estimation. The second configuration adapts to moderate-quality signals, providing acceptable measurement precision while maintaining reliability. This dual-configuration approach ensures the algorithm's versatility across varying signal quality conditions while maintaining measurement reliability.

5.2.4.3 Ablation analysis

To assess the impact of various quality control modules on cfPWV estimation, an ablation analysis was performed by systematically disabling specific thresholds. Disabling the BQT threshold allowed for the evaluation of how single-beat quality control influences the overall accuracy of cfPWV estimation. Similarly, disabling the RQT threshold assessed the effect of quality control applied to the entire recording on the final cfPWV estimate.

Additionally, we evaluated the computation of the PTT by implementing four distinct statistical approaches, applied to both individual beats and the entire recording:

$$PTT_{\text{mean\_mean}} = \frac{1}{N}\sum_{i=1}^{N}\left(\frac{1}{k_i}\sum_{j=1}^{k_1} PTT_{hbeat,1,j}, ..., \frac{1}{k_N}\sum_{j=1}^{k_N} PTT_{hbeat,N,j}\right) \quad (5.3)$$

$$PTT_{\text{mean\_median}} = \frac{1}{N}\sum_{i=1}^{N}\left(Median(PTT_{hbeat,1,j}), ..., Median(PTT_{hbeat,N,j})\right) \quad (5.4)$$

$$PTT_{\text{median\_mean}} = Median\left(\frac{1}{k_i}\sum_{j=1}^{k_1} PTT_{hbeat,1,j}, ..., \frac{1}{k_N}\sum_{j=1}^{k_N} PTT_{hbeat,N,j}\right) \quad (5.5)$$

$$PTT_{\text{median\_median}} = Median(Median(PTT_{hbeat,1,j}), ..., Median(PTT_{hbeat,N,j})) \tag{5.6}$$

where N represents the number of heartbeat and k the number of carotid-femoral pair in the specific heartbeat.

5.3 RESULTS

5.3.1 Validation of the algorithm

5.3.1.1 Validation of cfPWV estimation

The optimal configuration (K = 2.5, BQT = 15, and RQT = 15) using $PTT_{\text{median\_median}}$ achieved excellent accuracy with a mean difference of 0.25±0.77 m/s compared to applanation tonometry. Detailed performance metrics under different configurations are presented in Table 5.1. Recordings that did not meet the minimum quality criteria—based on the BQT and RQT thresholds—were automatically excluded from the analysis. The number of subjects and recordings reported in Table 5.1 refer only to those retained after this quality filtering step.

This approach ensures that the analysis is based on reliable signals, consistent with findings from a previous study [27], where only 15% of the measured signals were rated as good to excellent, making them immediately suitable for analysis.

Furthermore, to emphasize the advancements introduced by CAPE, we compared its performance against a previously published LDV-based method that was applied to the same dataset [23]. Unlike CAPE, the earlier method did not include any automatic signal quality assessment and depended on ECG-based detection. As shown in Table 5.2, CAPE achieved lower bias and standard deviation in cfPWV estimation, highlighting its increased accuracy and robustness.

Bland-Altman analysis (Figure 5.7) revealed a slight positive bias in both acceptable and excellent measurement configurations. For acceptable measurements, the bias was 0.39±1.23 m/s (95% limits of agreement: -2.02 to 2.80 m/s), while excellent measurements showed a bias of 0.25±0.77 m/s (95% limits of agreement: -1.26 to 1.76 m/s).

Table 5.1: Mean and standard deviation of the difference between the automatic methods and the tonometry or manual method. K: cross-correlation function; BQT: number of peak pairs in the heartbeat; RQT: number of good beats.

Performance measure	K	BQT	RQT	Mean of difference (m/s)	standard deviation of difference (m/s)	number of patients	number of recordings
Excellent	2.5	15	15	0.25	0.77	25	69
Acceptable	2.5	15	10	0.39	1.23	52	151

Table 5.2: Comparison of cfPWV estimation accuracy between CAPE and the method by Badhwar et al. [23] on the same dataset. STD refers to the standard deviation.

METHOD	BIAS (m/s)	STD (m/s)	KEY FEATURES
Badhwar et al. with ECG	0.58	1.14	ECG used; no quality filtering
Badhwar et al. without ECG	0.65	1.27	ECG-free; no quality filtering
CAPE (proposed method)	0.25	0.77	ECG-free; automatic quality assessment

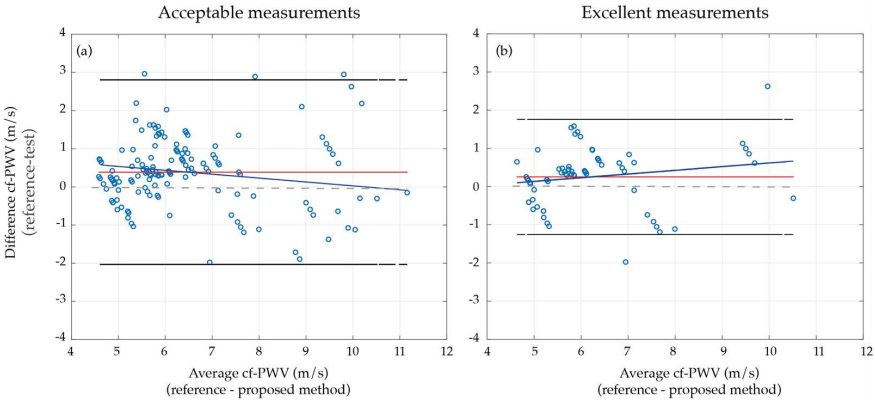

Figure 5.7: Bland-Altman analysis between the tonometry and the proposed algorithm, using the configuration for acceptable (a) and excellent (b) measurements. The red line represents the mean difference, while the black lines indicate the 95% limits of agreement, computed as the mean of difference $\pm$ 1.96 of the standard deviation difference. The gray dashed line represents the zero.

5.3.2 Threshold tuning and ablation analysis

To determine the optimal values for the quality thresholds BQT and RQT, an empirical tuning procedure was conducted. Various combinations of these parameters were systematically tested across different values of the correction factor K. The configuration that achieved the best balance between estimation accuracy (measured in terms of mean difference and standard deviation relative to applanation tonometry) and the number of retained subjects and recordings was identified as: $K = 2.5$, BQT = 15, and RQT = 15 (Table 5.3).

The ablation analysis, summarized in Table 5.4, highlights the critical role of the BQT and RQT thresholds in ensuring high-quality PWV estimation. The BQT was disabled to assess how the inclusion of lower-quality beats influences overall PWV estimation. The results indicated a significant deterioration in the accuracy of PWV measurements, as a substantial number of low-quality beats were incorporated into the analysis, leading to increased variability and potential inaccuracies in the calculated PWV.

Table 5.3: Tuning threshold result: Effects of the BQT, RQT, and K parameters on cfPWV estimation accuracy. Values report the mean and standard deviation of the difference with applanation tonometry. K: correlation threshold; BQT: number of peak pairs; RQT: number of high-quality beats.

Performance measure	K	BQT	RQT	Mean of difference (m/s)	standard deviation of difference (m/s)	Number of patients	Number of recordings
Acceptable	1	20	10	0.47	1.20	52	154
Excellent	1	20	15	0.38	0.70	26	58
Acceptable	2	20	10	0.32	1.20	44	125
Excellent	2	20	15	0.33	0.64	20	47
Acceptable	**2.5**	**15**	**10**	**0.39**	**1.23**	**52**	**151**
Excellent	**2.5**	**15**	**15**	**0.25**	**0.77**	**25**	**69**
Acceptable	3	15	10	0.27	1.20	37	102
Excellent	3	15	15	0.22	0.68	17	47

Additionally, the RQT was also disabled. This allowed recordings with insufficient valid beats to be considered in the analysis, negatively affecting the robustness of the PWV estimations. The data revealed that the absence of this threshold contributed to a marked increase in estimation error, particularly in recordings that were brief or contained excessive noise.

The findings from the ablation analysis underscore the necessity of implementing stringent quality control measures in cardiovascular signal analysis to enhance the reliability of PWV assessments.

The results obtained using the four approaches for computing the final delay, based on the module combination for excellent measurements (k = 2.5, BQT = 15, and RQT = 15), are summarized in Table 5.5, where PTT_{median_median} appears to be the most robust against outliers, displaying the smallest standard deviation computed between the LDV-based PTT estimation (performed with the four statistical approaches) and applanation tonometry.

As an extension of our previous analysis on the same dataset [23], we investigated the relationship between cf-PWV values – measured using both LDV and applanation tonometry (AT) – and age, body mass index (BMI), and systolic blood pressure (SBP). For this analysis, Spearman correlation coefficients (ρ) and corresponding p-values were computed for each modality. LDV-derived cf-PWV values were averaged per subject across all beats that met the "excellent" quality criterion (n = 25).

Table 5.4: Ablation Study Results: Effects of BQT and RQT modules on cfPWV estimations. K: cross-correlation function; RQT: number of peak pairs in the heartbeat; RQT: number of good beats.

BQT	RQT	Mean of difference (m/s)	standard deviation of difference (m/s)
X	✓	2.56	2.39
✓	X	0.75	4.36
✓	✓	**0.25**	**0.77**

Table 5.5: Comparison between LDV-based PTT estimation (performed over the entire recording) approaches and applanation tonometry. The best configuration is highlighted in bold. STD refers to the standard deviation.

Estimation method	MEAN OF DIFFERENCE (M/S)	STD OF DIFFERENCE (M/S)
$PTT_{\text{mean\_mean}}$	0.16	0.95
$PTT_{\text{mean\_median}}$	-0.25	2.23
$PTT_{\text{median\_mean}}$	0.25	0.88
$PTT_{\text{median\_median}}$	**0.25**	**0.77**

The scatterplots of cf-PWV versus age, BMI, and SBP for both LDV and AT modalities in Figure 5.8 highlight that the two measurement methods exhibit similar associations with physiological quantities. In detail, cf-PWV via LDV showed strong correlation with age and moderate correlation with SBP, consistent with physiological expectations (and with AT measurements as well). Although weaker, correlations with BMI were comparable between modalities. These findings further support the plausibility and potential generalizability of LDV-based cf-PWV estimation using the CAPE framework.

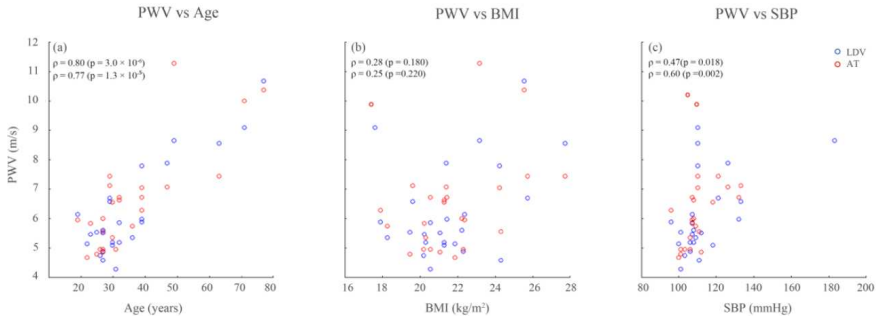

Figure 5.8: Scatterplots showing the association between cf-PWV values obtained from LDV (blue points) and applanation tonometry (AT, red points) with key physiological variables: (a) age (left); (b) body mass index—BMI; (c) systolic blood pressure—SBP.

5.3.3 Beat-to-beat analysis

Finally, the proposed algorithm performs the beat-to-beat analysis. Figure 5.9 presents an example of the PTT variability on a beat-by-beat basis. In this context, variability refers to the global assessment of PTT fluctuations across all beats, rather than a direct difference between consecutive beats. By evaluating these fluctuations, it is possible to qualitatively assess the robustness of the measurement.

As a final analysis, we present the time-varying trend of cfPWV, as shown in Figure 5.10. The results indicate that PWV exhibits beat-to-beat variability with a slow trend that could be ascribed to physiological

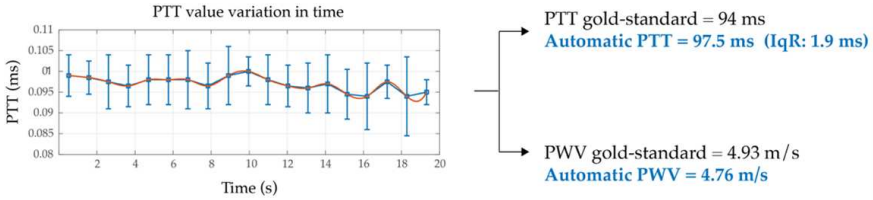

Figure 5.9: An example of PTT beat-to-beat variability with PTT and automatic PWV values from CAPE (blue) and applanation tonometry (black).

lower frequency activity such as breathing and/or so-called Mayer waves [217]. Breathing could influence intrathoracic pressure and modulate arterial blood pressure, potentially leading to cyclic changes in transit time.

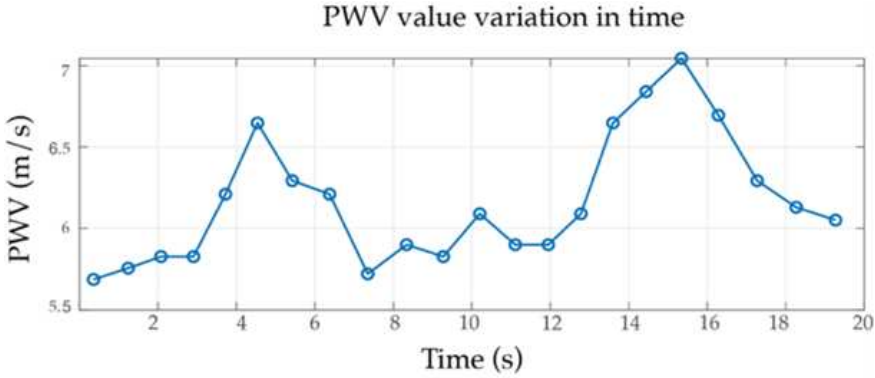

Figure 5.10: An example of the time-varying trend of cfPWV. Beats that are not classified as of good quality are excluded, and the values in between are interpolated to maintain the continuity of the trend.

5.4 DISCUSSION

This study presents CAPE, a near real-time, accuracy-controlled framework for cfPWV estimation using an LDV system. CAPE offers a continuous (beat-to-beat analysis) as well as an overall cfPWV estimation, providing a comprehensive understanding of cardiovascular dynamics. To ensure accuracy, CAPE applies a quality criterion that assesses the reliability of measurements in advance, based on the quality of heartbeats and recordings. It is designed to handle variable quality single pulses (heartbeats) and use only those that meet established standards for the cfPWV estimation, resulting in more reliable measurements. Indeed, by considering the number of cf-peak pairs (BQT) and the number of high-quality heartbeats (RQT), CAPE performs the cfPWV estimation, with a specific confidence level, classifying it as excellent, acceptable, or unreliable. This local-global

mechanism is critical in real-world conditions, where signals may be irregular or of suboptimal quality [27]. Furthermore, the dual-tuning architecture ensures flexibility, allowing CAPE to maintain performance across various signal recording levels and deliver either acceptable or high-accuracy measurements, based on data quality. CAPE is fully automated, once the signals are acquired the analysis proceeds without any other operator intervention, minimizing operator dependency and improving reproducibility in clinical applications.

CAPE demonstrated excellent accuracy with improved performance compared to a previous LDV-based study which using the same dataset [23] exhibited a standard deviation of 1.27 m/s versus CAPE's standard deviation of 0.77 m/s, when compared to applanation tonometry. These results underscore the importance of applying quality criteria to ensure the algorithm produces accurate measurements. However, the use of these criteria also led to a reduction in the analyzed dataset, as low-quality recordings were excluded from validation. Specifically, the sample size decreased to 25 patients when only measurements with an excellent confidence level were considered but increased to 52 patients with an acceptable confidence level. This consideration is in line with a previous study where a by-visual inspection quality assessment was implemented [27], and where only 15% of signals were rated from good to excellent, while 52% were classified as poor (20%) or suboptimal (32%).

CAPE's ability to perform cfPWV estimation within just 3 seconds of latency (tested on MacBook Pro 15, 2.6 GHz Intel Core i7 6 core) highlights its computational efficiency, making it an ideal candidate for integration into real LDV devices such as the CARDIS system. The preprocessing step, including acceleration calculation and signal filtering, takes approximately 1.7 seconds, while the quality assessment and fiducial point detection, along with PWV calculation, are completed in about 1.3 seconds. The clinical potential of our framework extends beyond standard PWV measurements. Its rapid processing capabilities make it suitable for continuous monitoring during surgical procedures, intensive care settings, and routine cardiovascular screening. The automated quality assessment feature could particularly benefit clinical research studies requiring large-scale arterial stiffness measurements, where operator expertise might vary across different centers.

Another key strength of the proposed pipeline is its ability to estimate cf-PWV without relying on an ECG signal, which is typically used to detect and synchronize fiducial points [27]. By eliminating the need for ECG, the method simplifies the setup and reduces patient preparation time, all

while preserving measurement accuracy. This makes it especially valuable in clinical settings where quick and efficient assessments are essential.

Finally, another key strength of the proposed pipeline is its ability to estimate cfPWV without relying on an ECG signal, which is typically used to detect and synchronize fiducial points [27]. By eliminating the need for ECG, the method simplifies the setup and reduces patient preparation time, all while preserving measurement accuracy. This makes it especially valuable in clinical settings where quick and efficient assessments are essential.

Despite the promising performance of CAPE, several limitations should be acknowledged. First, the thresholds used in the framework – such as BQT and RQT values – were set based on a single dataset (the CARDIS one). While these threshold values proved effective within this cohort, further validation is needed to assess their generalizability across diverse populations and measurement conditions, particularly in pathological cohorts such as the elderly, individuals with diabetes, or patients with advanced cardiovascular disease. Additionally, CAPE relies on template matching for fiducial point detection. Although this method performed well in CARDIS cohort [27], it may be sensitive to variations in signal morphology.

The framework's *local-global* quality assessment enhances the reliability of cfPWV estimation by filtering out poor-quality signals. However, this process also reduces the number of usable recordings, representing a trade-off between estimation accuracy and data availability. This trade-off should be taken into account when applying CAPE in real-world settings. Future studies should explore the robustness of the quality assessment approach, particularly in datasets characterized by lower signal quality or greater physiological heterogeneity.

Finally, the integration of machine learning or deep learning models [218]. could further enhance CAPE's adaptability by learning from signal variability, thus reducing the need for manual threshold tuning. These models could improve the algorithm's robustness, especially in populations with challenging physiologies. Future work may also include the development of a measurement uncertainty parameter, based on signal quality metrics, to complement the final cfPWV output.

5.5 CONCLUSION

This study introduces the CAPE framework, a near real-time, accuracy-controlled system for cfPWV estimation using LDV signals. CAPE provides continuous, beat-to-beat assessments of arterial stiffness, integrating quality control mechanisms to ensure reliable measurements

across varying signal qualities. By evaluating the number of cf-peak pairs (BQT) and high-quality heartbeats (RQT), CAPE classifies measurements into confidence levels, adapting to real-world conditions. The integration of CAPE within the CARDIS device represents a significant advancement in cfPWV estimation, offering an automated, near real-time solution for continuous cardiovascular monitoring and enhancing clinical assessments of arterial stiffness.

III

Investigating Heart-Carotid Pulse Transit Time for Arterial Stiffness Assessment

CHAPTERS

6 Heart-Carotid Pulse-Transit Time **127**

7 Deep-Learning Based ECG-free Heart-Carotid Pulse Transit Time Estimation **151**

CHAPTER 6

HEART-CAROTID PULSE-TRANSIT TIME

POSITIONING OF THE CHAPTER

This chapter is based on the publication *Heart-Carotid Pulse-Wave Velocity via Laser-Doppler Vibrometry as a Biomarker for Arterial Stiffening: a Feasibility Study* (Beeckman, S., Badhwar, S., Li, Y., Aasmul, S., Madhu, N., Khettab, H., Mousseaux, E., Gencer, U., Boutouyrie, P., Bruno, R. M., & Segers, P., Physiological Measurement, vol. 46(4), 22 April 2025, doi: https://doi.org/10.1088/1361-6579/adcb85) [219]. For this dissertation, Tables 6.5 and 6.6 were added to the discussion. The presented clinical investigational study protocol was determined by prof. Bruno, prof. Mousseaux and prof. Boutouyrie and executed by dr. Badhwar, dr. Gencer, dr. Khettab, dr. Gencer and in part also by the author. Methodology was provided for by prof. Li and ing. Aasmul. The analysis was conceptualized by the author and dr. Badhwar and performed by the author. The publication was written and proof-read by the author, dr. Badhwar, prof. Bruno and prof. Segers.

ABSTRACT

Objective: Large artery stiffening leads to an increase in cardiovascular risk and organ damage of the kidneys, brain or the heart. Biomarkers that

allow for early detection of this phenomenon are a point of interest in research, with pulse-wave velocity (PWV) having been proven useful in predicting and monitoring arterial stiffness. We previously introduced a laser Doppler vibrometry (LDV) prototype which can measure carotid–femoral PWV (cfPWV). In this work, we assess the feasibility of using the same device to infer heart-carotid pulse-transit time (hcPTT) as a first step towards measuring heart-carotid PWV (hcPWV). The advantage of hcPWV over cfPWV is that the ascending aorta, which is the most distensible segment of the aorta contributing most to total arterial compliance, is included in the arterial pathway.

Approach: Signals were simultaneously acquired from a location on the chest (near either the base or the apex of the heart) and the right carotid artery for 100 patients (45% female). Fiducial points on the heart waveforms are associated with opening and closure (second heart sound; S2) of the aortic valve, which can be combined with, respectively, the foot and dicrotic notch (DN) of the carotid waveform to retrieve hcPTT. Considering two distinct heart-signal measurement sites, four hcPTT estimations are evaluated in about 94% of all measurements.

Main results: Correlations between these and known predictors of arterial stiffness i.e. age, blood pressure and carotid–femoral PTT via applanation tonometry indicated that combining S2 from a heart-measurement site located at the base of the heart, with the carotid DN yields hcPTT providing convincing correlations with known determinants of arterial stiffness ($\rho = 0.377$ with age).

Significance: We conclude that LDV may provide a corollary biomarker of arterial stiffness, encompassing the ascending aorta.

6.1 INTRODUCTION

The large arteries, and specifically the aorta, play a central role in the blood circulation [49]. Their structure allows the vessel wall to distend during cardiac contraction, storing elastic energy, which is used during the consequent relaxation to drive blood flow after the pressure wave has passed [35, 49, 220]. This way, a near-continuous flow is assured further down the arterial tract, providing constant organ perfusion. This buffer or 'windkessel' function deteriorates significantly when large arteries stiffen, during a process called arteriosclerosis, leading to deregulated blood pressure, blood flow and consequent organ damage [7, 8, 75, 109]. Understanding the associated waveforms in blood pressure and flow related signals is vital in detecting and preventing this early vascular aging [221].

6.1.1 Carotid-femoral pulse-wave velocity

A metric that allows for quantifying arterial stiffening is pulse-wave velocity (PWV) [8, 11, 222], with especially carotid-femoral PWV (cfPWV) being studied and showing a significant relationship with arterial stiffness. It can be stated that cfPWV serves as the baseline biomarker regarding arterial stiffening [11]. The speed of the pulse-wave induced by heart-contraction increases with increased arterial stiffness. If one measures the arrival time of the pulse-wave at two distinct points on the arterial tract, separated by a distance dx, one can calculate PWV as in equation 6.1, where PTT is the delay in the pulse arrival time (PAT) across the two points. We refer to PTT as the pulse-transit time (PTT).

$$PWV = \frac{dx}{PTT} \tag{6.1}$$

Aside from the current state-of-the-art measurement methods of cfPWV, such as applanation tonometry and ultrasound [11, 184], we have been exploring an alternative approach based on laser-Doppler vibrometry (LDV) [20–22]. With this technique, skin displacement signals above large arteries such as the carotid and femoral arteries can be measured, from which the PAT and carotid-femoral PTT (cfPTT) can be estimated [18]. It was shown that cfPWV via LDV measurements had a high agreement with its tonometry-based counterpart [23]

6.1.2 Heart-carotid pulse-wave velocity

A drawback of cfPWV is that its arterial pathway does not include the ascending aorta, which is the most distensible aortic segment and consequently the region where the increase in arterial stiffness is expected to be most apparent. cfPWV is determined using a pathway spanning from the femoral artery up to the descending thoracic aorta. In this way, an important region of potential elastic behaviour changes is excluded from the metrics. Vlachopoulos et al. have shown that aortic stiffness is an independent predictor of cardiovascular-related mortality and disease [75], that also precedes the onset of hypertension [10].

This work proposes heart-carotid PTT (hcPTT) as an additional biomarker that includes the ascending aorta. Our hcPTT is measured via LDV, as seen in Figure 6.1, as opposed to the more frequent use of MRI to assess aortic stiffness [15, 123–129]. A similar experiment was conducted previously, using accelerometers placed on the chest at the mid-sternal precordial region, and in the neck above the carotid artery [223]. This experiment was able to evaluate the variation of the true central hcPTT during pharmacological and dynamic stress. In general, hcPTT is calculated between

the proximal measurement site (the heart), and the distal one of the carotid [224].

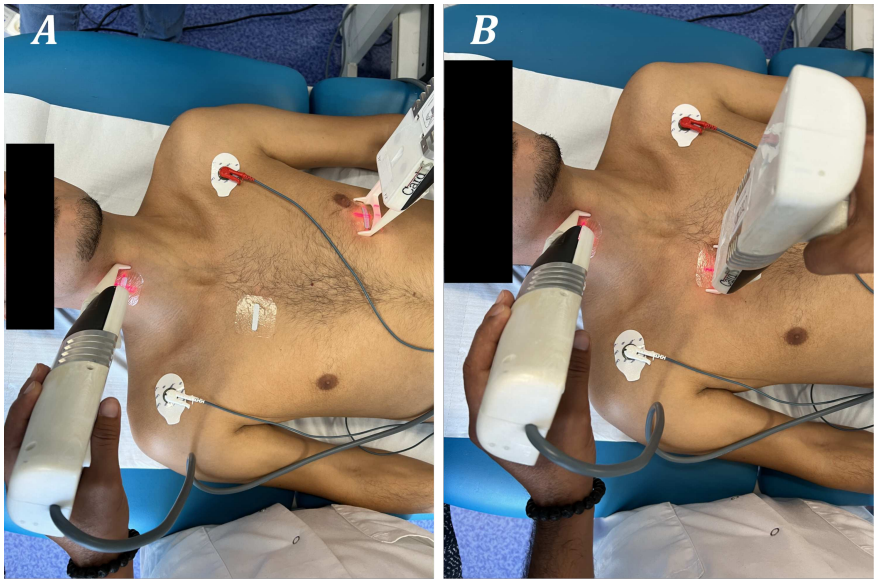

Figure 6.1: Overview of the two investigated methodologies to achieve hcPTT. Both panels show the LDV device's two handpieces measuring in parallel. The left panel shows a measurement on the carotid artery and the fifth left intercostal space. The right panel presents a measurement on the carotid artery and second right intercostal space.

Approaches for the proximal measurement site have been proposed, among them seismocardiography (SCG) [225–228]. SCG also measures skin acceleration, albeit via different technology and methodology, and could thus be interpreted as a form of reference for the currently unexplored LDV heart-waveforms. Phonocardiogram (PCG) methods via digital stethoscope have also been investigated for the proximal measurement [229]. Regarding the distal waveform, LDV can provide reliable waveforms at the carotid [18, 19, 26].

The specific research aims for this article are fourfold: assessing (i) correlation of hcPTT with relevant clinical parameters such as age and blood pressure; (ii) agreement of LDV with the golden standard for cfPTT, as measured by the Sphygmocor system; (iii) agreement between different estimates of hcPTT using LDV; (iv) investigation of the reproducibility of the LDV measurements. From these avenues, we propose an approach for the assessment of hcPTT while simultaneously quantifying the potential usefulness of hcPTT as a biomarker.

6.2 Materials & methods

6.2.1 The LDV-prototype specifications

In the context of a H2020 project (CARDIS, Grant agreement ID: 644798), a first LDV prototype was constructed, which has been extensively described in [19, 26, 230]. Briefly, the device includes two handpieces, with which skin displacement can be simultaneously measured at two different locations. Each handpiece captures data using six laser beams with a wavelength of 1550nm that are reflecting off of a retroreflective tape that is applied to the measurement site. The inter-beam distance is 5mm. The displacement signals obtained are differentiated twice, yielding skin acceleration. The time-point of the arrival of the pulse wave is then detected by selecting the appropriate features in the acceleration signals.

6.2.2 Study population and data collection

In this study, 100 patients with ages ranging from 18 to 90 years old, that could provide informed, written consent were recruited after their routine clinical care. Population statistics are listed in Table 6.1. Exclusion criteria for the InSiDe study were:

- Patients with skin lesions on the chest or neck or allergies to the adhesive that may affect placement of the patch.
- Patients with life-threatening conditions (metastatic cancer, end-stage renal failure, end-stage liver failure or end-stage heart failure).
- Patients with history of acute heart failure (NYHA class III-IV).
- Patients with progressive cardiovascular pathologies (unstable coronary artery disease, Peripheral artery disease, stroke, aortic dissection).
- Patients with arrhythmias leading to great heart rate variability during recordings.
- Pregnant or breastfeeding women.

The patients additionally underwent several tonometric and LDV measurements, with simultaneous recording of LDV signals at the two measuring sites as seen in Figure 6.1. Patients were placed in a supine position for entire duration of the protocol. Tonometric cfPTT data was collected via the Sphygmocor system, to serve as an established biomarker to compare the LDV-results to. The following measurements were performed:

Parameter (N=100)	Mean ± SD	Range
Age (years)	48 ± 17	[18, 81]
Sex (male %)	55	/
BMI (kg/m²)	26 ± 5	[17.24, 39.82]
Systolic BP (mmHg)	130 ± 20	[88, 219]
Diastolic BP (mmHg)	79 ± 15	[49, 136]

Table 6.1: Population statistics. SD refers to standard deviation.

- Carotid-femoral PTT with the Sphygmocor system (three repeated measurements, measuring 10 heartbeats each).
- Heart-carotid PTT, with the LDV probe measuring the heart signals aimed at the base of the heart (Base), as exemplified in panel B of Figure 6.1 (three repeated measurements, measuring 15 heartbeats each).
- Heart-carotid PTT, with the LDV probe measuring the heart signals aimed at the apex of the heart (Apex). An example of this is shown in panel A of Figure 6.1 (three repeated measurements, measuring 15 heartbeats each).

Electrocardiogram (ECG) data were also collected in parallel with the LDV measurements. Brachial systolic and diastolic blood pressure were gathered via state-of-the-art cuff-based technology.

Sphygmocor measurements were performed by continually recording ECG in parallel with the tonometry measurements. These alternate between measuring at the right carotid first, and then the right femoral artery. Transit time from the peak of the R-wave to the foot of the carotid pressure wave, and the peak of the R-wave to the foot of the femoral pressure wave, was used to calculate cfPTT. The intersecting tangent algorithm was used to assess the fiducial point of the foot of both pressure waveforms.

6.2.3 Analysis of heart-carotid LDV data

6.2.3.1 Data properties & preprocessing

For each measurement, six channels were measured for the carotid and heart measurement sites respectively. The signal length varied due to varying signal quality influencing the real-time heartbeat detection, but was capped at 60 seconds as a maximum measurement duration. All signals were passed through a second-order bandpass Butterworth filter with cutoff frequencies at 0.5 and 50Hz respectively, to filter out baseline wandering

and high-frequency signal distortion, and were then differentiated twice. The acceleration signals were then exported to the user at 10kHz and were resampled to 1kHz for post-processing computational purposes.

An example (patient 40, first Base-carotid measurement) is shown in Figure 6.2. As can be observed in the figure, signal quality can vary drastically between channels and/or handpieces since it is possible that only a few beams are placed on top of the target artery [27]. Panel B helps to visualize the arterial pathway between the measurement sites. The hcPTT to be quantified is the time delay between the pressure wave traveling from the aortic valve up to the right carotid artery, as demarcated in the figure panel.

A peak detection algorithm was applied to the ECG signal to detect the R waves of individual cardiac cycles. This allowed us to split the LDV signals into individual cardiac cycles, which will be called epochs in this work. Heart and carotid epochs that correspond to the same heartbeat are selected and matched to estimate the hcPTT based on the available temporal signal features. This is shown in Figure 6.2, panel C.

6.2.3.2 Heart-carotid pulse-transit time calculation

Similar to carotid-femoral, we intended to identify signal features in the LDV traces that correspond to the same physical event in the cardiac cycle, for both the heart and the carotid epochs. For the interpretation of cardiac LDV skin-acceleration signals, we relied on what was reported on SGC data [226, 227].

These SCG signals contain chest-skin acceleration in time, as measured by the application of accelerometers to the skin. From visual inspection of the data, it was found that the LDV signals mostly resembled the SCG waveforms as reported in literature. As indicated in panel C of Figure 6.2, several signal features and their respective fiducial points could be indicated. For the heart-signal epoch, there is the mitral valve closure (MC), isovolumic contraction (IVC), aortic valve opening (AO), rapid ventricular ejection (RE), aortic valve closure (AC), mitral valve opening (MO) and rapid ventricular filling (RF). In the carotid signal-epoch we indicated the foot-of-the wave and dicrotic notch (DN), corresponding to AO and AC respectively. Two hcPTT estimation methods were proposed.

First, the features corresponding to the opening of the aortic valve were identified. For the carotid signals, this is the well-established foot-of-the-wave waveform [11]. Opening of the aortic valve is less evident to assess from the cardiac LDV data. Analyzing reported SCG data, the second peak in the first region of elevated signal energy after the timepoint of the ECG R-peak is associated with AO [226, 227]. It was assumed that, because of

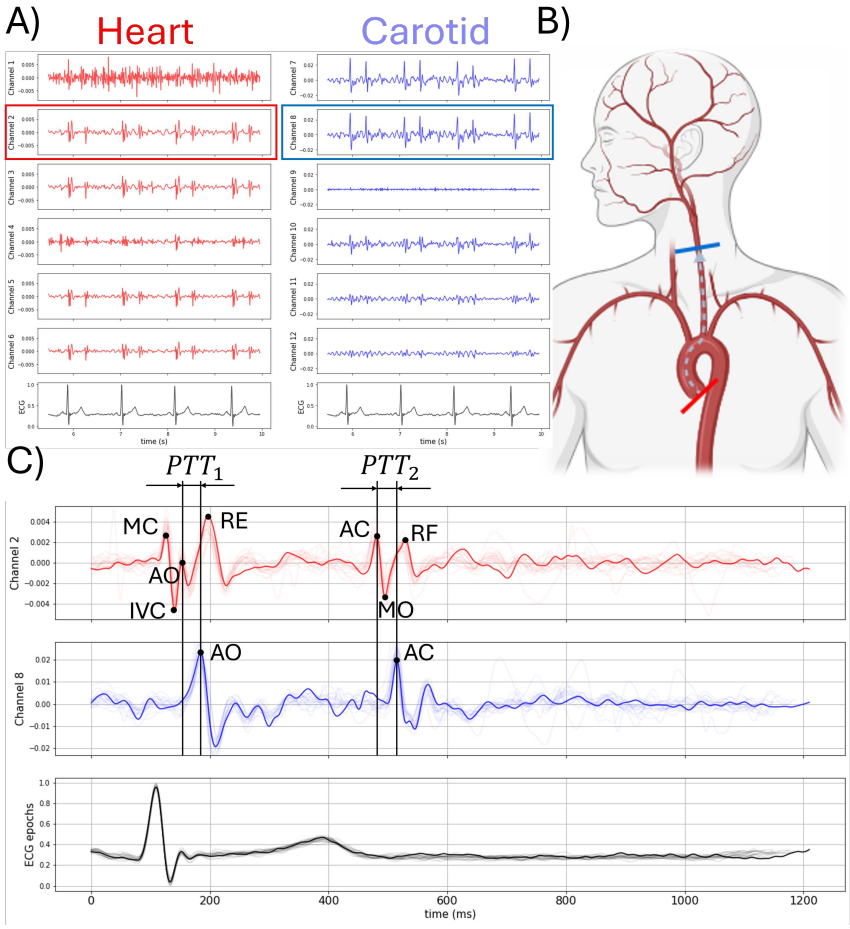

Figure 6.2: Panel A shows a 4.5-second segment of the first Base-carotid measurement of patient 40, performed during the study. The six channels in the right column represent carotid skin-acceleration in time. The left column contains base-of-the-heart skin acceleration in time. The bottom row shows the ECG measured in parallel with the LDV-channels. Panel B visualises the arterial pathway under investigation. Figure created with BioRender.com. Panel C displays a selection of carotid (middle plot) and heart (upper plot) channels that were split into epochs using the ECG, shown in the bottom plot. A randomly-picked carotid and heart epoch are both displayed on top of all individual epochs. Two combinations of temporal features that lead to two distinct hcPTT estimations are illustrated. See text for the definition of all indicated points. Y-axes show arbitrary units for all graphs.

the similarity between SCG and chest-LDV waveforms, the same peak in the LDV signal also corresponded to AO. The time delay between these carotid and heart features was then taken as a first hcPTT estimation (PTT_1).

Secondly, the features corresponding to the closure of the aortic valve are considered, see panel C of Figure 6.2. Again, this was straightfoward to assess from the carotid data, where the well-known DN [11] leads to a prominent second peak in the LDV acceleration signal. As for the heart signal, we again rely on what is known from SGC, where the first peak in the second region of visible signal perturbation (which we refer to as heartsound two, or S2) is associated with aortic valve closure [226, 227]. Analogously, the corresponding LDV feature could be identified. Combining both features yielded a second hcPTT estimation. In the following sections we will be referring to both these proposed methods as PTT_1 and PTT_2, respectively.

The following protocol was established to get PTT_1 and PTT_2, for Apex and Base measurements:

- For a given measurement (Base or Apex), the most qualitative channels (highest signal-to-noise ratio) of both handpieces respectively, were designated via visual inspection of signal quality.
- The R-wave peaks in the ECG trace were detected and utilised to split the selected channels into epochs.
- Signal averaging of the epochs yielded an average carotid and heart epoch.
- The five epochs per channel with the highest normalised cross-correlation coefficient with their average epoch were selected for hcPTT estimation.
- hcPTT estimation was performed via both methods described above to get PTT_1 and PTT_2 for the five selected epochs.
- Of these five values for both PTT_1 and PTT_2, the median values were taken as hcPTT estimates for the measurement.
- Of the three measurement hcPTT estimations per patient, the median value was again taken as final hcPTT estimation for the patient, and the standard deviation as a measure for inter-measurement hcPTT variability. If one (or two) of the three measurements could not be processed, the average value of the remaining hcPTT estimates was taken as the final hcPTT.

6.2.3.3 *Heart-carotid PTT with age and blood pressure*

Both hcPTT estimation methods were applied on the database, for both heart-measurement sites. This resulted in four hcPTT estimations. All four were compared to known biomarkers for arterial stiffness: age, brachial diastolic blood pressure (DBP), brachial systolic blood pressure (SBP) and cfPTT measured via the Sphygmocor system. The same correlations were additionally calculated for both male and female patients separately. All correlations were quantified using the Pearson-correlation coefficient and were considered significant for associated p-values < 0.05. Variability between measurements done per patient was investigated.

Additionally, the agreement between the four methods was investigated. This was done through correlation analyses that were performed between hcPTT's estimated on the two different heart-measurement sites. Correlations between PTT_1 and PTT_2, controlling for measurement site, were also investigated as well as any statistical difference between the two metrics which was done via paired t-tests and nonparametric Wilcoxon signed-ranks tests. Bland-Altman plots were made to evaluate any potential biases and to appraise the level of agreement between hcPTT estimation methods and between heart-measurement sites.

6.2.3.4 *Intra- and inter-operator variability*

In order to examine the reproducibility of the hcPTT biomarker, a separate batch of measurements was performed on 10 healthy volunteers by two distinct operators (OP1 & OP2). Similar to the protocol of the InSiDe-study described above, every volunteer was subject to three LDV measurements at both Base and Apex, performed by the two operators. This resulted in a total of 120 planned measurements. It was determined that only subjects with all three measurements being processable, were considered for the reproducibility analysis. hcPTT's were derived from the considered measured data as mentioned before, and compared in an intra- and inter-operator analysis.

Intra-operator variability was quantified as follows: every measurement resulted in a hcPTT estimate. The coefficient of variation (CV) was calculated on the three hcPTT estimates per subject. For a single method, e.g. Base PTT_2, this resulted in 10 CV values of which the mean was taken, together with its standard error (SE), as the metrics for evaluation. This was done for Base PTT_1, Base PTT_2, Apex PTT_1 and Apex PTT_2. Equations 6.2 and 6.3 show the formulas used to calculate CV and SE σ refers to the standard deviation and μ to the arithmetic mean. σ_{CV} is the standard deviation of the CV values for the $N = 10$ subjects.

$$CV = 100 * \frac{\sigma}{\mu} \tag{6.2}$$

$$SE = \frac{\sigma_{CV}}{\sqrt{N}} \tag{6.3}$$

The inter-operator variability was investigated using a Bland-Altman analysis [231], constructing Bland-Altman plots and recording relevant values i.e. bias, standard deviation of the differences and limits of agreement. Again, this was done for the four considered hcPTT methodologies.

6.3 Results

Of the total number of datasets gathered at each of the two measurement sites (600), 94%, 93.6%, 94.4% and 94.4% yielded a hcPTT for Base PTT_1, Base PTT_2, Apex PTT_1 and Apex PTT_2 respectively. On a per-patient level, 96 of the 100 patients yielded a final hcPTT for Base measurements. For the Apex measurements, 97 patients yielded a final hcPTT. Sphygmocor cfPTT reference values were gathered from 97 of the 100 patients.

6.3.1 Correlation with clinical parameters and sphygmocor cfPTT

Figure 6.3 shows the distributions of all four hcPTT estimates versus age, per patient. In case no error bar is visible, it is assumed that for two out of the three measurements no hcPTT estimate was possible (due to low signal quality or issues with the ECG). Panel A and B show the significant correlations, between age and Base PTT_1 ($\rho = -0.3, p = 0.003$) and PTT_2 ($\rho = -0.377, p < 0.001$) respectively. Panel C and D show the same correlations, but for the Apex measurement site ($\rho = -0.144, p = 0.16$ and $\rho = -0.149, p = 0.146$).

In Figure 6.4 the correlations are depicted for Base PTT_1 and PTT_2, with Sphygmocor cfPTT. This Figure highlights the strongest correlations found between LDV-based hcPTT and any other metric in the analysis. Base PTT_1 and Sphygmocor cfPTT yielded a correlation with $\rho = 0.359$ and $p < 0.001$, Base PTT_2 and Sphygmocor cfPTT yielded $\rho = 0.475$ and $p < 0.001$.

In Table 6.2, the Pearson-correlation coefficients between the considered hcPTT values and other parameters such as brachial SBP and DBP, and Sphygmocor cfPTT are displayed.

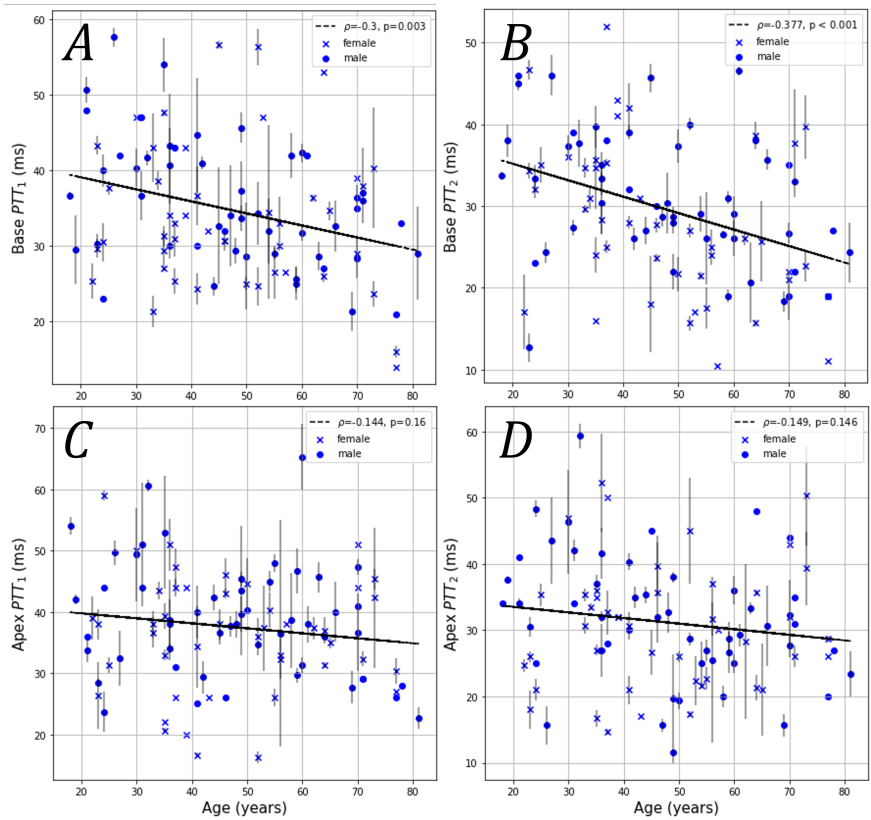

Figure 6.3: Correlations of the four proposed hcPTT estimations with age. Linear regression lines are drawn. The distinction between male and female patients has been visualised. Pearson-correlation coefficients and their p-values are given. Error bars represent the standard deviation of the resulting hcPTT values for the three measurements done per patient.

	Base PTT_1	*Base* PTT_2	*Apex* PTT_1	*Apex* PTT_2
Age	-0.3**	-0.377***	-0.144	-0.149
SBP	-0.259*	-0.18	-0.058	-0.1
DBP	-0.179	-0.098	-0.047	-0.125
cfPTT	0.359***	0.475***	0.167	0.196

Table 6.2: Pearson-correlation coefficients of the proposed hcPTT estimations with age, brachial SBP, and DBP, and cfPTT are shown. Highlighted with '*' are the statistically significant correlations with a p-value smaller than 0.05. ('**' and '***' refer to p-values smaller than 0.01 and 0.001 respectively)

6.3.2 Relation between hcPTT methods

Correlation between PTT_1 and PTT_2 for Base (N = 96) and Apex (N = 97) separately are investigated in Figure 6.5. The distributions are accompan-

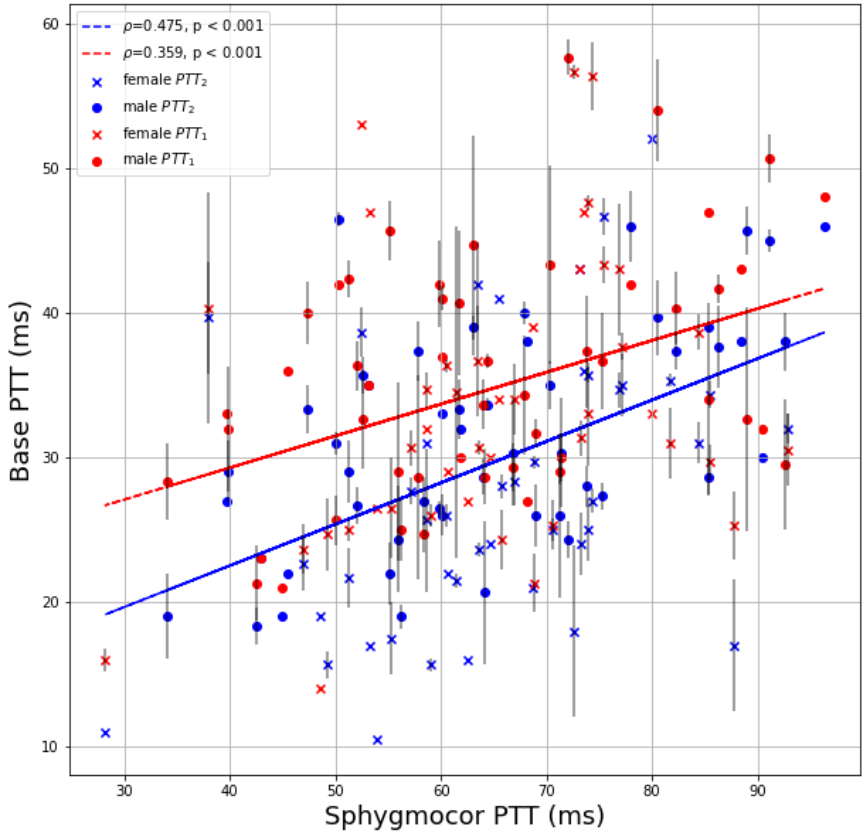

Figure 6.4: Correlations are depicted between both hcPTT estimation methods on Base measurements, and the golden standard of Sphygmocor cfPTT. Pearson correlations are given with their p-values for both cases. Linear regression lines are drawn in the relevant color.

ied by their respective Bland-Altman plots. The correlation between Base PTT_1 and Base PTT_2 yields the highest coefficient. the mean difference of these two is -5.08ms. Both the paired t-test ($T - statistic = 5.545, p < 0.001$) and Wilcoxon signed ranks test ($Test - Statistic = 950, p < 0.001$) suggest a significant difference between these two methods. The mean difference between Apex PTT_1 and Apex PTT_2 is -6.32ms. The paired t-test ($T - statistic = 5.315, p < 0.001$) and Wicoxon signed ranks test ($Test - Statistic = 879, p < 0.001$) provide similar results as with the Base hcPTT methods. The limits of agreement are large for both measurement sites.

Figure 6.6 explores the correlations between measurement sites while controlling for the hcPTT estimation methods (N = 96). PTT_2 reports the highest correlation between Base and Apex. Bland-Altman figures for these

cases show next to no bias (mean difference of 1.62 and 2.81 ms for PTT_2 and PTT_1 respectively), allthough a large variance is again observed. All correlations are given in Table 6.3.

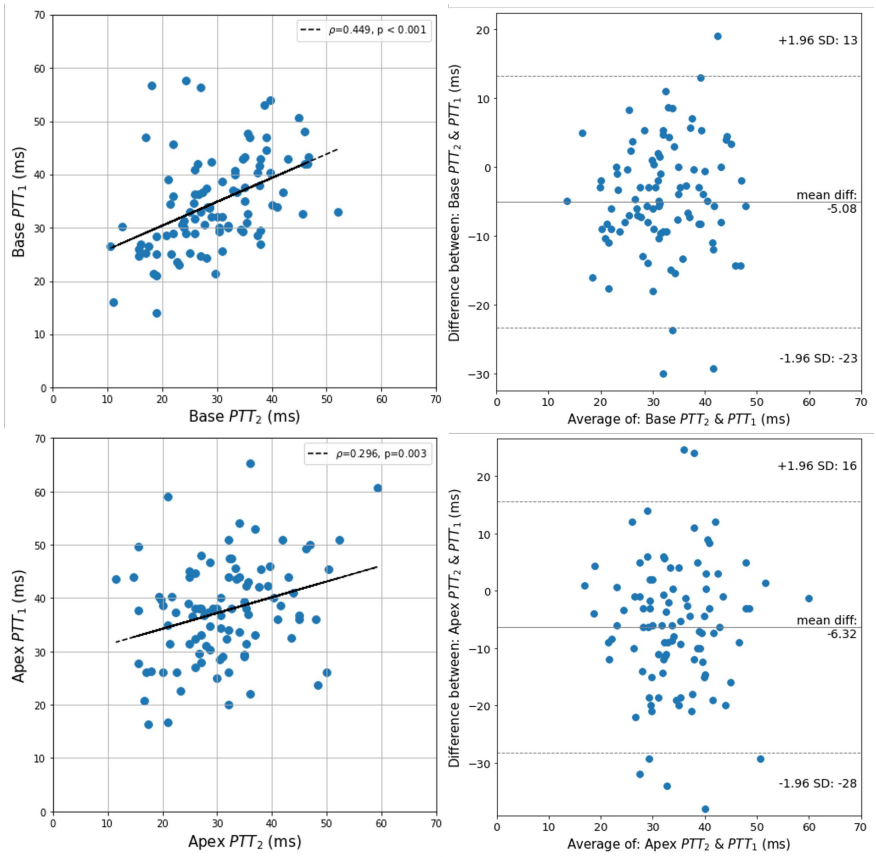

Figure 6.5: Correlations between the two proposed hcPTT-estimation methods are investigated while controlling for the heart-signal measurement site. Bland-Altman plots are displayed in addition. SD refers to the standard deviation of the differences between the two datasets.

6.3.3 Intra- and inter-operator variability

Not all data measured on the 10 subjects was fit for analysis. In one case, only two of the three measurements were conducted. Another two cases contained one measurement of inadequate signal quality each. This resulted in 111 out of the total 120 (92.5%) planned measurements that could be used.

The intra-operator variability is low ($CV < 15\%$) for both operators, for all four methodologies. Specifically OP2 has very low ($CV < 5\%$) variability. Especially the standard error of OP2 for Base PTT_1 suggests minimal

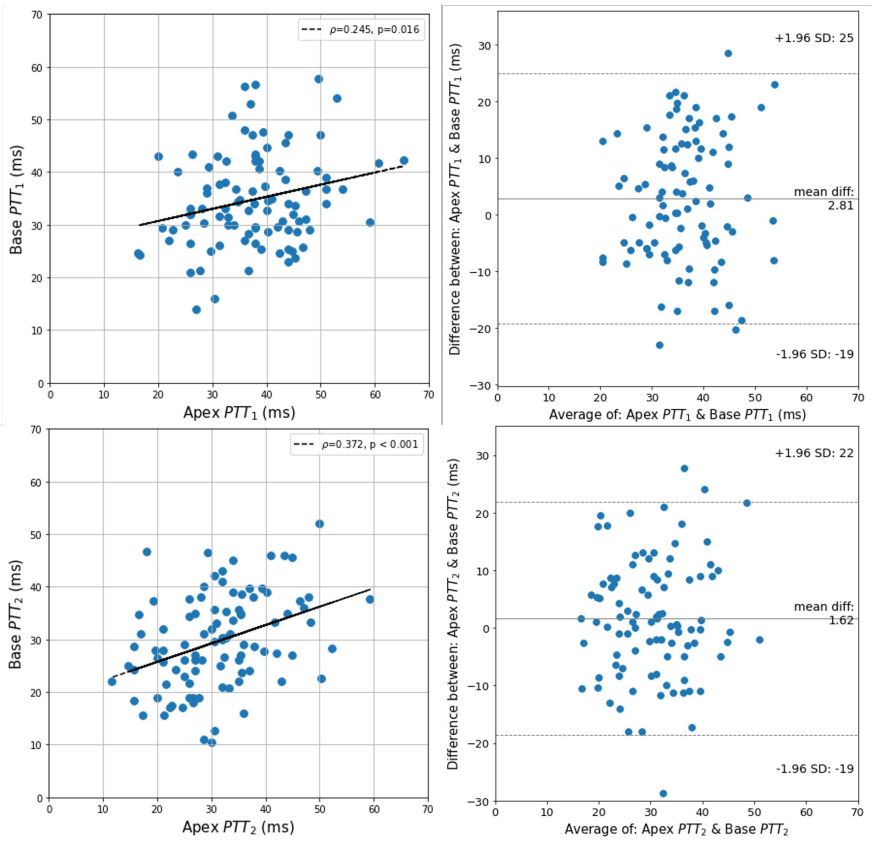

Figure 6.6: Correlations between the two heart-measurement sites are investigated while controlling for the hcPTT estimation method. Bland-Altman plots are displayed in addition.

	Base PTT_1	*Base* PTT_2	*Apex* PTT_1	*Apex* PTT_2
Base PTT_1	1	0.449***	0.245*	0.213*
Base PTT_2	0.449***	1	0.092	0.372***
Apex PTT_1	0.245*	0.092	1	0.296**
Apex PTT_2	0.213*	0.372***	0.296**	1

Table 6.3: Correlations between the four proposed hcPTT estimation methods. Highlighted with '*' are the statistically significant correlations with a p-value smaller than 0.05 ('**' and '***' refer to p-values smaller than 0.01 and 0.001 respectively).

variability in the estimate of its mean CV. The other standard errors range between 14.5% and 33% of their respective mean CV estimates. Mean CV and their standard errors are given in Table 6.4.

Figure 6.7 displays the Bland-Altman analysis done on the subject-level hcPTT estimates for OP1 and OP2. It was observed that both the bias and limits of agreement are smallest for Base PTT_2, suggesting that this hcPTT estimation method is the most reproducible between different operators. Notably, measurements taken at the Apex seem to produce results with higher biases, and wider limits of agreement, insinuating less reproducibility.

	Intra operator 1			*Intra operator 2*		
	mean CV (%)	*SE*	*N*	*mean CV (%)*	*SE*	*N*
Base PTT_1	5.43	1.11	9	4.15	0.51	10
Base PTT_2	5.49	1.98	10	8.04	3.18	10
Apex PTT_1	9.27	3.59	9	11.75	3.30	10
Apex PTT_2	5.83	2.51	9	8.22	3.84	9

Table 6.4: Mean CV's are reported per hcPTT-acquiring method, together with their standard errors. N indicates the number of included subjects in the analysis.

6.3.4 Sphygmocor cfPTT agreement with clinical parameters

Figure 6.8 shows the trends between Sphygmocor cfPTT and age ($\rho = -0.674, p < 0.001$), brachial SBP ($\rho = -0.512$, $p < 0.001$) and DBP ($\rho = -0.336$, $p = 0.001$). All correlations are statistically significant, with $N = 100$.

Figure 6.8 serves as a possible form of reference for hcPTT, with correlation values between cfPTT and age, SBP and DBP. We assume this because we consider cfPTT (and by extension: cfPWV), resulting from Sphygmocor measurements, as a golden standard for assessing vascular aging.

Currently it is not yet possible to approach the high correlation coefficient of $\rho = -0.674$ between Sphygmocor cfPTT and age when calculating hcPTT. At this time, we ascribe this effect to the different arterial pathway between both PTT's and increased complexity of the heart-LDV data. The proposed hcPTT's are clearly not yet interchangeable with Sphygmocor cfPTT, but could be considered as an additional metric that describes arterial stiffness in the ascending aorta, which is not included in the cfPWV pathway.

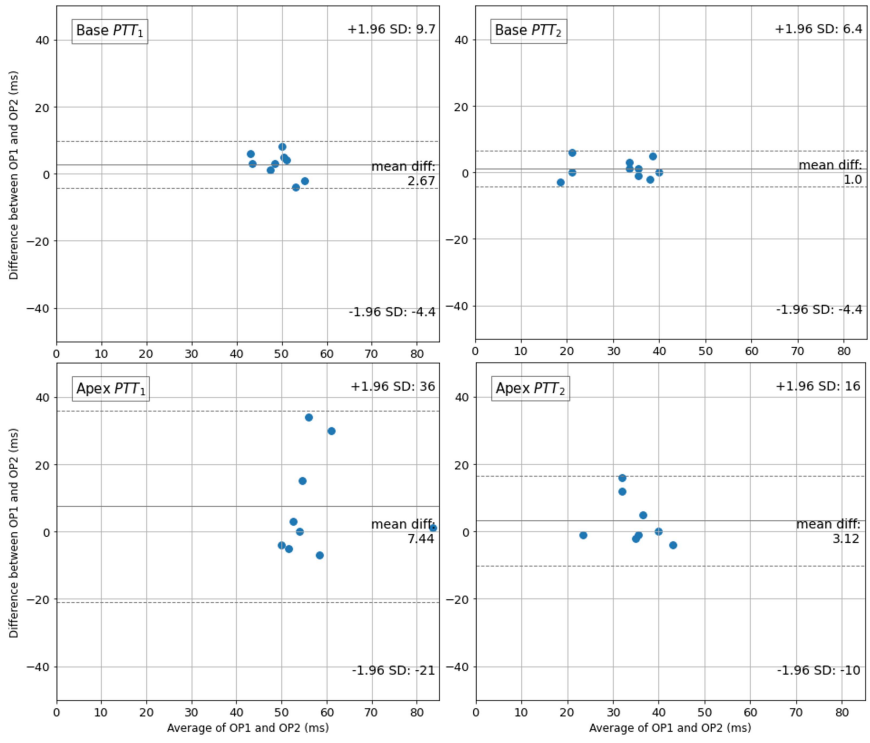

Figure 6.7: Bland-Altman plots are given for all four hcPTT methodologies. A comparison between hcPTT values, from measurements performed by two different operators, is made. SD refers to the standard deviation of the differences between the two datasets.

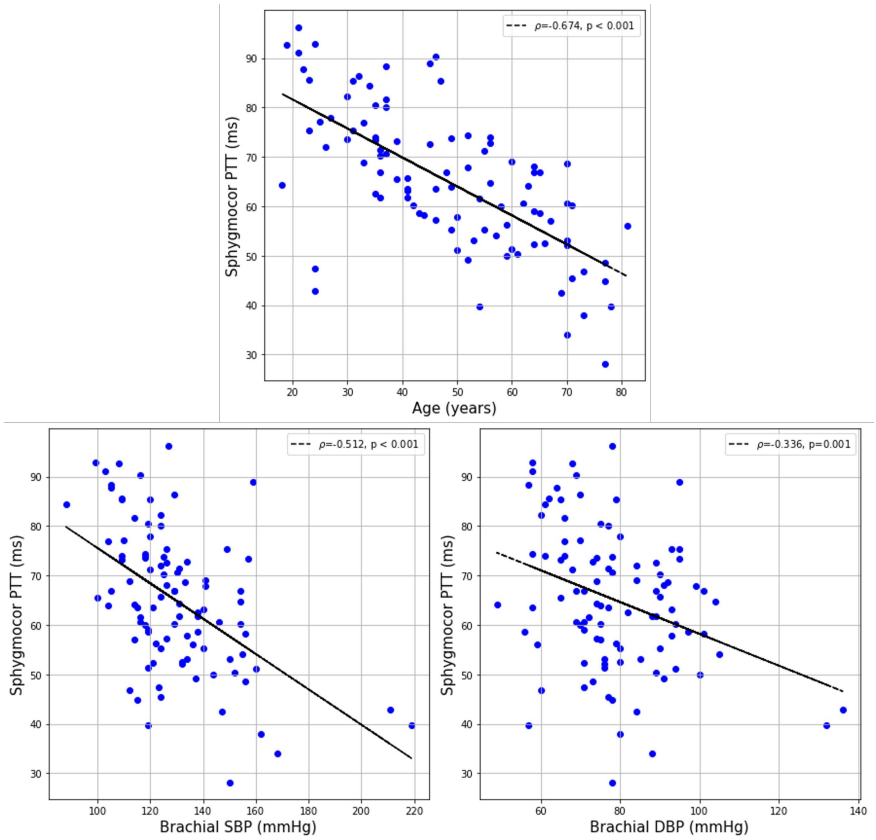

Figure 6.8: Figure depicting reference correlations of Sphygmocor cfPTT with age, brachial SBP and DBP. Linear regression lines are drawn and correlation coefficients are given alongside their p-values.

6.4 Discussion

Despite the compelling evidence of PWV as a biomarker of cardiovascular risk and target organ damage, its widespread application is still hampered by the difficulty of its measurement. LDV, picking up vibrations from the skin, has the potential to provide an easy technique to be broadly deployed, beyond specialized centers. Our team has been successful in using integrated silicon photonics solutions to develop a multi-sensor LDV system to simultaneously acquire signals from two distinct locations, and we previously demonstrated to be able to measure carotid-femoral PWV.

6.4.1 Feasibility of LDV-based hcPTT

In this study, we explored the use of our LDV-based prototype to also measure heart-carotid pulse transit times and demonstrated that it is feasible to capture signals from two different locations on the chest that seemingly demonstrate a high similarity to seismocardiographic signals and hence potentially allow identifying moments of aortic valve opening and closure. Combined with simultaneous measurements at the carotid artery, we could measure pulse transit times at aortic valve opening (PTT_1) and closure (PTT_2). PTT_2 using the 'Base' location on the chest provided the strongest correlations with age and blood pressure, and was also the measurement with the lowest inter- and intra-operator variability.

Irrespective of the exact method (PTT_1, PTT_2, Base or Apex), hcPTT could be estimated in about 94% of the population, with a very good inter- and intra-operator variability. These numbers, however, should be interpreted within the context of the study. It is observed from Figure 6.3 that several data-points show no error bars, which inherently means that of the three measurements for the considered heart-carotid measurement site, at least one did not yield a hcPTT estimate. Some measurements contained a faulty ECG trace (3.2% for Base and 2.8% for Apex measurements), but for the remainder 2.8% of measurements, this lack of a hcPTT could be attributed to a low signal quality or less interpretable waveforms for at least one of the measuring locations, with the carotid signals only failing for 5 measurements. The most difficult component in the estimation of hcPTT was the interpretation of the heart signals. Signal features associated with the first heartsound, on which PTT_1 was based, often fluctuated between patients in temporal and frequency content. The signal features corresponding with the second heartsound were not always as pronounced and sometimes difficult to detect. The ECG measurements in this feasibility study helped to identify signal features, but the method should become independent of the ECG. Any potential future work will implement algorithms for the automatic interpretation of the heart signals.

6.4.2 hcPTT as biomarker of arterial stiffness?

For hcPTT to be a biomarker of arterial stiffness, it should at least negatively correlate with its main predictor i.e. (chronological) age, as one may expect with an increased arterial stiffness. This is the case for hcPTT measured at the Base for both PTT_1 and PTT_2 (Figure 6.3 and Table 6.2), but not for values retrieved from apical data. We speculate that the consistent results for Base measurements are explained by the fact that the Base measurement site is anatomically closer to the aortic valve, leading to a better identifiability of the desired AO and AC features, with reduced distortion and delay of vibrations travelling to the measuring site. We found less pronounced correlations with brachial SBP, which was only significantly correlated with Base PTT_1, while brachial DBP did not significantly correlate with any of the measured hcPTT's.

These correlations are thus albeit modest, but it is important to consider that we are analysing hcPTT, and not heart-carotid PWV (hcPWV) which requires knowledge of the pathlength (see also further). As we expected, we found a positive correlation between cfPTT and hcPTT, with again the highest values for hcPTT assessed at the base ($\rho = 0.359$, $p < 0.001$ and $\rho = 0.475$, $p < 0.001$ for PTT_1 and PTT_2, respectively). Given that heart-carotid and carotid-femoral sample a very different trajectory along the arterial tree, it may not be surprising to find moderate correlations between both.

Another interesting observation is made when performing the correlation analysis of the proposed hcPTT's with Age, SBP, DBP and cfPTT, between male and female patients separately, as provided in Table 6.5. While for most cases, correlations are similar for male and female, this is not the case for the Apex measurements. correlations with Age and cfPTT are much higher and significant only for females. This phenomenon most likely presents itself as an anatomical difference between the two. For this work, it is another argument to prefer Base measurements over Apex.

While we only assessed hcPTT in this study, the ambition is to assess stiffness, and to eventually retrieve hcPWV, for which the pathlength is required. Nagasaki et al. calculate heart-carotid distance as a function of height (HT); $dx = 0.2473 \cdot HT - 18.999$ [232]. When this function is applied to the Base PTT_2 data of this study, the average hcPWV (± standard deviation) was 8.89 ± 3.21 m/s, with a range of 3.47 to 22.88 m/s. These values are plausible, but given the absence of a reference, it is difficult to evaluate the accuracy of these estimates. What we do know is that none of the hcPWV estimates provided stronger correlations with age or blood pressure than hcPTT. In this feasibility study, we wanted to exclude sources

Table 6.5: Pearson-correlation coefficients of the proposed hcPTT estimations, for male and female separately, with age, brachial SBP, and DBP, and cfPTT are shown. Significant correlations are marked with '*' ($p < 0.05$).

	Base PTT_1	*Base* PTT_2	*Apex* PTT_1	*Apex* PTT_2
Age (male)	-0.245	-0.34*	-0.004	0.065
Age (female)	-0.379*	0.476*	-0.297	-0.379*
SBP (male)	-0.251	-0.177	-0.066	-0.078
SBP (female)	-0.278	-0.189	-0.047	-0.12
DBP (male)	-0.176	-0.113	-0.099	-0.145
DBP (female)	-0.189	-0.085	0.004	-0.108
cfPTT (male)	0.377*	0.491*	0.03	0.046
cfPTT (female)	0.319*	0.49*	0.342*	0.392*

of uncertainty beyond the uncertainty related to the LDV measurements, which is why we opted to present the results in terms of hcPTT.

An interesting aspect of our technique is that we assess hcPTT at both diastolic (PTT_1) and end-systolic pressure (PTT_2). Given that elastic arteries typically stiffen with an increasing pressure [54], leading to lower PTT, one expects higher values for PTT_1 than for PTT_2. The Bland-Altman plots in Figure 6.5 demonstrate that this is effectively the case on average, with an average difference, for the Base measurements, of 5.08 ms. Using the estimated path lengths from Nagasaki et al., this time difference translates into an average hcPWV difference of 1.53 ± 2.84 m/s (range: -4.24 to 13.82 m/s). This is lower than the $\Delta PWV = 2.4$m/s (range: 0.8 to 4.4 m/s) stiffening reported by Hermeling et al. for the carotid artery [54].

However, an important consideration is that while we found this higher hcPTT at diastolic pressure on average, we did not find a systematic difference per subject (although the statistical tests performed did indicate a significant difference between PTT_1 and PTT_2). An important factor contributing to the observed variability is the complexity of the LDV signals originating from the aortic valve, but only being picked up at the skin-level. The effect of this on the time and frequency content of the observed epochs more than likely introduces inaccuracies in one or both PTT methods. Clearly PTT_1 is the most difficult to measure due to the complex waveform of S1 in the heart-LDV signals and the uncertainty on the identification of the exact timepoint of the opening of the aortic valve. While we are confident that further optimisation of our technique (measurements directly on the skin without retroreflective patch and further signal processing

enhancement) will further improve PTT_2 estimation, uncertainty on PTT_1 may remain too large to reliably quantify the stiffening between diastolic pressure and the dicrotic notch.

6.4.3 LDV-based hcPTT compared to other techniques

The following paragraphs provide an overview of the studies that we could identify in literature on (or including) heart-carotid PWV, demonstrating the relative paucity of articles investigating hcPTT or hcPWV. Table 6.6 provides a summary of the following paragraphs. Faita et al. conducted a feasibility study with N = 8, where they also combine signal features that correspond to the closure of the aortic valve via SCG at proximal and distal locations [223]. Nagasaki et al. also combine AC signal features but use a combination of ECG and PCG at proximal, and tonometry at distal locations [232]. Nagasaki et al. found hcPWV value of 8.45 ± 0.17 m/s, which had a correlation coefficient of 0.686 with age (N = 276). They calculated the distance dx as mentioned earlier.

Li et al. get to hcPTT via calculation of pulse-arrival time (PAT) using ECG and the foot of the systolic upstroke in the Doppler spectral envelope using ultrasound (US) at the left carotid [233]. The pre-ejection period was calculated the same way but with the ultrasound probe pointed at the aortic valve. They then calculated hcPTT as the difference between pulse-arrival time and pre-ejection period. They found hcPTT values of 22.65 ± 11.92 ms and 25.61 ± 10.18 ms for patients with a carotid intima-media thickness (CIMT) of over 0.8mm and lower than 0.8mm respectively (N = 85). The distance was calculated via the same way as Nagasaki et al. This led to hcPWV values of 2.47 ± 0.49 ms and 2.35 ± 0.47 ms in the high and low CIMT group, respectively.

Yang et al. calculate hcPTT as the time delay between the peak R wave in ECG, and the foot of the Doppler flow waveform with US [234]. They get to hcPWV by measuring dx with a tape measure on the body surface. This resulted in mean hcPWV values of 9.24 ± 1.93 m/s for their healthy controls, and 10.21 ± 4.18 m/s for patients with rheumatoid arthritis (N = 127). Ejiri et al. found a median hcPWV value of 12.04 m/s with a standard deviation of 3.36 m/s in an elderly population (mean age of 79.2 ± 4.1 years, N = 1351) [235].

When comparing between LDV and SCG, both methods require the application of an experimental tool to the skin. The used LDV prototype requires a piece of retroreflective tape, with SCG requiring the placement of accelerometers on the body. Currently, both technologies do not yet meet the expectations of clinicians and patients in that a vascular age assessment should come in the form of a quick, accessible and intuitive measurement.

Future LDV technology developments aim for measurements without the need of the retroreflective patch (InSiDe project).

Table 6.6: A framing of this work within the present literature. SCG = seismocardiography, PCG = phonocardiography, US = ultrasound, AC = aortic valve closure, PAT = pulse arrival time, PEP = pre-ejection period.

	Method	*Pathway*	*Strategy*	*PTT Method*	*Age*	*N*
This work	LDV	heart-carotid	Skin acceleration features	Time domain: AC	0.377	100
Faita 2009	SCG	heart-carotid	Skin acceleration features	Time domain: AC	/	8
Nagasaki 2011	ECG, PCG-tonometry	heart-carotid	Time domain features	Time domain: AC	0.686	276
Li 2015	ECG, US	heart-carotid	Time domain features	PAT-PEP	/	85
Yang 2019	ECG, US	heart-carotid	Time domain, US spectra	PAT-peak R wave	0.235	127
Ejiri 2024	ECG, PCG	heart-carotid	Time domain	Time domain: AC	/	1351

6.4.4 Study limitations

The eventual transition from hcPTT to hcPWV is only possible if hcPTT has been shown to indicate a change in arterial stiffness. A reliable distance metric dx has to be derived first, as to avoid adding errors to the hcPWV biomarker. Because of the shorter pathlength between both measurement sites, small distance errors will cause large relative hcPWV errors.

We did not investigate the technical reproducibility of this study. We strive towards hcPTT based on fully automated algorithms, removing the need of manual hcPTT estimation.

The most important limitation, however, is the absence of a proven reference method for LDV-derived hcPTT. The literature survey shows that no single method of estimating hcPTT (or hcPWV) is acceptable for this role. A future study could consider using established methods that capture flow- or distensibility data at the aortic valve and carotid simultaneously, with a high enough temporal resolution, in order to acquire reference hcPTT data.

6.5 Conclusions

This work represents a feasibility study, investigating hcPTT as a potential and not well-known biomarker for arterial stiffening, sampling the properties of the large, proximal aorta and carotid artery using LDV technology to detect the pulse transit time from the heart to the carotid artery. It was found that most robust hcPTT is retrieved from the base of the heart, and measurements are repeatable, with significant though moderate correlations with known predictors of arterial stiffness. Future work should focus on further refinement of the method - especially regarding the identification of aortic valve opening and closure from chest measurements – and on more precise validation against metrics of proximal aortic stiffness. We believe this work adds to the legitimacy of heart-carotid PWV as a biomarker that could be used in conjunction with cfPWV in the future.

CHAPTER 7

DEEP-LEARNING BASED ECG-FREE HEART-CAROTID PULSE TRANSIT TIME ESTIMATION

POSITIONING OF THE CHAPTER

This chapter is a copy of the publication under review *Deep-Learning Based ECG-free Heart-Carotid Pulse Transit Time Estimation from Laser Doppler Vibrometry* (Beeckman, S., Badhwar, S., Bruno, R. M., Li, Y., Aasmul, S., Seoni, S., Segers, P. & Madhu, N.). The presented analysis was conceptualized by prof. Segers, prof. Madhu and the author and performed by the author. The article was proof-read and finetuned by the author, dr. Badhwar, prof. Segers and prof. Madhu.

ABSTRACT

Assessment of arterial stiffness is important in the diagnosis and management of cardiovascular diseases. A strong biomarker for arterial stiffness is pulse-wave velocity (PWV) – the speed at which a heartbeat-induced pulse wave travels through the large arteries. By measuring the pulse-transit time (PTT) – the time delay between the arrival of the pulse wave – at two points on the arterial pathway, PWV can be estimated. PTT can be calculated from skin-displacement signals, measured via laser Doppler

vibrometry (LDV). This process requires an accurate indication of heartbeat onsets, to be able to utilize the correct signal features or fiducial points that lead to PTT. Typically, electrocardiography (ECG) is a reliable, parallel measurement to segment LDV signals. However, common practice for LDV does not include ECG, necessitating alternative means for identifying heartbeat cycles from LDV signals. Proposed solution is a deep neural network (DNN) which returns an ECG-proxy for each LDV signal, containing information on the timing of the heartbeats. Heart-carotid PTT can then be calculated after segmenting the signals based on the predicted heartbeat timing. This PTT was additionally calculated via two other techniques i.e. a state-of-the-art template matching algorithm and a reference technique in which PTT was calculated via manual inspection of the data. The DNN was able to correctly predict the onset of 72% and 75% of heartbeats present in the test and validation sets respectively. When applied to unseen data of 100 subjects (45 female), it provided PTT values for 68 subjects that correlated well with the reference ($\rho = 0.71$). In comparison, a state-of-the-art knowledge-driven approach yielded a similar correlation ($\rho = 0.69$) but was only able to return PTT values for 46 subjects. An ECG-based ground truth method reached a correlation of $\rho = 0.62$ for 91 subjects. Finally, the DNN demonstrates potential for broader biomedical LDV applications beyond heart-carotid PTT, provided that carotid signals are incorporated.

7.1 INTRODUCTION

The large arteries, particularly the aorta, play a crucial role in blood circulation [49]. Their structural properties enable the vessel wall to distend during cardiac contraction, storing elastic energy that is subsequently released during relaxation to maintain blood flow after the pulse wave has passed [35, 49, 220]. This mechanism ensures a near-continuous flow further along the arterial system, supporting constant organ perfusion. However, this buffering or 'windkessel' function deteriorates significantly when large arteries stiffen due to arteriosclerosis, resulting in dysregulated blood pressure, altered blood flow, and subsequent organ damage [7, 8, 75, 109]. Understanding the shape and content of blood pressure and flow-related signals is essential for detecting and preventing early vascular aging as well as other related cardiovascular diseases (CVD), as CVD risk increases with an increase in large artery stiffness [10, 75, 221].

7.1.1 Pulse transit time estimation

Common practice for the assessment of arterial stiffness is via the speed of the pressure wave which travels through the arterial tree following heart contractions [8, 11, 222]. This pulse-wave velocity (PWV) increases with

increased stiffness. By measuring the distance dx between two measurement sites, and the time delay between the arrival of the pressure wave at these sites (i.e., the pulse transit time – PTT)), the PWV is obtained as:

$$PWV = \frac{dx}{PTT} \tag{7.1}$$

Current state-of-the-art for measuring PWV is through applanation tonometry, magnetic resonance or ultrasound applied to the carotid and femoral arteries [11, 127–129, 184]. These methods, while reliable, have a number of challenges associated with them: (i) they require specialized operator training, (ii) are typically located at dedicated medical facilities or hospitals, (iii) can be expensive to acquire and (iv) there is a widely held consensus in the medical community that none of the aforementioned diagnostic methods can effectively identify a significant portion of at-risk individuals, both in primary care and secondary prevention settings [1]. Furthermore, individuals classified as low or moderate risk may remain undiagnosed.

As such, there is an interest in deploying the optimal diagnosis to institute a *timely* preventative therapy among those that are currently considered to be at low or moderate risk. We have been investigating laser-Doppler vibrometry (LDV) as an alternative technology to address these challenges [20–22, 212]. LDV measures skin displacement at the location of large subcutaneous arteries such as the carotid and the femoral. By differentiating the displacement signal twice, skin acceleration is obtained. From these data, PTT can be estimated [18, 19]. It was demonstrated that these PTT and their corresponding PWV values strongly correlate with tonometry [23, 25].

The LDV-prototype used to measure all data presented in this work was developed during the H2020 CARDIS project (Grant agreement ID: 644798). It consists of two handpieces (Figure 7.1), where each handpiece has 6 built-in laser beams with a wavelength of 1550 nm that illuminate the measurement site on the skin. The distance between beams is 5 mm. Retroreflective tape was applied to the skin to ensure sufficient reflection. Further details can be found along with an extensive description of the device in [19, 26, 230].

Several arterial pathways can be considered for estimating PTT, to use as additional biomarkers for large artery stiffness assessment and its associated CVD risk prediction. One such is the heart-carotid, whose PTT is calculated on a pathway spanning from the aortic valve at the base of the heart, up to the (right) carotid artery [223, 233]. Previous work using LDV

has investigated the correlation of heart-carotid (hc) PWV with known predictors of arterial stiffness i.e. chronological age and blood pressure in a population of 100 patients with CVD [219]. Figure 7.1 depicts the heart-carotid measurement and illustrates the arterial pathway that is investigated.

This study builds upon previous work on heart-carotid PTT via LDV, with focus on techniques to calculate heart-carotid PTT from heart-carotid LDV measurements that were considered for implementation in an LDV prototype set-up. In this previous work, hcPTT values were estimated manually through visual inspection. The aim of this study is to investigate improved approaches for automated heart-carotid PTT estimation.

7.1.2 Automated PTT estimation

We subsequently use PTT to refer to heart-carotid PTT. Manual PTT estimation serves as the reference. This manual method required electrocardiography (ECG), measured in parallel with LDV, for R-peak detection so the LDV signals could be segmented into individual heartbeats (or epochs). This made both the identification and combination of the relevant fiducial points for PTT calculation significantly easier.

However, parallel ECG measurements can be cumbersome, are not included in the LDV-device functionality and will not be included in future wireless and user-friendly iterations of the prototype. A system including both LDV and ECG decreases the envisioned ease-of-use for clinical personnel and increase the average time to get patient measurements. ECG was measured during this study for research purposes only. The exact timing of heartbeats provided by ECG is essential for manual PTT calculation. However, automated PTT estimation – especially in the absence of the ECG reference – requires other solutions. Similarity-search or pattern-recognition techniques exist e.g. template matching (TM) [145–147] or matrix profile [27]. Drawbacks of these techniques are the requirement of a preconstructed template and the occasional identification of the wrong recurring waveforms respectively. Our work aims to boost the current state-of-the-art.

The proposed approach in this work is based on a deep neural network (DNN) trained and tested on the available LDV databases. The DNN was trained for a signal-to-signal mapping, using LDV data as input and returning a proxy signal for ECG, preserving information on cardiac gating. In general, neural networks have been applied to biomedical signals before, such as seismocardiography (SCG) [236, 237], ECG [238, 239], electroencephalography (EEG) [240], photoplethysmography (PPG) [241, 242] and many others [178, 243–245], but not yet on clinical LDV data. Some interesting work published in the literature contain inspiration for the grand

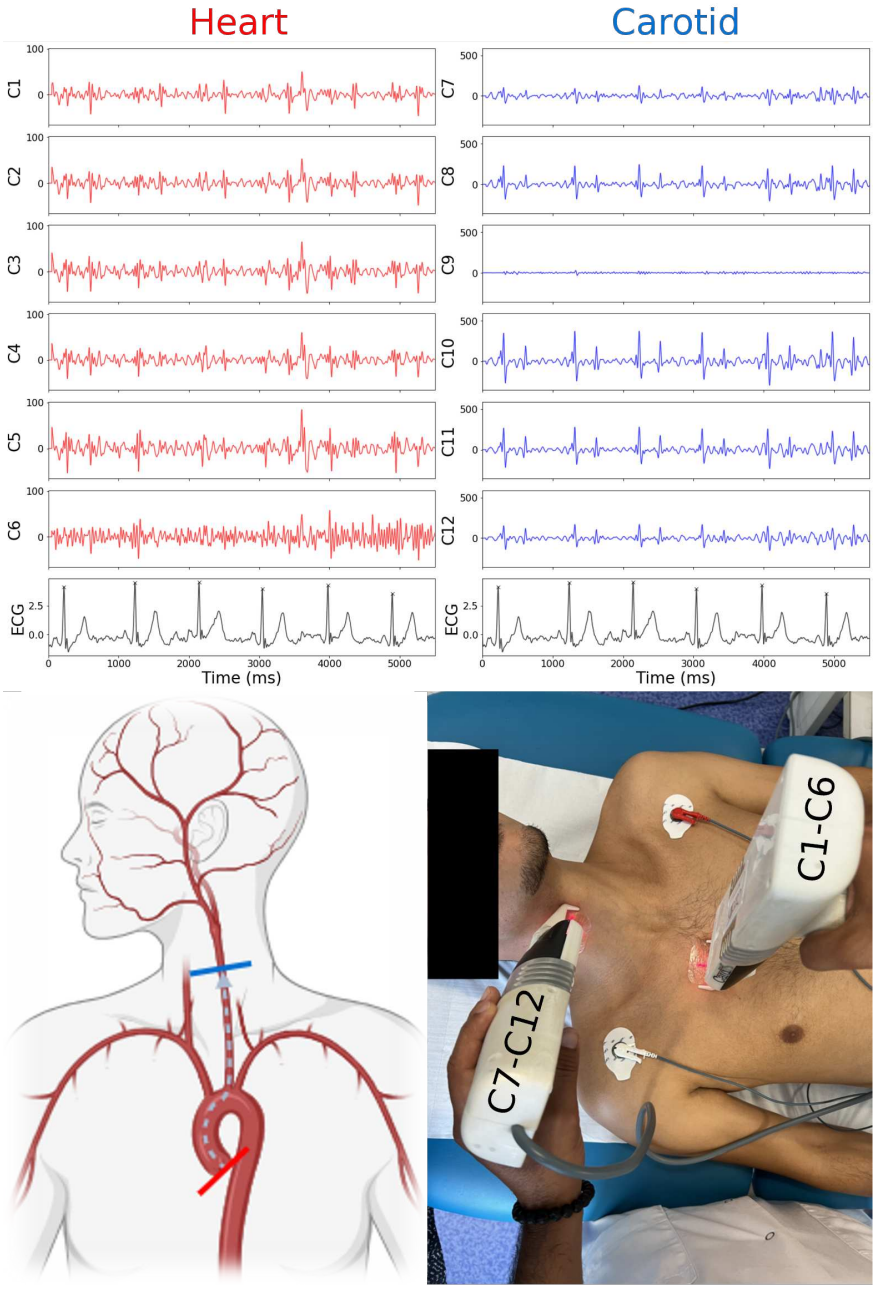

Figure 7.1: Figure showing an example heart-carotid LDV measurement using the prototype handpieces. The top panel contains skin acceleration signals with the first column containing 6 heart signals (channel 1 = C1, etc.) and the second one the 6 carotid signals. Each handpiece contains 6 channels for a higher probability of at least one channel containing useful signal quality. The bottom row shows the ECG measured in parallel, to illustrate the rhythmic correspondence between ECG and LDV signals. The bottom-left panel sketches the anatomy of the considered arterial pathway. The bottom-right panel is a picture taken during the measurement, depicting the prototype as well as two ECG electrodes.

scope of the DNN-related methods in this work such as working with a transformed target signal as opposed to raw ECG [246, 247].

To validate our findings a template-matching based method is also presented as a classical machine learning benchmark technique. We hypothesize that the data-driven DNN approach would outperform TM in both accuracy and representation i.e. (i) The DNN provides a useful alternative to ECG for robust automated heartbeat onset detection, leading to PTT estimations, (ii) the correlation of DNN-derived PTT values with the manual reference will be higher than for TM and (iii) the number of subjects whose data can be processed to obtain a reliable PTT estimate will be higher than for TM.

7.2 METHODS

Both carotid and heart handpieces have $M = 6$ channels. For any handpiece, the LDV (discrete-time) acceleration signal at a channel $m \in \{1, 2, \ldots, M\}$ is modeled as:

$$x_m(n) = s_m(n) + v_m(n)\,, \tag{7.2}$$

where $s_m(n)$ is the underlying signal *in channel m* and $v_m(n)$ is the noise in that channel. The accompanying ECG signal is denoted as ECG(n). Index n refers to the sample index with N being the total signal length in samples.

7.2.1 Applied principle for PTT calculation

All PTT calculation methods based on LDV signals for a given measurement have the same workflow:

1. Select the carotid and heart channels that will be used.
2. Segment each selected signal into separate heartbeats.
3. For each heart-carotid channel combination, combine fiducial points that correspond to the same heartbeat to estimate the PTT for that combination.
4. Calculate a final PTT value from all available PTT estimates.

7.2.2 Manual PTT estimate (reference method)

Manual PTT estimation served as ground truth to benchmark the automated PTT estimation algorithms. Using ECG(n), the LDV signals were segmented into separate heartbeats or *epochs*. This simplified the combining of fiducial points in both carotid and heart LDV signals for PTT estimation [219]. The physiological event underlying the relevant fiducial points

is the closure of the aortic valve (AC). This event is associated with a region of elevated signal energy typically referred to as the second heartsound (S2). The fiducial point in the heart signal is then taken as the first perturbation before the minimum value during S2. The carotid fiducial point is taken as the second distinct peak in the carotid epoch, a.k.a. the carotid dicrotic notch (DN). This signal feature also corresponds to AC. PTT is then calculated from the time difference between heart and carotid fiducial points, as illustrated in Figure 7.2.

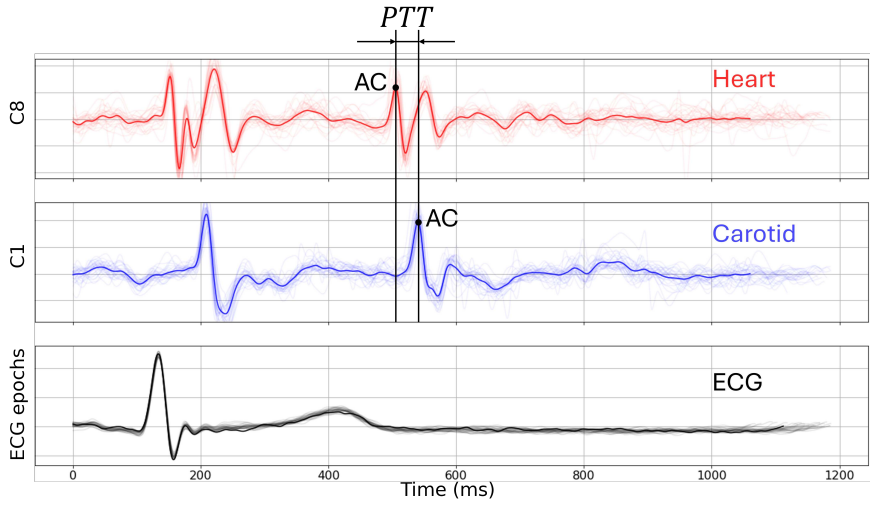

Figure 7.2: Example of an ECG-based heartbeat segmentation of a carotid and heart channel combination (channel numbers 1 and 8). The top graph displays LDV-heart epochs of which one is highlighted. The middle graph shows the same for the carotid site. Fiducial points that were used to identify the timing of AC are indicated. PTT is calculated from a combination of the indicated heart and carotid fiducial points. The bottom graph contains individual epochs of the $ECG(n)$ signal that was used for LDV-signal segmentation.

7.2.3 ECG-based automated PTT estimation

For the sake of comparison, an experiment was conducted wherein PTT values were calculated on data that was segmented into separate heartbeats (or *epochs*) delineated by the I available R peaks in ECG(n). For this naive method, all heart-carotid channel combinations were included, leading to $M^2 = 36$ combinations that were all segmented.

Every channel combination has I epochs. PTT was calculated on the same fiducial points as the reference (manual) PTT method, as in Figure 7.2. The key difference however was that the fiducial point detection was done in an automated manner. The carotid DN was identified by taking the

point of maximum acceleration within a window of 300 to 550 ms in the epochs of the selected carotid channel. The fiducial point corresponding to the aortic valve closure in the heart epochs was taken as the first peak before the absolute minimum within a window of 250 to 500 ms in heart channel epochs. The values of these windows were set based on the time between closure of the mitral valve (corresponding to the timepoint of the associated R-peak in ECG) and the closure of the aortic valve. This varies between 250-300 ms for healthy individuals, but can be elongated due to aging or disease [248, 249].

PTT_j were then calculated for each valid beat, yielding a total of J estimates. Only PTT values within a physiological range (5 ms to 60 ms) were considered valid, and the median of these values was used as the representative PTT for the recording, as in (7.3):

$$PTT = \text{median}(\boldsymbol{PTT}), \tag{7.3}$$

$$\text{with PTT} = \left[\text{PTT}_1, \text{PTT}_2, \ldots, \text{PTT}_J\right]^T.$$

This method is not practical for clinical implementation, as the additional ECG set-up would hamper the potential speed of LDV measurements, and decrease its appeal for widespread adoption.

7.2.4 Template matching-based PTT estimation

Without the ECG trace to identify heartbeat onsets and segment accordingly, the identification of required fiducial points is more challenging. One potential solution to this challenge was a similarity-search algorithm based on *template matching*.

First, a criterion was designed to remove channels with poor signal quality, as signal quality can vary significantly between channels of one handpiece [27]. A signal-to-noise-ratio (SNR) estimate was computed as follows, and applied to all M-channels per handpiece. First, the input signal power was obtained as:

$$P_{x,m} = \frac{1}{N}\sum x_m^2(n), \tag{7.4}$$

which represents the joint power of the target signal and noise. A median-filtered version of the input signal was next computed using a (non-causal) window of 5 samples:

$$\tilde{x}_m(n) = \text{median}(x_m(n-2), x_m(n-1), x_m(n), x_m(n+1), x_m(n+2)) \tag{7.5}$$

Noise was approximated as $v_m(n) = x_m(n) - \tilde{x}_m(n)$ and its power was estimated:

$$P_{v,m} = \frac{1}{N}\sum(x_m(n) - \tilde{x}_m(n))^2 \tag{7.6}$$

Thereby, the SNR was estimated as:

$$\mathrm{SNR}_m = \frac{P_{x,m}}{P_{v,m}} - 1 = \frac{P_{s,m}}{P_{v,m}} \tag{7.7}$$

The maximum SNR_m and standard deviation of SNR_m values per handpiece were calculated. Channels whose SNR_m deviated from the maximum value by more than one standard deviation were excluded from the analysis. The remaining carotid and heart channels were pair-wise combined for PTT estimation.

A template for the foot-of-the-wave waveform in carotid LDV acceleration signals was constructed as outlined in [27]. This waveform corresponds to a large peak in the acceleration signal, indicating the arrival of a pulse wave. For one heartbeat, two peaks are typically observed. The first one is referred to as the foot of the wave, while the second one corresponds to the dicrotic notch. The constructed template was cross-correlated with a sliding window on each considered carotid channel of the heart-carotid channel combination. A heartbeat onset was assumed when the cross-correlation exceeded an empircally set threshold ([27]).

For every detected beat, fiducial points corresponding to (AC) were searched for in physiologically relevant windows. For the carotid DN, this window spanned between 250 and 500 ms after the detected heartbeat onset. The fiducial point in the heart signal, corresponding to AC, lay within a window of 200 to 450 ms after the onset of the corresponding beat at the carotid. Similar to section 7.2.3, these windows were set with physiological cardiac timing in mind but were altered slightly due to the construction of the template. Indices at which template matching detects a beat are situated up to 50 ms later in time than the corresponding R-peaks [27].

In this way, *both* heart and carotid fiducial points depended on the template matching at the carotid level. The construction and application of a heart-signal template was deemed unsuitable due to the observed inter-subject variability in the heart-signal morphology. The carotid dicrotic notch was found as the maximum value in its window. The aortic valve closure timing in the heart signal was taken as the first peak to the left of the minimum value in its respective window.

To ensure the quality of the resulting PTT values, a criterion was set on the variability in fiducial point timing. The method flagged the data as

unreliable if either the timepoints at which the carotid DN was found, or the timepoints for the heart fiducial points had a standard deviation exceeding 60 ms. In these cases, the channel combination was dropped.

PTT values were calculated in the same way as in section 7.2.3. The final PTT was calculated as in (7.3), but was rejected if the total number of PTT estimates J was smaller than or equal to an empirical threshold of 15. This value was set to exclude several measurements where signal quality was extremely poor, and the few PTT estimation made resulted from random, noisy waveforms being combined as opposed to physiologically sound features.

7.2.5 Data-driven PTT approach

There is an obvious need for robust segmentation of LDV signals. The importance of this need warrants a data-driven approach, realized through the development of a DNN. This DNN was trained using 4-second carotid LDV-signal segments as input. Any selected carotid channel was segmented into 4-second segments with 50% overlap. This returned for e.g. a signal of length 20 seconds, 9 overlapping segments. For every such LDV segment, the model provided an equally long output signal $\hat{E}'(n)$ of 4 seconds. The individual output signals $\hat{E}'(n)$ were then concatenated using windowed overlap-add with perfect reconstruction condition [193], resulting in a model prediction $\hat{E}'_m(n)$ for carotid channel m.

The target signal had to be a signal from which segmentation of LDV signals into heartbeats was feasible. Raw ECG, while rich in information on cardiac timing, was deemed too complex to accurately predict with the available data. For our application, only the timing of R-peaks is needed, while ECG contains many more features that are not relevant for this work. From visual inspection of the measured data, it was observed that the ECG traces also contained noise. Hence, a transformation aimed at reducing complexity while conserving cardiac timing information was engineered first.

7.2.5.1 ECG-proxy as learning target

To derive a suitable learning target for the DNN, the ECG was transformed, taking care to conserve the information on the timing of the R-peaks. First, the ECG trace is replaced by a pulse train formed by Kronecker's delta functions at the location of the original R-peaks. Denote this as:

$$\mathrm{ECG}'(n) = \sum_i \delta(n - n_{p,i}), \tag{7.8}$$

where $n_{p,i}$ is the sample-index of the $i-$th R-peak. This does not yet suffice however, as this pulse train is too sparse. Such a sparse target signal is

not optimal for model training with the mean squared error (MSE) loss function.

Subsequently, this simplified ECG trace is convolved with a Gaussian filter, to yield the target signal $E'(n)$:

$$E'(n) = \mathrm{ECG}'(n) * g(n) = \sum_i g(n - n_{p,i}), \tag{7.9}$$

where $g(n)$ is the Gaussian filter:

$$g(n) = \frac{1}{\sigma\sqrt{2\pi}} \exp\left\{(-\frac{n^2}{2\sigma^2}\right\}). \tag{7.10}$$

This transformed signal is contrasted with the original trace in 7.3. For the model training, the mean-squared error (MSE) between the target $E'(n)$ and model-output $\hat{E}'(n)$ signals is calculated as:

$$\mathrm{MSE} = \frac{1}{N}\sum(E'(n) - \hat{E}'(n))^2 \tag{7.11}$$

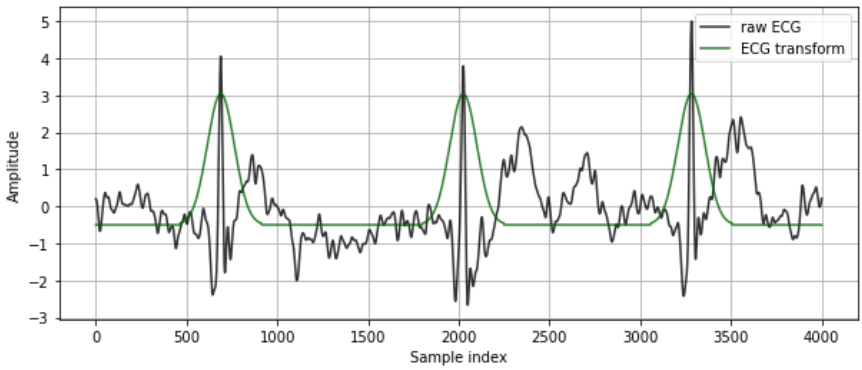

Figure 7.3: Example of the transformation from raw ECG ($\mathrm{ECG}(n)$) to a target signal with reduced complexity ($E'(n)$) for a randomly picked LDV segment. Data are z-normalized. $\sigma = 75$ samples.

7.2.5.2 DNN structure and training

The DNN architecture was inspired by state-of-the-art for biomedical image processing, where U-nets are often used because of their multi-scale feature extraction, end-to-end learning and strong generalization with limited dataset sizes, amongst others [175]. The proposed model is adjusted for 1D data but largely retains the structure of the U-net architecture. It has

four convolutional layers in the encoder- and decoder blocks, and an added transformer layer in the bottleneck [250]. Addition-based skip connections were also included. This architecture (Figure 7.4) ensures the conservation of short- and long-term temporal context, allowing it to effectively learn the complex non-linear transformation between input and target. The model has 25k learnable parameters.

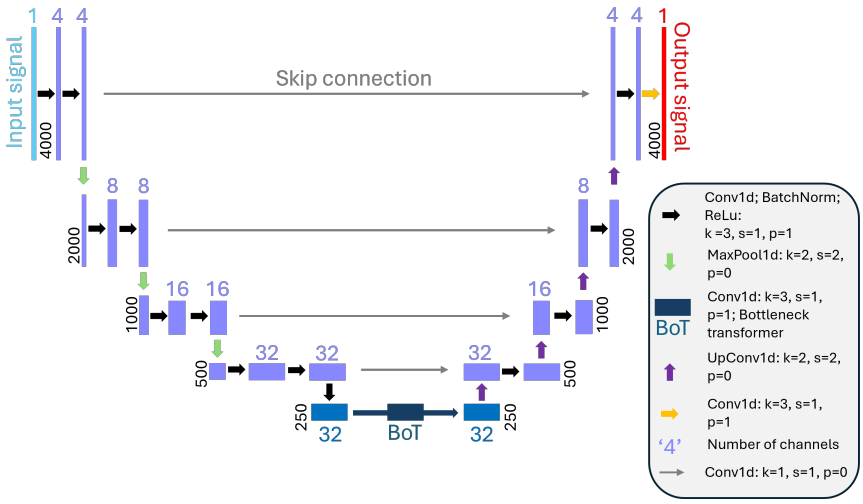

Figure 7.4: DNN-model architecture: each blue box represents a feature map with a number of channels equal to the number displayed on top of it. The 1D-data dimension is noted at the bottom of the relevant boxes. Arrows and notations corresponding to different operations are listed. k, s and p refer to kernel size, stride and padding respectively.

During training, the calculated loss on the validation set was evaluated to identify the stopping criterion. Model performance was also evaluated via an auxiliary metric, the R-peak score Q_R. This is the ratio of the number of R-peaks that are present in the target signal I to the number of those peaks that were also detected in the model output $\hat{I}$ (within a window of 30 ms before or after the corresponding target R-peak, as illustrated in Figure 7.5):

$$Q_R = \frac{\hat{I}}{I} \tag{7.12}$$

To illustrate this, an example datapoint is presented (Figure 7.5). Peaks are found via a simple find-peaks algorithm that has the criteria of a minimum amplitude $A_{min} = 1$ (all data is z-normalized) and that the peaks should be separated by at least 500 ms. Also indicated in the target and model-output signals are the temporal windows around the target R-peak instances, where a corresponding peak should occur in a correctly predicted output. It should

be noted that the example datapoint in Figure 7.5 is unseen data, and completely independent of the training set. This well showcases the generalization capability of the proposed DNN.

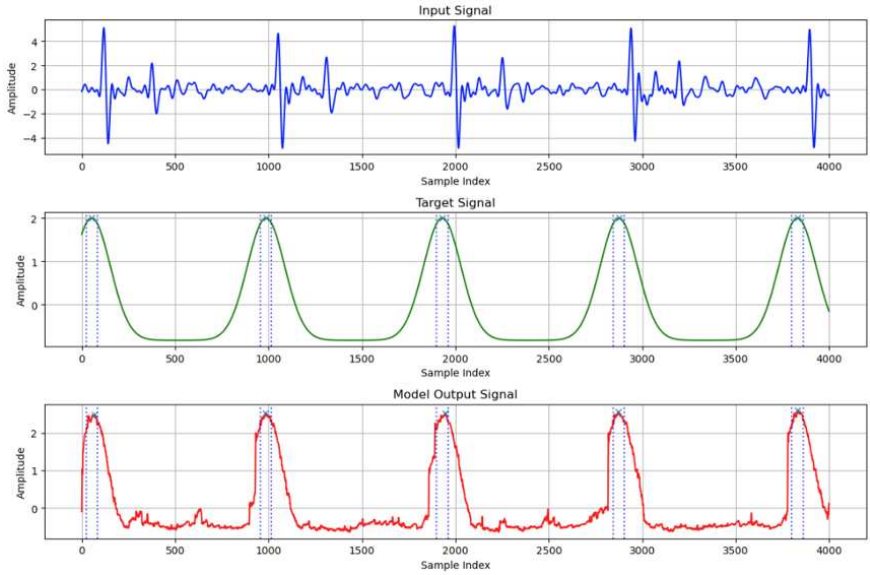

Figure 7.5: Example of model prediction on an unseen datapoint. The top graph shows the carotid-LDV segment that serves as model input. Its corresponding $E'(n)$ segment is displayed in the middle graph, and serves as target signal for this datapoint. The model prediction or output, is shown in the bottom plot. The vertical dotted lines indicate the tolerance window around target-signal peaks wherein output-signal peaks are desired for an acceptable model performance. Q_R in this case is 100%.

7.2.5.3 Application to PTT calculation

The DNN-based ECG-proxy estimate is used to segment the LDV-signal $x_m(n)$ into separate heartbeats or epochs. In order to get to a PTT estimate, additional steps are required: starting from the $M = 6$ heart and carotid LDV channels for a given measurement, first a check on individual channel signal quality was implemented using SNR-based estimations. For the heart signals, SNR was calculated as detailed in Section 7.2.3.

Carotid SNR was calculated differently. The DNN was used to generate predictions $\hat{E}'_m(n)$ for all $M = 6$ carotid channels. A simple peak-finding function was applied to $\hat{E}'_m(n)$. The only restraints provided to the function were again; a minimum distance of 500 ms between consecutive peaks, and a minimum height of A_{min}. For every detected peak i at $\hat{n}^m_{p,i}(n)$, an individual, bounded, SNR-based metric $\zeta_{m,i} \in [0,1]$ is calculated as follows:

$$\zeta_{m,i} = \frac{\text{SNR}}{\text{SNR}+1} = \frac{P^m_s}{P^m_s + P^m_v}\,, \tag{7.13}$$

where P_s^m is now computed from $\hat{E}'_m(n)$ within a window spanning -2σ to $+2\sigma$ centered around $\hat{n}^m_{p,i}$. σ comes from the definition of $g(n)$, where a window of 4σ centered on the peak of the predicted gaussian waveform is assumed to contain correctly predicted model output signal content:

$$P_s^m = \sum_{n=\hat{p}_i-2\sigma}^{\hat{p}_i+2\sigma} \hat{E}'^2_m(n) \tag{7.14}$$

$\zeta_{m,i}$ was calculated on a segment of $\hat{E}'_m(n)$ around $\hat{p}_i$, as in (7.13) – (7.15).

The signal plus noise component $P_s + P_v$ is approximated as the energy of $E'(n)$ within a window between the previous and next peak locations. Specifically, denoting by $d_i^m = \hat{n}^m_{p,i+1} - \hat{n}^m_{p,i}$ the distance, in samples, between the current and next successive peak and analogously defining $d_{i-1} = \hat{n}^m_{p,i} - \hat{n}^m_{p,i-1}$, we define:

$$P_s^m + P_v^m = \sum_{n=\frac{d_{i-1}}{2}}^{\frac{d_i}{2}} \hat{E}'^2_m(n)\,. \tag{7.15}$$

Note that due to heart rate variability, typically $d^m_{i-1} \neq d^m_i$. An average ζ_m is then calculated for each carotid channel: $\boldsymbol{\zeta} = \Big[\zeta_1, \zeta_2, \ldots, \zeta_M\Big]^T$.

$$\zeta_m = \frac{1}{\hat{I}} \sum \zeta_{m,i} \tag{7.16}$$

For both the heart and carotid side, only channels with a ζ_m within one standard deviation of the maximum ζ_m were considered for further analysis. The $\hat{E}'_m(n)$ of the carotid channel with the maximum ζ_m was used for segmentation. Further, only the peaks with a $\zeta_{m,i} > 0.4$ were kept for further processing. All included heart and carotid channels were segmented into individual epochs based on these detected peaks. Each heart channel was iteratively combined with each carotid channel.

At this point, the DNN-based *pseudo-ECG transform* allowed us to detect heartbeat onsets, followed by carotid and heart signal segmentation. The next step towards PTT calculation was designed to be similar to that described in section 7.2.4 for the template-matching method. Briefly, Fiducial points had to be identified in the segmented epochs within physiologically sound windows. The signal features corresponding to the fiducial points are the same for this method, previously exemplified in Figure 7.2.

However, taking the tolerance window for Q_R into account, slightly wider windows were used for this method as compared with those used for

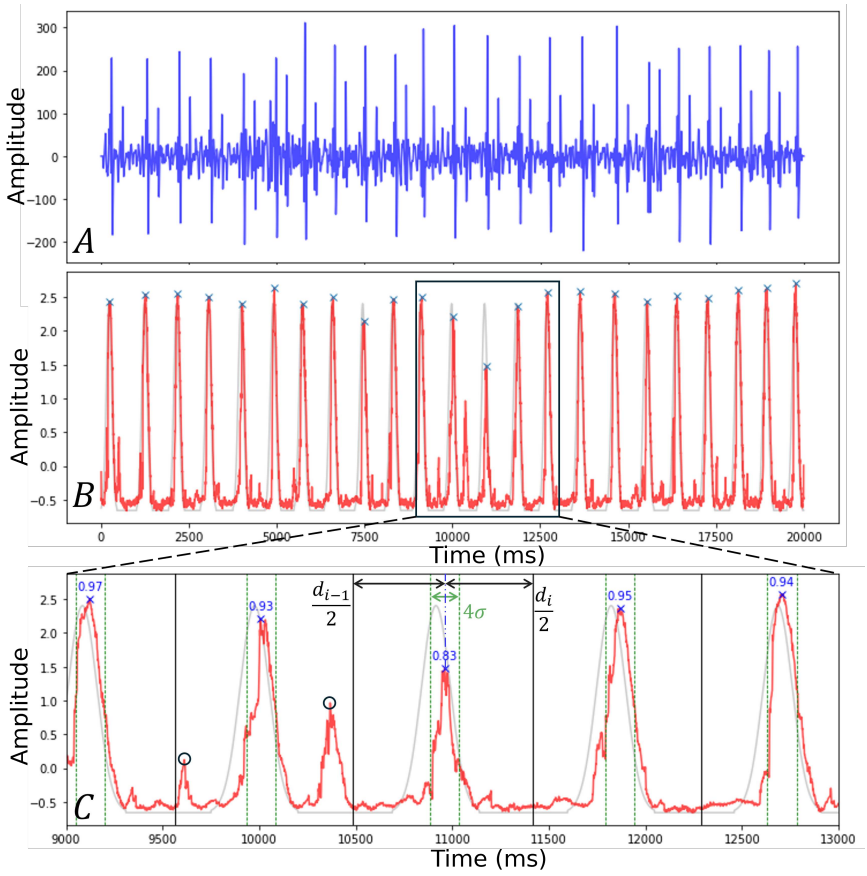

Figure 7.6: Panel A: Example LDV carotid skin-acceleration signal. Panel B: $\hat{E}'_m(n)$ for the example signal. The ground truth $E'(n)$ is displayed for reference in gray in the background. Panel C: An illustrative segment of $\hat{E}'_m(n)$ is shown in which the detected beats are indicated. The ζ_i values for detected peaks are displayed together with the boundaries within which signal (vertical dashed lines) power P_s and signal plus noise (full vertical lines) power $P_s + P_v$ are calculated. The gray graph is the corresponding $E'(n)$. The two smaller peaks indicated with 'o' were excluded from the analysis based on the set criteria on amplitude and proximity to other peaks in time.

the template matching. The fiducial points and window values are the same as for the ground-truth method with ECG, outlined in section 7.2.3. The above steps are illustrated for one measurement in Figure 7.7. The PTT can then be estimated as detailed in section 7.2.3 and 7.2.4.

A final difference between this method and the TM-based approach is the acceptance criterion for the final PTT. Here, if J is the total number of PTT estimates, the final PTT estimate is rejected if $J \leq \gamma N$, where N is the total sample length of the measured LDV signals. The threshold factor γ was set to 0.0025 (corresponding roughly to 50 PTT estimates over a 20s long segment, sampled at 1kHz – consistent with previous work on the CARDIS database, where this criterion yielded the best results [23].

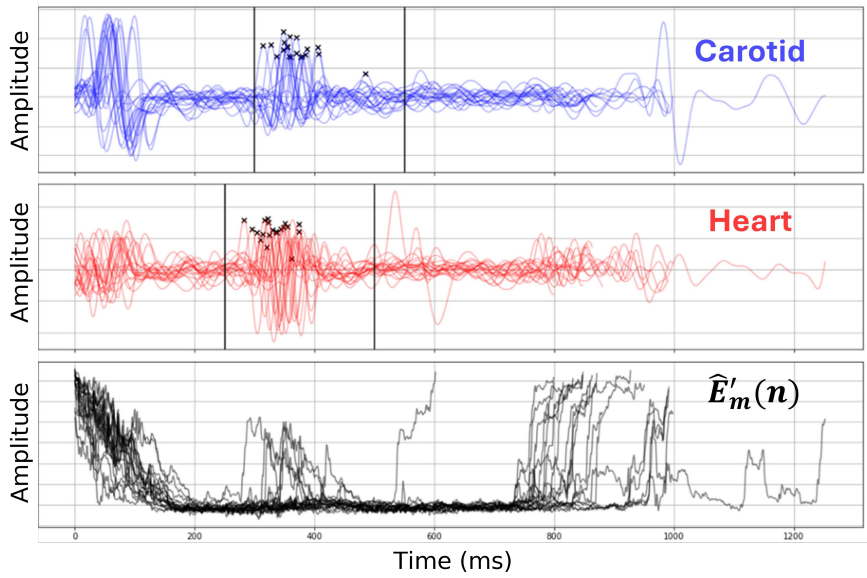

Figure 7.7: One heart-carotid channel combination is illustrated. Both channels were split into epochs according to the detected peaks in the preferred $\hat{E}'_m(n)$ (channel with highest ζ_m). Its epoch-wise representation is given in the bottom plot. Carotid (top) and heart (middle) epochs are drawn together with the window limits between which the search desired fiducial points. These points are indicated.

7.2.6 Experiment

Two separate databases were used (demographic data reported in Table 7.1). The first one, the CARDIS database, was measured during the CARDIS project [23]. 100 hypertensive patients (age range: 23-73 years, 50% female) were included with three measurements made for each measurement set-up, consisting of carotid-carotid (i.e. the two LDV

handpieces mounted on top of eachother, both pointed at the carotid artery) and carotid-femoral measurements. For this database, an expert visually scored all carotid signals on a 5-point scale ranging from 1 (very bad) to 5 (very good) [27]. 67 subjects had at least one measurement with at least one qualitative carotid channel (score 4 or 5) that could be included in the DNN training and evaluation process. Other data was discarded for the purpose of this analysis.

All signals of higher signal quality (visually scored 4 or 5 on the 5-pointer scale outlined in previous work [27]) were selected and split into 70 – 15 – 15 percent subsets. The 70% data stack served as a training set, while the two 15% stacks served as validation and testing sets respectively. Care was taken to ensure that data from the same subject were not present in both training and validation or test sets, thus avoiding data leakage. This yielded 6055 4-second segments for the training set, 1431 segments for the validation set and 1432 segments for the test set. The training data was provided by 45 subjects. The validation and testing data together entailed 22 subjects. Each segment had a corresponding, ground truth, ECG trace ($ECG(n)$), measured in parallel. This served to generate the training target as detailed in Section 7.2.5.1.

The second database (INSIDE) was cultivated during the H2020 In-SiDe project (Grant agreement ID: 871547). Of importance for this work: 100 patients (age range: 18-81 years, 45% female) were included, each of whom had 3 heart-carotid measurements taken. One handpiece was pointed at the right common carotid artery, with the other pointed at the base of the heart i.e. the second right intercostal space, depicted in Figure 7.1. This measurement site was yielded better signal quality when compared with others, in previously exploratory work. PTT values for these data were previously estimated by manual segmentation based on $ECG(n)$, followed by a manual combination of fiducial points. The proposed PTT estimation using the DNN-based segmentation and SNR metrics, as well as the previously proposed template-matching (TM) based method in section 7.2.4, were tested on this database. For the DNN, this database is comprised completely of unseen data. The skin acceleration data used across the two databases was resampled to a 1kHz sampling rate.

7.3 Results

First, the performance of the DNN is investigated through evaluation of the Q_R metric. From visual inspection of the data, it was observed that signal quality can vary, even between the selected higher-quality segments for the training, testing and validation sets [27]. There is also the presence

InSiDe (N=100)		
Variable	Mean ± SD	Range
Age (years)	48 ± 17	[18, 81]
Sex (male %)	55	/
BMI (kg/m²)	26 ± 5	[17.24, 39.82]
Systolic BP (mmHg)	130 ± 20	[88, 219]
Diastolic BP (mmHg)	79 ± 15	[49, 136]
CARDIS (N=100)		
Variable	Mean ± SD	Range
Age (years)	43 ± 19	[19, 85]
Sex (male %)	50	/
BMI (kg/m²)	23 ± 3.6	[17.63, 31.6]
Systolic BP (mmHg)	118 ± 14.7	[96, 183]
Diastolic BP (mmHg)	64.5 ± 9.2	[45, 99]

Table 7.1: Population statistics for both LDV databases. SD refers to standard deviation.

of motion artifacts, obscuring underlying heartbeat-related waveforms required by the DNN for an accurate prediction. The DNN model reached Q_R values of 75% on the validation set and 72.84% on the test set. This is visualized in Figure 7.8.

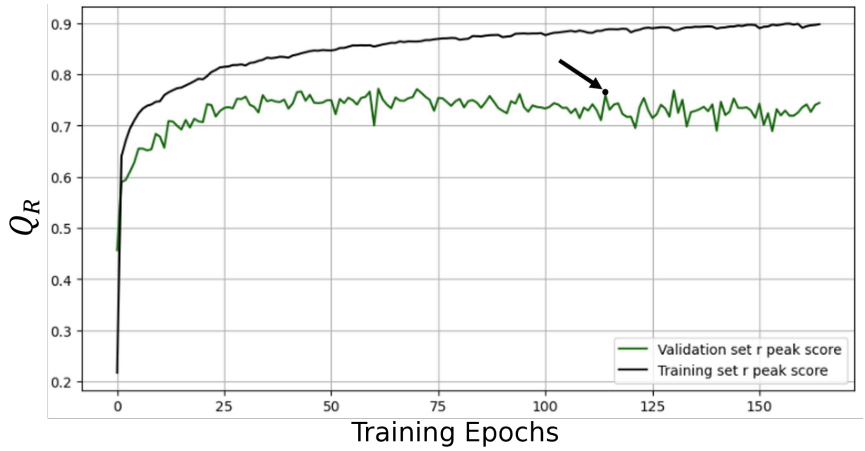

Figure 7.8: R-peak score evolution during the DNN training for both training and validation sets. The epoch at which the training process was halted is indicated.

Following DNN hearbeat onset detection, the performance of PTT estimation is assessed. All results pertaining the automated PTT methods are

displayed in Figure 7.9. Panel A shows the results when the automated PTT algorithm using ground-truth ECG(n) for signal segmentation is utilized. A total of 215 datapoints stemming from 91 subjects are represented. The correlation coefficient with the ground truth (manual PTT values) is $\rho = 0.62$, $p < 0.001$

Panel B shows the results for the template-matching based PTT method. Out of the 100 subjects included in the INSIDE study, for 46 subjects the method yielded a final PTT estimate from at least one of the three heart-carotid LDV measurements. In total, 78 measurements had a final result, as seen on the panel. The correlation coefficient between the manual PTT and their corresponding automated PTT values is $\rho = 0.69$, $p < 0.001$.

Panel C in Figure 7.9 shows the datapoints of measurements with a final PTT value via the DNN-based method. These are plotted against and correlated with their corresponding manual PTT estimates. A total of 127 datapoints belonging to 68 subjects were displayed. A correlation coefficient of $\rho = 0.71$, $p < 0.001$ was found.

7.4 Discussion

7.4.1 DNN-model validation for heartbeat onset prediction

The U-net inspired configuration was scaled in accordance with the prevalence of available training data. At 25k trainable parameters, the model is relatively small and we did not observe overfitting.

Carotid signals were chosen as inputs to the model, instead of the heart-signals measured at the chest. This choice was partially driven by our more detailed understanding of the carotid LDV waveforms as compared to the newly investigated heart signals. This is because the bulk of the existing LDV research focuses on carotid-femoral PTT (and consequently PWV) [19, 23, 25, 27]. Thus, selection of good quality data was deemed most feasible at the carotid site for this study. The carotid signals also seemed to be more consistent in quality, experiencing less pronounced effects on signal content from altered physiology due to cardiovascular disease. Due to these reasons, signal-quality scores per measured signal for the carotid signals in the CARDIS database were previously acquired [27]. This allowed for selection of good to very good quality data, making the training, testing and validation data representative for the type of data that future applications of improved LDV-prototypes will provide.

Our application requires only the detection of the onset of heartbeats, so the R peaks of the $ECG(n)$ are critical and need to be reliably predicted by the DNN. Therefore a target signal containing information only on the

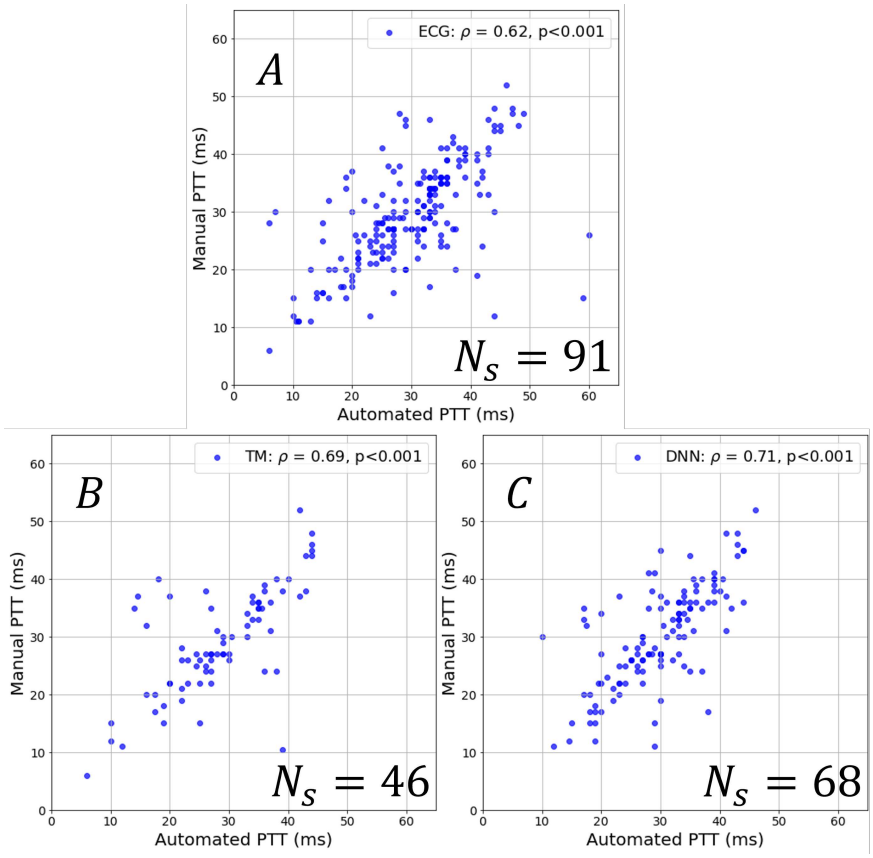

Figure 7.9: Results comparing automated PTT estimates with manual PTT estimates. Panel A displays the ECG-based automated PTT estimates. Panel B shows TM-based automated PTT values and panel C shows those obtained using the DNN-based $\hat{E}'(n)$ for segmentation. Correlation coefficients and corresponding p-values are indicated. N_S refers to the total number of unique subjects for whom a final PTT estimate was obtained by the corresponding methods.

timepoints of these R peaks is sufficient and simplifies the relation to be learnt between input and target signals. Additionally, this transformation allows us to train the DNN with the straightforward, well-known MSE loss function, which would be challenging with a more sparse $ECG(n)$. The transformation from raw ECG to the series of Gaussian pulses in $E'(n)$ was, thus, beneficial for model performance. For the Gaussian filter, $\sigma = 75$ was empirically found to be a good trade-off.

The R-peak score Q_R counts a correctly detected R-peak location in the $\hat{E}'(n)$ if it corresponds to an R-peak in the associated raw ECG signal (or the corresponding peak in $E'(n)$) within a 60 ms window centered on that R-peak. A Q_R value of 72-75% for unseen data indicates that our

model performs well in detecting heartbeat onsets, especially considering the sensitivity of LDV data to motion artifacts, which can be visually inspected and influence signal quality.

It is important to note that a reliable PTT estimate does not require exhaustive processing of every single beat in a given measurement. Final DNN-based PTT estimates were accepted if, for a $T_s = 20$ s signal, $J = 50$ PTT estimates were made across all considered channel combinations. Even if only $M = 3$ carotid and $M = 3$ heart channels pass their respective SNR criteria, this results in 9 channel combinations. Assuming a heart rhythm of 60 bpm (a realistic lower bound), with 20 beats in the T_s measurement, this leads to $9 \times 20 = 180$ total beat-pairs considered for PTT calculation. In this scenario, J is well below 72-75% of 180, implying that the DNN-based method can return reliable PTT values based on a smaller subset of the available data from one LDV measurement.

We observed that the majority of the accepted R-peak locations in $\hat{E}'(n)$ do not perfectly coincide with the ground-truth peaks. The reason why we accept these timeshifts (maximum of 30 ms before or after the ground-truth peak) is because of the windowing in the later stages of PTT-estimation processing. The set windows, to locate the desired fiducial points, are wide enough to account for this margin of error. These windows also take into account the inter-subject variability in time between features such as the carotid foot of the wave and the dicrotic notch.

7.4.2 TM- vs DNN-based PTT estimation

It is clear from Figure 7.9 that using the raw ECG for signal segmentation leads to an acceptable final PTT value for most subjects. This method would indeed be the most inclusive, if ECG could readily be measured alongside LDV, which is not the case. However, subjects with objectively poor signal-quality measurements are also included, leading to more outliers and a somewhat lower correlation coefficient with the reference when compared to TM and the DNN-based method. This is to be expected, as there are no severe quality criteria included with this ground-truth method while there are several in place for the other, ECG-independent methods.

To evaluate the discrepancies between the TM and DNN-based approaches, they were both correlated to the reference. While the correlation between reference and TM-based PTT values is indicative enough to be interpreted as a validation for the method, the number of criteria that were put in place to ensure a reliable result leads to many measurements being discarded. This yields results for only 31.2% of data (i.e. for 46 subjects), which is a significant drawback.

The DNN-based method implemented similar criteria on the quality of the input signals and the DNN output, also to guarantee results that are as robust as possible. Doing so, this method yielded results for 50.8% of the measurements corresponding to results for 64 subjects. The correlation between manual and both automated PTT values was also stronger for the DNN method compared to the TM-based approach. These results imply that the DNN method is not only more in line with our chosen reference, but also more inclusive and subsequently more applicable in practice.

An explanation for the discrepancy between the number of subjects represented by the TM-based and DNN-based automated PTT estimation methods can be derived from Figure 7.10. The figure shows a segment of carotid LDV data of lower signal quality, i.e. less pronounced and differently shaped physiologically relevant peaks and low SNR. For this segment, the carotid foot was detected by TM where the algorithm found matches. Using the DNN, an $\hat{E}'(n)$ was generated on the same segment. As can be seen, TM failed to indicate the correct waveforms. Conversely, while not perfect by any means, the DNN output does place peaks in acceptable proximity to the ECG R peaks, that can be identified in an automated manner. This specific case illustrates general observed trends: the TM is more susceptible to signal quality degradations as opposed to the DNN, demonstrating the power of representations learnt by data-driven methods.

7.4.3 Future applications

All measurements in both CARDIS and InSiDe studies were conducted using the CARDIS prototype. This device has a few drawbacks such as the requirement of retroreflective tape on the measurement site to ensure enough reflection of the incident laser beams. This likely has an effect on signal quality that can only be resolved by improving the hardware. A new LDV prototype is set to be released within the scope of the InSiDe project that aims to achieve this and thereby improve measurement signal quality. With this, the DNN-based technique can be expected to perform even better.

Other project objectives for InSiDe are the development of algorithms for estimating carotid-femoral pulse-wave velocity, investigating carotid stenosis and cardiac arrythmia [26, 230, 251]. For the latter especially, but not exclusively, the DNN could prove useful as its output contains information on the relative heartbeat onset timing within a given measurement. One could generalize the potential use of the DNN to any cardiac application of LDV, potentially even for non-carotid signals (given a retraining of the DNN on e.g. heart or femoral artery LDV measurements).

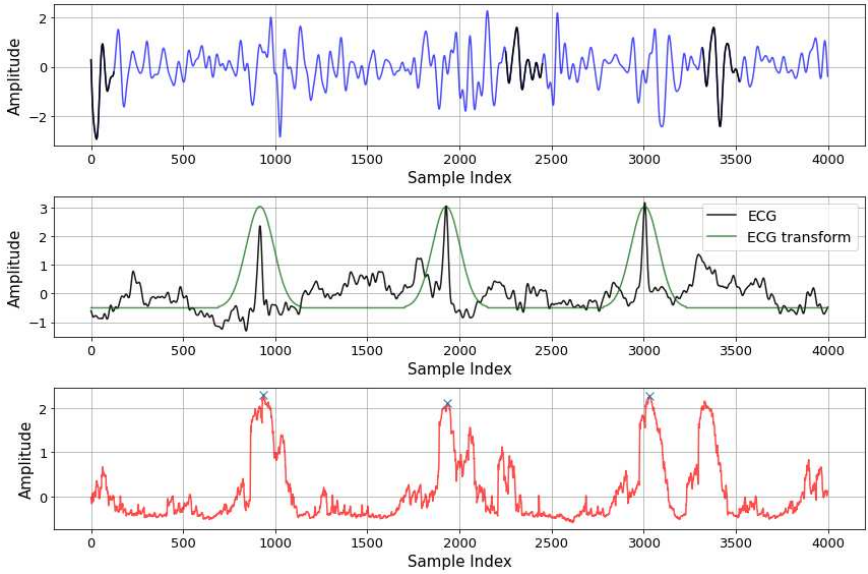

Figure 7.10: An example Figure presenting a low-quality carotid signal (blue) and its corresponding ECG (black, second panel). Indicated in black on the first panel are the waveforms in the LDV signal that were identified by template matching. The detected waveforms do not correspond with actual heartbeats here. DNN output is shown in red, in which detected peaks are marked. These peaks do correspond with heartbeat onsets as can be seen from the R peaks in the ECG signal.

7.4.4 Remaining challenges

Given the relative niche application of LDV within the current state of the art and especially the paucity of other studies investigating heart-carotid PTT, there is little literature to compare the results of this work to. However, as the technology and prototype builds progress, so would the average signal quality and with it the DNN performance.

7.5 Conclusion

A DNN was trained for the purpose of heartbeat onset prediction in LDV signals measured at the carotid artery. The model training was efficiently done by way of a transformation applied to raw ECG signals that were measured in parallel with the LDV signals. This transformation consisted of Gaussian pulses at the location of the ECG R peaks, conserving only information of their timing and facilitating a simplified loss-function application. With the information provided by the DNN, robust signal segmentation in the absence of ground-truth ECG was possible. From the segmented heartbeats, fiducial points were identified which led to heart-carotid PTT values. These DNN-based PTT values correlated better with reference PTT

values than the classical TM-based method. The DNN method also yielded results for significantly more subjects than TM. We conclude that the DNN method provides added value in the form of a complexity-reducing target signal transformation and robust heartbeat segmentation, which performed well when applied to LDV-derived heart-carotid PTT estimation and could be expanded for other cardiac applications.

IV

Conclusions

CHAPTERS

8 Conclusions and Perspectives **177**

CHAPTER 8

CONCLUSIONS AND PERSPECTIVES

Having discussed the several avenues of efforts made in the previous chapters of this dissertation, a comprehensive discussion on the larger scope is in order. This chapter will convene the individual results and conclusions of the dedicated analyses of the different chapters and review them globally for the reader.

8.1 SIGNAL QUALITY

Beginning with LDV signal quality, a metric was derived based on temporal signal features. The primary contributors to the quality metrics were the number and shape of recurring patterns over time, applicable to both matrix-profile and template-matching metrics. Logistic regression models were also trained using these new quality metrics to classify signals according to their respective qualities. Although these models performed well for their intended application, they were not integrated into the updated software packages for enhanced graphical user interface functionality. Instead, a real-time signal quality indicator was deemed more beneficial than post-measurement signal quality classification. This decision is rational, as real-time feedback allows the operator to make adjustments to their own and the subject's positioning for improved results.

The final implementation of real-time signal-quality feedback utilized the template matching metric. Despite the nearly identical performance of both metrics, template matching was preferred due to its lower computational resource requirements and seamless integration. Another advantage

of template matching was its perceived lower susceptibility to detection errors, particularly in detecting incorrect waveforms, such as mistaking the carotid dicrotic notch or motion artefacts for the wave foot. However, subsequent analyses following the publication of the paper on which chapter 3 is based revealed that both template matching and matrix profile experienced this issue. This error could occur even in objectively high-quality measurements, though it was more commonly observed in lower-quality signals.

Another method for improving signal quality was our 'beamforming' and beamforming-derived independent component analysis, reported in chapter 4. This approach utilized spatial features, as opposed to the previous temporal features, by combining multiple channels from the same handpiece to create a single, enhanced signal. When tested for carotid-femoral PTT estimation, it produced values closer to Sphygmocor reference values compared to a benchmark method that individually combined all channels across handpieces for PTT estimation. Notably, spurious artefacts were effectively suppressed through the blind, segmented weighting of the different spatial components used to construct the enhanced signals. PTT estimation methods using matrix profile or template matching, which are known to be affected by such artefacts, benefit from the spatial filtering provided by beamforming. With further optimization, these methods could be incorporated into future software updates for the LDV system to improve carotid-femoral PTT estimation.

Real-time carotid-femoral PWV can be estimated using the algorithm described in chapter 5. The results corresponded with gold-standard (arterial tonometry) reference values, demonstrating that carotid-femoral PWV can be reliably calculated from LDV measurements. Still, there is no such thing as a *free lunch* in signal processing. If signal quality is insufficient, template matching may fail to detect heartbeats, resulting in either no PWV value or an erroneous one.

Ultimately, even with the implementation of the real-time quality feedback system, the average signal quality did not show noticeable improvement. Visual inspection of data collected with this added functionality for the heart-carotid feasibility study revealed that much of the data were difficult or impossible to process into a PTT value, both automatically and manually. This was particularly true for carotid-femoral measurements, similar to observations during the CARDIS study. Although the real-time quality feedback functioned effectively, it did not sufficiently guide the operator towards obtaining better measurements. Poor signal quality typically did not improve with increased pressure or device repositioning, although it is to be kept in mind that data were generated with the CARDIS

device which requires retroreflective patches, limiting repositioning options. Given that the device cannot compensate for factors such as excess body weight, which affect the signal-to-noise ratio for femoral signals, it can be concluded that there are inherent limitations to the physiologically relevant information present in the skin vibrations of subjects with poor real-time signal quality. While LDV technology is capable of detecting nanometer-scale vibrations, it falls short for this specific application if the detected vibrations do not correspond to meaningful physiological signals.

One potential reason for the persistent difficulty in consistently obtaining high-quality measurements could be the necessity of the retroreflective patch. As previously mentioned, the CARDIS device operates at a wavelength where the reflected laser-beam amplitude is insufficient when illuminating bare skin. While the retroreflective patch resolves this reflection issue, it is not unreasonable to assume that it interferes with the biomechanics of skin vibrations. It remains to be seen whether a hardware update to a future prototype that eliminates the need for the patch will yield signals with higher signal-to-noise ratio and better interpretability.

8.2 The potential of heart-carotid PWV

Part III explored the study of heart-carotid PWV as a potential alternative or supplementary biomarker to carotid-femoral PWV. The primary motivations for this experiment were to incorporate the elastic region of the ascending aorta into the considered pathlength and to address the scarcity of extensive literature on heart-carotid PTT and PWV. Additionally, heart signals measured by the LDV device generally exhibited clear features, higher signal-to-noise ratio, and greater reliability compared to femoral measurements.

To minimize potential errors, a manual PTT estimation method was employed, involving visual inspection of signals to identify fiducial points. PWV was not calculated because the distance between the heart and carotid measurement sites was unknown, preventing an accurate estimation of the heart-carotid pathlength. Although several distances were measured alongside the LDV, they could not be validated due to the absence of a reference for heart-carotid PTT values. This challenge, which remains unresolved, was initially thought to be surmountable. According to the clinical study protocol, LDV measurements were conducted after an MRI. The intention was to calculate PTT between the aortic valve and carotid artery using MRI data. However, this was not feasible because the MRI coils only covered the thoracic area and did not extend to the carotid measurement site. Even approximations, such as PTT between the aortic valve and brachiocephalic

trunk, could not be reliably assessed due to the low temporal resolution of the MRI data. Alternative technologies offering superior temporal resolution and accounting for the entire heart-to-carotid arterial pathlength should be explored.

LDV-derived heart-carotid PTT values could be correlated with established predictors of arterial stiffness, such as age and blood pressure. The experimental correlations indicated a clear preference for specific heart measurement sites (i.e. the base of the heart) and temporal signal features (the dicrotic notch) for fiducial point detection and combination in PTT calculation. However, the results did not reveal the strength of the potential biomarker. The correlations were not sufficiently high for serious clinical consideration, which usually requires them to fall in the 0.7-0.8 range. These mediocre correlations suggest that while LDV heart measurements contain physiological information, this data is distorted by the multiple tissue layers between the measurement site and the origin of the vibrations (i.e., the aortic valve).

The project goal of investigating heart-carotid PWV was not fully achieved, but significant initial progress was made. Further investigation is necessary, but current evidence does not suggest that heart-carotid PWV is a strong, independent biomarker like carotid-femoral PWV. Consequently, we conclude that while heart-carotid LDV measurements contain some physiologically relevant information, it is insufficient for this application and should be redirected towards other uses. However, this remains to be confirmed by testing with a device without the requirement of retro-reflective tape. Heart signals may still be valuable for detecting cardiac arrhythmias or ventricular dysfunction, though this remains speculative at this stage. Additionally, other more compact and efficient technologies, such as digital stethoscopes, already perform well for these applications.

8.3 DEEP LEARNING APPLICATION AND FINDINGS

ECG is highly effective for heartbeat detection, which facilitates LDV signal segmentation and subsequently simplifies signal feature detection. Our experiments utilized carotid signals, but with comprehensive visual classification of heart measurements based on signal quality (as was done with carotid and femoral signals in chapter 3), similar experiments could be conducted using a DNN trained on heart signals. This would extend the application of the model presented in Chapter 7 from heart-carotid measurements to purely cardiac measurements. LDV signal segmentation following heartbeat detection remains beneficial for various cardiac fields beyond arterial

stiffness assessment, and is equally applicable to other carotid-related studies. The current model could also be employed in carotid stenosis detection, albeit as a component of a larger algorithm.

A significant strength of our approach lies in the utilization of a compact network comprising 25,000 trainable parameters. This network, trained on CARDIS data and validated with new data measured within the InSiDe project (though with the same CARDIS device), exhibits robust generalization capabilities despite the InSiDe dataset being unseen data. Enhancing the model's representational capacity would naturally involve expanding both the training and validation datasets. The model's performance with limited training data, especially considering the small number of subjects, underscores its efficacy.

The DNN-based method demonstrates significant advantages over template-matching based algorithms due to its robustness against variations in carotid acceleration signal morphology, including artefacts. Unlike the prior approach, which depended heavily on sharp accelerations at the wave foot and dicrotic notch – features that are not consistently present – the DNN method reduces dropout in usable beat-pairs. It effectively compensates for the absence or reduced prominence of the double spike pattern (e.g., when only one prominent LDV peak is present), facilitating the identification of whether the single peak corresponds to the wave foot or the dicrotic notch.

A key insight from Chapter 7 with broader applicability is the methodology for training DNNs on signals characterized by sparsity or sparse features. While the primary application involved high-quality skin acceleration signals acquired via LDV, the principles outlined are transferable to other biomedical domains that involve irregular or spurious signal characteristics – such as SCG, PPG or non-cardiac signals e.g. electrooculography (eye blinks) or respiratory monitoring. Another generalizable contribution is the use of simplified proxy targets to facilitate model training. This strategy can enhance generalization performance, particularly in scenarios constrained by limited dataset sizes, a common challenge in many medical signal processing applications.

8.4 Alternative tools for arterial pulse detection

This dissertation has primarily concentrated on the application of LDV for arterial pulse detection and vascular stiffness assessment. However, alternative methodologies have been proposed within the literature for a straightforward detection of the arterial pulse at a relevant measuring site for addressing similar physiological measurements.

An initial alternative to LDV is photoplethysmography (PPG), a widely adopted technique in clinical practice due to its rapid acquisition and operational simplicity [252]. PPG works by shining an infrared or green light into the skin and measuring the amount of light either absorbed or reflected by blood vessels with a photodetector. As blood volume changes with each heartbeat, the light absorption fluctuates, allowing the device to detect pulse waves and derive cardiovascular metrics like heart rate, PTT or pulse arrival time [218, 225, 241, 252, 253]. PPG has demonstrated efficacy in pulse detection across various anatomical sites, including finger, wrist and earlobe, and across various different wearables [253].

A notable commercially available example is the pOpmètre device, which simultaneously acquires PPG signals from the finger and toe to estimate PTT, employing a methodology analogous to that described in preceding chapters [254, 255]. This approach yields PWV measurements that correlate strongly with those obtained via arterial tonometry (e.g. SphygmoCor) [256], particularly when the foot of the PPG waveform is used for timing reference [257]. However, PPG is not without limitations. It is susceptible to non-stationary noise such as motion artifacts, exhibits reduced reliability in mobile or ambulatory settings due to inconsistent sensor-skin contact, and lacks standardized metrics for signal quality assessment [252]. pOpmètre results can be challenging to interpret physiologically because it aims to measure aortic pulse wave velocity from measurements along two distinct peripheral arterial pathways – from the heart to the finger, and from the heart over the aorta to the toe – rather than along a single central arterial segment. As such, the pOpmètre device amplifies the problem that also exists for carotid-femoral PWV, with pulse waves travelling along two partially parallel pathways rather than a single one.

Seismocardiography (SCG), which involves placing accelerometers on the sternum, yields mechanical cardiac signals that are comparable in morphology and timing to those obtained via LDV [225, 227, 258]. Recent advancements in sensor technology and the integration of artificial intelligence-based signal processing algorithms have contributed to a resurgence of interest in SCG as a viable tool for non-invasive cardiac monitoring [258]. Still, SCG is a technically elegant but clinically immature modality. It holds promise for enhancing cardiac diagnostics, especially in wearable health tech, but its clinical utility is currently constrained by signal variability, lack of standardization, and limited interpretability. For SCG to become mainstream, it needs robust validation, automated interpretation tools, and integration with multimodal data (e.g., ECG, PPG) – as our LDV technology.

Building upon the arterial tonometry techniques outlined in Section 2.2.1, recent research efforts have explored the development of multi-sensor, cuffless, and wearable tonometry systems [259, 260]. These devices, characterized by their flexible and mobile form factors, offer promising potential for continuous and unobtrusive monitoring. However, current implementations are primarily oriented toward blood pressure estimation. While local PWV can be derived from these systems, it is typically integrated into the device's signal processing framework as an intermediate parameter to enhance the accuracy of blood pressure measurements [260]. Conventional PWV assessment using two measurement sites is not currently integrated into the functional capabilities of these devices.

An emerging approach for assessing and monitoring vascular health involves the use of ultrasound patch technology [261–263]. Unlike tonometry or LDV, which acquire signals at the skin surface, these devices operate directly at the level of the blood vessel or cardiac tissue, enabling more direct and potentially accurate physiological measurements. In patch format, this modality supports long-term, motion-resilient monitoring of localized arterial or cardiac parameters. Compared to conventional ultrasound systems, these patches are significantly less operator-dependent and more compact, although their application and upkeep still demand a certain degree of technical proficiency. Ultrasound-based measurements may also yield signals that are more readily interpretable than those obtained via LDV, owing to their higher signal-to-noise ratio and the direct visualization of anatomical structures. A notable limitation remains the cost, driven by the need for compact, high-capacity batteries and integrated computational resources, which currently constrains their scalability and widespread clinical adoption.

To further illustrate the diversity of pulse detection technologies, the Withings smart scale is among the few consumer-grade devices that incorporates a (aortic-leg) PWV measurement into its functionality [264, 265]. The device estimates PWV by combining ballistocardiography, detecting micro-variations in body weight caused by left ventricular ejection, with impedance plethysmography at the feet to assess peripheral blood volume changes. While its agreement with reference systems such as SphygmoCor is generally favorable, comparisons with other methodologies can be challenging due to the upright posture required during measurement, which contrasts with the supine position typically used in clinical assessments.

Looking ahead, integrating LDV with complementary technologies may offer promising avenues for enhancing cardiovascular assessment. The current LDV configuration relies on two prototype handpieces, which

inherently doubles the potential for hardware-related error due to the early-stage nature of the system. A more streamlined approach could involve a single, optimized LDV handpiece positioned at the carotid artery, used in conjunction with a PCG device – such as a digital stethoscope – to estimate heart-carotid PTT. Additional hybrid configurations, such as combining LDV at the thorax with tonometry or ultrasound at the carotid site, may also yield accurate PTT measurements. Furthermore, alternative PWV pathways, including heart-to-finger or heart-to-toe, could become feasible through integrated LDV-PPG systems. These hypotheses warrant further investigation to validate the role of LDV as a supportive component in multimodal cardiovascular monitoring frameworks.

8.5 THE INSIDE-ALPHA DEVICE

In February 2025, a first new LDV prototype resulting from the InSiDe project became available. Although its use is currently restricted to research purposes within a laboratory setting, and clinical investigations are not yet permitted, the device has been distributed across the consortium in several iterations. Figure 8.1 depicts this device being used on the author.

The primary advantages of this new device are as follows: (i) It features a more compact and lightweight design, reducing the number of laser channels to four, thereby enabling four simultaneous beams to illuminate the target. (ii) The device operates effectively on bare skin, achieved by modifying the laser wavelength and incorporating an adjustable set of lenses to focus the beams, although automatic autofocusing has not yet been implemented. (iii) The device includes a wireless connection to the processing unit (laptop), although the power connection still requires wiring. (iv) The laptop is equipped with software that allows operators to observe the measured signals in (pseudo) real-time. These signals are accompanied by quality indicators, aiding the operator in making necessary manual adjustments.

Despite the numerous challenges, resulting delays, and design compromises, the *existence* of the InSiDe-alpha device is a testament to the substantial efforts made to advance clinical LDV aspirations. While the device is not yet perfect, its functionality validates the potential for further research and development of an LDV-based solution for accessible arterial stiffness assessment (among others). The future of this technology depends on the positive interpretation of the provided scientific evidence and financial support of those willing to invest in its continued development.

8.6 FINAL THOUGHTS

The potential of laser Doppler vibrometry for medical applications is evident, not only from the findings presented in this dissertation but also from

Figure 8.1: The InSiDe-alpha device in action while performing a measurement at the base of the heart of the author (March 5, 2025). Luckily for him, as can be seen from the sparse signals on the associated laptop, he seems to still be alive.

numerous previous studies [18–23, 26, 230]. This potential justified a dedicated set of efforts, spanning two distinct EU-funded projects. Despite the substantial progress made, it must be acknowledged that laser Doppler vibrometry technology is not yet mature enough for clinical implementations. Over eight years of resource investment have resulted in a device that meets many of the valid requirements of clinical personnel, yet it still falls short in some areas. To name a few: the device still requires a wired connection to a power supply, the 'autofocus' optical system has not yet been implemented to operate automatically and requires manual setting, and the device has not been tested to operate with two handpieces measuring simultaneously. This suggests that the envisioned laser Doppler vibrometry application may not be fully achievable at this stage. The transition from a prototype clinical investigational device to a marketable, licensed medical device is a lengthy process, and persistent signal-quality issues temper a more optimistic outlook.

Nevertheless, the work presented in this dissertation is meaningful. Quality metrics based on established similarity-search algorithms remain relevant beyond carotid-femoral laser Doppler vibrometry measurements. Beamforming and beamforming-derived independent component analysis can enhance multi-sensor array medical signals with similar spatial multi-dimensionality intentions, as demonstrated by the CARDIS device. This approach increases the likelihood of obtaining at least one sensor/channel with a sufficiently high signal-to-noise ratio for further processing.

Furthermore, the investigation of heart-carotid pathlength for arterial stiffness assessment is of significant importance to the field, even if the outcome does not indicate that non-invasive assessment of heart-carotid pulse wave velocity assessed from LDV shows great promise. References to heart-carotid pulse wave velocity in the literature are typically as one of several metrics measured by a single device for broader clinical studies [225, 232, 233, 235]. The research validating the functionality of heart-carotid pulse wave velocity in these devices remains protected and copyrighted.

Finally, the deep neural network method demonstrates promise and utility beyond the application of automated heart-carotid pulse transit time calculation. Predicting heartbeat onset timing can be highly valuable without relying on carotid laser Doppler vibrometry data. The general principles discussed can be extended beyond the specific purpose of handheld, laser Doppler vibrometry based technology. Therefore, while we remain hopeful for the future of laser Doppler vibrometry, the CARDIS and InSiDe devices, the added value of the research presented herein does not solely depend on the clinical aspirations of laser Doppler vibrometry technology.

V

Appendices

CHAPTERS

A Appendix **189**

APPENDIX

PROJECT SCOPE AND ETHICAL CONSIDERATIONS

All work done in this article, was performed within the scope of the H2020-project: InSiDe (Grant agreement ID: 871547).

The author's have confirmed that any identifiable participants in this study have given their consent for publication.

The InSide study was approved by the National Ethics Committee and the French National Drug Agency on 28.11.2022, Clinicaltrial.gov number: NCT05711693.

The CARDIS study was approved by the National Ethics Committee and the French National Drug Agency on 26.02.2018, Clinicaltrial.gov number: NCT03446430.

ACKNOWLEDGEMENTS

BIBLIOGRAPHY

[1] C. Cawley and J. W. McEvoy, 'European guidelines for risk assessment in the primary prevention of cardiovascular disease', in *Contemporary Cardiology*, Cham: Springer International Publishing, 2022, pp. 35–58.

[2] J. W. McEvoy et al., '2024 ESC guidelines for the management of elevated blood pressure and hypertension', en, *Eur. Heart J.*, vol. 45, no. 38, pp. 3912–4018, 2024.

[3] C. W. Tsao et al., 'Heart disease and stroke statistics-2023 update: A report from the american heart association', en, *Circulation*, vol. 147, no. 8, e93–e621, 2023.

[4] D. S. Kazi et al., 'Forecasting the economic burden of cardiovascular disease and stroke in the united states through 2050: A presidential advisory from the american heart association', en, *Circulation*, vol. 150, no. 4, e89–e101, 2024.

[5] SCORE2 working group and ESC Cardiovascular risk collaboration, 'SCORE2 risk prediction algorithms: New models to estimate 10-year risk of cardiovascular disease in europe', en, *Eur. Heart J.*, vol. 42, no. 25, pp. 2439–2454, 2021.

[6] SCORE2-OP working group and ESC Cardiovascular risk collaboration, 'SCORE2-OP risk prediction algorithms: Estimating incident cardiovascular event risk in older persons in four geographical risk regions', en, *Eur. Heart J.*, vol. 42, no. 25, pp. 2455–2467, 2021.

[7] J. A. Chirinos, P. Segers, T. Hughes and R. Townsend, 'Large-artery stiffness in health and disease: Jacc state-of-the-art review', *Journal of the American College of Cardiology*, vol. 74, no. 9, pp. 1237–1263, 2019.

[8] S. Laurent et al., 'Expert consensus document on arterial stiffness: Methodological issues and clinical applications', *European heart journal*, vol. 27, no. 21, pp. 2588–2605, 2006.

[9] G. F. Mitchell et al., 'Changes in arterial stiffness and wave reflection with advancing age in healthy men and women: The Framingham Heart Study', *Hypertension*, vol. 43, no. 6, pp. 1239–1245, 2004.

[10] G. F. Mitchell et al., 'Arterial stiffness and cardiovascular events: The framingham heart study', en, *Circulation*, vol. 121, no. 4, pp. 505–511, 2010.

[11] P. Segers, E. R. Rietzschel and J. A. Chirinos, 'How to measure arterial stiffness in humans', *Arteriosclerosis, thrombosis, and vascular biology*, vol. 40, no. 5, pp. 1034–1043, 2020.

[12] D.-W. An et al., 'Derivation of an outcome-driven threshold for aortic pulse wave velocity: An individual-participant meta-analysis', en, *Hypertension*, vol. 80, no. 9, pp. 1949–1959, 2023.

[13] K. Stone et al., 'Reimagining the value of brachial-ankle pulse wave velocity as a biomarker of cardiovascular disease risk-a call to action on behalf of VascAgeNet', en, *Hypertension*, vol. 80, no. 10, pp. 1980–1992, 2023.

[14] T. Ohkuma et al., 'Brachial-ankle pulse wave velocity and the risk prediction of cardiovascular disease: An individual participant data meta-analysis', en, *Hypertension*, vol. 69, no. 6, pp. 1045–1052, 2017.

[15] A. Redheuil et al., 'Reduced ascending aortic strain and distensibility: Earliest manifestations of vascular aging in humans', en, *Hypertension*, vol. 55, no. 2, pp. 319–326, 2010.

[16] M. Couade et al., 'Quantitative assessment of arterial wall biomechanical properties using shear wave imaging', en, *Ultrasound Med. Biol.*, vol. 36, no. 10, pp. 1662–1676, 2010.

[17] M. Butlin and A. Qasem, 'Large artery stiffness assessment using SphygmoCor technology', en, *Pulse (Basel)*, vol. 4, no. 4, pp. 180–192, 2017.

[18] Y. Li, P. Segers, J. Dirckx and R. Baets, 'On-chip laser doppler vibrometer for arterial pulse wave velocity measurement', *Biomedical optics express*, vol. 4, no. 7, pp. 1229–1235, 2013.

[19] Y. Li et al., 'Silicon photonics-based laser doppler vibrometer array for carotid-femoral pulse wave velocity (pwv) measurement', *Biomedical Optics Express*, vol. 11, no. 7, pp. 3913–3926, 2020.

[20] A. Campo and J. Dirckx, 'Dual-beam laser doppler vibrometer for measurement of pulse wave velocity in elastic vessels', in *22nd Congress of the International Commission for Optics: Light for the Development of the World, Puebla, Mexico*, International Society for Optics and Photonics, vol. 8011, 2011, 80118Y.

[21] A. D. Kaplan, J. A. OrSullivan, E. J. Sirevaag, P.-H. Lai and J. W. Rohrbaugh, 'Hidden state models for noncontact measurements of the carotid pulse using a laser doppler vibrometer', *IEEE Transactions on Biomedical Engineering*, vol. 59, no. 3, pp. 744–753, 2012.

[22] M. De Melis et al., 'A noncontact approach for the evaluation of large artery stiffness: A preliminary study', *American journal of hypertension*, vol. 21, no. 12, pp. 1280–1283, 2008.

[23] S. Badhwar et al., 'Clinical validation of carotid-femoral pulse wave velocity measurement using a multi-beam laser vibrometer: The CARDIS study', en, *Hypertension*, vol. 81, no. 9, pp. 1986–1995, 2024.

[24] Y. Li et al., 'Six-beam homodyne laser doppler vibrometry based on silicon photonics technology', *Opt. Express*, vol. 26, no. 3, pp. 3638–3645, 2018.

[25] L. Marais et al., 'Measurement of aortic stiffness by laser doppler vibrometry: The cardis study', *Journal of Hypertension*, vol. 37, e88, 2019.

[26] Mancini, Viviana and Bergersen, Aslak W. and Valen-Sendstad, Kristian and Segers, Patrick, 'Computed poststenotic flow instabilities correlate phenotypically with vibrations measured using laser Doppler vibrometry : perspectives for a promising in vivo device for early detection of moderate and severe carotid stenosis', eng, *JOURNAL OF BIOMECHANICAL ENGINEERING-TRANSACTIONS OF THE ASME*, vol. 142, no. 9, p. 13, 2020.

[27] S. Seoni et al., 'Template matching and matrix profile for signal quality assessment of carotid and femoral laser doppler vibrometer signals', *Frontiers in Physiology*, vol. 12, 2022.

[28] Reference Values for Arterial Stiffness' Collaboration, 'Determinants of pulse wave velocity in healthy people and in the presence of cardiovascular risk factors: 'establishing normal and reference values'', en, *Eur. Heart J.*, vol. 31, no. 19, pp. 2338–2350, 2010.

[29] L. M. Van Bortel et al., 'Expert consensus document on the measurement of aortic stiffness in daily practice using carotid-femoral pulse wave velocity', en, *J. Hypertens.*, vol. 30, no. 3, pp. 445–448, 2012.

[30] N. Stergiopulos, J. J. Meister and N. Westerhof, 'Simple and accurate way for estimating total and segmental arterial compliance: The pulse pressure method', en, *Ann. Biomed. Eng.*, vol. 22, no. 4, pp. 392–397, 1994.

[31] J. A. Chirinos, Ed., 'Textbook of arterial stiffness and pulsatile hemodynamics in health and disease'. San Diego, CA: Academic Press, 2022.

[32] W. W. Nichols, M. O'Rourke, C. Vlachopoulos and E. R. Edelman, 'McDonald's blood flow in arteries'. Boca Raton: CRC Press, 2022.

[33] G. H. ten Velden, G. Elzinga and N. Westerhof, 'Left ventricular energetics. heat loss and temperature distribution of canine myocardium', en, *Circ. Res.*, vol. 50, no. 1, pp. 63–73, 1982.

[34] G. Elzinga and N. Westerhof, 'Matching between ventricle and arterial load. an evolutionary process', en, *Circ. Res.*, vol. 68, no. 6, pp. 1495–1500, 1991.

[35] N. Westerhof, J.-W. Lankhaar and B. E. Westerhof, 'The arterial windkessel', *Medical & biological engineering & computing*, vol. 47, no. 2, pp. 131–141, 2009.

[36] J.-J. Wang, A. B. O'Brien, N. G. Shrive, K. H. Parker and J. V. Tyberg, 'Time-domain representation of ventricular-arterial coupling as a windkessel and wave system', en, *Am. J. Physiol. Heart Circ. Physiol.*, vol. 284, no. 4, H1358–68, 2003.

[37] O. S. Randall, N. Westerhof, G. C. van den Bos and B. Alexander, 'Reliability of stroke volume to pulse pressure ratio for estimating and detecting changes in arterial compliance', *Journal of Hypertension. Supplement : Official Journal of the International Society of Hypertension*, vol. 4, no. 5, S293–S296, 1986.

[38] D. Chemla et al., 'Total arterial compliance estimated by stroke volume-to-aortic pulse pressure ratio in humans', en, *Am. J. Physiol. Heart Circ. Physiol.*, vol. 274, no. 2, H500–H505, 1998.

[39] S. S. Franklin et al., 'Hemodynamic patterns of age-related changes in blood pressure. the framingham heart study', en, *Circulation*, vol. 96, no. 1, pp. 308–315, 1997.

[40] G. de Simone et al., 'Age-related changes in total arterial capacitance from birth to maturity in a normotensive population', en, *Hypertension*, vol. 29, no. 6, pp. 1213–1217, 1997.

[41] D. G. Devos et al., 'Mr pulse wave velocity increases with age faster in the thoracic aorta than in the abdominal aorta', *Journal of Magnetic Resonance Imaging*, vol. 41, pp. 765–772, 3 2015.

[42] R. M. Bruno et al., 'Early and supernormal vascular aging: Clinical characteristics and association with incident cardiovascular events', en, *Hypertension*, vol. 76, no. 5, pp. 1616–1624, 2020.

[43] A. Benetos et al., 'Pulse pressure: A predictor of long-term cardiovascular mortality in a french male population', en, *Hypertension*, vol. 30, no. 6, pp. 1410–1415, 1997.

[44] D. Meier, S. Maier and P. Bösiger, 'Quantitative flow measurements on phantoms and on blood vessels with MR', en, *Magn. Reson. Med.*, vol. 8, no. 1, pp. 25–34, 1988.

[45] V. Bikia et al., 'Noninvasive cardiac output and central systolic pressure from cuff-pressure and pulse wave velocity', en, *IEEE J. Biomed. Health Inform.*, vol. 24, no. 7, pp. 1968–1981, 2020.

[46] J. D. MacDougall, D. Tuxen, D. G. Sale, J. R. Moroz and J. R. Sutton, 'Arterial blood pressure response to heavy resistance exercise', en, *J. Appl. Physiol.*, vol. 58, no. 3, pp. 785–790, 1985.

[47] M. L. R. Harkness, R. D. Harkness and D. A. McDonald, 'The collagen and elastin content of the arterial wall in the dog', en, *Proc. Biol. Sci.*, vol. 146, no. 925, pp. 541–551, 1957.

[48] A. Avolio, D. Jones and M. Tafazzoli-Shadpour, 'Quantification of alterations in structure and function of elastin in the arterial media', en, *Hypertension*, vol. 32, no. 1, pp. 170–175, 1998.

[49] H. Wolinsky and S. Glagov, 'A lamellar unit of aortic medial structure and function in mammals', *Circulation research*, vol. 20, no. 1, pp. 99–111, 1967.

[50] S. E. Greenwald, 'Ageing of the conduit arteries', en, *J. Pathol.*, vol. 211, no. 2, pp. 157–172, 2007.

[51] D. H. Bergel, 'The dynamic elastic properties of the arterial wall', en, *J. Physiol.*, vol. 156, no. 3, pp. 458–469, 1961.

[52] M. R. Roach and A. C. Burton, 'The reason for the shape of the distensibility curves of arteries', en, *Can. J. Biochem. Physiol.*, vol. 35, no. 8, pp. 681–690, 1957.

[53] A. C. Burton, 'Relation of structure to function of the tissues of the wall of blood vessels', en, *Physiol. Rev.*, vol. 34, no. 4, pp. 619–642, 1954.

[54] E. Hermeling et al., 'The change in arterial stiffness over the cardiac cycle rather than diastolic stiffness is independently associated with left ventricular mass index in healthy middle-aged individuals', en, *J. Hypertens.*, vol. 30, no. 2, pp. 396–402, 2012.

[55] J. A. G. Rhodin, 'Architecture of the vessel wall', in *Comprehensive Physiology*. Hoboken, NJ, USA: John Wiley & Sons, Inc., 1980, pp. 1–31.

[56] A. S. Greene, P. J. Tonellato, J. Lui, J. H. Lombard and A. W. Cowley Jr, 'Microvascular rarefaction and tissue vascular resistance in hypertension', en, *Am. J. Physiol. Heart Circ. Physiol.*, vol. 256, no. 1, H126–H131, 1989.

[57] P. Lacolley, V. Regnault, P. Segers and S. Laurent, 'Vascular smooth muscle cells and arterial stiffening: Relevance in development, aging, and disease', en, *Physiol. Rev.*, vol. 97, no. 4, pp. 1555–1617, 2017.

[58] H. W. Weizsacker and J. G. Pinto, 'Isotropy and anisotropy of the arterial wall', en, *J. Biomech.*, vol. 21, no. 6, pp. 477–487, 1988.

[59] D. Valdez-Jasso et al., 'Analysis of viscoelastic wall properties in ovine arteries', en, *IEEE Trans. Biomed. Eng.*, vol. 56, no. 2, pp. 210–219, 2009.

[60] G. A. Holzapfel and H. W. Weizsäcker, 'Biomechanical behavior of the arterial wall and its numerical characterization', en, *Comput. Biol. Med.*, vol. 28, no. 4, pp. 377–392, 1998.

[61] G. J. Langewouters, K. H. Wesseling and W. J. Goedhard, 'The static elastic properties of 45 human thoracic and 20 abdominal aortas in vitro and the parameters of a new model', en, *J. Biomech.*, vol. 17, no. 6, pp. 425–435, 1984.

[62] P. Segers et al., 'Functional analysis of the common carotid artery', en, *J. Hypertens.*, vol. 22, no. 5, pp. 973–981, 2004.

[63] J. C. Bramwell and A. V. Hill, 'The velocity of pulse wave in man', *Proceedings of the Royal Society of London. Series B, Containing Papers of a Biological Character*, vol. 93, no. 652, pp. 298–306, 1922.

[64] O. Frank, 'Die elastizitat der blutegefasse', en, *Zeitschrift für Biologie.*, vol. 71, pp. 255–272, 1920.

[65] A. Moens, Ed., 'Die Pulskurve'. Leiden, The Netherlands: E.J. Brill, 1878.

[66] D. J. Korteweg, 'Ueber die fortpflanzungsgeschwindigkeit des schalles in elastischen röhren', en, *Ann. Phys.*, vol. 241, no. 12, pp. 525–542, 1878.

[67] D. Bergel, 'The properties of blood vessels', en, *Biomechanics, its Foundations and Objectives*, pp. 105–139, 1972.

[68] T. Mirault et al., 'Carotid stiffness change over the cardiac cycle by ultrafast ultrasound imaging in healthy volunteers and vascular Ehlers-Danlos syndrome', en, *J. Hypertens.*, vol. 33, no. 9, 1890–6, discussion 1896, 2015.

[69] B. Spronck et al., 'Pressure-dependence of arterial stiffness', en, *J. Hypertens.*, vol. 33, no. 2, pp. 330–338, 2015.

[70] P. Segers, J. Mynard, L. Taelman, S. VERMEERSCH and A. Swillens, 'Wave reflection: Myth or reality?', eng, *ARTERY RESEARCH*, vol. 6, no. 1, pp. 7–11, 2012.

[71] S. Laurent et al., 'Protocol of the SPARTE study: A strategy for preventing cardiovascular and renal events based on ARTErial stiffness', en, *Artery Res.*, vol. 26, no. 4, pp. 250–260, 2020.

[72] C. M. McEniery et al., 'Normal vascular aging: Differential effects on wave reflection and aortic pulse wave velocity: The Anglo-Cardiff collaborative trial (ACCT)', en, *J. Am. Coll. Cardiol.*, vol. 46, no. 9, pp. 1753–1760, 2005.

[73] B. Spronck and J. D. Humphrey, 'Arterial stiffness: Different metrics, different meanings', en, *J. Biomech. Eng.*, vol. 141, no. 9, p. 091 004, 2019.

[74] S. Laurent et al., 'Aortic stiffness is an independent predictor of all-cause and cardiovascular mortality in hypertensive patients', en, *Hypertension*, vol. 37, no. 5, pp. 1236–1241, 2001.

[75] C. Vlachopoulos, K. Aznaouridis and C. Stefanadis, 'Prediction of cardiovascular events and all-cause mortality with arterial stiffness: A systematic review and meta-analysis', *Journal of the American College of Cardiology*, vol. 55, no. 13, pp. 1318–1327, 2010.

[76] F. Cuomo, S. Roccabianca, D. Dillon-Murphy, N. Xiao, J. D. Humphrey and C. A. Figueroa, 'Effects of age-associated regional changes in aortic stiffness on human hemodynamics revealed by computational modeling', en, *PLoS One*, vol. 12, no. 3, e0173177, 2017.

[77] T. L. Zhou, R. M. A. Henry, C. D. A. Stehouwer, T. T. van Sloten, K. D. Reesink and A. A. Kroon, 'Blood pressure variability, arterial stiffness, and arterial remodeling', en, *Hypertension*, vol. 72, no. 4, pp. 1002–1010, 2018.

[78] B. J. van Varik, R. J. M. W. Rennenberg, C. P. Reutelingsperger, A. A. Kroon, P. W. de Leeuw and L. J. Schurgers, 'Mechanisms of arterial remodeling: Lessons from genetic diseases', en, *Front. Genet.*, vol. 3, p. 290, 2012.

[79] A. J. Cocciolone, J. Z. Hawes, M. C. Staiculescu, E. O. Johnson, M. Murshed and J. E. Wagenseil, 'Elastin, arterial mechanics, and cardiovascular disease', *REVIEW Extracellular Matrix in Cardiovascular Pathophysiology Am J Physiol Heart Circ Physiol*, vol. 315, pp. 189–205, 2018.

[80] J. D. Humphrey, 'Vascular adaptation and mechanical homeostasis at tissue, cellular, and sub-cellular levels', en, *Cell Biochem. Biophys.*, vol. 50, no. 2, pp. 53–78, 2008.

[81] D. Ambrosi et al., 'Growth and remodelling of living tissues: Perspectives, challenges and opportunities', *Journal of the Royal Society Interface*, vol. 16, 157 2019.

[82] C. Cavinato, S. I. Murtada, A. Rojas and J. D. Humphrey, 'Evolving structure-function relations during aortic maturation and aging revealed by multiphoton microscopy', *Mechanisms of Ageing and Development*, vol. 196, 2021.

[83] S. M. Arribas, A. Hinek and M. C. González, 'Elastic fibres and vascular structure in hypertension', en, *Pharmacol. Ther.*, vol. 111, no. 3, pp. 771–791, 2006.

[84] M. J. Sherratt, 'Tissue elasticity and the ageing elastic fibre', en, *Age (Dordr.)*, vol. 31, no. 4, pp. 305–325, 2009.

[85] L. Horny, T. Adamek and R. Zitny, 'Age-related changes in longitudinal prestress in human abdominal aorta', en, *Arch. Appl. Mech.*, vol. 83, no. 6, pp. 875–888, 2013.

[86] B. M. Kaess et al., 'Aortic stiffness, blood pressure progression, and incident hypertension', en, *JAMA*, vol. 308, no. 9, pp. 875–881, 2012.

[87] A. P. Avolio et al., 'Role of pulse pressure amplification in arterial hypertension: Experts' opinion and review of the data', en, *Hypertension*, vol. 54, no. 2, pp. 375–383, 2009.

[88] J. A. Chirinos and P. Segers, 'Noninvasive evaluation of left ventricular afterload: Part 2: Arterial pressure-flow and pressure-volume relations in humans', en, *Hypertension*, vol. 56, no. 4, pp. 563–570, 2010.

[89] J. I. E. Hoffman and G. D. Buckberg, 'The myocardial oxygen supply:demand index revisited', en, *J. Am. Heart Assoc.*, vol. 3, no. 1, e000285, 2014.

[90] T. Coutinho, L. M. Mielniczuk, K. Srivaratharajah, R. deKemp, G. A. Wells and R. S. Beanlands, 'Coronary artery microvascular dysfunction: Role of sex and arterial load', *Int. J. Cardiol.*, 2018.

[91] T. Weber and J. A. Chirinos, 'Pulsatile arterial haemodynamics in heart failure', en, *Eur. Heart J.*, vol. 39, no. 43, pp. 3847–3854, 2018.

[92] J. A. Chirinos, 'Deep phenotyping of systemic arterial hemodynamics in HFpEF (part 2): Clinical and therapeutic considerations', en, *J. Cardiovasc. Transl. Res.*, vol. 10, no. 3, pp. 261–274, 2017.

[93] J. A. Chirinos et al., 'Arterial properties as determinants of time-varying myocardial stress in humans', en, *Hypertension*, vol. 60, no. 1, pp. 64–70, 2012.

[94] M. F. O'Rourke and T. Yaginuma, 'Wave reflections and the arterial pulse', *Hypertension*, vol. 6, no. 5, pp. 571–577, 1984.

[95] W. F. Hamilton, 'The patterns of the arterial pressure pulse', *American Journal of Physiology*, vol. 141, no. 2, pp. 289–297, 1944.

[96] J. A. Chirinos et al., 'Arterial stiffness, central pressures, and incident hospitalized heart failure in the chronic renal insufficiency cohort study', en, *Circ. Heart Fail.*, vol. 7, no. 5, pp. 709–716, 2014.

[97] S. Kobayashi et al., 'Influence of aortic impedance on the development of pressure-overload left ventricular hypertrophy in rats', en, *Circulation*, vol. 94, no. 12, pp. 3362–3368, 1996.

[98] T. C. Gillebert and W. Y. Lew, 'Influence of systolic pressure profile on rate of left ventricular pressure fall', en, *Am. J. Physiol. Heart Circ. Physiol.*, vol. 261, no. 3, H805–H813, 1991.

[99] P. Zamani et al., 'Resistive and pulsatile arterial load as predictors of left ventricular mass and geometry: The multi-ethnic study of atherosclerosis', en, *Hypertension*, vol. 65, no. 1, pp. 85–92, 2015.

[100] J. Hashimoto, B. E. Westerhof, N. Westerhof, Y. Imai and M. F. O'Rourke, 'Different role of wave reflection magnitude and timing on left ventricular mass reduction during antihypertensive treatment', en, *J. Hypertens.*, vol. 26, no. 5, pp. 1017–1024, 2008.

[101] M. F. O'Rourke and M. E. Safar, 'Relationship between aortic stiffening and microvascular disease in brain and kidney: Cause and logic of therapy', en, *Hypertension*, vol. 46, no. 1, pp. 200–204, 2005.

[102] J. Hashimoto and S. Ito, 'Central pulse pressure and aortic stiffness determine renal hemodynamics: Pathophysiological implication for microalbuminuria in hypertension', en, *Hypertension*, vol. 58, no. 5, pp. 839–846, 2011.

[103] R. R. Townsend et al., 'Aortic PWV in chronic kidney disease: A CRIC ancillary study', en, *Am. J. Hypertens.*, vol. 23, no. 3, pp. 282–289, 2010.

[104] M. L. Meyer et al., 'Association of central arterial stiffness and pressure pulsatility with mild cognitive impairment and dementia: The atherosclerosis risk in communities Study-Neurocognitive study (ARIC-NCS)', en, *J. Alzheimers. Dis.*, vol. 57, no. 1, pp. 195–204, 2017.

[105] M. P. Pase et al., 'Aortic stiffness and the risk of incident mild cognitive impairment and dementia', en, *Stroke*, vol. 47, no. 9, pp. 2256–2261, 2016.

[106] A. Sehgal, B. J. Allison, F. Crispi and S. Menahem, 'Influence of accelerated arterial aging in growth-restricted cohorts on adult-onset cardiovascular diseases', en, *Am. J. Physiol. Heart Circ. Physiol.*, vol. 325, no. 1, H89–H105, 2023.

[107] J. D. Humphrey, D. G. Harrison, C. A. Figueroa, P. Lacolley and S. Laurent, 'Central artery stiffness in hypertension and aging: A problem with cause and consequence', en, *Circ. Res.*, vol. 118, no. 3, pp. 379–381, 2016.

[108] R. A. Payne, I. B. Wilkinson and D. J. Webb, 'Arterial stiffness and hypertension: Emerging concepts', en, *Hypertension*, vol. 55, no. 1, pp. 9–14, 2010.

[109] Y. Ben-Shlomo et al., 'Aortic pulse wave velocity improves cardiovascular event prediction', en, *J. Am. Coll. Cardiol.*, vol. 63, no. 7, pp. 636–646, 2014.

[110] A. Pandey et al., 'Arterial stiffness and risk of overall heart failure, heart failure with preserved ejection fraction, and heart failure with reduced ejection fraction: The health ABC study (health, aging, and body composition)', en, *Hypertension*, vol. 69, no. 2, pp. 267–274, 2017.

[111] C. W. Tsao et al., 'Relation of central arterial stiffness to incident heart failure in the community', en, *J. Am. Heart Assoc.*, vol. 4, no. 11, 2015.

[112] R. V. for Arterial Stiffness' Collaboration, 'Determinants of pulse wave velocity in healthy people and in the presence of cardiovascular risk factors:'establishing normal and reference values'', *European heart journal*, vol. 31, no. 19, pp. 2338–2350, 2010.

[113] A. Milan et al., 'Current assessment of pulse wave velocity', en, *J. Hypertens.*, vol. 37, no. 8, pp. 1547–1557, 2019.

[114] J. E. Sharman et al., 'Validation of a generalized transfer function to noninvasively derive central blood pressure during exercise', en, *Hypertension*, vol. 47, no. 6, pp. 1203–1208, 2006.

[115] R. Kelly, C. Hayward, A. Avolio and M. O'Rourke, 'Noninvasive determination of age-related changes in the human arterial pulse', en, *Circulation*, vol. 80, no. 6, pp. 1652–1659, 1989.

[116] P. Salvi, G. Lio, C. Labat, E. Ricci, B. Pannier and A. Benetos, 'Validation of a new non-invasive portable tonometer for determining arterial pressure wave and pulse wave velocity', en, *J. Hypertens.*, vol. 22, no. 12, pp. 2285–2293, 2004.

[117] C. H. Chen et al., 'Estimation of central aortic pressure waveform by mathematical transformation of radial tonometry pressure. validation of generalized transfer function', en, *Circulation*, vol. 95, no. 7, pp. 1827–1836, 1997.

[118] M. Karamanoglu, M. F. O'Rourke, A. P. Avolio and R. P. Kelly, 'An analysis of the relationship between central aortic and peripheral upper limb pressure waves in man', en, *Eur. Heart J.*, vol. 14, no. 2, pp. 160–167, 1993.

[119] I. B. Wilkinson et al., 'Reproducibility of pulse wave velocity and augmentation index measured by pulse wave analysis', en, *J. Hypertens.*, vol. 16, no. Supplement, pp. 2079–2084, 1998.

[120] P. D. Gatehouse et al., 'Applications of phase-contrast flow and velocity imaging in cardiovascular MRI', en, *Eur. Radiol.*, vol. 15, no. 10, pp. 2172–2184, 2005.

[121] J. A. Chirinos and P. Segers, 'Noninvasive evaluation of left ventricular afterload: Part 1: Pressure and flow measurements and basic principles of wave conduction and reflection', en, *Hypertension*, vol. 56, no. 4, pp. 555–562, 2010.

[122] P. D. Gatehouse et al., 'Flow measurement by cardiovascular magnetic resonance: A multi-centre multi-vendor study of background phase offset errors that can compromise the accuracy of derived regurgitant or shunt flow measurements', en, *J. Cardiovasc. Magn. Reson.*, vol. 12, no. 1, p. 5, 2010.

[123] M. Z. Bensalah et al., 'Geometry is a major determinant of flow reversal in proximal aorta', en, *Am. J. Physiol. Heart Circ. Physiol.*, vol. 306, no. 10, H1408–16, 2014.

[124] A. Dogui et al., 'Consistency of aortic distensibility and pulse wave velocity estimates with respect to the Bramwell-Hill theoretical model: A cardiovascular magnetic resonance study', en, *J. Cardiovasc. Magn. Reson.*, vol. 13, no. 1, p. 11, 2011.

[125] P. Ou et al., 'Increased central aortic stiffness and left ventricular mass in normotensive young subjects after successful coarctation repair', en, *Am. Heart J.*, vol. 155, no. 1, pp. 187–193, 2008.

[126] P. Ou et al., 'Angular (gothic) aortic arch leads to enhanced systolic wave reflection, central aortic stiffness, and increased left ventricular mass late after aortic coarctation repair: Evaluation with magnetic resonance flow mapping', en, *J. Thorac. Cardiovasc. Surg.*, vol. 135, no. 1, pp. 62–68, 2008.

[127] W. Y. Kim et al., 'Subclinical coronary and aortic atherosclerosis detected by magnetic resonance imaging in type 1 diabetes with and without diabetic nephropathy', en, *Circulation*, vol. 115, no. 2, pp. 228–235, 2007.

[128] S. G. C. van Elderen et al., 'Aortic stiffness is associated with cardiac function and cerebral small vessel disease in patients with type 1 diabetes mellitus: Assessment by magnetic resonance imaging', en, *Eur. Radiol.*, vol. 20, no. 5, pp. 1132–1138, 2010.

[129] A. Brandts et al., 'The effect of hypertension on aortic pulse wave velocity in type-1 diabetes mellitus patients: Assessment with MRI', en, *Int. J. Cardiovasc. Imaging*, vol. 28, no. 3, pp. 543–550, 2012.

[130] Y. Amraoui and N. A. J. Lieven, 'Laser vibrometry based detections of delaminations in aerospace composites', in *Proceedings of the 23rd Congress of the International Council of the Aeronautical Sciences (ICAS)*, Paper ICAS 2002-8.3.5, Toronto, Canada, 2002.

[131] B. J. Halkon, 'An international review of laser doppler vibrometry: Making light work of vibration measurement', *Optics and Lasers in Engineering*, vol. 99, pp. 11–22, 2017.

[132] M. Duperron et al., 'Hybrid integration of laser source on silicon photonic integrated circuit for low-cost interferometry medical device', in *Optical Interconnects XVII*, H. Schröder and R. T. Chen, Eds., San Francisco, California, United States: SPIE, 2017.

[133] G. R. Naik and W. P. d. Santos, 'Biomedical signal processing', en. Boca Raton: CRC Press, 2023.

[134] R. B. Northrop, 'Signals and Systems Analysis In Biomedical Engineering, Second Edition' (Biomedical Engineering), 2nd ed. Boca Raton, FL: CRC Press, 2010.

[135] V. Bajaj, G. R. Sinha and C. Chakraborty, Eds., 'Biomedical signal processing for healthcare applications', en. London, England: CRC Press, 2021.

[136] H. Nyquist, 'Certain topics in telegraph transmission theory', *Transactions of the American Institute of Electrical Engineers*, vol. 47, no. 2, pp. 617–644, 1928.

[137] N. M. Saad, A. R. Abdullah and Y. F. Low, 'Detection of heart blocks in ECG signals by spectrum and time-frequency analysis', in *2006 4th Student Conference on Research and Development*, Shah Alam, Malaysia: IEEE, 2006.

[138] A. Mueen, E. Keogh, Q. Zhu, S. Cash and B. Westover, 'Exact discovery of time series motifs', *Society for Industrial and Applied Mathematics - 9th SIAM International Conference on Data Mining 2009, Proceedings in Applied Mathematics*, vol. 1, pp. 469–480, 2009.

[139] Y. Zhu et al., 'Matrix profile II: Exploiting a novel algorithm and GPUs to break the one hundred million barrier for time series motifs and joins', *Proceedings - IEEE International Conference on Data Mining, ICDM*, pp. 739–748, 2017.

[140] Y. Zhu, M. Imamura, D. Nikovski and E. Keogh, 'Matrix Profile VII: Time Series Chains: A New Primitive for Time Series Data Mining', *Ieee Icdm*, 2017.

[141] C.-C. M. Yeh et al., 'Time series joins, motifs, discords and shapelets: a unifying view that exploits the matrix profile', *Data Mining and Knowledge Discovery*, vol. 32, no. 1, pp. 83–123, 2018.

[142] Y. Zhu et al., 'The Swiss army knife of time series data mining: ten useful things you can do with the matrix profile and ten lines of code', *Data Mining and Knowledge Discovery*, vol. 34, no. 4, pp. 949–979, 2020.

[143] F. Madrid, S. Imani, R. Mercer, Z. Zimmerman, N. Shakibay and E. Keogh, 'Matrix profile XX: Finding and visualizing time series motifs of all lengths using the matrix profile', *Proceedings - 10th IEEE International Conference on Big Knowledge, ICBK 2019*, pp. 175–182, 2019.

[144] S. Omachi and M. Omachi, 'Fast template matching with polynomials', *IEEE TRANSACTIONS ON IMAGE PROCESSING*, vol. 16, no. 8, 2007.

[145] C. Won-Du and I. Chang-Hwan, 'Enhanced template matching using dynamic positional warping for identification of specific patterns in electroencephalogram', *Journal of Applied Mathematics*, vol. 2014, 2014.

[146] C. Jiun-Hung, C. Chu-Song and C. Yong-Sheng, 'Fast algorithm for robust template matching with m-estimators', *IEEE TRANSACTIONS ON SIGNAL PROCESSING*, vol. 51, no. 1, 2003.

[147] O. Shinichiro and O. Masako, 'Fast template matching with polynomials', *IEEE TRANSACTIONS ON IMAGE PROCESSING*, vol. 16, no. 8, 2007.

[148] F. Shaffer and J. P. Ginsberg, 'An overview of heart rate variability metrics and norms', *Front. Public Health*, vol. 5, 2017.

[149] U. Rajendra Acharya, K. Paul Joseph, N. Kannathal, C. M. Lim and J. S. Suri, 'Heart rate variability: A review', en, *Med. Biol. Eng. Comput.*, vol. 44, no. 12, pp. 1031–1051, 2006.

[150] M. Boyer, L. Bouyer, J.-S. Roy and A. Campeau-Lecours, 'Reducing noise, artifacts and interference in single-channel EMG signals: A review', en, *Sensors (Basel)*, vol. 23, no. 6, p. 2927, 2023.

[151] R. Martinek et al., 'Advanced bioelectrical signal processing methods: Past, present and future approach-part i: Cardiac signals', en, *Sensors (Basel)*, vol. 21, no. 15, p. 5186, 2021.

[152] A. E. Abouelregal, R. A. Alharb, M. Yaylacı, B. O. Mohamed and S. F. Megahid, 'Analysis of temperature changes in living tissue using the modified fractional thermal conduction model under laser heat flux on the skin surface', en, *Contin. Mech. Thermodyn.*, vol. 37, no. 1, 2025.

[153] J. Martel, N. Rouleau, N. J. Murugan, W.-C. Chin, D. M. Ojcius and J. D. Young, 'Effects of light, electromagnetic fields and water on biological rhythms', en, *Biomed. J.*, p. 100 824, 2024.

[154] J. Agrawal, M. Gupta and H. Garg, 'A review on speech separation in cocktail party environment: Challenges and approaches', en, *Multimed. Tools Appl.*, vol. 82, no. 20, pp. 31 035–31 067, 2023.

[155] R. Sharma and H. K. Meena, 'Emerging trends in EEG signal processing: A systematic review', en, *SN Comput. Sci.*, vol. 5, no. 4, 2024.

[156] N. Ille et al., 'Ongoing EEG artifact correction using blind source separation', en, *Clin. Neurophysiol.*, vol. 158, pp. 149–158, 2024.

[157] R. Nersisson and M. M. Noel, 'Heart sound and lung sound separation algorithms: A review', en, *J. Med. Eng. Technol.*, vol. 41, no. 1, pp. 13–21, 2017.

[158] B. D. Van Veen and K. M. Buckley, 'Beamforming: A versatile approach to spatial filtering', *IEEE ASSP Magazine*, vol. 5, no. 2, pp. 4–24, 1988.

[159] N. Madhu, 'Acoustic source localization: Algorithms, applications and extensions to source separation', Ph.D. dissertation, Ruhr-Universität Bochum, 2009.

[160] R. Ranta and N. Madhu, 'Reference estimation in EEG: Analysis of equivalent approaches', *IEEE Signal Processing Letters*, vol. 19, no. 1, pp. 12–15, 2012.

[161] A. Hyvärinen, E. Oja and J. Karhunen, 'Independent Component Analysis'. New York: John Wiley & Sons, 2001.

[162] A. Ivannikov, T. Kärkkäinen, T. Ristaniemi and H. Lyytinen, 'Spatially weighted averaging for ERP denoising in EEG data', in *Proc. Intl. Symp. Communication, Control, Signal Proc. (ISCCSP)*, 2010.

[163] J. V. Stone, 'Independent component analysis' (A Bradford Book), en. Cambridge, MA: Bradford Books, 2019.

[164] A. Hyvärinen, 'Independent component analysis: Recent advances', en, *Philos. Trans. A Math. Phys. Eng. Sci.*, vol. 371, no. 1984, p. 20 110 534, 2013.

[165] T. Tu et al., 'Towards conversational diagnostic AI', 2024.

[166] K. Saab et al., 'Advancing conversational diagnostic AI with multimodal reasoning', 2025.

[167] N. Jones, 'AI now beats humans at basic tasks - new benchmarks are needed, says major report', en, *Nature*, vol. 628, no. 8009, pp. 700–701, 2024.

[168] S. Domínguez-Almendros, N. Benítez-Parejo and A. R. Gonzalez-Ramirez, 'Logistic regression models', *Allergologia et Immunopathologia*, vol. 39, no. 5, pp. 295–305, 2011.

[169] T. Nick and K. Campbell, 'Logistic regression', *Discovering Statistics Using SPSS*, vol. 404, no. 4, pp. 731–735, 2012.

[170] P. C. Austin and E. W. Steyerberg, 'Interpreting the concordance statistic of a logistic regression model: Relation to the variance and odds ratio of a continuous explanatory variable', *BMC Medical Research Methodology*, vol. 12, pp. 1–8, 2012.

[171] N. Siddique, P. Sidike, C. Elkin and V. Devabhaktuni, 'U-Net and its variants for medical image segmentation: Theory and applications', *arXiv [eess.IV]*, 2020.

[172] W. Jiangtao, N. I. R. Ruhaiyem and F. Panpan, 'A comprehensive review of U-Net and its variants: Advances and applications in medical image segmentation', 2025.

[173] N. S. Punn and S. Agarwal, 'Modality specific U-Net variants for biomedical image segmentation: A survey', en, *Artif. Intell. Rev.*, vol. 55, no. 7, pp. 5845–5889, 2022.

[174] T. L. B. Khanh et al., 'Enhancing U-Net with spatial-channel attention gate for abnormal tissue segmentation in medical imaging', en, *Appl. Sci. (Basel)*, vol. 10, no. 17, p. 5729, 2020.

[175] O. Ronneberger, P.Fischer and T. Brox, 'U-net: Convolutional networks for biomedical image segmentation', in *Medical Image Computing and Computer-Assisted Intervention (MICCAI)*, ser. LNCS, (available on arXiv:1505.04597 [cs.CV]), vol. 9351, Springer, 2015, pp. 234–241.

[176] A. H. Reynolds, *Convolutional neural networks (cnns)*, Accessed: 2025-05-14, 2017.

[177] V. Dumoulin and F. Visin, 'A guide to convolution arithmetic for deep learning', 2016.

[178] J. S. Khan, M. Kaushik, A. Chaurasia, M. K. Dutta and R. Burget, 'Cardi-Net: A deep neural network for classification of cardiac disease using phonocardiogram signal', en, *Comput. Methods Programs Biomed.*, vol. 219, no. 106727, p. 106 727, 2022.

[179] S. A. Deevi, C. P. Kaniraja, V. D. Mani, D. Mishra, S. Ummar and C. Satheesh, 'HeartNetEC: A deep representation learning approach for ECG beat classification', en, *Biomed. Eng. Lett.*, vol. 11, no. 1, pp. 69–84, 2021.

[180] B. Subba Reddy, N. Dasari Ramesh Gari Amrutha, S. Sripathi, B. Surineni, N. Patel and S. Voriganti, 'CADNet: Cardiac arrhythmia detection and classification using unified principal component analysis and 1D-CNN model', en, *Res. Biomed. Eng.*, vol. 40, no. 2, pp. 317–329, 2024.

[181] S. Kiranyaz, M. Zabihi, A. B. Rad, T. Ince, R. Hamila and M. Gabbouj, 'Real-time phonocardiogram anomaly detection by adaptive 1D convolutional neural networks', en, *Neurocomputing*, vol. 411, pp. 291–301, 2020.

[182] G. F. Mitchell et al., 'Arterial stiffness, pressure and flow pulsatility and brain structure and function: The age, gene/environment susceptibility–reykjavik study.' eng, *Brain : a journal of neurology*, vol. 134, no. Pt 11, pp. 3398–3407, 2011.

[183] M. O'Rourke and R. Kelly, 'Wave reflection in the systemic circulation and its implications in ventricular-function', *Journal of Hypertension*, vol. 11, no. 4, pp. 327–337, 1993.

[184] T. Pereira, C. Correia and J. Cardoso, 'Novel methods for pulse wave velocity measurement', *Journal of medical and biological engineering*, vol. 35, no. 5, pp. 555–565, 2015.

[185] L. Scalise and U. Morbiducci, 'Non-contact cardiac monitoring from carotid artery using optical vibrocardiography', *Medical Engineering and Physics*, vol. 30, no. 4, pp. 490–497, 2008.

[186] U. Morbiducci, L. Scalise, M. De Melis and M. Grigioni, 'Optical vibrocardiography: A novel tool for the optical monitoring of cardiac activity', *Annals of biomedical engineering*, vol. 35, no. 1, pp. 45–58, 2007.

[187] K. Jensen-Urstad, N. Storck, F. Bouvier, M. Ericson and L. E. Lindblad, 'Heart rate variability in healthy subjects is related to age and gender', pp. 235–241, 1997.

[188] J. Zhang, 'EFFECT OF AGE AND SEX ON HEART RATE VARIABILITY IN HEALTHY SUBJECTS', pp. 374–379, 2007.

[189] M. Pinotti, N. Paone, F. A. Santos and E. P. Tomasini, 'Carotid artery pulse wave measured by a laser vibrometer', in *Third International Conference on Vibration Measurements by Laser Techniques: Advances and Applications*, International Society for Optics and Photonics, vol. 3411, 1998, pp. 611–616.

[190] J. W. Rohrbaugh, E. J. Sirevaag and E. J. Richter, 'Laser doppler vibrometry measurement of the mechanical myogram', *Review of Scientific Instruments*, vol. 84, no. 12, p. 121 706, 2013.

[191] Z. Zimmerman et al., 'Matrix profile XVIII: Time series mining in the face of fast moving streams using a learned approximate matrix profile', *Proceedings - IEEE International Conference on Data Mining, ICDM*, vol. 2019-November, pp. 936–945, 2019.

[192] R. Rockwell and L. Goldman, 'Research on human skin laser damage thresholds', eng, *Report DERM-LL-74-1003, USAF School of Aerospace Medicine, Brooks Air Force Base TX*, 1974.

[193] S. Beeckman et al., 'Enhancing multichannel laser-doppler vibrometry signals with application to (carotid-femoral) pulse transit time estimation', en, *Annu. Int. Conf. IEEE Eng. Med. Biol. Soc.*, vol. 2023, pp. 1–7, 2023.

[194] H. L. V. Trees, 'Detection, Estimation, and Modulation Theory. Part 4. Optimum Array Processing'. New York: John Wiley & Sons, 2002.

[195] P. Vary and R. Martin, 'Digital Speech Transmission'. New York: John Wiley & Sons, 2006.

[196] M. Ringnér, 'What is principal component analysis?', English, *Nature Biotechnology*, vol. 26, no. 3, pp. 303–304, 2008.

[197] R. M. Gray and L. D. Davisson, 'An Introduction to Statistical Signal Processing'. Cambridge University Press, 2004.

[198] D. Ventzas and N. Petrellis, 'Peak searching algorithms and applications', *Proceedings of the IASTED International Conference on Signal and Image Processing and Applications, SIPA 2011*, 2011.

[199] T. I. Laakso, V. Välimäki, M. Karjalainen and U. K. Laine, 'Splitting the unit delay - tools for fractional delay filter design', *IEEE Signal Processing Magazine*, vol. 13, no. 1, 1996.

[200] O. Vardoulis, T. G. Papaioannou and N. Stergiopulos, 'Validation of a novel and existing algorithms for the estimation of pulse transit time: Advancing the accuracy in pulse wave velocity measurement', en, *Am. J. Physiol. Heart Circ. Physiol.*, vol. 304, no. 11, H1558–67, 2013.

[201] P. Boutouyrie, M. Briet, C. Collin, S. Vermeersch and B. Pannier, 'Assessment of pulse wave velocity', en, *Artery Res.*, vol. 3, no. 1, p. 3, 2008.

[202] F. S. Hu et al., 'A region-matching method for pulse transit time estimation: Potential for improving the accuracy in determining carotid femoral pulse wave velocity', en, *J. Hum. Hypertens.*, vol. 29, no. 11, pp. 675–682, 2015.

[203] A. Valerio et al., 'A region-based cross-correlation approach for tonometric carotid–femoral pulse wave velocity assessment', en, *Biomed. Signal Process. Control*, vol. 93, no. 106161, p. 106 161, 2024.

[204] M. Butlin et al., 'Carotid-femoral pulse wave velocity assessment using novel cuff-based techniques: Comparison with tonometric measurement', en, *J. Hypertens.*, vol. 31, no. 11, 2237–43, discussion 2243, 2013.

[205] A. Milan et al., 'Current assessment of pulse wave velocity', en, *J. Hypertens.*, vol. 37, no. 8, pp. 1547–1557, 2019.

[206] O. Gu, B. He, L. Xiong, Y. Zhang, Z. Li and X. Lang, 'Reconstructive interpolation for pulse wave estimation to improve local pwv measurement of carotid artery', en, *Med. Biol. Eng. Comput.*, vol. 62, no. 5, pp. 1459–1473, 2024.

[207] L. Soukup et al., 'Comparison of noninvasive pulse transit time determined from doppler aortic flow and multichannel bioimpedance plethysmography', en, *Med. Biol. Eng. Comput.*, vol. 57, no. 5, pp. 1151–1158, 2019.

[208] M. Kozakova et al., 'The impact of age and risk factors on carotid and carotid-femoral pulse wave velocity', en, *J. Hypertens.*, vol. 33, no. 7, pp. 1446–1451, 2015.

[209] C. Tang, P. Lee, Y. Chuang and C. Huang, 'Measurement of local pulse wave velocity for carotid artery by using an ultrasound-based method', en, *Ultrasonics*, vol. 102, no. 106064, p. 106 064, 2020.

[210] A. L. Wentland, T. M. Grist and O. Wieben, 'Review of mri-based measurements of pulse wave velocity: A biomarker of arterial stiffness', en, *Cardiovasc. Diagn. Ther.*, vol. 4, no. 2, pp. 193–206, 2014.

[211] J. Mura et al., 'Non-invasive local pulse wave velocity using 4d-flow MRI', en, *Biomed. Signal Process. Control*, vol. 71, no. 103259, p. 103 259, 2022.

[212] U. Morbiducci, L. Scalise, M. D. Melis and M. Grigioni, 'Optical vibrocardiography: A novel tool for the optical monitoring of cardiac activity', *Annals Biomedical Engg.*, vol. 35, no. 1, pp. 45–58, 2007.

[213] Y. Chen, C. Wen, G. Tao, M. Bi and G. Li, 'Continuous and noninvasive blood pressure measurement: A novel modeling methodology of the relationship between blood pressure and pulse wave velocity', en, *Ann. Biomed. Eng.*, vol. 37, no. 11, pp. 2222–2233, 2009.

[214] B. Spronck et al., '2024 recommendations for validation of noninvasive arterial pulse wave velocity measurement devices', en, *Hypertension*, vol. 81, no. 1, pp. 183–192, 2024.

[215] M. A. Mansournia, R. Waters, M. Nazemipour, M. Bland and D. G. Altman, 'Bland-Altman methods for comparing methods of measurement and response to criticisms', en, *Glob. Epidemiol.*, vol. 3, no. 100045, p. 100 045, 2021.

[216] J. Martin B. and D. Altman, 'Statistical methods for assessing agreement between two methods of clinical measurement', en, *Lancet*, vol. 327, no. 8476, pp. 307–310, 1986.

[217] C. Julien, 'The enigma of mayer waves: Facts and models', en, *Cardiovasc. Res.*, vol. 70, no. 1, pp. 12–21, 2006.

[218] S. M. T. U. Raju et al., 'DNN-BP: A novel framework for cuffless blood pressure measurement from optimal PPG features using deep learning model', en, *Med. Biol. Eng. Comput.*, vol. 62, no. 12, pp. 3687–3708, 2024.

[219] S. Beeckman et al., 'Heart-carotid pulse-wave velocity via laser-doppler vibrometry as a biomarker for arterial stiffening: A feasibility study', *Physiol. Meas.*, 2025.

[220] K. H. Parker, 'A brief history of arterial wave mechanics', en, *Med. Biol. Eng. Comput.*, vol. 47, no. 2, pp. 111–118, 2009.

[221] J. Alastruey et al., 'Arterial pulse wave modeling and analysis for vascular-age studies: A review from VascAgeNet', en, *Am. J. Physiol. Heart Circ. Physiol.*, vol. 325, no. 1, H1–H29, 2023.

[222] P. Boutouyrie and R.-M. Bruno, 'The clinical significance and application of vascular stiffness measurements', en, *Am. J. Hypertens.*, vol. 32, no. 1, pp. 4–11, 2019.

[223] F. Faita, V. Gemignani, E. Bianchini, R. M. Bruno, T. Bombardini and L. Ghiadoni, 'P9.04 a new method for continuous monitoring of central arterial stiffness during stress', en, *Artery Res.*, vol. 3, no. 4, p. 167, 2009.

[224] R. Mukkamala et al., 'Toward ubiquitous blood pressure monitoring via pulse transit time: Theory and practice', *IEEE Transactions on Biomedical Engineering*, vol. 62, no. 8, pp. 1879–1901, 2015.

[225] C. Yang and N. Tavassolian, 'Pulse transit time measurement using seismocardiogram, photoplethysmogram, and acoustic recordings: Evaluation and comparison', *IEEE Journal of Biomedical and Health Informatics*, vol. 22, no. 3, pp. 733–740, 2018.

[226] R. S. Crow, P. Hannan, D. Jacobs, L. Hedquist and D. M. Salerno, 'Relationship between Seismocardiogram and Echocardiogram for Events in the Cardiac Cycle', *American Journal of Noninvasive Cardiology*, vol. 8, no. 1, pp. 39–46, 2017.

[227] P. Balali, J. Rabineau, A. Hossein, C. Tordeur, O. Debeir and P. van de Borne, 'Investigating cardiorespiratory interaction using ballistocardiography and seismocardiography-a narrative review', en, *Sensors (Basel)*, vol. 22, no. 23, p. 9565, 2022.

[228] N. Di Lascio et al., 'Non-invasive assessment of carotid PWV via accelerometric sensors: Validation of a new device and comparison with established techniques', en, *Eur. J. Appl. Physiol.*, vol. 114, no. 7, pp. 1503–1512, 2014.

[229] H. Park, Q. Wei, S. Lee and M. Lee, 'Novel design of a multimodal technology-based smart stethoscope for personal cardiovascular health monitoring', en, *Sensors (Basel)*, vol. 22, no. 17, p. 6465, 2022.

[230] V. Mancini et al., 'Detecting carotid stenosis from skin vibrations using laser doppler vibrometry - an in vitro proof-of-concept', en, *PLoS One*, vol. 14, no. 6, e0218317, 2019.

[231] D. Giavarina, 'Understanding bland altman analysis', en, *Biochem. Med. (Zagreb)*, vol. 25, no. 2, pp. 141–151, 2015.

[232] T. Nagasaki et al., 'Clinical utility of heart-carotid pulse wave velocity in healthy japanese subjects', en, *Biomed. Aging Pathol.*, vol. 1, no. 2, pp. 107–111, 2011.

[233] C. Li et al., 'Heart-carotid pulse wave velocity a useful index of atherosclerosis in chinese hypertensive patients', en, *Medicine (Baltimore)*, vol. 94, no. 51, e2343, 2015.

[234] Y. Yang et al., 'Stiffening of aorta is more preferentially associated with rheumatoid arthritis than peripheral arteries', en, *Rheumatol. Int.*, vol. 39, no. 10, pp. 1711–1721, 2019.

[235] K. Ejiri et al., 'Association of segment-specific pulse wave velocity with vascular calcification: The ARIC (atherosclerosis risk in communities) study', en, *J. Am. Heart Assoc.*, vol. 13, no. 2, e031778, 2024.

[236] J. Yao, S. Tridandapani, W. F. Auffermann, C. A. Wick and P. T. Bhatti, 'An adaptive seismocardiography (SCG)-ECG multimodal framework for cardiac gating using artificial neural networks', en, *IEEE J. Transl. Eng. Health Med.*, vol. 6, p. 1 900 611, 2018.

[237] M. Nikbakht et al., 'Synthetic seismocardiogram generation using a transformer-based neural network', en, *J. Am. Med. Inform. Assoc.*, vol. 30, no. 7, pp. 1266–1273, 2023.

[238] B. Pourbabaee, M. J. Roshtkhari and K. Khorasani, 'Deep convolutional neural networks and learning ECG features for screening paroxysmal atrial fibrillation patients', *IEEE Trans. Syst. Man Cybern. Syst.*, vol. 48, no. 12, pp. 2095–2104, 2018.

[239] U. R. Acharya, H. Fujita, S. L. Oh, Y. Hagiwara, J. H. Tan and M. Adam, 'Application of deep convolutional neural network for automated detection of myocardial infarction using ECG signals', en, *Inf. Sci. (Ny)*, vol. 415-416, pp. 190–198, 2017.

[240] S. Rajwal and S. Aggarwal, 'Convolutional neural network-based EEG signal analysis: A systematic review', en, *Arch. Comput. Methods Eng.*, 2023.

[241] Y. Zheng, C. Wu, P. Cai, Z. Zhong, H. Huang and Y. Jiang, 'TinyPPG: A lightweight deep neural network for real-time detection of motion artifacts in photoplethysmogram signals on edge devices', en, *Internet of Things*, vol. 25, no. 101007, p. 101 007, 2024.

[242] A. Habib, M. A. Motin, T. Penzel, M. Palaniswami, J. Yearwood and C. Karmakar, 'Performance of a convolutional neural network derived from PPG signal in classifying sleep stages', en, *IEEE Trans. Biomed. Eng.*, vol. 70, no. 6, pp. 1717–1728, 2023.

[243] O. Faust, Y. Hagiwara, T. J. Hong, O. S. Lih and U. R. Acharya, 'Deep learning for healthcare applications based on physiological signals: A review', en, *Comput. Methods Programs Biomed.*, vol. 161, pp. 1–13, 2018.

[244] B. Bozkurt, I. Germanakis and Y. Stylianou, 'A study of time-frequency features for CNN-based automatic heart sound classification for pathology detection', en, *Comput. Biol. Med.*, vol. 100, pp. 132–143, 2018.

[245] A. Meintjes, A. Lowe and M. Legget, 'Fundamental heart sound classification using the continuous wavelet transform and convolutional neural networks', in *2018 40th annual international conference of the IEEE engineering in medicine and biology society (EMBC)*, IEEE, 2018, pp. 409–412.

[246] P. Suresh, N. Narayanan, C. V. Pranav and V. Vijayaraghavan, 'End-to-end deep learning for reliable cardiac activity monitoring using seismocardiograms', in *2020 19th IEEE International Conference on Machine Learning and Applications (ICMLA)*, Miami, FL, USA: IEEE, 2020.

[247] M. Haescher, F. Hopfner, W. Chodan, D. Kraft, M. Aehnelt and B. Urban, 'Transforming seismocardiograms into electrocardiograms by applying convolutional autoencoders', in *ICASSP 2020 - 2020 IEEE International Conference on Acoustics, Speech and Signal Processing (ICASSP)*, Barcelona, Spain: IEEE, 2020.

[248] A. S. Alhakak et al., 'Changes in cardiac time intervals over a decade and the risk of incident heart failure: The copenhagen city heart study', en, *Int. J. Cardiol.*, vol. 386, pp. 141–148, 2023.

[249] T. Biering-Sørensen, R. Mogelvang, M. C. de Knegt, F. J. Olsen, S. Galatius and J. S. Jensen, 'Cardiac time intervals by tissue doppler imaging m-mode: Normal values and association with established echocardiographic and invasive measures of systolic and diastolic function', en, *PLoS One*, vol. 11, no. 4, e0153636, 2016.

[250] O. Petit, N. Thome, C. Rambour, L. Themyr, T. Collins and L. Soler, 'U-Net transformer: Self and cross attention for medical image segmentation', in *Machine Learning in Medical Imaging*, ser. Lecture notes in computer science, Cham: Springer International Publishing, 2021, pp. 267–276.

[251] V. Mancini, A. W. Bergersen, J. Vierendeels, P. Segers and K. Valen-Sendstad, 'High-frequency fluctuations in post-stenotic patient specific carotid stenosis fluid dynamics: A computational fluid dynamics strategy study', en, *Cardiovasc. Eng. Technol.*, vol. 10, no. 2, pp. 277–298, 2019.

[252] J. Park, H. S. Seok, S.-S. Kim and H. Shin, 'Photoplethysmogram analysis and applications: An integrative review', en, *Front. Physiol.*, vol. 12, p. 808 451, 2021.

[253] B. W. Nelson and N. B. Allen, 'Accuracy of consumer wearable heart rate measurement during an ecologically valid 24-hour period: Intraindividual validation study', en, *JMIR MHealth UHealth*, vol. 7, no. 3, e10828, 2019.

[254] M. Hallab et al., 'Rigidité artérielle mesurée par popmètre® chez les patients à risque cardiovasculaire, lien aux plaques d'athérome carotidien', fr, *Ann. Cardiol. Angeiol. (Paris)*, vol. 62, no. 3, pp. 189–192, 2013.

[255] M. Hallab, S. Pichierri, J.-M. Boin, M. Tramblay, P. Chevalet and G. Berrut, 'Un nouvel index pour évaluer le vieillissement artériel indépendamment de la pression artérielle : Popscore®', fr, *Ann. Cardiol. Angeiol. (Paris)*, vol. 61, no. 3, pp. 184–187, 2012.

[256] H. Obeid, H. Khettab, P. Boutouyrie, S. Laurent and M. Hallab, '10.5 comparison of arterial stiffness assessed by popmètre® with arterial stiffness assessed by applanation tonometry: A clinical study', en, *Artery Res.*, vol. 16, no. C, p. 72, 2016.

[257] H. Obeid, H. Khettab, M. Hallab, P. Boutouyrie and S. Laurent, 'CO-25: Evaluation of different methods for determining the time delay of the arterial pulse wave: Application to the popmetre ®', *Ann. Cardiol. Angeiol. (Paris)*, vol. 64, S12–S13, 2015.

[258] A. Taebi, B. E. Solar, A. J. Bomar, R. H. Sandler and H. A. Mansy, 'Recent advances in seismocardiography', en, *Vibration*, vol. 2, no. 1, pp. 64–86, 2019.

[259] M. Deng et al., 'Flexible adaptive sensing tonometry for medical-grade multi-parametric hemodynamic monitoring', en, *Npj Flex. Electron.*, vol. 8, no. 1, 2024.

[260] J. Li et al., 'Thin, soft, wearable system for continuous wireless monitoring of artery blood pressure', en, *Nat. Commun.*, vol. 14, no. 1, p. 5009, 2023.

[261] H. Hu et al., 'A wearable cardiac ultrasound imager', en, *Nature*, vol. 613, no. 7945, pp. 667–675, 2023.

[262] M. Lin et al., 'A fully integrated wearable ultrasound system to monitor deep tissues in moving subjects', en, *Nat. Biotechnol.*, vol. 42, no. 3, pp. 448–457, 2024.

[263] C. Wang et al., 'Monitoring of the central blood pressure waveform via a conformal ultrasonic device', en, *Nat. Biomed. Eng.*, vol. 2, no. 9, pp. 687–695, 2018.

[264] S. R. Collier et al., 'Withings body cardio versus gold standards of pulse-wave velocity and body composition', en, *J. Pers. Med.*, vol. 10, no. 1, p. 17, 2020.

[265] M. Butlin, F. Shirbani, E. Barin, I. Tan, B. Spronck and A. P. Avolio, 'Cuffless estimation of blood pressure: Importance of variability in blood pressure dependence of arterial stiffness across individuals and measurement sites', *IEEE Transactions on Biomedical Engineering*, vol. 65, no. 11, pp. 2377–2383, 2018.